RADIO ASTRONOMY

SARA 2023 Annual Eastern Conference
and
Global Symposium on Amateur Radio Astronomy

It is the mission of the Society of Amateur Radio Astronomers (SARA) to: Facilitate the flow of information pertinent to the field of Radio Astronomy among our members; Promote members to mentor newcomers to our hobby and share the excitement of radio astronomy with other interested persons and organizations; Promote individual and multi station observing programs; Encourage programs that enhance the technical abilities of our members to monitor cosmic radio signals, as well as to share and analyze such signals; Encourage educational programs within SARA and educational outreach initiatives. Founded in 1981, the Society of Amateur Radio Astronomers, Inc. is a membership supported, non-profit [501(c) (3)], educational and scientific corporation.

Cover Photo:
Various SARA Members and GBO Staff

Contents

Congratulations to Jay Wilson
for a fantastic Eastern Conference!

Jay took on organizing the first live Eastern Conference since 2019. It also included a fantastic hybrid live /zoom format that worked great. Thanks to Ted Cline and Charles Osborne for moderating the online sessions and Chip Csufitchi for managing the technical setup.

Congratulate the new officers and Board members:

Treasurer: Tom Jacobs (appointed and approved by the board)
Assistant Treasurer: Donna Hallin (appointed and approved by the board)
Board: Paul Butler
Board: Dr. Wolfgang Herrmann (reelected)
Board: Ted Cline
Board: Charles Osborne (reelected)

Education Co-chairs: Ken Redcap and Tom Hagen (appointed and approved by the board)

Thanks to Tom Jacobs for serving on the board and then volunteering for the treasurer position.

Special thanks to outgoing treasurer, Brian O'Rourke. He did a fantastic job at the hardest position in the SARA organization.

Also, to our long-term Education Chair, Jon Wallace, who has been serving in that position for almost 20 years!

SARA is run by fantastic volunteers! Let me know if you would like to join the administrative side of the organization.

Thanks!
Rich
SARA President

Editor's Notes

We are always looking for basic radio astronomy articles, radio astronomy tutorials, theoretical articles, application and construction articles, news pertinent to radio astronomy, profiles and interviews with amateur and professional radio astronomers, book reviews, puzzles (including word challenges, riddles, and crossword puzzles), anecdotes, expository on "bad astronomy," articles on radio astronomy observations, suggestions for reprint of articles from past journals, book reviews and other publications, and announcements of radio astronomy star parties, meetings, and outreach activities.

Subscribe to the SARA YouTube Channel

SARA has a YouTube channel at: https://www.youtube.com/channel/UC-SzptAQZ-20c9CkRb9ZPxw/videos

We are also looking to add content to the site. Anyone who wants to help produce a series of 5 - minute videos relating to radio astronomy technology or observations please contact me. (drrichrussel@netscape.net)
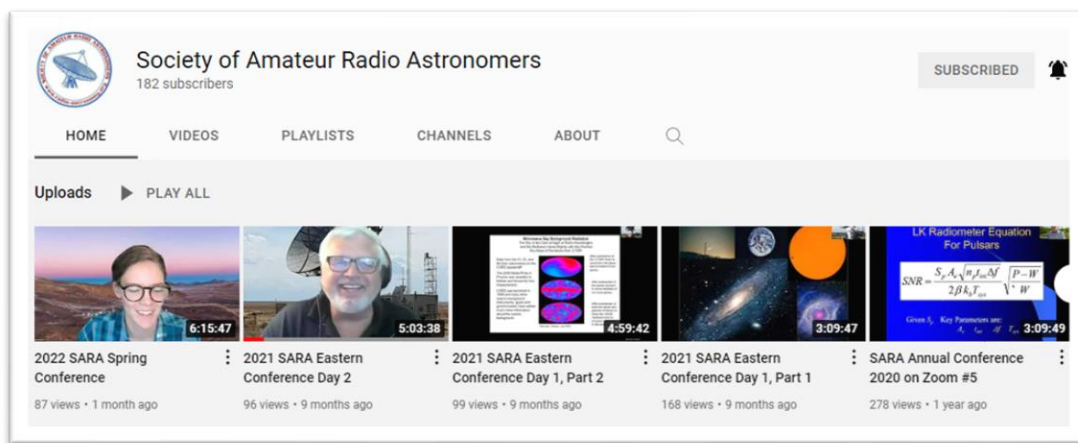
Observation Reports

We are now accepting 1-2 page observation reports. These reports should include the astronomical object's RA/DEC plus UTC of the observation. Also include the telescope configuration, process used to observe the object and results. Picture of the setup and plots of the observation are a plus to the report.

If you would like to write an article for Radio Astronomy, please follow **the newly updated Author's Guide** on the SARA web site:
 http://www.radio-astronomy.org/publicat/RA-JSARA_Author's_Guide.pdf.

Let us know if you have questions; we are glad to assist authors with their articles and papers and will not hesitate to work with you. You may contact your editors any time via email here: edit@radio-astronomy.org.

The editor(s) will acknowledge that they have received your submission within two days. If they do not reply, assume they did not receive it and please try again.

Please consider submitting your radio astronomy observations for publication: any object, any wavelength. Strip charts, spectrograms, magnetograms, meteor scatter records, space radar records, photographs; examples of radio frequency interference (RFI) are also welcome.
Guidelines for submitting observations may be found here: http://www.radio-astronomy.org/publicat/RA-JSARA_Observation_Submission_Guide.pdf

2024 SARA Western Conference
Dallas, Texas, USA on 8 and 9 April 2024

The 2024 SARA Western Conference will be held at Dallas, Texas at the University of Texas campus on Monday and Tuesday, 8 and 9 April 2024.   A total solar eclipse will be visible from the Dallas area on the afternoon of April 8, and observation of the eclipse will be a main event of the conference.
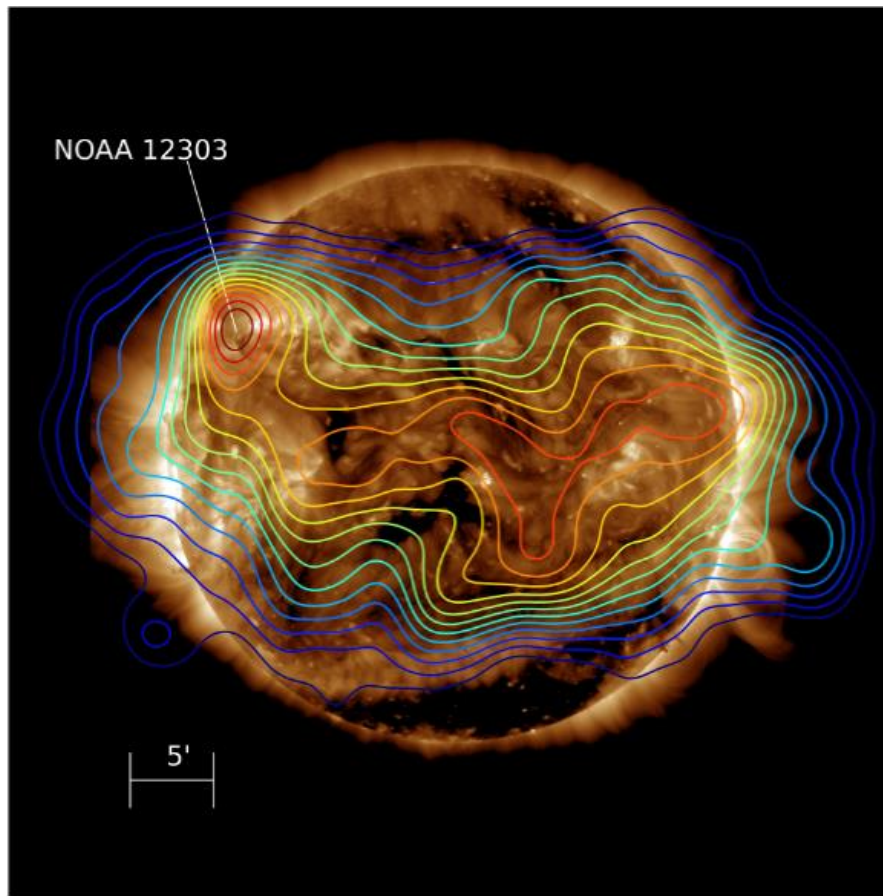
2015 Solar Eclipse LOFAR contours: LOFAR contours 50-95% (blue to red) of the peak intensity on top of a Solar Dynamics Observatory/Atmospheric Imaging Assembly 193 Å image. The contours are from a multifrequency LOFAR map (140-160 MHz) and the 193 Å EUV image is from 11:05 UT, during 2015 March 20 partial solar eclipse in Europe, 80% totality.

Call for papers: Papers are welcome on subjects directly related to radio astronomy including hardware, software, education and tutorials, research strategies, observations and data collection and philosophy. If you wish to present a paper please email a letter of intent, including a proposed title and abstract to the conference coordinator at westernconf@radio-astronomy.org no later than 1 February 2024.

Be sure to include your full name, affiliation, postal address, and email address, and indicate your willingness to attend the conference either in person or virtually to present your paper. Submitters will receive an email response, typically within one week. Final advance presentations should be submitted to the Western Conference coordinator for inclusion in the proceedings no later than March 15, 2024. Due to the work required to prepare the proceedings, this should be considered a hard deadline.

Presentations and proceedings: In addition to presentations by SARA members, we will have a keynote speech by Dr. Lindsay King of the University of Texas Physics and Astronomy Dept., who will be hosting the conference. They have arranged a National Science Foundation grant to support it.

Basic schedule: The conference will be entirely held on the University of Texas Dallas campus.   Virtual attendance at the conference using Zoom will be possible at a reduced rate for those who cannot attend in person.

Contact: Please contact conference coordinator David Westman if you have any questions or if you would like to help with the conference: westernconf@radio-astronomy.org.

Getting there: Many major airlines have flights to Dallas/Ft. Worth International Airport.

Registration: Registration for in person attendance at the 2024 Western Conference is just US$75.00. The reduced rate to attend the conference online using Zoom is $15. You must be a SARA member to register for the conference. The in-person conference rate will include lunch at the conference site on Monday and Tuesday. Payment can be made through PayPal, www.paypal.com by sending payment to treas@radio-astronomy.org.   If you need to send a check for registration, please send it to:

   SARA Treasurer
    c/o Thomas Jacobs
    P. O. Box 4245
    Wilmington, NC 28406.
Please include in comments that the payment is for the **2024 Western Regional Conference**.

Hotel reservations: Further work on hotel reservations is being done at this time.   New arrangements will be posted soon (we hope!)

Monday night dinner: We will make a group dinner reservation at a local restaurant for Monday night.

Additional Information: Additional details will be published online at www.radio-astronomy.org and in the SARA journal, *Radio Astronomy*, as we get closer to the conference date.

SARA Student & Teacher Grant Program

All, SARA has a grant program that is, sad to say, very underutilized. We will provide kits or money to students and teachers including college students to help them with a radio telescope project. SARA can supply any of the following kits:

[1] SuperSID
[2] Scope in a Box
[3] IBT (Itty Bitty Telescope)
[4] Radio Jove kit
[5] Inspire
[6] Sky Scan

We can also provide up to five hundred dollars ($500.00 USD) for an approved radio telescope project.

We have on occasion provided more money based on the merits of the project and the SARA Grant Committee approval.

More information on the grant program can be found at the URL below.
SARA Student and Teacher Project Grants | Society of Amateur Radio Astronomers (radio-astronomy.org)

All that is required is the SARA grant request form be filled out and sent in. If it needs more work for approval, we will work with the students to help ensure their success.

Please pass the word that SARA will fund any legitimate radio telescope project anywhere in the world.

If you have a question, contact me at crowleytj at hotmail dot com.
Tom Crowley - SARA Grant Program Administrator

NEW Drake's Lounge Australia

This new zoom forum is geared to the Melbourne, Australia time zone (UTC+10) in order to improve coordination with our Australia, New Zealand, and Japanese members. The meetings are scheduled for the 4rth Friday of every month, 9 AM Melbourne time (2000 UTC December 23). A zoom announcement will be sent out to all SARA members before the meeting.

Radio Telescope Observation Party (RTOP)

RTOP is designed to demonstrate how to take observations using various radio telescopes. It will also cover how to record and analyze data.

RTOP is every month on the 1st Sunday at 2 pm Eastern time (1800 UTC). ZOOM email notifications will be sent to all members.

Drake's Lounge

Join the SARA community as we discuss the latest astronomy and radio astronomy news. The lounge also provides a forum to share and get advice on your radio astronomy projects from very experienced amateur radio astronomers.

Drake's Lounge is every month on the 3rd Sunday at 2 pm Eastern time (1800 UTC). ZOOM email notifications will be sent to all members.

Vintage SARA

CHARLES OSBORNE, SARA HISTORIAN
Pisgah Astronomical Research Institute at 60

I ran across the meeting group shot on the following page and thought today's SARA members would enjoy this look into SARA member involvement at PARI twenty-two years ago. It was an Astronomy in Education professional meeting at PARI on August 11th 2001.

I'm in the green striped shirt on left side beside Don Cline. Paul Shuch N6TX is in the blue SETI League shirt. Behind Paul is David Fields N4HBO (Roane State). Beside him is SARA's Founder Jeff Lichtman KI4GIY. Beside him is Carl Lyster WA4ADG. The SARA Journal Editor at the time John Manone is second from right. On back row in middle in red shirt is SARA member John Bernard W4JSS (Clemson). SARA member Ben Malphrus (Morehead State Univ).

Several of the RadioJOVE team are on the back row. Third from right is Jim Thieman. Sixth from right is Chuck Higgins (Middle Tennessee State University). Probably others I missed.

Most of the other people in this picture are Astronomy or Physics Professors from: Clemson, Furman, UNC Chapel Hill, Roan State University, Morehead State University, Appalachian State University, Middle Tennessee State University, Arecibo, and others.

The girl beside Paul Shuch is Mercedes Lopez-Morales who was PARI's first remote astronomy student working on her PHD. I was her remote hands if something went wrong with an observation and things needed to be rebooted or investigated to be sure it was safe to continue with the observation. Today she is Deputy Associate Director of Science at the Harvard Smithsonian Center for Astrophysics and has been there for 11 years. Prior to that she was at the Space Telescope Science Institute.

In the green shirt on far left is Dr David Moffett of Furman University. He was one of the key professors doing early Pulsar work at PARI. Today he is the Physics Department head at Furman. While getting his PHD he was at a sister observatory in Tasmania using a near duplicate 85foot dish to the one at PARI. Originally both dishes were part of the worldwide NASA Satellite Tracking and Data Network (STDN) used during the Apollo program.

It's notable that October 28th is the 60th anniversary of the opening of the NASA Rosman Research Station which would eventually become the Pisgah Astronomical Research Institute 25 years ago. Saturday Oct.28th will be an Open House Celebration of this. www.pari.edu

The lady behind Don Cline and Ben Malphrus is Dr Carmen Pantoja (Univ. Puerta Rica). She'll figure prominently in helping to get SARA access to have a regional meeting at Arecibo Observatory starting not long after this picture was taken.

David Szondy ~ Neutron images reveal zinc as culprit in Arecibo radio telescope collapse

https://newatlas.com/space/neutron-images-find-zinc-culprit-arecibo-radio-telescope-collapse/

https://www.thorntontomasetti.com/news/arecibo-collapse-forensic-report-released

https://www.ornl.gov/news/neutrons-prove-bond-villain-did-not-cause-arecibo-telescope-collapse
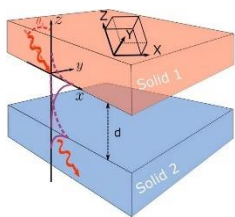
University of Jyväskylä ~ Physicists demonstrate how sound can be transmitted through vacuum

https://phys.org/news/2023-08-physicists-transmitted-vacuum.html

https://dx.doi.org/10.1038/s42005-023-01293-y

Andy Tomaswick ~ A New Paper Shows How to Change an Asteroid into A Space Habitat – In Just 12 Years

https://www.universetoday.com/162697/a-new-paper-shows-how-to-change-an-asteroid-into-a-space-habitat-in-just-12-years/

David W. Jensen, "Autonomous Restructuring of Asteroids into Rotating Space Stations", February 2023, https://arxiv.org/ftp/arxiv/papers/2302/2302.12353.pdf

Tereza Pultarova ~ Powerful sun storm knocks out radio transmissions across North America

https://www.space.com/x-class-solar-flare-radio-blackout-august-2023
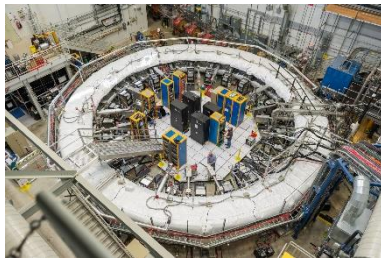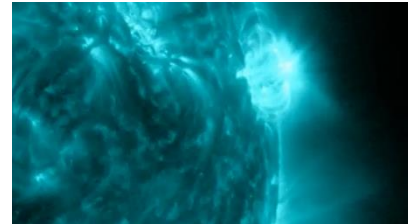
Tracy Marc ~ Muon g-2 doubles down with latest measurement, explores uncharted territory in search of new physics

https://news.fnal.gov/2023/08/muon-g-2-doubles-down-with-latest-measurement/

https://muon-g-2.fnal.gov/result2023.pdf

Astronomy(.com) Staff ~ Where is the center of the universe?

https://www.astronomy.com/science/ask-astro-where-is-the-center-of-the-universe/
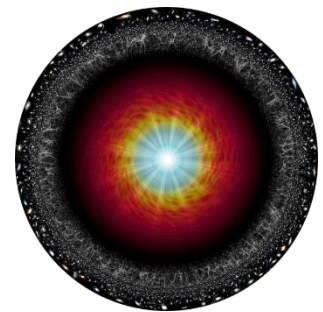
Mark Zastrow ~ Predictions for the next 50 years of astronomy

https://www.astronomy.com/science/the-next-50-years-of-astronomy/

Sejong University ~ Smoking-gun evidence for modified gravity at low acceleration from Gaia observations of wide binary stars

https://phys.org/news/2023-08-smoking-gun-evidence-gravity-gaia-wide.html

https://dx.doi.org/10.3847/1538-4357/ace101
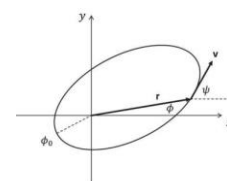
orbital plane
(face-on view)
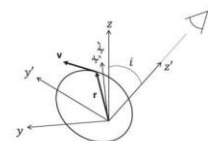
observer's view
(3D geometry)

Robert Lea ~ Our Milky Way galaxy was not always a spiral. Here's how it changed shape

https://www.space.com/galaxy-shape-shifting-milky-way-mystery-solved

https://academic.oup.com/mnras/article/522/3/3588/7152347

Ethan Siegel ~ New JWST data confirms, worsens the Hubble tension

https://bigthink.com/starts-with-a-bang/jwst-confirms-worsens-hubble-tension/

University of Birmingham ~ New Exoplanet Discovery Challenges Established Astronomical Theories

https://scitechdaily.com/new-exoplanet-discovery-challenges-established-astronomical-theories/

https://doi.org/10.1093/mnrasl/slad097

University of Ottawa ~ Visualizing the mysterious dance: Quantum entanglement of photons captured in real-time

https://phys.org/news/2023-08-visualizing-mysterious-quantum-entanglement-photons.html

https://dx.doi.org/10.1038/s41566-023-01272-3
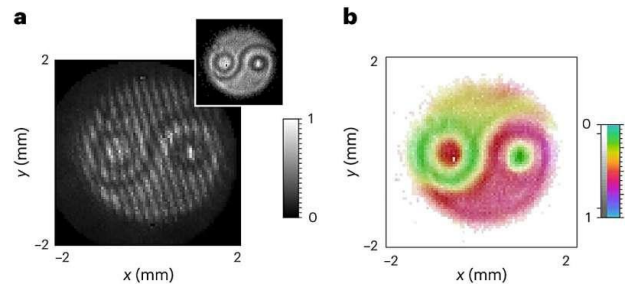
Stevens Institute of Technology ~ Physicists use a 350-year-old theorem to reveal new properties of light waves

https://phys.org/news/2023-08-physicists-year-old-theorem-reveal-properties.html

https://dx.doi.org/10.1103/PhysRevResearch.5.033110
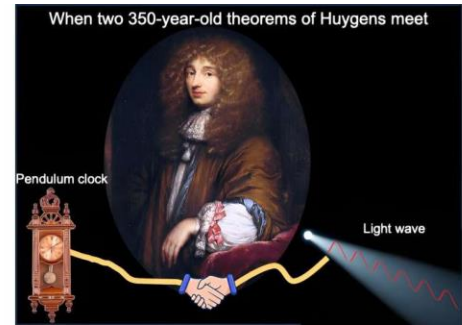
Dr Alfredo Carpineti ~ Quantum Entanglement Waves Detected for The First Time

https://www.iflscience.com/quantum-entanglement-waves-detected-for-the-first-time-70410

https://journals.aps.org/prl/abstract/10.1103/PhysRevLett.131.086701
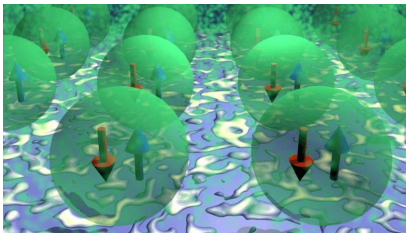
Ethan Siegel ~ Is there a 5th fundamental force of nature?

https://bigthink.com/starts-with-a-bang/5th-fundamental-force/
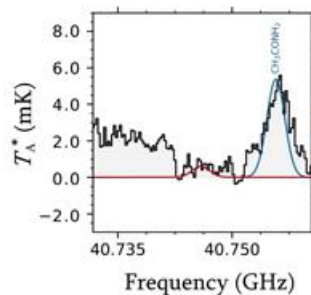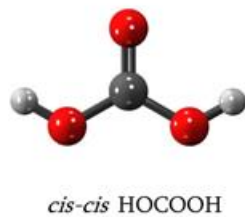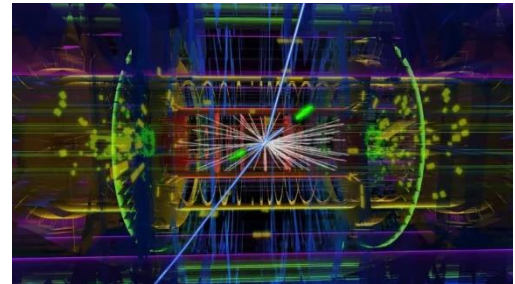
Miguel Sanz Novo, Et. Al ~ Discovery of the Elusive Carbonic Acid (HOCOOH) in Space

https://iopscience.iop.org/article/10.3847/1538-4357/ace523

Paul Scott Anderson ~ Are the TRAPPIST-1 exoplanets habitable, or not?

https://earthsky.org/space/trappist-1-exoplanets-habitability/

https://www.nature.com/articles/s41586-023-06258-3

Li Yuan ~ Researchers develop oversampled channelization technology for radio astronomy wideband digital signal

https://phys.org/news/2023-08-oversampled-channelization-technology-radio-astronomy.html

https://dx.doi.org/10.1088/1674-4527/acd73b

Andy Tomaswick ~ Floating Seismometers Could Help Peer into The Core of Venus

https://www.universetoday.com/162854/floating-seismometers-could-help-peer-into-the-core-of-venus/

https://agupubs.onlinelibrary.wiley.com/doi/pdf/10.1029/2022GL100978

David L. Chandler ~ Could the Universe be a giant quantum computer?

https://www.nature.com/articles/d41586-023-02646-x

Technical Knowledge and Education: (September-October 2023)

Julian Barbour – The Janus Point: A New Theory of Time

https://www.science.org/doi/10.1126/science.abf2440

https://www.amazon.com/Janus-Point-New-Theory-Time/dp/0465095461
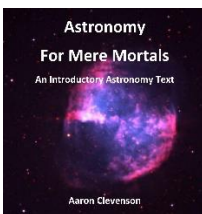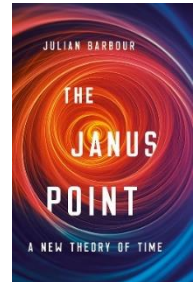
Aaron Clemson ~ Astronomy for Mere Mortals – An Introductory Astronomy Text

Astronomy for Mere Mortals: a complete introductory textbook, available free, updated annually. You may print it, or if you would like a printed copy, please contact the author, Aaron Clevenson, at aaron@clevenson.org

Published by the Astronomical League, https://www.astroleague.org/navigating-the-night-sky-guides/
https://www.astroleague.org/wp-content/uploads/2023/09/Astronomy-For-Mere-Mortals-v-23.pdf

SARA ~ ezRA – Easy Radio Astronomy Analysis Tutorials:
- *Simple Overview: https://youtu.be/sgid9zn9KkY*
- *Analysis 1- Introduction and Data Collectors*: https://youtu.be/ig_jPTuS8ZA
- *Analysis 2- Spreadsheet Analysis*: https://youtu.be/HkrIN9d6Hd8
- *Analysis 3- Signal Progression*: https://youtu.be/VIp7L6gIZPY
- *Analysis 4- More Plots and ezb file*: https://youtu.be/K02MADafOhc
- *Analysis 5- Interference Filters*: https://youtu.be/FeFk9EvITtc

- ✿ *Analysis 6- ezSky*: https://youtu.be/UNwS0f9X7kE
- ✿ *Analysis 7- AntXTVT and VLSR* : https://youtu.be/0ezig90GNBc
- ✿ *Analysis 8- ezGal*: https://youtu.be/i0St2X7ODKM

SARA ~ *Radio Astronomy Video Series: Constants, Variables and Formulas, Radio Astronomy Formulas:*
- ✿ *Introduction to Radio Astronomy: https://youtu.be/AOgvjRXnins*
- ✿ *Lesson 1- Parabolic Dish Gain*: https://www.youtube.com/watch?v=2bx5K9jUc_w
- ✿ *Lesson 2 -Parabolic Dish Half Power Beamwidth*: https://www.youtube.com/watch?v=XWOMRrwjkl8
- ✿ *Lesson 3 -Thermal Noise*: https://youtu.be/MMJ6Xvapt10
- ✿ *Lesson 4 -Focal Length and f/D*: https://youtu.be/Am6t06KqFPE
- ✿ *Lesson 5 -Feed Illumination Angle*: https://youtu.be/4RZzPzVBSJ4
- ✿ *Lesson 6 -Pointing Offset Gain Loss*: https://youtu.be/dQ8wAaTtm40
- ✿ *Lesson 7 -Measuring System Temperature (TSys)*: https://youtu.be/4gVUFFxra-U
- ✿ *Lesson 8 -Coax Attenuation Interpolation*: https://youtu.be/3B8hV6vFyo8
- ✿ *Lesson 9 -Pulsar math including electron density, distance, and age*: https://youtu.be/Bymdp--_3JU
- ✿ *Lesson 10 -Distance Math - AU, Parallax, Parsecs and Light Years*: https://youtu.be/6fo0y3fDOZs
- ✿ *Lesson 11 -Doppler Frequency and Relative Velocity Calculations*: https://youtu.be/8zKloAVpnJc
- ✿ *Lesson 12 -Pointing to the Milky Way using a Compass and Protractor*: https://youtu.be/33xeUSji94U
- ✿ *Lesson 13 -Radiometer Equation Basics*: https://youtu.be/vAyypJ8f2z8
- ✿ *Lesson 14 -Noise Figure and Noise Factor Calculations*: https://youtu.be/GD6wZhW5NPA
- ✿ *Lesson 15 -Interpreting Stokes Parameters*: https://youtu.be/wUVsbfURIsg
- ✿ *Lesson 16 -Velocity Factor, Speed of Light in a Coax Cable: https://youtu.be/WWuqRyb4Ad8*
- ✿ *Lesson 17 -Interferometry Fringe Spacing: https://youtu.be/rYhUKFn7IWg*

National Radio Astronomy Observatory ~ 39ᵗʰ Annual New Mexico Symposium

https://web.cvent.com/event/73aa6b1b-b349-407a-a0dc-9302e0c3639c/summary

Dark skies and remote sites have attracted world-class astronomical facilities to the Southwest and supported a wide range of research since the mid-1900s. Regional achievements span areas in both science and technology including optical and radio interferometry, as well as new understanding of solar physics, planetary science, star and galaxy formation and evolution, and the creation and evolution of our universe. To support the network of scientific research in the Southwest and encourage interdisciplinary discussions, the National Radio Astronomy Observatory (NRAO) is sponsoring the 39th Annual New Mexico Symposium on Friday, 17 November 2023.

Date and Location: The Symposium will be held in-person on Friday, 17 November 2023, at the NRAO Domenici Science Operations Center, and will be streamed online. We anticipate to fill the symposium day with presentations from 8:30am to 5:00pm MST, including poster sessions.

Symposium Dinner: NRAO will be hosting a post-meeting dinner, starting with pre-dinner drinks at 5:30pm MST. The dinner will be held at the Macey Center from 6pm MST. The dinner event will be free to officially registered symposium participants.

Jansky Lecture: The 58th annual Karl G. Jansky Lecture will be presented by Dr. Paul Vanden Bout from the NRAO on "Millimeter Astronomy at NRAO - Some Personal Reminiscences". The public lecture is free to attend by any member of the public and will be held at the Macey Center on the NMT campus in Socorro, starting at 7pm MST. A reception will follow the lecture.

Code of Conduct: The National Radio Astronomy Observatory is committed to providing a safe and welcoming environment for our employees, visitors, and guests, and has adopted a Code of Conduct that includes prohibitions against discrimination and harassment of any kind, including sexual harassment. Learn more at http://go.nrao.edu/conduct.

Register: https://web.cvent.com/event/73aa6b1b-b349-407a-a0dc-9302e0c3639c/summary

Contact: Lori Appel (lappel@nrao.edu)

SARA 2023 Annual Eastern Conference
and
Global Symposium on Amateur Radio Astronomy

Lectures

Tour

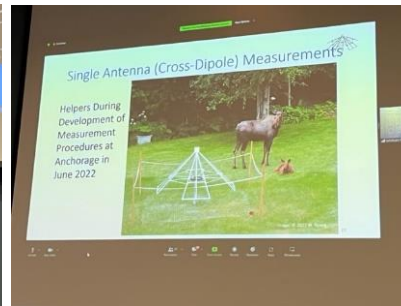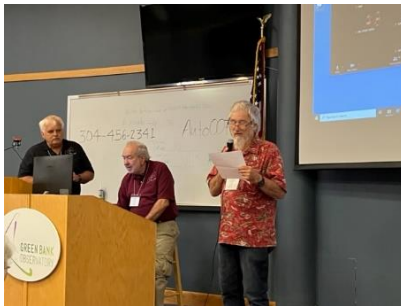# People

$$N = R_* \, f_p \, n_e \, f_\ell \, f_i \, f_c \, L$$
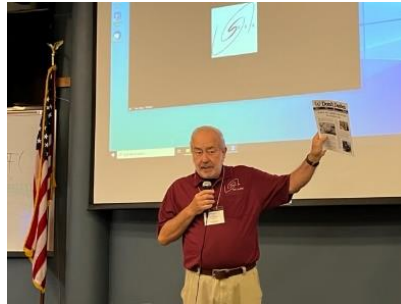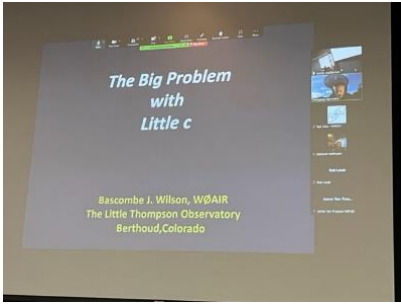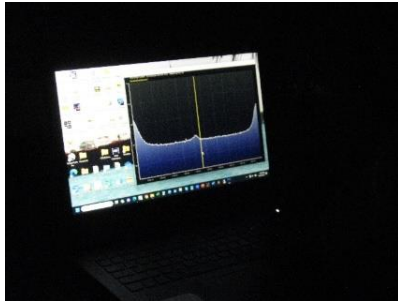
Online

Green Bank

Looking forward to the 2024 Conference!

SuperSID

SuperSID
Collaboration of Society of Amateur Radio Astronomers and Stanford Solar Center

- Stanford provides data hosting, database programming, and maintains the SuperSID website
- Society of Amateur Radio Astronomers (SARA) sells the SuperSID monitors for 48 USD to amateur radio astronomers and the funds are then used to support free distribution to students all over the world (image below as of Fall 2017)
-
- Jonathan Pettingale at SARA is responsible for building and shipping the SuperSID monitor kits: SuperSID@radio-astronomy.org
- SuperSID kits may be ordered through the SARA SuperSID webpage: http://radio-astronomy.org/node/210

- Questions about the SuperSID project may be directed to Steve Berl at Stanford: steveberl@gmail.com

- Jaap Akkerhuis at Stanford is responsible for the SuperSID software and SARA has provided financial support for his efforts

- SuperSID website hosted by Stanford: http://solar-center.stanford.edu/SID/sidmonitor/
- SuperSID database: http://sid.stanford.edu/database-browser/

- The data is searchable by time, station, date, and multiple plots may be placed on the same graph for comparison.

SID Monitor Distribution
1078 instruments
82 countries
7 continents

Algeria - 2	Denmark - 3	Mexico - 21	Slovenia - 2
Antarctica - 1	Egypt - 3	Mongolia - 10	South Africa - 8
Australia - 7	Ethiopia - 14	Mozambique - 2	Spain - 1
Austria - 3	France - 9	Namibia - 1	Sri Lanka - 1
Azerbaijan - 2	Gabon - 1	Netherlands - 5	Sweden - 3
Bangladesh - 1	Germany - 30	New Zealand - 7	Switzerland - 4
Bhutan - 1	Greece - 7	Nigeria - 57	Taiwan - 4
Bolivia - 1	Guyana - 1	Pakistan - 4	Thailand - 5
Bosnia-Herzegovina - 2	Hungary - 1	Peru - 10	Tunisia - 9
Brazil - 11	India - 33	Philippines - 3	Turkey - 2
British Virgin Islands - 1	Indonesia - 2	Poland - 2	Uganda - 5
Bulgaria - 2	Iran - 4	Portugal - 3	UK - 32
Burkino Faso - 1	Iraq - 1	Rep of Congo - 3	Uruguay - 9
Canada - 33	Ireland - 9	Romania - 4	US Virgin Islands - 2
Chile - 1	Italy - 42	Russia - 3	USA - 491
China - 38	Kenya - 23	Rwanda - 1	Uzbekistan - 2
Columbia - 9	Korea (South) - 2	S Africa - 4	Venezuela - 2
Croatia - 7	Lebanon - 11	Senegal - 1	Vietnam - 1
Cypress - 1	Libya - 1	Serbia - 1	Zambia - 2
Czech Republic - 1	Malaysia - 19	Singapore - 3	
D Rep of Congo - 4	Malta - 1	Slovak Repub - 2	

-

28

SuperSID Space Weather Monitor
Request Form

	Your information here
Name of site/school *(if an institution)*:	
Choose a site name: <mark>*(3-6 characters) No Spaces*</mark>	
Primary contact person:	
Email:	
Phone(s):	
Primary Address:	Name School or Business Street Street City State/Province Country Postal Code
Shipping address, if different:	Name School or Business Street Street City State/Province Country Postal Code
Shipping phone number:	
Latitude & longitude of site:	Latitude: _____ Longitude: _____

I understand that neither Stanford nor the Society of Amateur Radio Astronomers is responsible for accidents or injuries related to monitor use.   I will assure that a surge protector and other lightning protection devices are installed if necessary.

Signature: _____ _____   **Date:** _____

I will need:

What	Cost	How many?
SuperSID distribution USB Power	$48 (assembled)	
USB Sound card 96 kHz sample rate *(or provide this yourself)*	$40 *(optional)*	
Antenna wire (120 meters) *(or you can provide this yourself)*	$23 *(optional)* with connectors attached and tested	
RG 58 Coax Cable (9 meters) *(or provide this yourself)*	$14 *(optional)* with connectors attached and tested	
Shipping	US $12 Canada & Mexico $40 all other $60	
	TOTAL	$

_____   I have included a $_____ check (payable to SARA)
_____   I will make payment thru www.paypal.com **to** treas@radio-astronomy.org

or

_____ If you are a Minority-serving institution, in a Developing or economically deprived nation, and/or you are using the monitor with students for educational purposes, you may qualify for obtaining a monitor at reduced or no cost. Check here if you wish to apply for this designation. Then tell us how you want to use the SuperSID monitor. Include type of site, number of students involved, whether public or private school, grade levels, etc. and describe your program. The goal of the SuperSID project is to provide as many students with systems as possible. If you are able to pay for a system, even if you qualify for a free one, please do so and help support our goal.

_____

_____

_____

For more details on the Space Weather Monitor project, see: **http://sid.stanford.edu**

To set up a SuperSID monitor you will need:

[1]   Access to power and an antenna location that is relatively free of electric interference (could be indoors or out)

[2]   A **PC**** with the following minimal specifications:

  a. A sound card that can record (sample) up to 96 kHz, or a USB port to connect such a sound card (for North and South America)
      i. All other countries can use AC97 sound card with 48 kHz record (sample) rate. Most computers made after 1997 will have AC97.
  b. Windows 2000 or more recent operating system
  c. 1 GHz Processer with 128 mb RAM
  d. Ethernet connection & internet browser (desirable, but not required)
  e. Standard keyboard, mouse, monitor, etc.

[3]   An inexpensive antenna that you build yourself. You'll need about 120 meters (400 feet) of **insulated** wire. Solid wire is easier to wind than stranded. Magnet wire will work but be more fragile. You can use anything from #18 to #26 size wire. The antenna frame can be made of wood, PVC pipe, or similar materials. We'll provide instructions. You can purchase the wire from us or obtain your own.

[4]   RG58 coax cable with a BNC connector at one end to run from the antenna to the SuperSID receiver. 9 meters is recommended, but the length will depend on where you place the antenna. You can purchase the coax from us or obtain your own.

[5]   Surge protector and other protection against a lightning strike

Return this form to: SuperSID@radio-astronomy.org
or mail to: SARA
                   Brian O'Rourke, SARA Treasurer
                   337 Meadow Ridge Rd,
                   Troy, VA 22974-3256

Announcing Radio JOVE 2.0

The Radio JOVE Team

Radio JOVE students and amateur scientists from around the world observe and analyze natural radio emissions of Jupiter, the Sun, and our galaxy using their own easy to construct radio telescopes.

Our Project announces Radio JOVE 2.0, where participants assemble a 16-24 MHz radio spectrograph to observe solar, Jupiter, Galactic, and Earth-based natural radio emissions and share their observations with fellow participants.

In the Beginning

Radio JOVE started as a NASA sponsored educational outreach project in 1999. We developed a radio telescope kit suitable for receiving signals from Jupiter, the Sun, the Galaxy, and Earth-based radio emissions. The original kit comprised a radio receiver (RJ1.1) and a dual dipole antenna for 20.1 MHz. An important goal was to teach electronic principles including how to build, solder, and assemble the radio receiver and antenna.
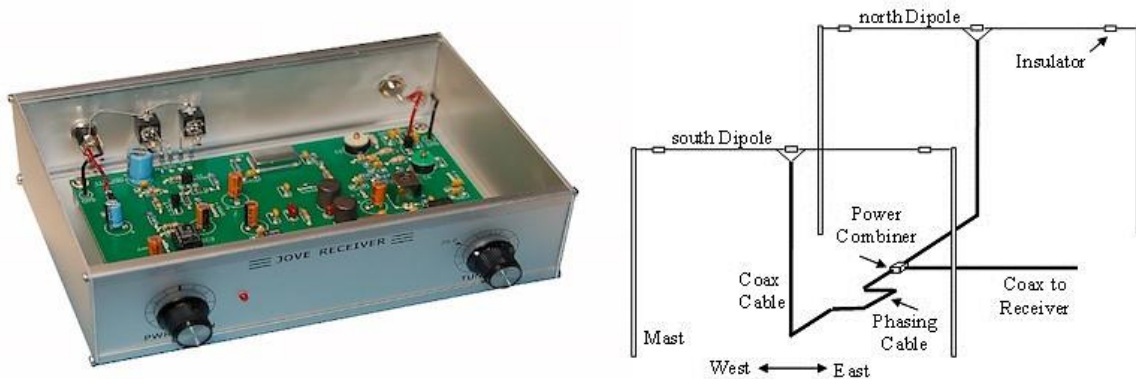

Figure 1. A Radio JOVE RJ1.1 receiver and a schematic of the dual-dipole antenna.

In addition to the hardware, three software packages were developed. These were Radio Jupiter Pro (Jupiter emission prediction program), Radio-SkyPipe (strip chart program) and Radio Sky Spectrograph (control and display of radio spectrograph data).
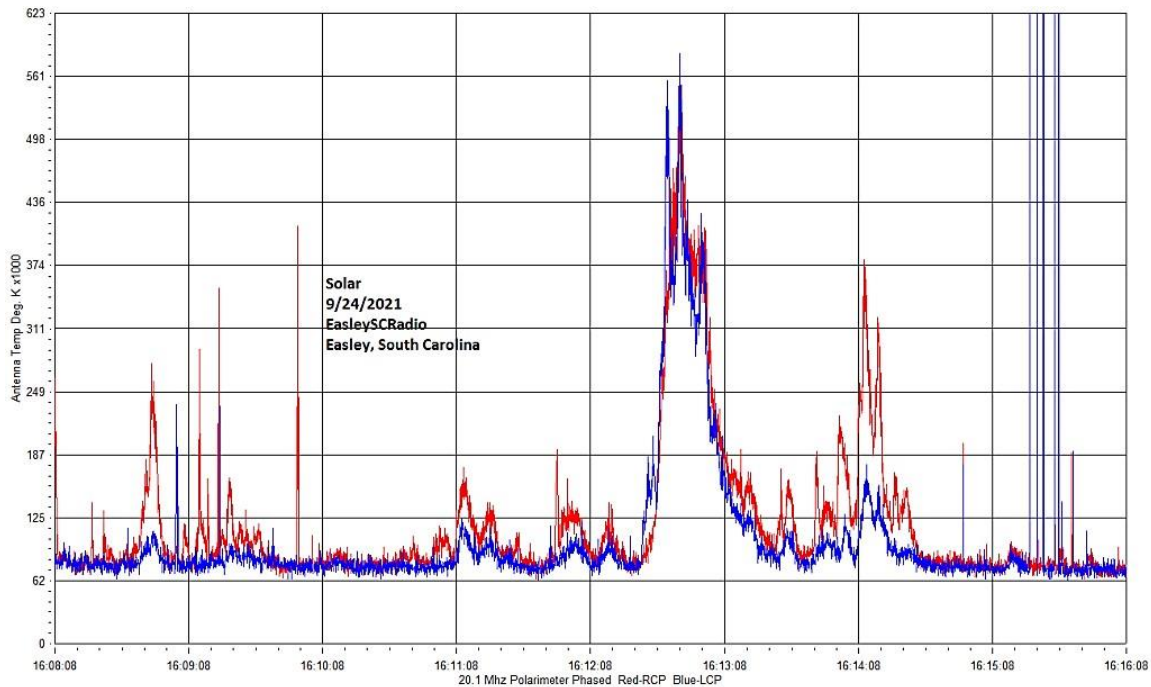
Figure 2. A SkyPipe strip chart showing multiple solar bursts using a JOVE receiver. John Cox, SC.

The Growth of Radio JOVE

As of Autumn 2021, over 2,500 kits have been sold at cost to schools and individuals around the world. Thousands of data submissions from observers have been made to the Radio JOVE data archive.

The Radio JOVE web site has always provided a wealth of information describing observation methods and various educational materials intended to teach radio astronomy techniques and scientific methods. Biannual newsletters are produced, and several telephone help sessions are held each year.

A sub-group of experienced observers known as the Spectrograph Users Group (SUG) evolved from the core JOVE group. These observers developed data collection and analysis techniques using more advanced equipment and techniques. SUG members have contributed to articles published in peer-reviewed scientific journals. This group remains active under the Radio JOVE listserv at https://groups.io/g/radio-jove/.

Moving Forward with New Technology

In the past, Radio JOVE provided the hands-on experience of building a radio kit. We have many RJ1.1 receivers in operation successfully contributing scientifically valuable data. It has, however, become increasingly difficult to obtain parts for the RJ1.1 receiver kits and we therefore decided to replace the RJ1.1 receiver with a new SDR-based design for the receiver portion of our radio telescope kits. While we continue to support the hardware and software for the original RJ1.1 receivers, the only kits now available for purchase from Radio JOVE contain this newly designed system.

In recent years, new technologies have made software defined radios (SDRs) ever more affordable. These radios can operate on a single frequency like the original JOVE receiver but can also generate spectrograms which depict radio activity as a function of both time and frequency. Such displays offer new insights into our studies of the Sun, Jupiter, the Galaxy, and both natural and artificial Earth-based radio emissions.
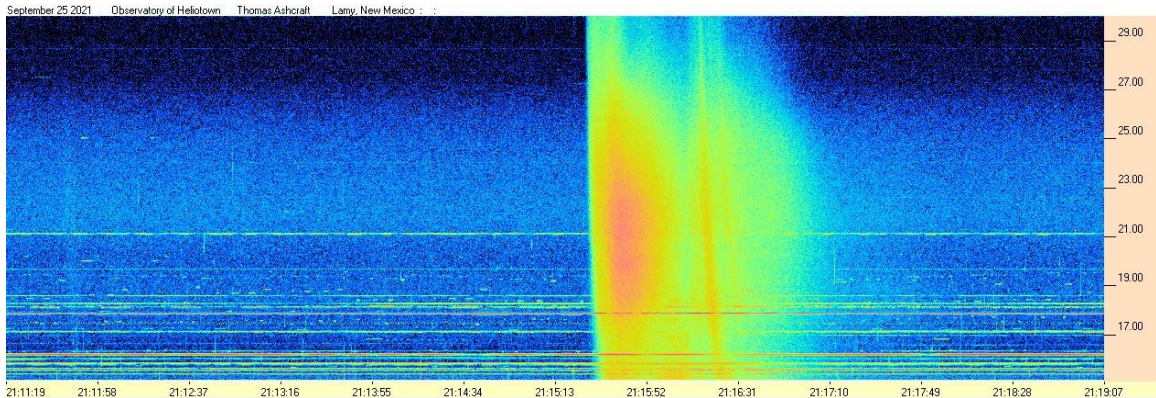
Figure 3. Radio spectrogram showing multiple solar bursts received by Tom Ashcraft in New Mexico. Horizontal scale is time, and the vertical scale is frequency. Amplitude is displayed using different colors corresponding to the strength of signals.

Radio JOVE continues to sell radio telescope packages including an antenna, receiver, and software; however, the receiver is now a commercially built SDR.

Figure 4. The JOVE team has had considerable success with the SDRPlay RSP1A unit and will provide support for using this instrument for our radio astronomy program. Not all SDR types can be supported, but it is our intent to provide support for some other SDRs as they become available during this period of rapid SDR development.

It continues to be our goal to introduce new observers to the scientific method and help them experience the thrill of receiving cosmic radio signals. Through a series of educational training modules and observing and analysis projects we aim to guide new observers to levels where they can contribute to Citizen Science projects.

 We continue to support our large user base that uses JOVE RJ1.1 receivers – both in terms of technical support for the receivers but also with new and exciting observing projects for both RJ1.1 and SDR users.

We welcome both new and experienced observers to the JOVE 2.0 program as we share the excitement of receiving, studying, and understanding radio signals from our corner of the galaxy.

Please see the Radio JOVE web site at https://radiojove.gsfc.nasa.gov for more information.

RADIO JOVE 2.0 RADIO TELESCOPE KIT ORDER FORM

Order Online using PayPal™

* * * Please allow 2 to 3 weeks for delivery. * * *

IMPORTANT: Before you order the Jove receiver kit and/or the antenna kit, we suggest that you read the on-line manuals. You will need to provide additional materials and tools to complete the antenna. The cost of additional materials for the antenna support structure (masts, etc.) may be in the range of US$75 to US$100. Also note that the optimal antenna height can be up to 20ft, depending upon your latitude.

Item # RJK2u – Complete 2.0 Kit: Receiver + Unbuilt Antenna Kit + Software This kit includes an SDRplay RSP1A, USB Cable, SMA/BNC cable, F-adapter, unbuilt Antenna Kit (RJA), printed assembly manuals, and Radio-Sky Spectrograph (RSS) software. Note: Kit does not include antenna support structure. **Price: $215 + Shipping (See reverse for shipping)**	**Item # RJK2p** – Complete 2.0 Kit: Receiver + Professionally Built Antenna Kit + Software This kit includes an SDRplay RSP1A, USB Cable, SMA/BNC cable, F-adapter, Professionally Built Antenna Kit (RJA2), printed assembly manuals, and Radio-Sky Spectrograph (RSS) software. Note: Kit does not include antenna support structure. **Price: $384 + Shipping (See reverse for shipping)**
Item # RJA – Unbuilt Antenna Kit The RJA Radio JOVE Antenna Kit includes a printed construction manual, stranded copper easy-to-solder antenna wire, ceramic insulators, RG-59 easy-to-solder coax cable, screw-on Fconnectors, and a power combiner. Note: Kit does not include antenna support structure. Assembly requires a soldering gun and other tools. **Price: $90 + Shipping (See reverse for shipping)**	**Item # RJA2** – Professionally Built Antenna Kit The RJA2 Radio JOVE Antenna Kit includes a printed installation manual, two professionally assembled dipole antennas constructed of #14 Copperweld wire with Budwig center insulators and center support rope attachment points, high quality RG-6 coax with pre-installed commercial grade connectors, and a power combiner. Note: Kit does not include antenna support structure. **Price: $249 + Shipping (See reverse for shipping)**
Item # LTJ2 – Listening to Jupiter, 2nd Ed. by R. S. Flagg PDF download of Richard Flagg's book "Listening to Jupiter, 2nd Ed., 2005". The file is downloaded from a secure website. **Price: $10 + $0 shipping (PDF file download)**	**Item # RJR2** – Radio JOVE 2.0 Receiver-Only Kit This kit includes one SDRplay RSP1A SDR receiver, USB Cable, SMA/BNC cable, and F-adapter, printed assembly manuals, and Radio-Sky Spectrograph (RSS) software. **Price: $135 + Shipping (See reverse for shipping)**

RADIO JOVE 2.0 RADIO TELESCOPE KIT ORDER FORM (continued)

Order Online at https://radiojove.net/kit/order_form.html OR
Complete this form and mail with payment

Payment may be made by Credit Card via PayPal™, U.S. Check, U.S. Money Order, International Money Order in U.S. funds drawn on a U.S. bank, or Western Union Money Transfer made payable to **The Radio JOVE Project**. No bank-to-bank wire transfers are accepted. Purchase Orders are accepted from U.S. Institutions.

Send to: The Radio JOVE Project
1301 East Main St
MTSU Box 412
 Murfreesboro, TN 37132, USA
 email: chiggins@mtsu.edu
FEIN: 20-5239863

Item	Description	Quantity	Item Price	Shipping (see below)	Subtotal
RJK2u	Complete Radio JOVE 2.0 Kit Receiver + unbuilt Antenna		$215		
RJK2p	Complete Radio JOVE 2.0 Kit Receiver + Professionally Built Antenna		$384		
RJA2	Professionally Built Antenna-Only Kit		$249		
RJA	Unbuilt Antenna-Only Kit		$90		
RJR2	Receiver-Only Kit		$135		
LTJ2	Listening to Jupiter, 2nd Ed., by R.S. Flagg (PDF download)		$10	$0	
				Total:	

Shipping Fees for Radio JOVE: We ship all packages using USPS Priority Mail flat rate boxes.
U.S.A.: $17.00
Canada: $57.00
All Other International Shipping: $85.00

 Ship to: (Please print clearly)

Name: _____

Address: _____

City, State, Postal Code: _____

Province, Country: _____

Email: _____

Visit the Radio JOVE web site and fill out the team application form at https://radiojove.net/sign_up_form.php even if you are just an interested individual so that you can receive important information about kit updates, online services, and activities within the project as they occur!

The British Astronomical Association

A company limited by guarantee

Registered Charity No. 210769

PO Box 702, Tonbridge, TN9-9TX 020-7734 4145
www.britastro.org

Founded in 1890

Please send questions, reports, and observations to John Cook: jacook@jacook.plus.com

BAA Radio Astronomy Section, Director: Paul Hearn

RADIO SKY NEWS   **2023 JULY**

VLF SID OBSERVATIONS

July has been another very busy month for solar activity, although not quite as high as the peak in May. We have recorded 117 C-class flares and 34 M-class, the only X-class flare shown in the SWPC data being just before midnight on July 2nd. This was too late even for the 24kHz trans-Atlantic path. Once again many of the flares were multiple peaked, some with rather confusing timings. The M1.0 flare on the 14th has fairly consistent peak times in our recordings, from 09:37 to 09:46, while the satellite X-ray data gives a peak at 09:13, ending by 09:18.
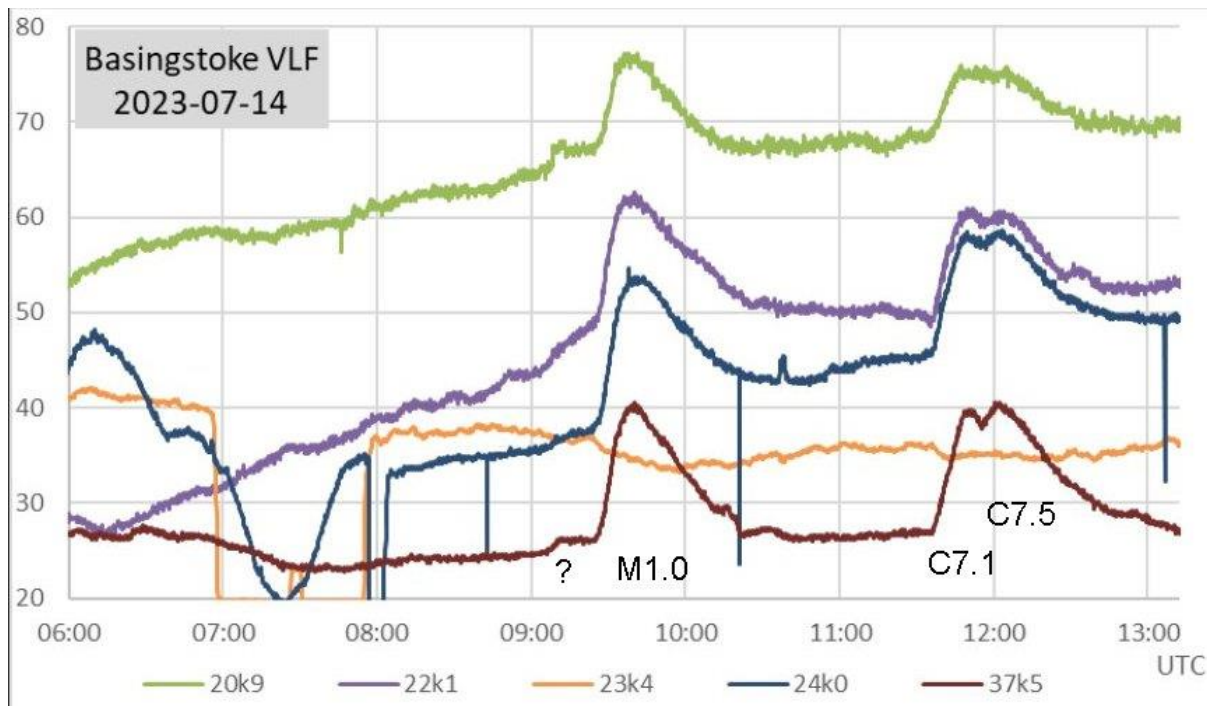
This recording by Paul Hyde clearly shows the stronger SID at around 09:40, preceded by a much weaker SID nearer to 09:13. It also shows the C7.1 and C7.5 flares merged into a twin-peaked SID on most signals, but less clear at 20.9kHz. The 23.4kHz signal also appears very unresponsive to all of these events. Both of the C-flares were from AR13372, while the M1.0 was from AR13363, both very large and complex sunspot groups.

On the 30th, two M1.8 flares from AR13390 merged into a single SID in all of our observations. The chart from Mark Prescott shows the activity:
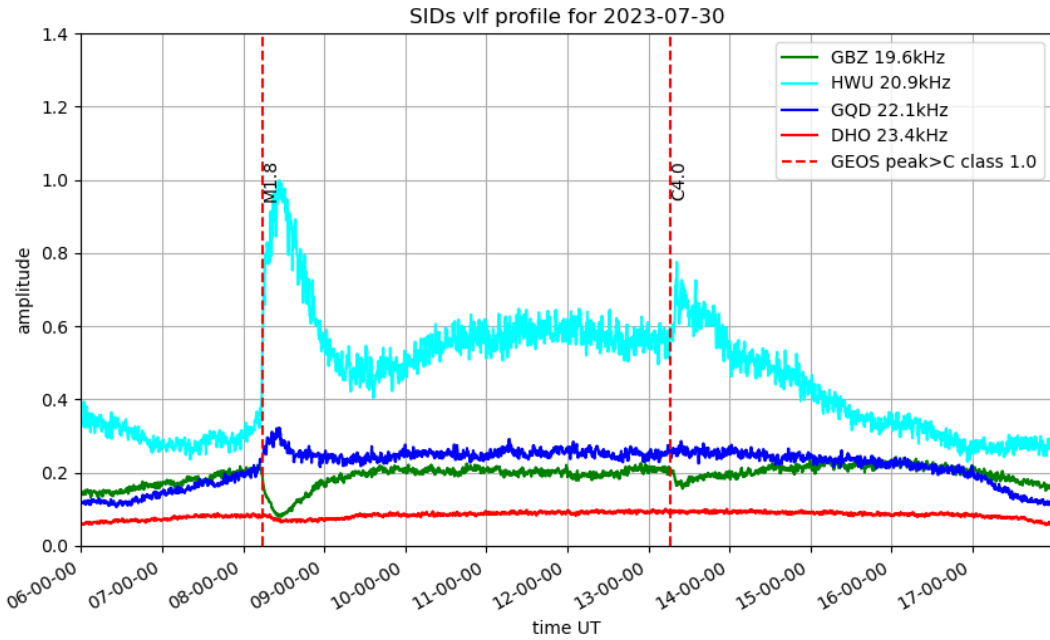
The satellite X-ray data lists identical flares peaking at 08:14 and 08:22. There is just a hint of the first peak visible in the rising edge of the flare in Mark's recording. AR13390 was a fairly small sunspot group near to the solar East limb at the time.
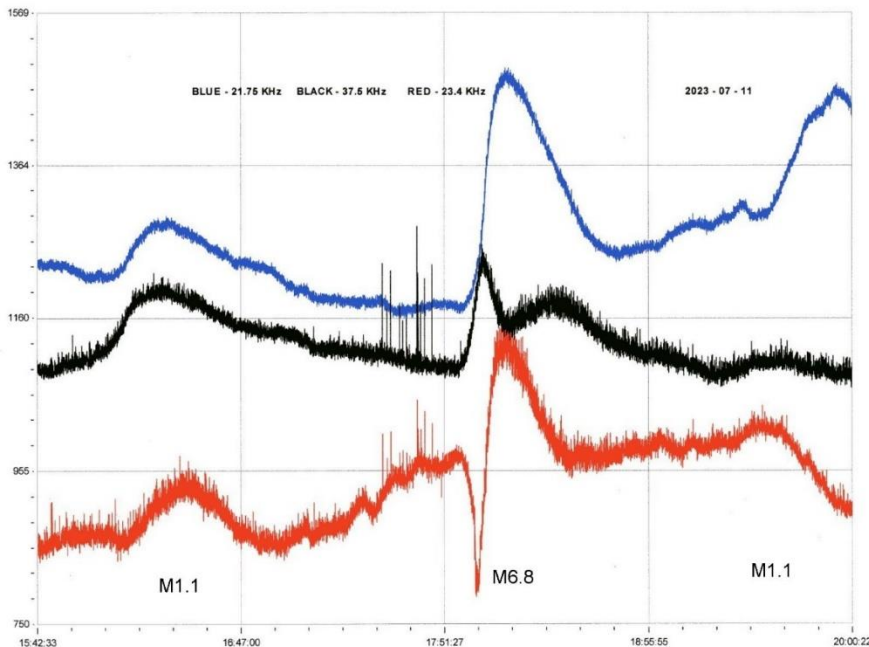
The strongest of the M-flares were recorded on the 11th and 12th, the M6.8 on the 11th shown in this recording by Colin Clements. The 21.75kHz signal from France (blue) has a good symmetrical SID, while the 23.4kHz signal from Germany (red) and 37.5kHz signal from Iceland (black) show mirror image spike and wave SIDs. The combination clearly shows the effects of the ground / sky path phase reversal from the strong flare. The M6.9 flare on the 12th had a faster rise time, producing the classic 'Sharks Fin' SID.
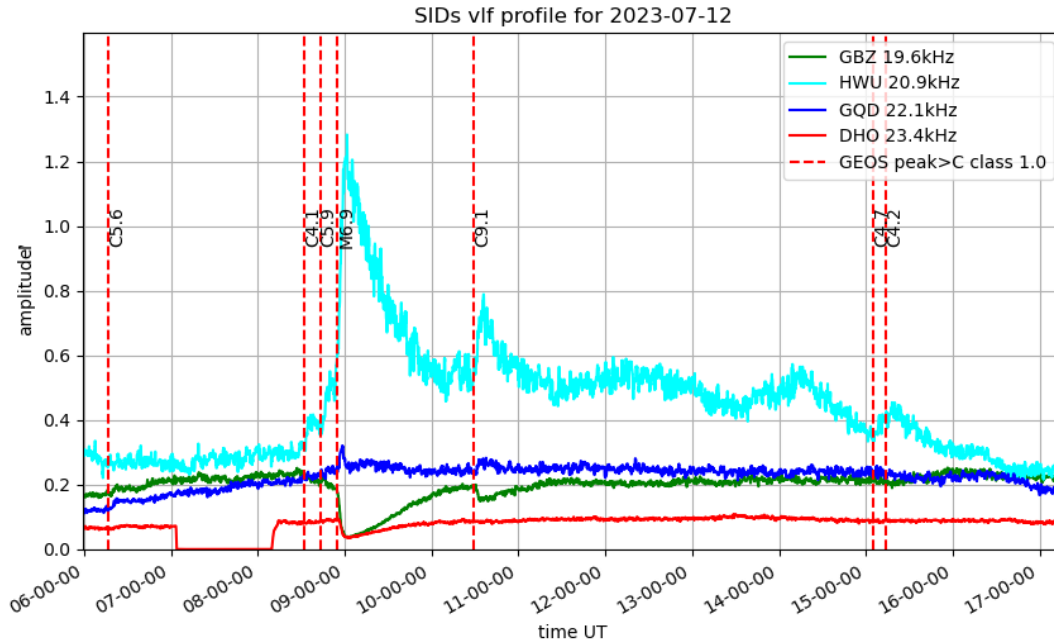
Mark Prescott's recording shows this well, along with the rest of the day's activity.

Mark Edwards noted a strong oscillation from about 16:15UT on the 14th, on 19.6kHz and 22.1kHz. There were also some disturbances at other frequencies, probably related to the stormy weather conditions.

MAGNETIC OBSERVATIONS

39
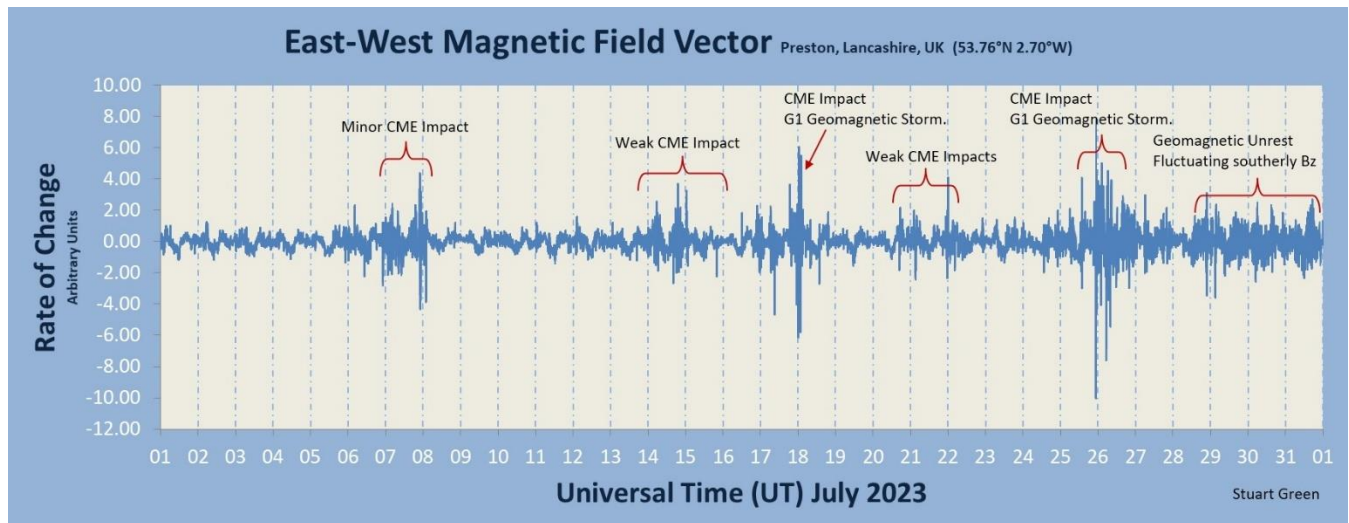
Stuart Green's summary of July's magnetic activity again shows mostly minor disturbances but getting stronger in the last week. There were plenty of CMEs associated with the strong flaring, but again mostly not Earth directed. No SFEs were recorded either, perhaps reflecting the more complex flare structures recorded.

The small disturbance on the 5th and 6th was from a CME glancing blow and lasted a few days. The CME impact on the 14th was stronger, producing a short active period shown in the recording by Roger Blackwell:
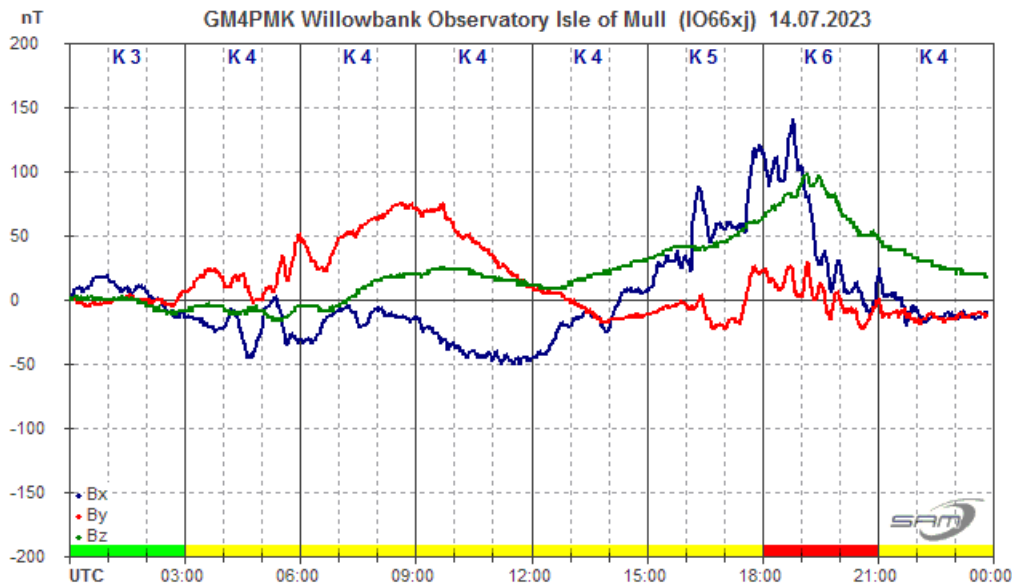
This activity faded in strength but continued over the 15th and 16th.
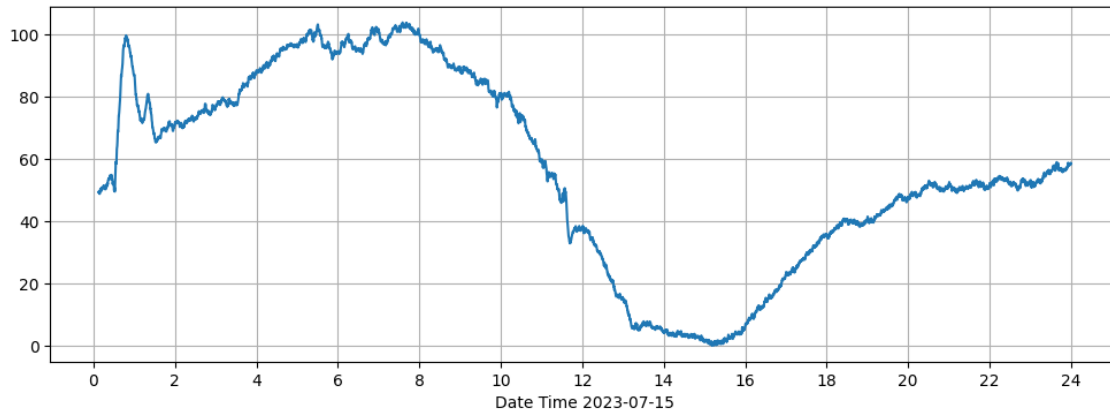
Callum Potter's chart shows this very mild disturbance on the 15th, following the end of the strong activity after 02UT. The source of the CME is not clear but presumed to be from a flare on the 11th.

Steyning Magnetometer (50.8 North, 0.3 West)
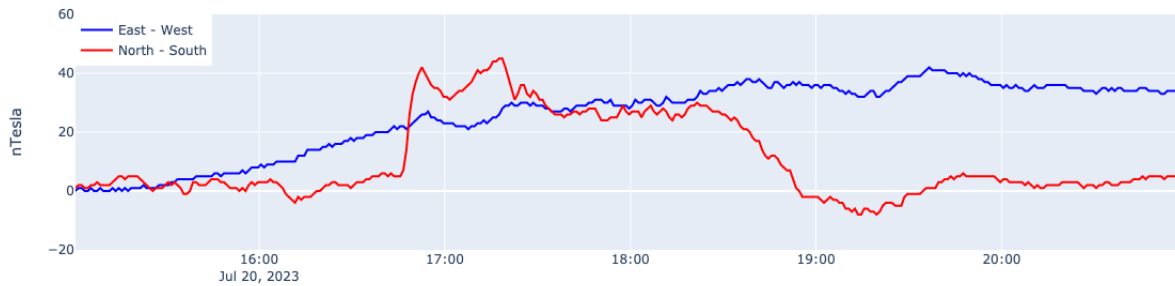
Nick Quinn's recording from the afternoon of the 20th shows what might be a CME impact around 16:45 – 16:50, continuing until 19:00. Stuart Green's summary chart does not show any specific source at this time, although the disturbance does appear to be real and not local interference. A similar effect was also recorded by Roger Blackwell. The STCE report does suggest that a CME from a flare on the 17th could impact by the 20th. Nick also recorded a clearer CME impact late on the 25th:

Steyning Magnetometer (50.8 North, 0.3 West)
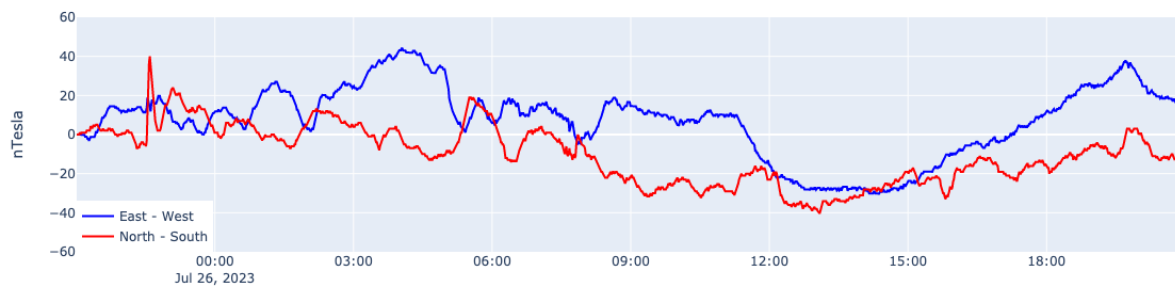
The recording shows a fairly strong disturbance through most of the 26th. The disturbance continued to the end of the month, with a turbulent solar wind adding to the CME.

Magnetic observations received from Roger Blackwell, Stuart Green, Callum Potter, Nick Quinn and John Cook.

SOLAR EMISSIONS

RED - 151 MHz   BLUE - 408 MHz   BLACK - 610 MHz   2023 - 07 - 16
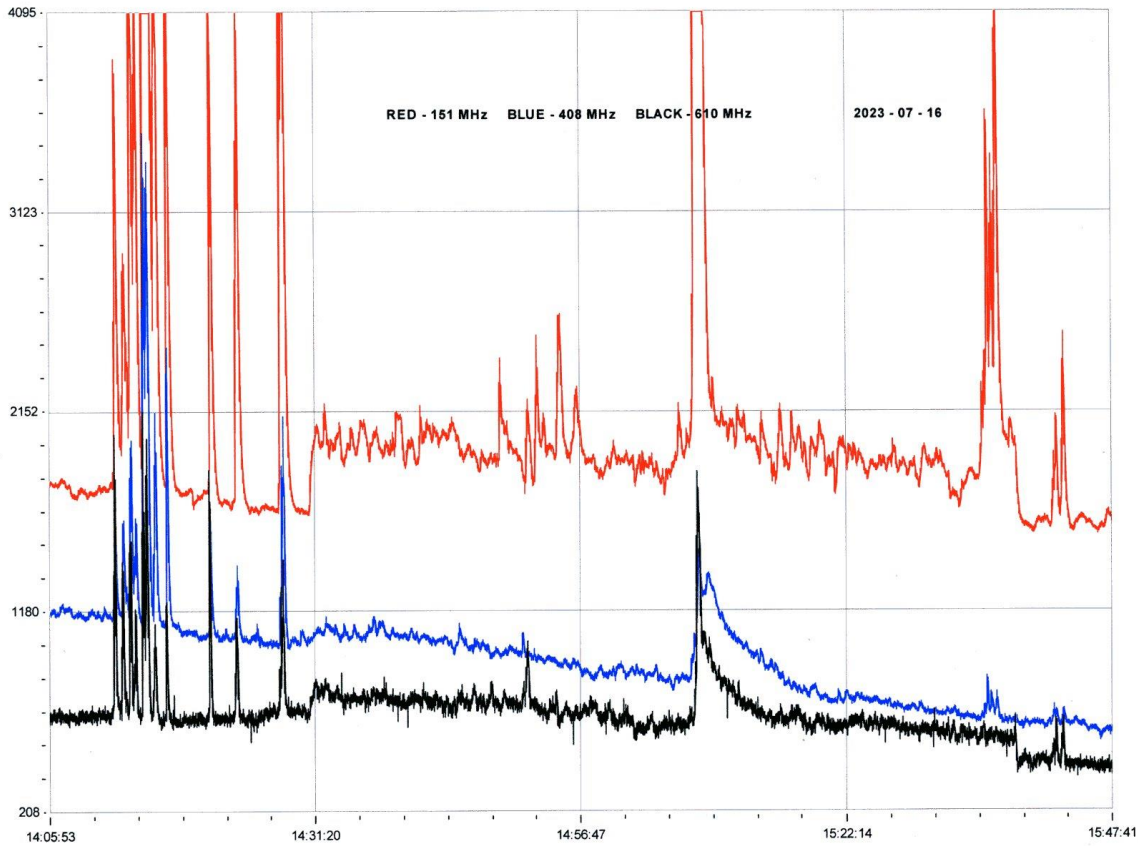
There was a burst of activity on the BAA-RAG forum regarding a solar noise burst in the afternoon of the 16th. Colin Clements recorded this activity at VHF / UHF, showing activity at all three frequencies. The C3.0 flare at 14:05UT produced a series of noise spikes over about 20 minutes, followed by a small rise in the background level. The SID-like burst on 408 and 610MHz is from the M1.7 flare at 15:10UT and is the source of the forum discussion. The SWPC alert lists a type IV radio burst at 15:09, matching well with Colin's recording. 610MHz shows more of a spike at the start of the burst, and also shows another strong spike around 15:35. This may be related to the earlier flare, as no further flare activity is listed until 16:27.

1027UT Type III
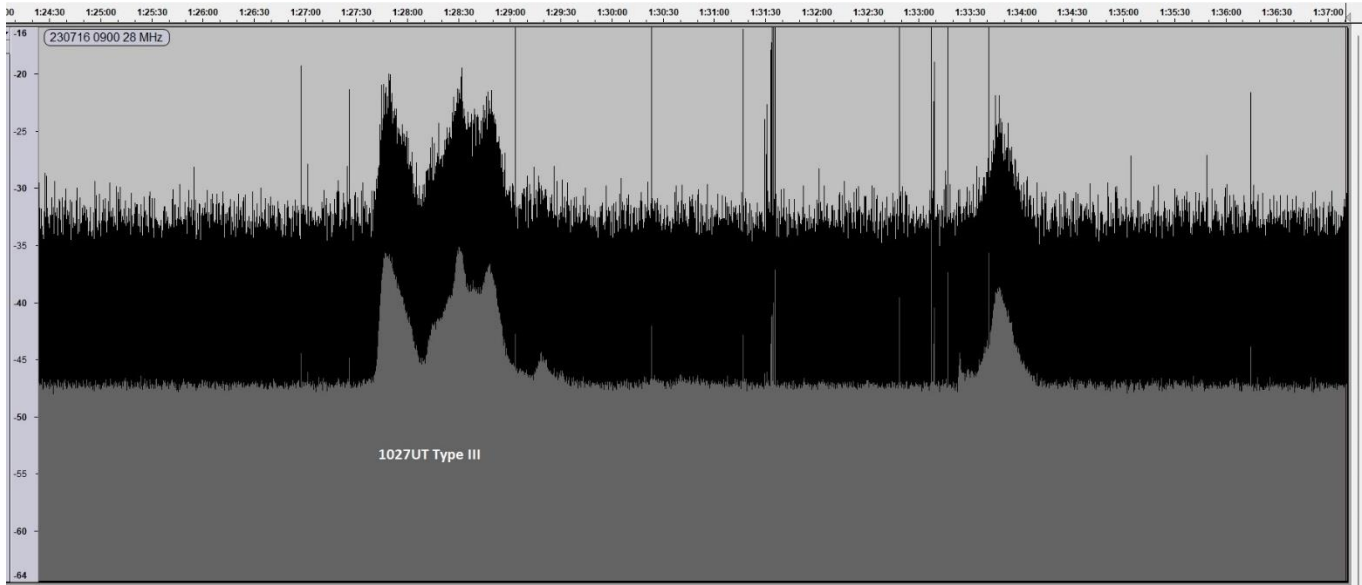
Colin Briden made a 28MHz recording earlier on the 16th showing a type III emission. This matches the C2.9 flare that we recorded starting at about 10:27 and peaking at 10:40UT. The first set of bursts rise about 12dB above the background level.

Colin Clements also recorded a very noisy outburst on the 13th, mostly at 151 and 408MHz:

RED - 151 MHz   BLUE - 408 MHz   BLACK - 610 MHz   2023 - 07 - 13
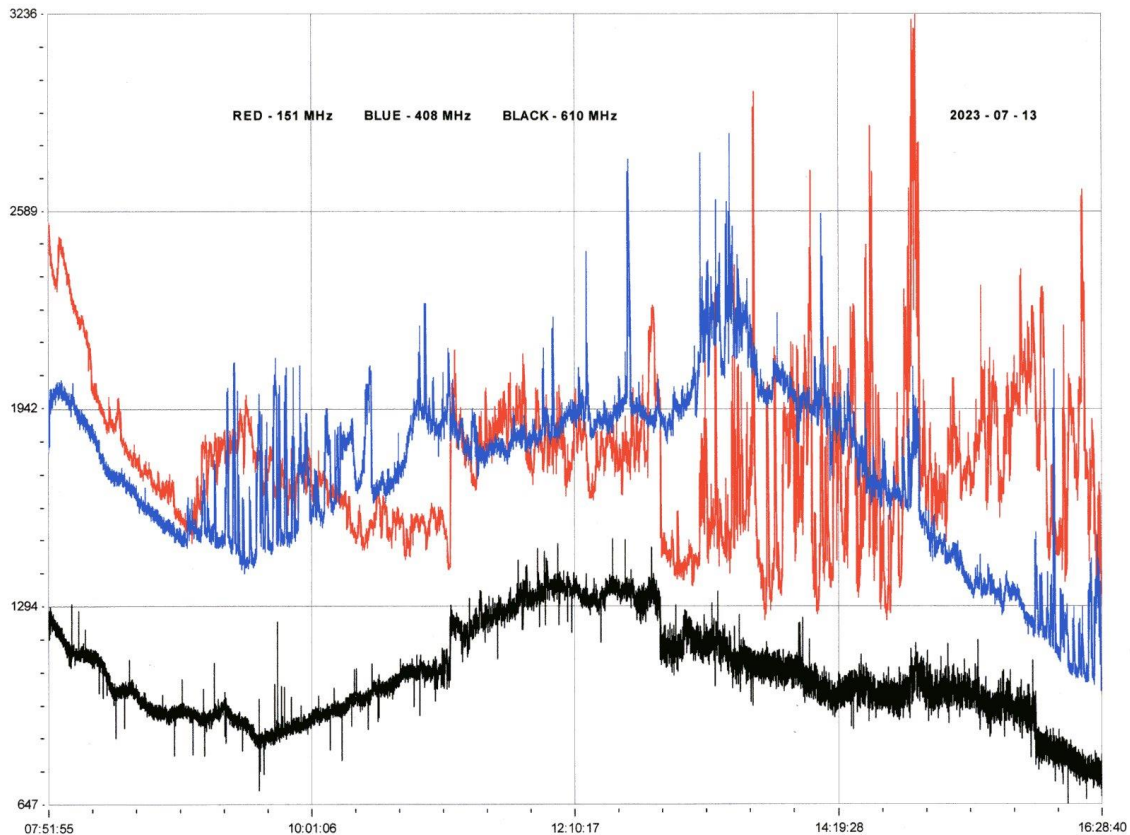
The chart covers 07:52 to 16:29, including the C4.7 flare at 11:27 and the C9.7 at 12:40. The X-ray data shows a number of unclassified flares in this period, along with a C5.1 at 09:55 that we did not record as a SID. The

complexity makes this chart very difficult to analyse, but the peaks in 151 and 408MHz do match with these timings. The activity at 610MHz is rather unusual, just showing a rise in the background level around midday.

MUONS

Muon count rate 2023 bins=300s, elev=125m, NW Kent UK

%deviation from mean 2023 bins=300s, elev=125m, NW Kent UK

Muon count adjusted for temperature & atmospheric pressure 2023 bins=300s, elev=125m

GEOS 16 X-ray flux (max time)

22-07 to 23-07 Muon count (+background)   bins=24h, NW Kent, UK

Mark Prescott has provided his Muon data for July, along with a summary of the last 12 months. A local thunderstorm has caused a minor peak in the data, a problem faced with SID recording as well. The 12-month summary shows a gradual decrease in Muon counts as the level of solar activity has increased, an effect that was expected due to its effect on the Earth's atmosphere/ionosphere/magnetosphere. It will be interesting to see how this continues with the solar cycle over the next few years. Solar maximum is predicted in 2025 or 2024.

VLF SID OBSERVATIONS

The strong solar activity in July continued into early August, but then faded away by mid-month. We recorded 68 classified flares in August, compared with 150 in July. There were however two X-class flares recorded, although they were rather late in the evening for the European signals. The background X-ray flux shown in the satellite data was also fairly high, so many of the smaller C-class flares were missed. Many of the stronger flares were also multiple peaked again, giving plenty of unclassified SIDs.
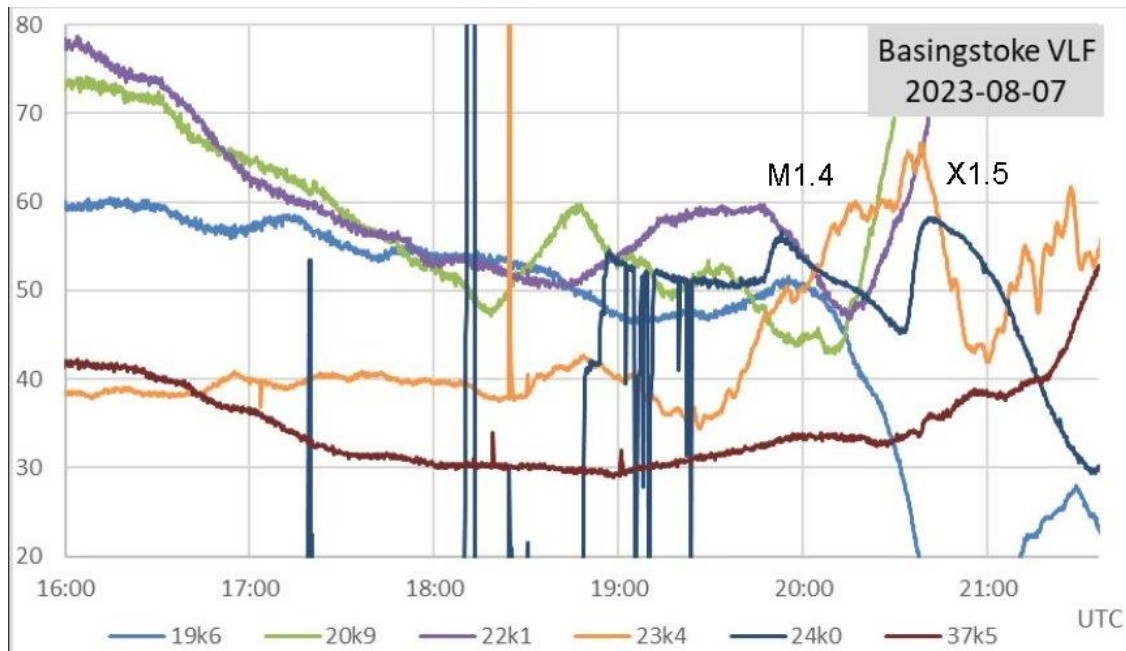
This recording by Paul Hyde shows the X1.5 flare peaking at 20:41UT on the 7th. Most of the signals shown are suffering from the sunset, but the 24kHz trans-Atlantic signal shows a clear SID together with the earlier M1.4 flare. The signal had been off for much of the day, but luckily had come back on in time to catch these flares. 37.5kHz from Iceland shows a very small response. The peak of the earlier M1.0 flare is right on the left edge of the chart. This was a double peaked flare, both peaks of a similar magnitude. It was also a very slow flare, starting around 15:30 with peaks at 16:10 and 16:30. This is shown in the recording by Mark Prescott, along with the rest of the day's activity:

SIDs vlf profile for 2023-08-07

SID events recorded on 08Aug2023 monitored DHO 23.4kHz — Roberto Battaiola
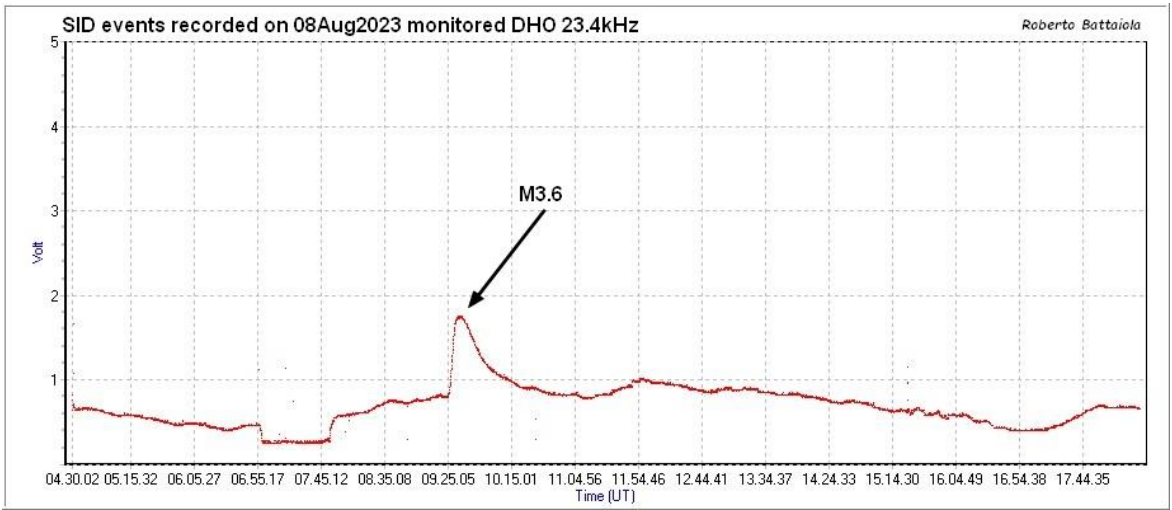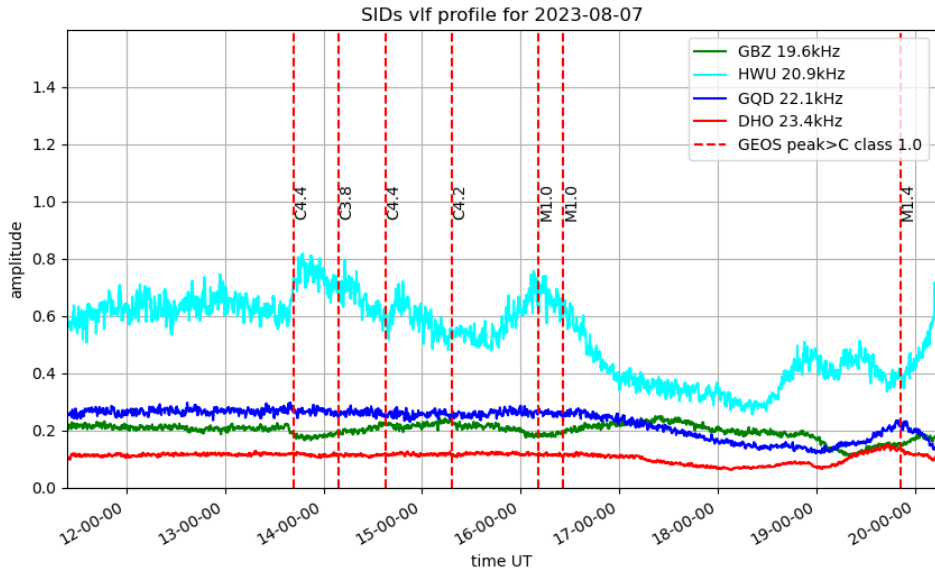
Activity started to decline after this, with just two flares recorded on the 8th. The first of these is shown in this recording by Roberto Battaiola at 23.4kHz. The M3.6 flare at 09:31 produced a clear SID, although the C8.7 flare at 18:12 was too close to the sunset to show on this signal.

SIDs vlf profile for 2023-08-03
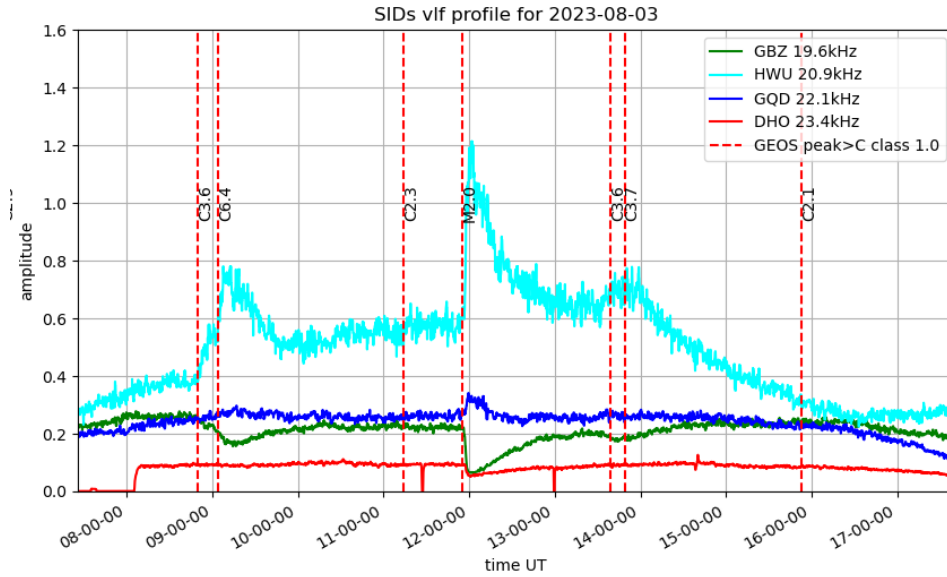
Mark Prescott's recording from the 3rd shows the strong M2.0 flare close to midday, its long decay time covering the later C-class flares at 20.9kHz. The earlier C2.3 flare is also well hidden.
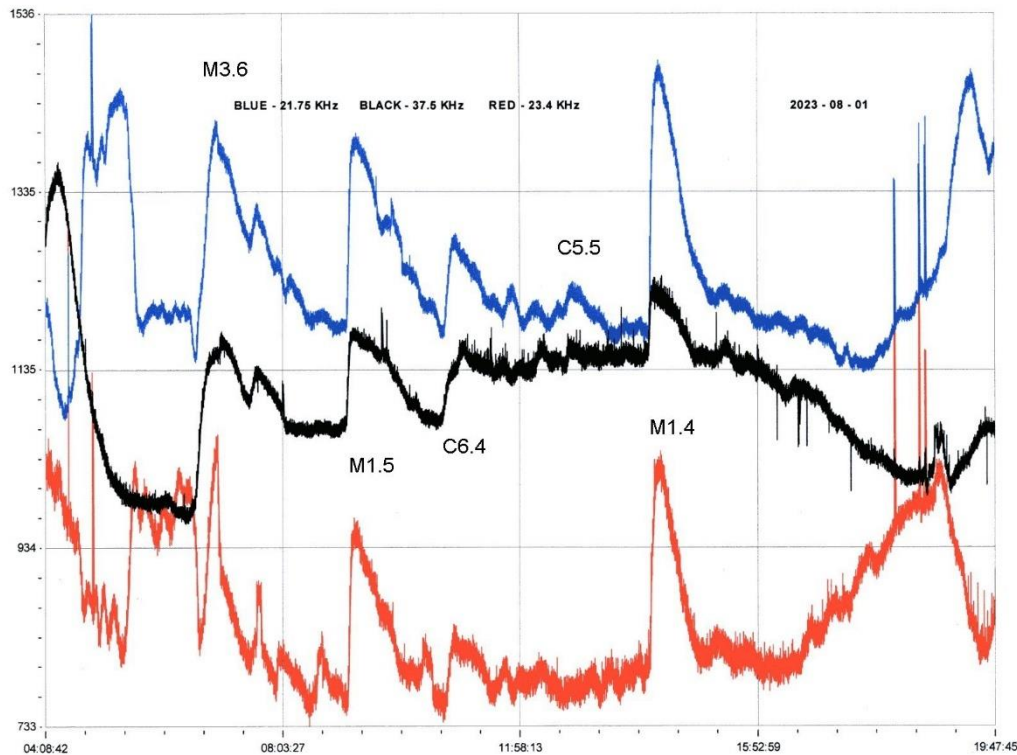
The 1st was one of the busiest days for flares, shown in the recording by Colin Clements. The stronger M-flares are easy to see with clear SIDs, but 21.75kHz (blue) in particular shows many smaller peaks between them. The satellite data shows that the majority of these flares were all from AR13380, an active region very close to the west limb of the sun at the time.

Oscillations 2023 August 10th
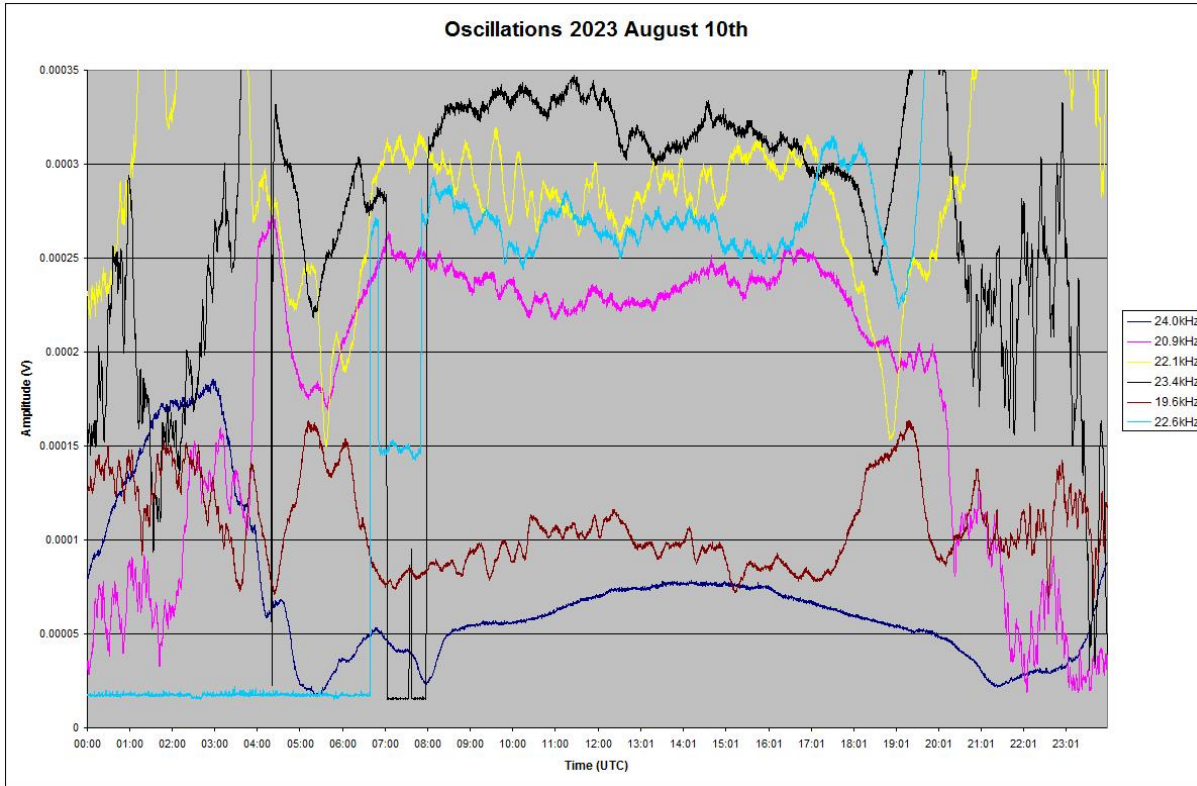
The recording from the 10th by Mark Edwards shows some significant oscillations on all of the European signals throughout the day, while 24kHz just shows a normal quiet diurnal curve. The two British signals, 19.6 and 22.1kHz show the most distinct pattern, followed by the French signal at 20.9kHz. This appears to be due to the more active weather pattern over Europe compared to the North Atlantic. Satellite data shows just a few small flares during the day. Mark also recorded oscillations on the 4th, again leaving 24kHz with a clean diurnal curve showing the two small SIDs.

MAGNETIC OBSERVATIONS

East-West Magnetic Field Vector Preston, Lancashire, UK (53.76°N 2.70°W)

48
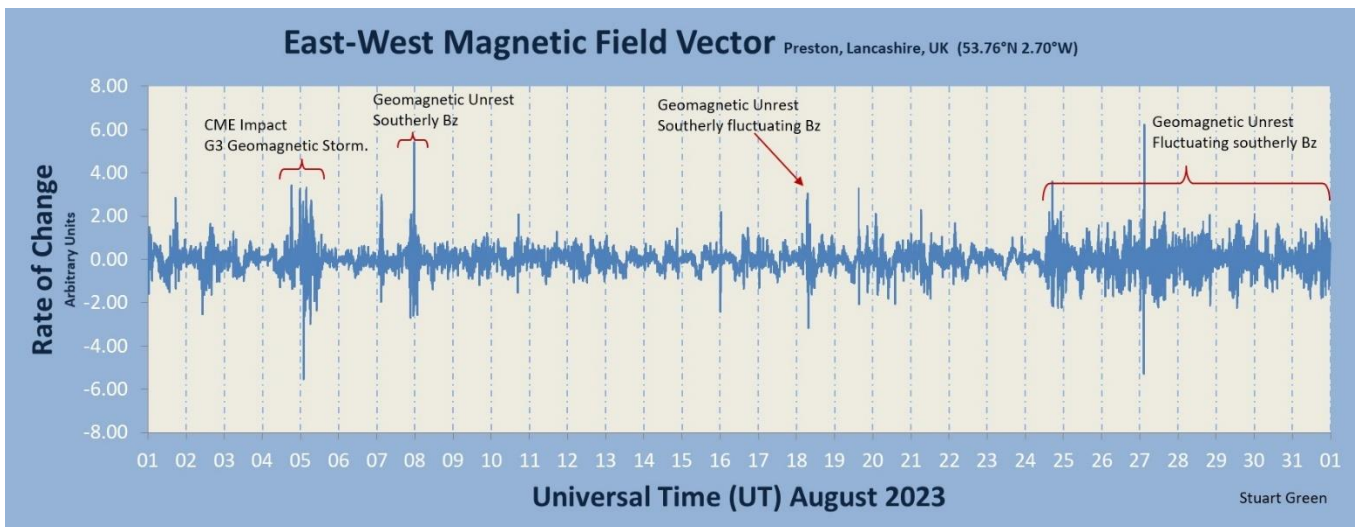
Stuart Green's summary of the magnetic activity in August shows a mostly quiet month, disturbances mostly due to the solar wind. The CME impact on the 5th appears to be from a filament eruption, as the satellite images show a full halo CME from near the centre of the visible disc. The strong flares were from active regions much nearer to the limb. Whatever the source, it gave rise to the most active magnetic disturbance of the month, shown in Roger Blackwell's recording:
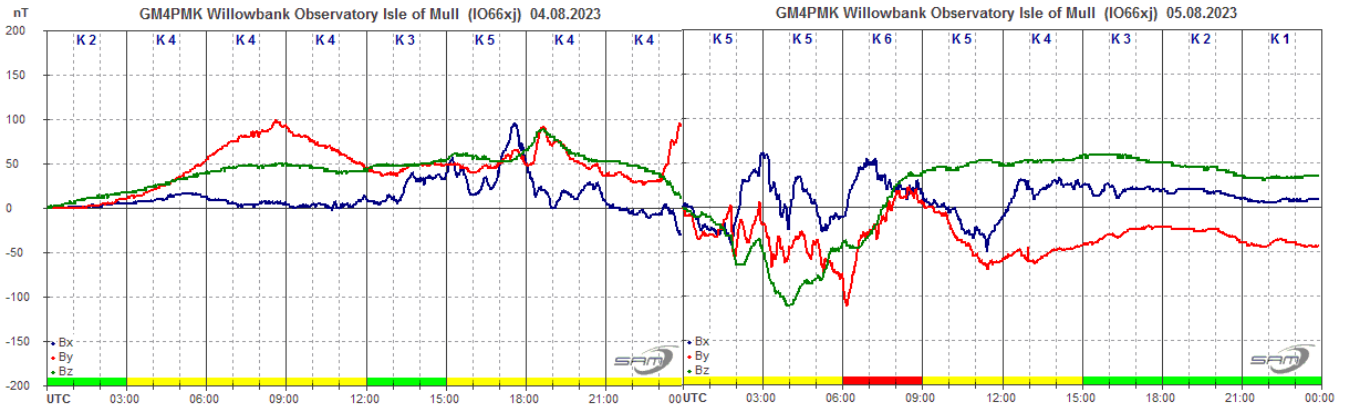
The sensor is reset at midnight, and so there is an offset between the 4th and 5th clearly seen in the afternoon of the 5th. Nick Quinn (Steyning) and Callum Potter (Wasbister) also made recordings of the disturbance with respectively, two and singe axis sensors:

The rest of the month was much quieter, with disturbance mainly from a more active solar wind. Nick Quinn's recording shows a mild disturbance starting on the 7th:

Steyning Magnetometer (50.8 North, 0.3 West)
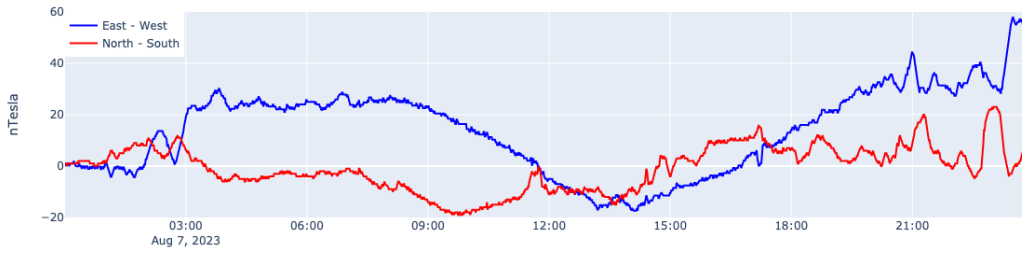
Wasbister Magnetometer (59.17N,3.06W)
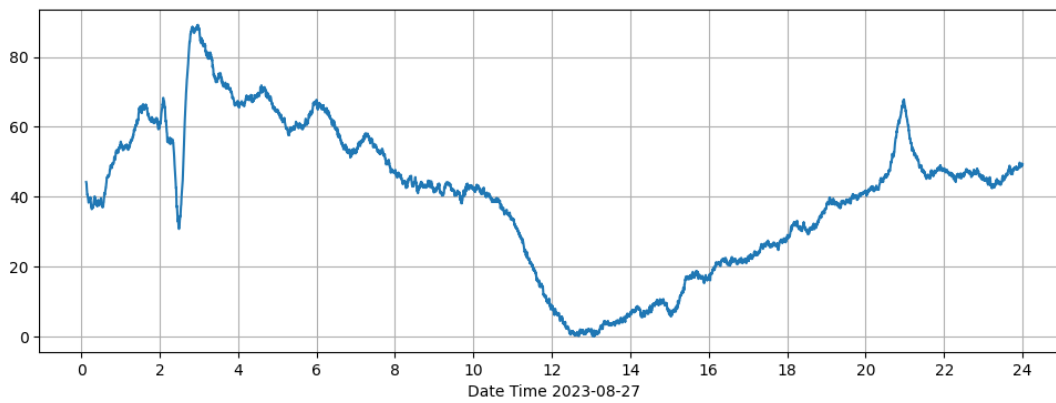
Callum Potter's chart shows more solar wind disturbance on the 27th, possibly aided by CME glancing blows. The sharp pulse around 02:30 looks like a CME impact, although it was not recorded by other observers, so may just be from the solar wind.

Magnetic observations received from Roger Blackwell, Stuart Green, Callum Potter, Nick Quinn and John Cook.
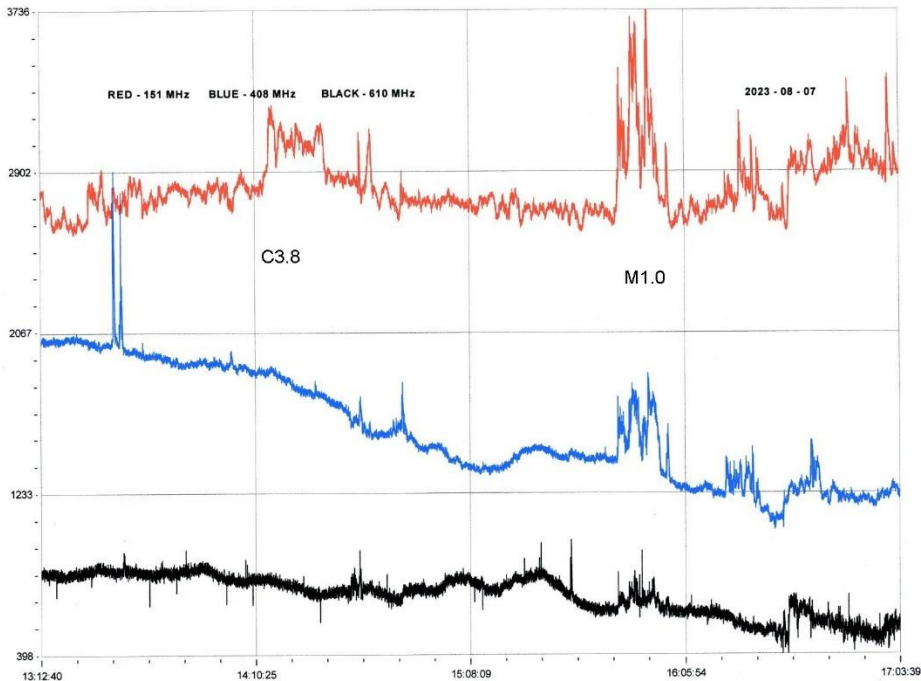
SOLAR EMISSIONS

Colin Clements recorded some VHF/UHF emissions associated with flare activity on the 7th. The 151MHz burst just after 14:10UT matches the timing of a C3.8 flare that occurred between the pair of C4.4 flares that we recorded. The stronger 151MHz burst aligns with the M1.0 flare and is accompanied by smaller signals at 408MHz and 610MHz. The SID recording by Mark Prescott already illustrated shows that this was a very slow flare, and so links to the complex noise peaks after 16UT in Colin's recording.

Colin recorded similar activity from the M1.7 flare on the 2nd, with a strong 151MHz signal and much less response at 408MHz and 610MHz.

MUONS

51

Muon count adjusted for temperature & atmospheric pressure 2023 bins=300s, elev=125m

GEOS 16 X-ray flux (max time)
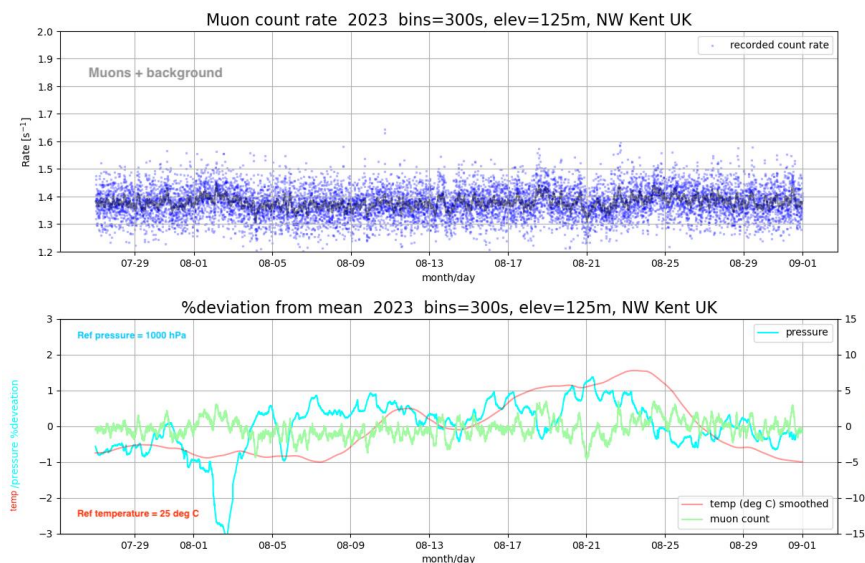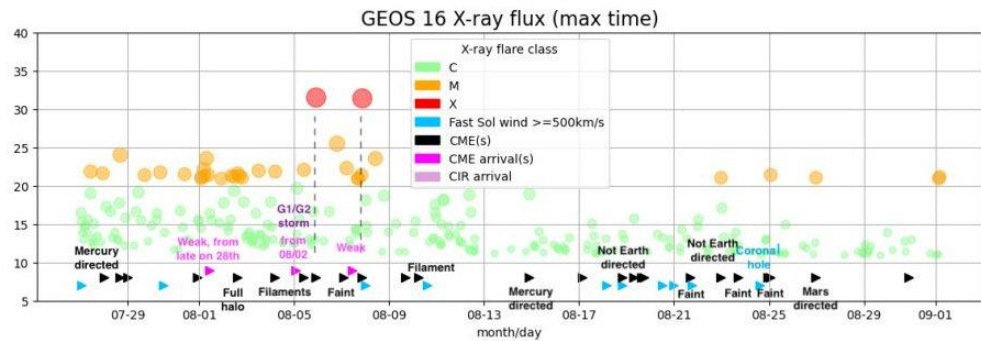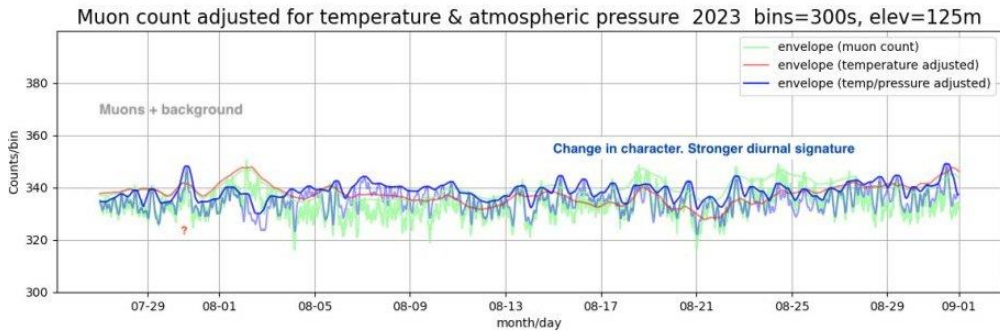
Mark Prescott recorded the Muon flux during August, noting the strong change in behaviour after the 13th. During the period of high flare activity, the muon counts are highly variable. After the 13th when the flare activity declined, the diurnal curve is much clearer on most days.

2022/07 - 2023/07 Muon count (+background) adjusted for temperature/pressure   bins=300s, elev=125m, NW Kent UK
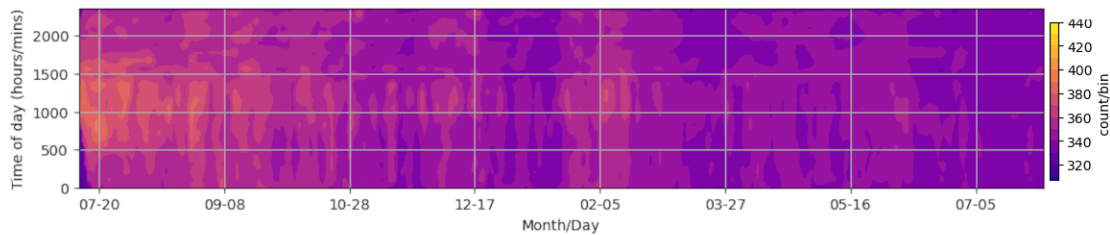
2022/07 - 2023/07 Muon count (+background) Mean daily count   bins=24h, elev=125m, NW Kent UK
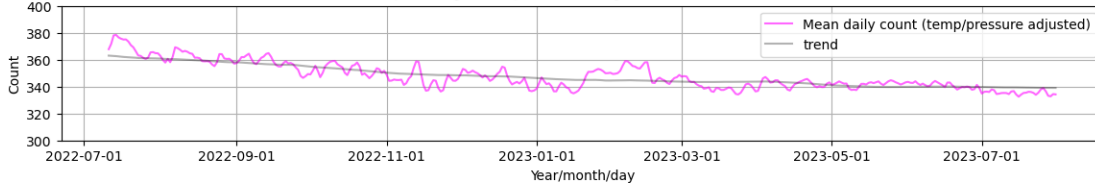
Mark has also produced a chart showing the change in Muon count over the last 12 months. From 2022 July 1 to 2023 July 31 the temperature / pressure corrected mean daily count has fallen by about 6.8%.

PERSEID METEORS

Colin Clements made meteor recordings from the 10th to 14th using the GRAVES radar signal. A low level of activity was seen in the afternoon of the 10th, increasing very slightly overnight into the 11th. Similar activity was again seen overnight 11th to 12th. Much stronger activity was recorded in the evening of the 12th, increasing again in the early hours of the 13th. The afternoon of the 13th was very quiet, but then the strongest activity was recorded from about 21UT on the 13th to 14UT on the 14th when recording ended.
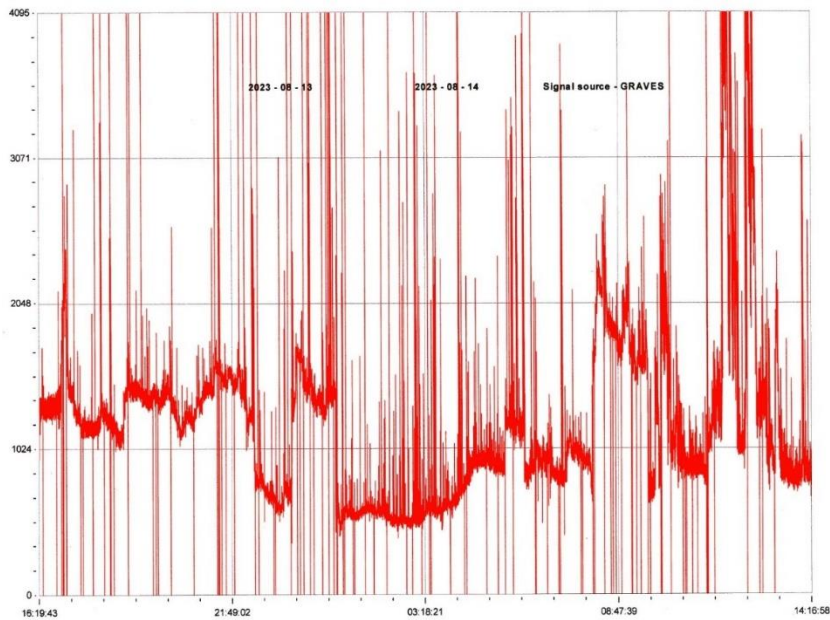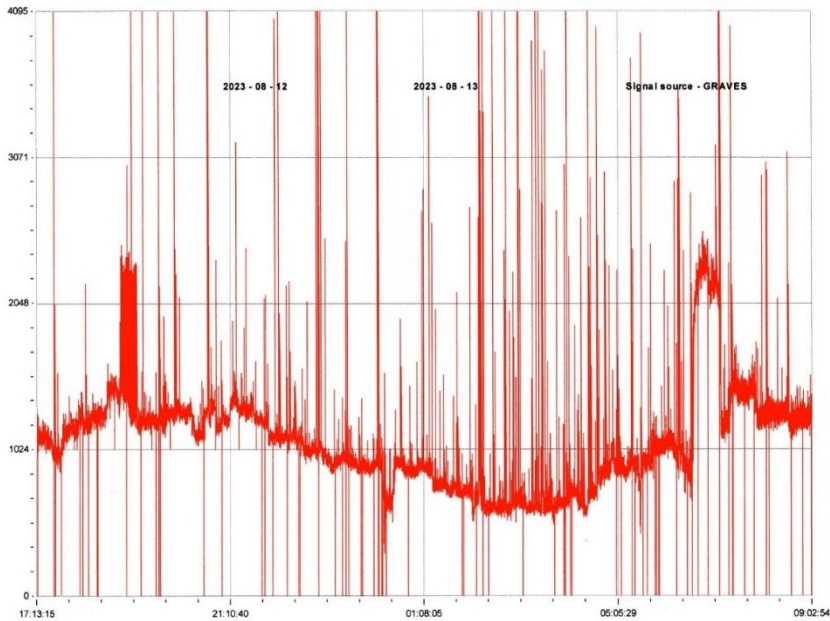
BARTELS CHART

KEY: DISTURBED. | ACTIVE | SFE | B, C, M, X = FLARE MAGNITUDE. | Synodic rotation start (carrington's).

Rotation																													
2552		7	8	9	10	11	12	13	14	15	16	17	18	19	20	21	22	23	24	25	26	27	28	29	30	2020 October 1	2	3	
2553		4	5	6	7	8	9	10	11	12	13	14	15	16 CC	17	18	19	20	21	22	23	24	25	26	27 C	28	29 BCCC	30	
2554		31	2237 2020 November 1 B	2	3	4 B	5 CBCC	6 CBC	7 B	8	9	10 C	11 C	12	13	14	15	16	17	18	19	20	21	22 CC	23	24	25	26 C
2555		27	28 C	29 CM	30	2020 December 1	2	3	4	5	6 C	7	8	9	10	11	12	13	14 C	15	16	17	18	19	20	21	22	23
2556		24	25	26	27	28	29	30	31	2021 January 1	2	3	4	5	6	7	8	9	10	11	12	13	14	15	16	17	18	19
2557		20	21	22	23	24	25	26	27	28	29	30	31	2021 February 1	2	3	4	5	6	7	8	9	10	11	12	13	14	15
2558		16	17	18	19	20	21	22	23	24	25	26	27	28	2021 March 1	2	3	4	5	6	7	8	9 C	10	11	12	13	14
2559		15 B	16	17	18	19	20	21	22	23	24	25	26	27	28	29	30	31	2021 April 1	2	3	4	5	6	7	8	9	10
2560		11	12	13	14	15	16	17 B	18	19	20	21	22 C	23 CCCC	24	25	26	27	28	29	30	2021 May 1	2	3	4	5	6	7 M
2561		8 CC	9 CC	10	11	12 C	13	14	15	16	17	18	19	20	21 C	22 CCMM	23 CCBM	24	25	26 CCCC	27 C	28	29	30	31	2021 June 1	2	3
2562		4	5	6	7	8 CCC	9 CCB	10	11	12	13	14	15	16	17	18	19	20	21	22	23	24 C	25	26	27	28 CBC	29	30 CC
2563		2021 July 1	2	3 MCXM	4 MC	5	6	7	8	9 CCB	10	11	12	13	14 C	15	16 C	17	18	19	20	21	22	23	24	25	26	27
2564		28	29	30	31	2021 August 1	2	3	4	5	6	7	8	9	10	11	12	13	14	15	16	17	18	19 CCC	20	21 C	22	23
2565		24 C	25	26	27 CCCC	28 MCCC	29 CC	30 C	31	2021 September 1	2	3	4	5	6	7 CC	8 C	9	10	11	12	13	14	15	16	17	18	19
2566		20	21 C	22 MM	23	24	25 C	26	27 C	28	29 C	30	2021 October 1	2	3	4	5	6	7	8	9 M	10	11	12	13	14	15	16
2567		17	18	19	20	21	22	23	24	25	26 CCCM	27 CCCC	28 CMMX	29 CC	30 CCC	31	2021 November 1	2	3 CC	4	5	6	7	8	9	10	11	12
2568		13 C	14	15	16	17	18	19	20	21	22	23	24	25	26	27	28	29	30	2021 December 1	2	3	4	5 M	6	7	8	9
2569		10	11	12	13	14	15 CCC	16 CC	17 C	18	19	20 CM	21 M	22 MCC	23	24 CC	25 CCCM	26	27	28	29	30	31	2022 January 1	2	3	4	5
2570		6	7	8	9	10	11	2253 12	13 C	14 C	15	16	17	18	19	20	21	22	23	24	25 C	26 CC	27	28 C	29 BCCC	30	31	1 C
2571		2022 February 2 CC	3	4 CC	5	6	7	8	9 C	10	11	12 MCCC	13	14 CCM	15	16	17	18	19	20	21	22	23	24	25	26	27	28 C
2572		2022 March 1 CM	2	3	4	5	6 C	7 C	8	9	10	11 CCCC	12 C	13	14 M	15 CCMC	16	17	18	19	20 CC	21	22 CC	23 CCCC	24 C	25	26 C	27 C
2573		28 CMC	29 MCCC	30 CCCC	31 CCCX	2022 April 1 CCCC	2 CCMM	3 CC	4 C	5	6 C	7 CC	8 C	9	10	11 CBCC	12	13	14	15	16 MMCC	17 CCCM	18 CCCM	19 MMCC	20 CCCC	21 CMCC	22 CMC	23 C
2574		24	25 MCCC	26 CCCC	27 CCC	28 CC	29 MCCM	30 MMXM	2022 May 1 CCCC	2	3 MCX	4 BMCM	5 CMMC	6 CC	7 CC	8 CCC	9 C	10 CCX	11 CCMM	12 CCCM	13 CCCC	14 CCCC	15 C	16 CMC	17 CCCC	18 CCCC	19 CMMM	20 CMM
2575		21 CCC	22 CC	23 C	24 CC	25 CCM	26 CC	27 CC	28 CC	29	30	31	2022 June 1	2	3	4	5	6	7 C	8	9 CC	10 CCMC	11 C	12	13 C	14 CCCC	15 C	16 C
2576		17 CCCC	18 CCC	19 C	20 CC	21 C	22 CC	23 CC	24 C	25	26	27	28	29	30	2022 July 1	2 BC	3 C	4 CC	5	6	7 M	8	9 CCCC	10 CCCC	11 CM	12 CCCC	13 CCC
2577		14 CMCM	15 CCC	16 MCM	17 CCCC	18	19 C	20 CCCC	21	22 CCCC	23 C	24	25	26 C	27 C	28	29	30	31	2022 August 1	2 CC	3 C	4	5	6 CC	7	8	9
2578		10	11 C	12 CC	13	14	15	16 CMMM	17 MCC	18 CCCM	19 CMMM	20 CCCM	21 C	22 C	23	24	25 CCCM	26 CMMM	27 CCCM	28 CMM	29	30 C	31	2022 September 1 C	2 CC	3 CCCC	4 CCCC	5 CCMC
2579		6 CC	7	8	9 C	10 CCCC	11 CCCC	12 CCCC	13 MCCC	14 MM	15 M	16 CC	17 C	18 MCCC	19 M	20 CCCC	21 CCCM	22 CCCC	23	24 CCC	25 CCCC	26	27 CC	28 CCMM	29 CC	30 CMMC	2022 October 1	2
2580		2022 October 3 CMMM	4 M	5 C	6 CM	7 C	8	9 CM	10 MMCC	11 CC	12 C	13 M	14 C	15 C	16 C	17	18 CC	19	20 CB	21	22 CC	23 C	24 C	25	26	27	28	29
2581		30	31	2022 November 1	2	3	4	5	6	7	8	9	10 C	11 MCCM	12 CC	13 C	14 C	15 CCC	16 CC	17 CC	18 CCC	19 M	20	21	22 CCC	23	24	25
2582		26	27	28	29 C	30	2022 December 1	2 C	3	4 M	5	6	7	8	9	10 C	11 MMMM	12 CMCM	13 MMMC	14	15 CC	16 CCC	17 M	18 C	19 C	20	21	
2583		23 CC	24 C	25	26 CM	27	28 CM	29 CCCM	30 C	31	2023 January 1	2	3	4	5	6 MM	7	8	9 MCMM	10 MC	11 MCMC	12 MC	13 CCC	14 CM	15 C	16	17	18 MC
2584		19 MMC	20 CC	21 CC	22 CMCM	23 C	24	25 MCM	26 CMCC	27	28 C	2023 February 1 CC	2 C	3	4 C	5 C	6 C	7 CC	8 CM	9 MMMM	10 MCCM	11 MMXM	12 MMMM	13 CCCM	14 CCM
2585		15 CCCC	16 C	17 CX	18 C	19 CC	20 CMCC	21 MCCM	22 CCCM	23 CMCC	24 CC	25 CCM	26 CCMM	27 CC	28 CC	2023 March 1 CC	2 CCCC	3 MCCX	4 CMMC	5 CCMC	6 MCCC	7 C	8 MC	9 CCC	10 CCCC	11 C	12	13
2586		14 C	15	16	17 CCCM	18 C	19 CCC	20 C	21 C	22	23 C	24	25 CC	26 CCC	27 CC	28 MC	29 M	30 CC	31	2023 April 1	2	3	4	5 CC	6 MC	7	8	9 CCCC
2587		10 MCCC	11 MC	12 CCC	13 CCCC	14 CCMC	15 CCCC	16 C	17 CC	18 CCC	19 CCC	20 CCCC	21 M	22 CC	23	24 CC	25	26 C	27 M	28 CC	29 CCCC	30 CCM	2023 May 1 CCMC	2 CCCC	3 MMMM	4 MCCC	5 CMM	6 CC
2588		7 C	8 CCCM	9 MCMM	10 MCCC	11 CCCC	12 C	13 C	14	15 CCCM	16 CCCC	17 MMMM	18 MCCM	19 MMMM	20	21 CCCM	22 C	23 CCC	24	25 CC	26 MC	27	28 C	29 MC	30 MMMC	31 CMMC	2023 June 1 C	
2589		3 CC	4 CCCC	5 C	6 CCCC	7 CMCC	8 CC	9 CM	10	11	12	13 CCCC	14 CCC	15 C	16 MCMM	17 CC	18 M	19 MC	20 CCMX	21 CMMC	22 CMCC	23 C	24 CCMC	25 CCCC	26 CCMC	27 CMCC	28 MCC	29 CCCM
2590		2023 July 30 CCCC	1 CCCC	2 CCCC	3 MCCC	4 MC	5 CCCM	6 CCM	7 MC	8 C	9 CCC	10 CCCC	11 MMMM	12 MMCC	13 CCCM	14 MCCC	15 MMMC	16 MCMM	17 CCC	18 MMMM	19 CMCM	20 C	21 C	22 CC	23 CC	24 C	25 CCCM	26 CMCM
2591		27 CMCC	28 CMCC	29 CCCM	30 MC	31 CMCC	2023 August 1 MMMM	2 MMMM	3 CMCC	4 CC	5 MMCX	6 CM	7 CMMX	8 MC	9	10 CCCC	11 CCCC	12 C	13	14 C	15 CC	16 CCC	17	18 C	19 CC	20 CCC	21	22
2592		23 CCC	24 C	25 C	26 C	27	28	29	30 C	31	2023 September 1	2	3	4 C	5	6	7	8	9	10	11	12	13	14	15	16	17	18
2593		19	20	21	22	23	24	25	26	27	28	29	30	2023 October 1	2	3	4	5	6	7	8	9	10	11	12	13	14	15

VLF flare activity 2005/23

BAA RA Section Autumn programme 2023

Monday Nov. 13th 19:30 GMT (19:30 UTC)	**Prof. Sean Paling** STFC UKRI Boulby Underground Lab.	Deep Science at Boulby Underground Laboratory **The search for Dark Matter and Beyond**.
Christmas lecture **Fri. Dec. 1st.** 19:30 GMT (19:30 UTC)	**Prof Clive Tadhunter** Department of Physics and Astronomy University of Sheffield	**Active Galactic Nuclei** (AGN) emit at least as much radiation by themselves as the integrated light of all the stars in a typical galaxy, yet this radiation is produced in a region that is smaller than the solar system.

Neutral Hydrogen Receiver Low Noise Amplifier Noise Figure Measurement

Written by: Stephen Bentley
Date: 13 Sept. 2023

1.0 Preamble

The low noise amplifier (LNA) for the radio astronomy neutral hydrogen receiver is a critical component within the receiver. The gain and noise figure performance of the LNA will in part determine the limit of sensitivity of the receiving system. This report presents a measurement technique to obtain the LNA noise figure.

2.0 LNA specifications

The LNA is a component supplied to the ASV from Radio Astronomy Supplies in the US. Figure 1 shows the physical item in a partially assembled state with the lid removed from the enclosure to reveal the internal circuitry. The LNA design uses a discrete circuit that operates from a 12 volt DC power supply.
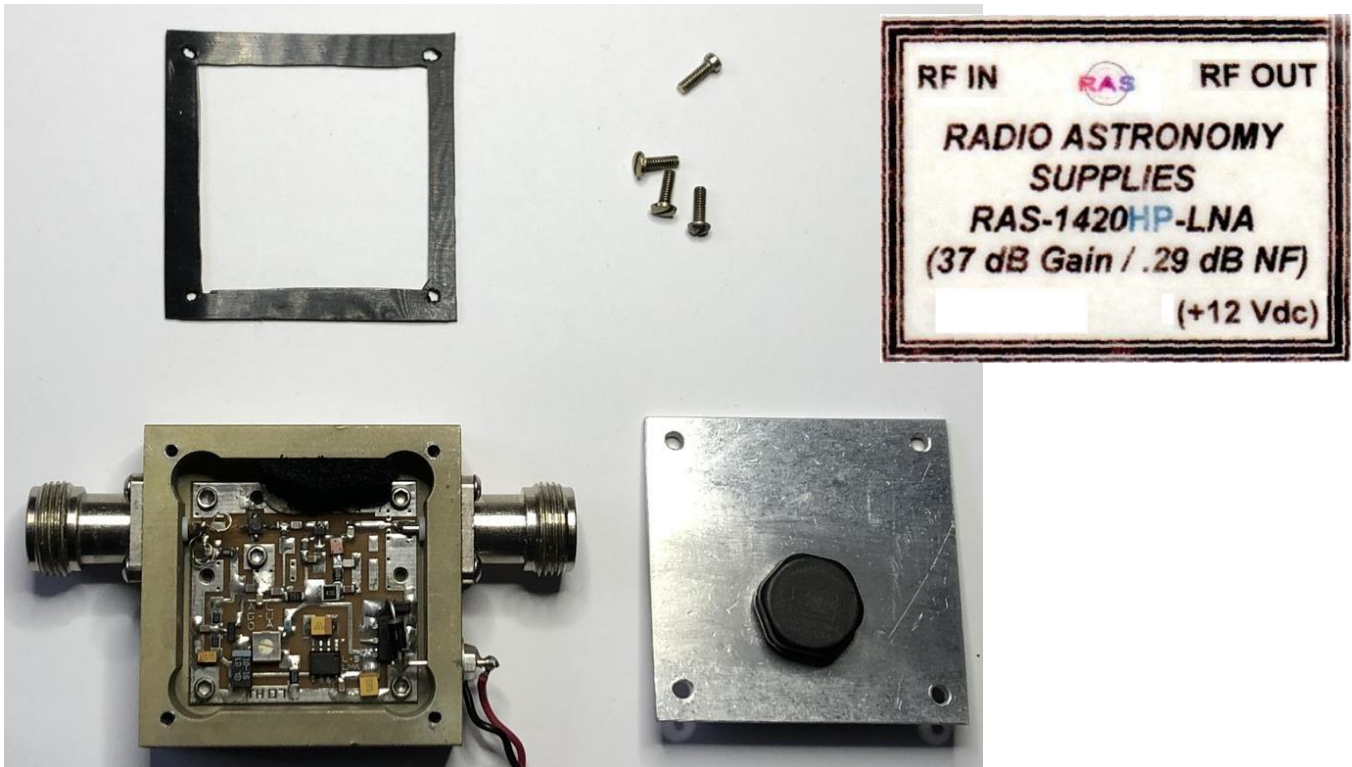

Figure 1. Low Noise Amplifier Module

In the top right of Figure 1 is the label supplied with the LNA. This indicates the gain and expected noise figure (NF). The LNA should have a gain of 37 dB and a noise figure of 0.29 dB which is an exceptional result and suggests

quality components have been used in the design. The author has performed prior measurements of the LNA to provide additional measurements to fully qualify the LNA. The specification for the LNA can therefore be presented as shown in Table 1.

Frequency:	1420 MHz
Gain:	37.17 dB (measured)
NF:	0.29 dB (implied)
Current Consumption (12 Volts):	58.5 mA
Gain versus temperature:	- 0.036 dB per degrees C. (measured)

Table 1 LNA Specifications

3.0 LNA and Front End Assembly

The LNA will not be used in isolation within the neutral hydrogen receiver. To provide a means of calibration a stable reference noise signal generator is provided which may be switched into circuit so that the receiver response can checked regularly. Therefore, an RF switch is placed ahead of the LNA. The switch induces a small RF loss which will degrade the overall noise figure of the LNA assembly. Shown in Figure 2 is a block diagram of the LNA and Front End assembly with the RF switch and reference noise signal generator.
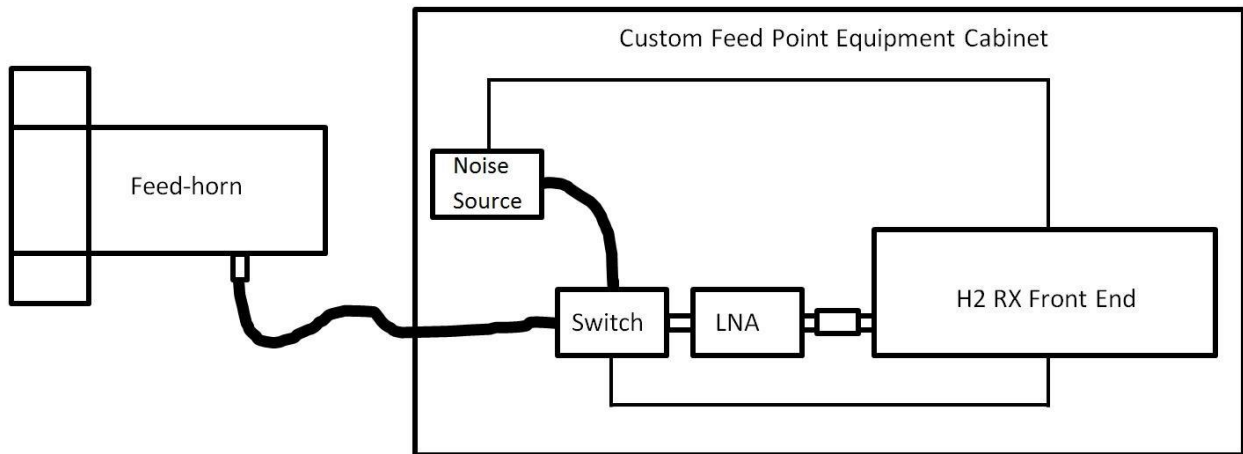

Figure 2. LNA and Front End Assembly

The RF switch is a MiniKits EME225 relay and the author has measured the insertion loss of the RF switch to be 0.2 dB.

The LNA, RF switch and Reference Noise Signal Generator are all housed within a separate airtight enclosure. Figure 3 shows an internal view of the LNA enclosure. This complete assembly is what will be measured to obtain the LNA noise figure. Therefore, the measured noise figure will include the impact of the RF switch and the various RF adapters and connectors. The 400 mm length of coax cable at the output of the LNA will also be part of the measurement.
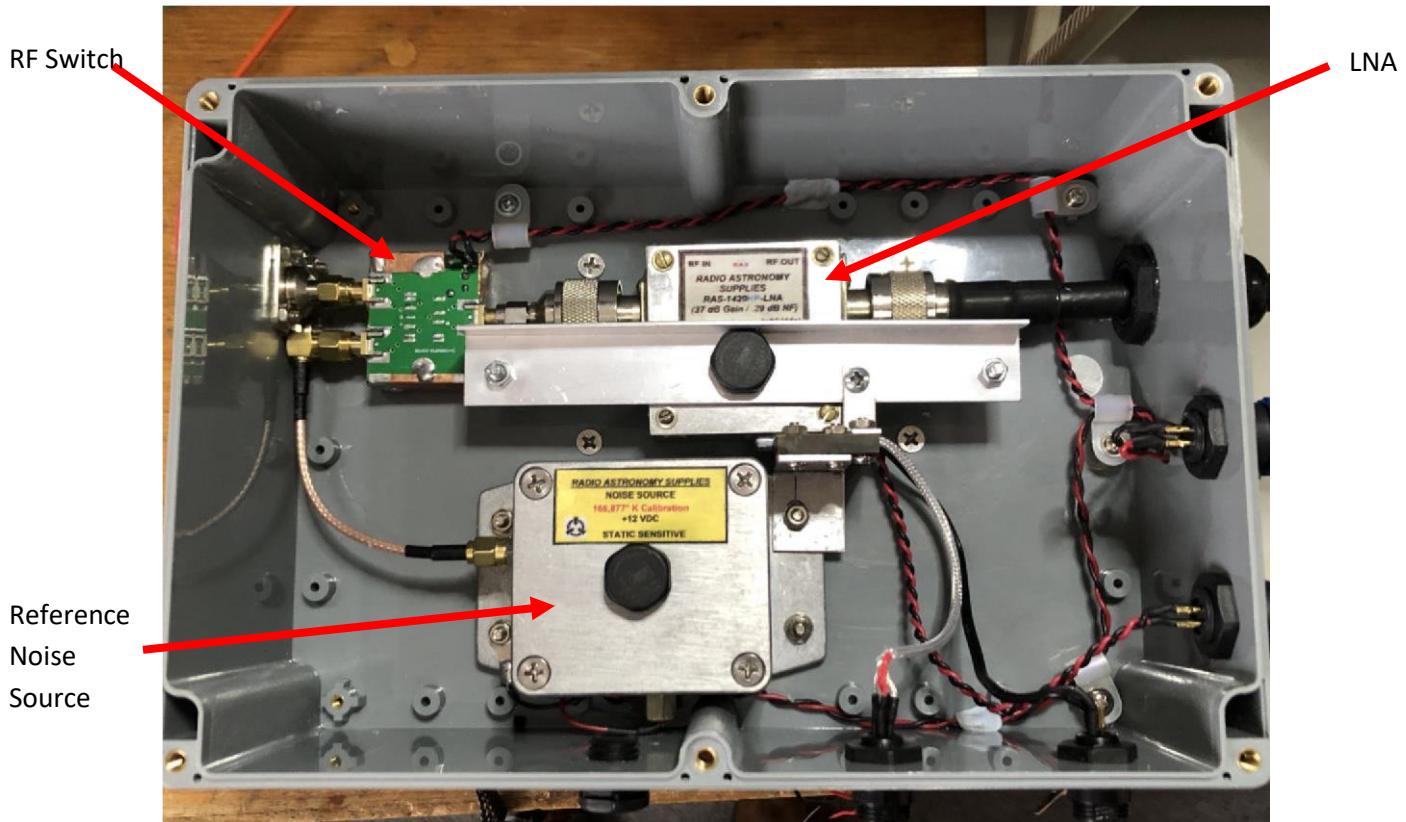
Figure 3. LNA, RF Switch and Reference Noise Signal Generator Enclosure

4.0 Noise Figure Measurement

The author owns a HP8560A spectrum analyzer which will be used to measure the noise figure of the LNA assembly. The noise figure of an amplifier is given by equation 1 shown below.

$$NF = 10log_{10}N_o - 10log_{10}(G) - 10log_{10}(kTB)$$

1

Where
N_0 is the Noise power output
G is the Gain of the amplifier
K is Boltzmann's constant which is 1.3806 x 10^{-23} J/K
T is temperature in Kelvin
B is the measurement bandwidth in Hertz

Equation 1 can be further broken down to simplify the terms. This is shown in Equation 2. Here the Log (KTB) term has been separated into 2 terms, one just relating to temperature and the other relating to bandwidth.

$$NF = 10log_{10}N_o - 10log_{10}(G) - 10log_{10}(4.00x10^{-18}) - 10log_{10}(B)$$

2

At room temperature (say 17 C) T becomes 290K. KT therefore becomes 4 x 10^{-18} milli Joules. Milli Joules has been used here because we also want to express the Noise figure in terms relative to dBm or dB relative to 1 milliwatt. The resolution bandwidth of the spectrum analyzer can be set to 10 Hertz therefore B is 10. If a resolution bandwidth of 1 Hz was possible, the last term becomes 0 and can be eliminated from Equation 2.

The temperature term in equation 2 can be calculated to produce equation 3 shown below.

$$_3 \ NF = N_o \, [\text{dBm}] - G[\text{dB}] + 174 \, dBm$$

Therefore, to determine the noise figure of the LNA assembly, the gain needs to be measured, and the amplifier output noise level in dBm when the amplifier has the input terminated with a 50 Ohm dummy load at room temperature. The gain was already known as being 37.17dB however this was once again verified before performing the noise measurement. It is also pointed out here that the gain is the total system gain which includes the RF switch, connectors, and cables. The 50 Ohm dummy load was a high quality Huber + Suhner device with a specified VSWR better than 1:1.05 at 1.4 GHz.

Shown in Figure 4 is a screen capture of the spectrum analyzer during the noise measurement process. At this capture, the video averaging had completed 6 sweeps. The settings on the spectrum analyzer are summarized in table 2 below.

Centre Frequency: 1420 MHz
RF attenuator: 0dB
Span: 10 KHz
Resolution BW: 10 Hz (minimum setting)
Video BW: 1 Hz
Amplitude Scale: 1dB/div.
Video Averaging: On (100 sweeps)
Marker: Noise Measurement

Table 2. Spectrum Analyzer Settings for Noise Measurement

Although the resolution bandwidth could not be set to 1 Hz, it was not necessary to subtract the additional 10 dB from the noise figure measurement. This is because the spectrum analyzer marker feature already provides a direct reading of noise in terms of dBm/Hz.
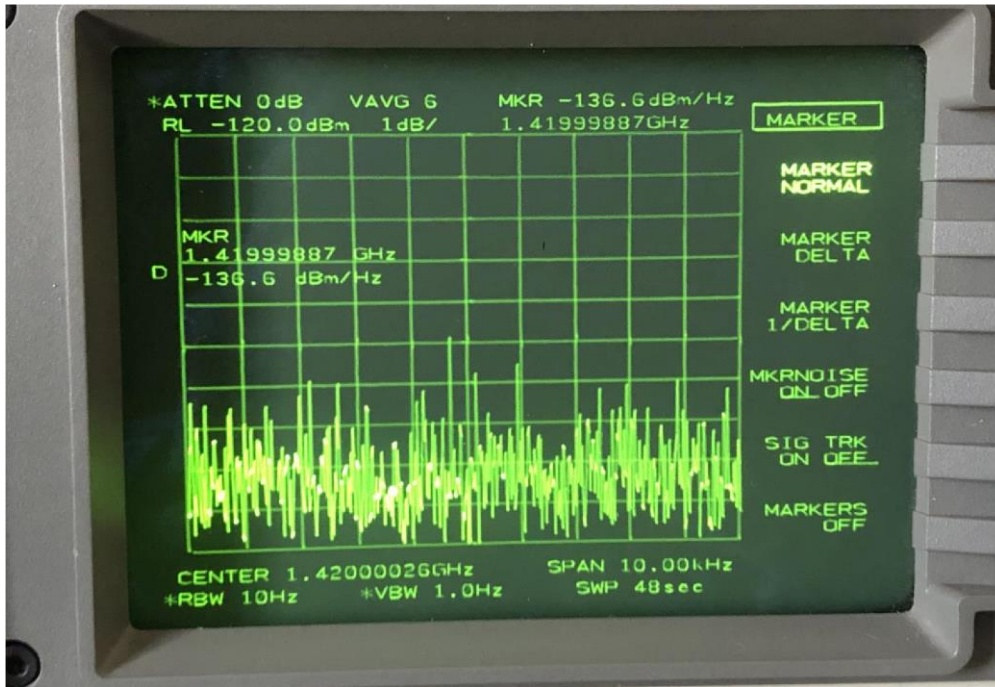
Figure 4. Spectrum Analyzer Noise Measurement (6 Sweeps)

It took approximately 80 minutes to complete 100 sweeps of the video averaging. Figure 5 is a screen capture at the conclusion of 100 sweeps of the video averaging. The measurement then stabilized with a value -136.3 dBm/Hz.
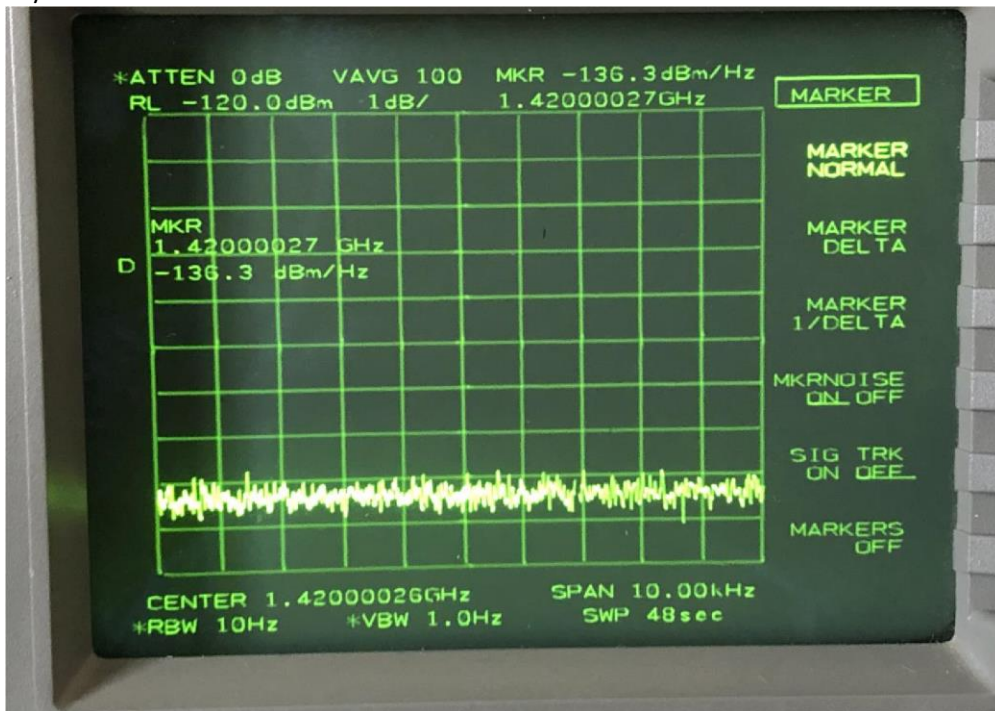

Figure 5. Spectrum Analyzer Noise Measurement (100 Sweeps)

Placing the known values into equation 3, we get the result shown in equation 4.

4   NF = - 136.3dBm – 37.17dB + 174dBm

                    NF = 0.53dB

There will be a tolerance on this value which may be of the order of +/- 0.2dB.
The prior measurement of the insertion loss of the RF switch (0.2dB) can be subtracted from the result in equation 4 to produce a NF = 0.33dB for the LNA alone. This is very close to the specified performance of the LNA which is stated to be 0.29dB.

5.0 Conclusion
The LNA and RF switch assembly is expected to have a noise figure of about 0.5dB +/- 0.2dB. This is a degraded result from the ideal 0.29 dB if the LNA was to be used without the RF switch and reference noise signal generator. Therefore, a slightly degraded receiver sensitivity will occur. There will be further degradation of the noise figure with the inclusion of the coax cable between the antenna feed-horn and the input to the LNA. This is expected to be quite low, however, as the cable and connector loss should be less than 0.07dB.

6.0 Acknowledgements
The measurement technique and mathematical derivations presented in this report were obtained from an instructional video found on YouTube. The video was produced by a qualified RF engineer, Mr. Stephen K. Remillard. This link is provided for the YouTube video.

   https://www.youtube.com/watch?v=-LfzJjxdtTE

Investigating the Performance of a Semi-Professional Magnetometer for Space Weather Research: 13 Years of Measurements from a Backyard in Anchorage

William H. Barndt, Doğacan S. Öztürk, Whitham Reeve

University of Alaska Fairbanks, Geophysical Institute, Space Weather UnderGround (SWUG)

whbarndt@alaska.edu, dsozturk@alaska.edu

May 23rd, 2023

Space weather is an important field of study for Alaska as it can impact the everyday lives of Alaskans. One way that Space Weather can cause disruptions is through geomagnetically induced currents (GICs) which can occur along power transmission lines, pipelines, and railroads. Geomagnetic disturbance measurements are one way of studying when and where GICs can occur, which is essential for safeguarding Alaska's infrastructure. The Space Weather UnderGround (SWUG) project, founded by Charles Smith at the University of New Hampshire, was created to increase measurements of geomagnetic disturbances by deploying low-cost arrays of magnetometers using Simple Aurora Monitors (SAMs) provided by Whitham Reeve. In 2020, the University of Alaska Fairbanks developed their own SWUG program for understanding these geomagnetic disturbance effects in Alaska. This project's research was motivated by investigating the capabilities of SAM-III, for understanding Space Weather related disturbances. I obtained a unique dataset of SAMIII data, curated by Whitham Reeve, spanning at least one solar cycle, and developed tools and datasets to analyze and study it by first comparing it to Narod science-grade magnetometers deployed across Alaska as a part of the Geophysical Institute Magnetometer Array (GIMA). I (Barndt) investigated the dependencies of this semi-professional magnetometer scientifically and operationally by analyzing its relation to the solar cycle and subsurface temperature at Eagle River close to where it is deployed. With these analyses, I was able to evaluate the performance of SAM-III and provide guidance for optimizing its performance for GIC research.

Introduction

Whitham Reeve curated over 13 years of Simple Aurora Monitor (SAM) magnetometer data from 2009 to present – 2 years of a 1-axis SAM, from 2009 to 2010, and 12 years of a 3-axis SAM (called SAM-III) data, from 2010 to 2022. The focus of this project was to conduct a preliminary investigation into the scientific and operational dependencies of SAM-III given this large-spanning dataset. The first goal was to compare the data provided with a science-grade magnetometer nearby for a qualitative and quantitative comparison. This was chosen to be a Narod magnetometer in Trapper Creek, a part of the Geophysical Institute Magnetometer Array (GIMA). Given that the SAM-III data encompasses a whole solar cycle, we would then look at solar sunspot information investigate its scientific dependencies since the number of sunspots correlates with which stage of the solar cycle the sun is located, the two major stages being the solar maximum or the solar minimum. Lastly, understanding that SAM-III magnetometers have temperature dependencies, we would look at the subsurface temperature nearby to see its impact operationally.

Geomagnetic Disturbances

Geomagnetic disturbances in Earth's magnetosphere can occur due to interactions with the solar wind and space weather events and can generate Geomagnetically Induced Currents (GICs). These GICs can cause significant impact to long ground-based conductive infrastructure such as damage to high-voltage power transmission systems or railway systems and increased corrosion of gas and oil pipelines. [1] One way of measuring these geomagnetic disturbances is using a magnetometer. As a reminder, geomagnetically induced currents are governed by Faraday's Law of Induction, equation (1), in electrodynamics which states that a change in the magnetic field with time can cause a change in the electric field in space, which can constitute a current.

$$\nabla \times \mathbf{E} = -\partial \mathbf{B}/\partial t \tag{1}$$

Space Weather UnderGround (SWUG) Program

The Space Weather UnderGround (SWUG) Program, founded by Dr. Charles Smith at the University of New Hampshire, is an educational outreach program geared towards undergraduate and high school students to build and deploy a cost-effective and research-capable array of magnetometers across Alaska. The magnetometers used by SWUG are called Simple Aurora Monitors (SAMs).

3-Axis Simple Aurora Monitor (SAM-III)

3-Axis Simple Aurora Monitor (SAM-III) is a semi-professional magnetometer designed by Dirk Langenbach and Karsten Hansky and developed by Reeve Engineers, founded by Whitham Reeve, who distributes SAM-III kits to both the University of Alaska Fairbanks and the University of New Hampshire SWUG programs. [2] SAM-III is a magnetometer kit that consists of a main controller printed circuit board (PCB), keyboard PCB, a Liquid Crystal Display (LCD) module, three fluxgate magnetometer sensors and includes an option for a temperature sensor. Generally, magnetometers have a dependency on temperature, and it varies with magnetometer setups. The SAM-III fluxgate magnetometer sensor is very sensitive to temperature variations. The temperature coefficient is approximately −100 to −150 nT/°C (the minus sign indicates that the amplitude increases as the temperature decreases). (pg. 66) [3] SAM-III's sensor has a range of approximately ±50,000 nT with a resolution of 1 – 2 nT. (pg. 2) [3] The data typically has a temporal resolution of 1 second however the data provided by Whitham Reeve had a temporal resolution of 10 seconds.

Methodology

The SAM-III dataset provided by Whitham Reeve included .log, .sam, .png, and .txt files for each day for the years 2010 through 2022. The .log files include information on the number of correct and erroneous lines of readings for that day and what the erroneous lines were read as. The .sam files give metadata on the components, date, location, author and what each reading is for each component subtracted by a baseline. The .png files show a time series plot of baseline subtracted data for each component for that day, these are created from the .sam files. Lastly, the .txt files include the raw magnetometer data for each reading and each component. [4] These .txt files are the files that were parsed through to use for this project. This data included the 'datetime' of the reading and x, y, and z components of the magnetic field.

The tools used for parsing and analyzing the data were the Python programming language with the Pandas data analysis library [5]. Using these tools, I created a toolset of scripts to work with this data. In Figure 1 you can see the Architecture Diagram of the scripts created during the duration of the project.

The SAM-III dataset included various files on measurement information but the .txt files for each day were used to extract the magnetometer data. In the diagram, I represented these .txt files as the RAW SAIII .txt files and created the SAM-III_data_parser.py script to process the files into a Python readable format. After parsing the .txt files, the non-erroneous data was read into a panda DataFrame with the rows representing each measurement and columns representing the date, time and magnetic field component information for each measurement. It was then exported to a .pickle file, a serialized representation of the Pandas DataFrame object, used for ease of transfer and internal Python readability, so the raw data can be manipulated and, if needed, reviewed with ease. Afterwards, the raw SAM-III data .pickle files are then processed to a standard data format, used so that both magnetometer's data can be analyzed on a similar footing. This format first baseline subtracts all of the readings, where, for each day, each reading is subtracted by the first reading of that day. This allows normalization of the values to directly see the changes for that day and to be able to compare it to measurements from other instruments easier. Then, a new coordinates system, made of *H*, *D*, and *Z* components, is calculated from the *x*, *y*, and *z* coordinate measurements. Figure 2 is a visualization of this coordinate system. The *Z*-component is the same as in the *x*, *y*, *z* system however *x* and *y* transformed using equations (2) and (3).

$$H = \sqrt{X^2 + Y^2} \tag{2}$$

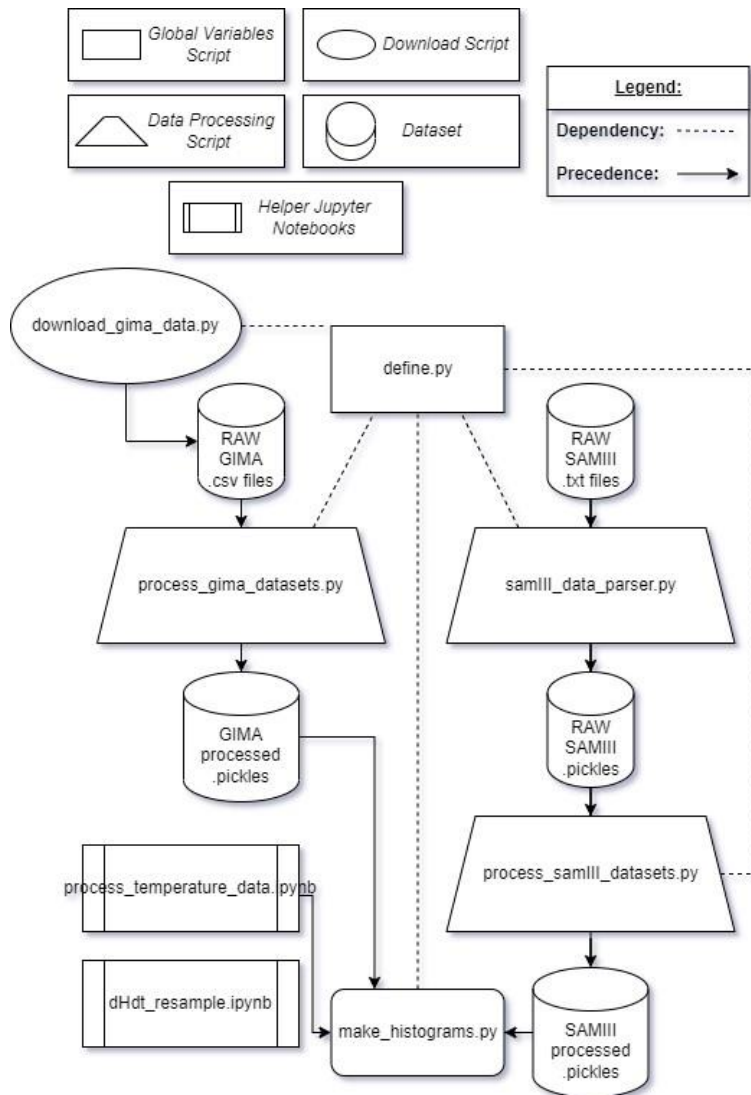$$D = \tan^{-1}\left(\frac{y}{x}\right) \tag{3}$$

Figure 1: Architecture Diagram of the scripts used during the project. [6]

This coordinate system is useful because geomagnetic activity and disturbances occur more often in the horizontal component than the *z*-component which allows us to couple the *x* and *y* measurements into one value. With this *H*-component, δH, the difference in the current *H* and the previous, is calculated and δt, the difference in time, is calculated to then calculate $\partial H/\partial t$, the change in the *H*-component in time for each reading.

B: total field
H: horizontal component
X: northward component
Y: eastward component
Z: vertical component
D: declination
I: inclination
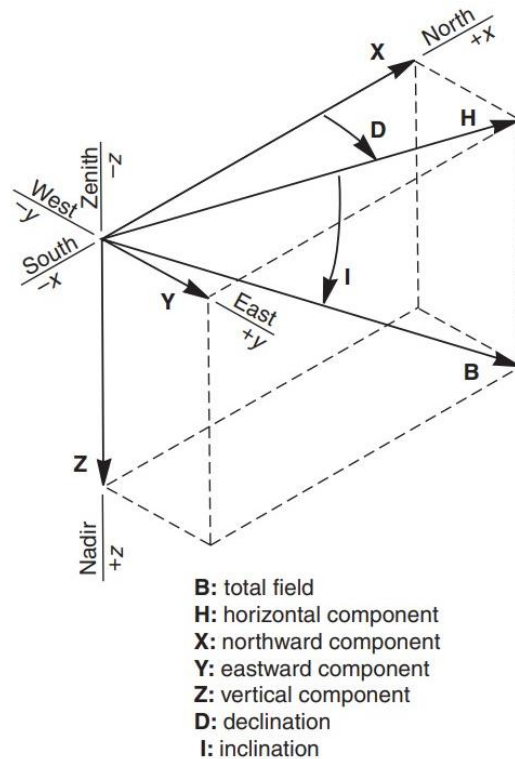
Figure 2: *H*, *D*, *Z* Coordinate System. [7]

Geophysical Institute Magnetometer Array (GIMA)

The Geophysical Institute Magnetometer Array (GIMA) is comprised of thirteen science-grade magnetometer stations dispersed across Alaska. Each station includes a Narod ring-core, fluxgate magnetometer [8], GPS clock and data logger which then transfers the data collected to the Geophysical Institute for verification, to archive and make available to the broader space weather science community. [9] This data can be retrieved publicly from the GI's website [10] and it can be shown graphed as the *H*, *D*, *Z* components with the median of the day subtracted from the readings. As of May 23rd, 2023, the *H*, *D*, *Z* components of GIMA physically correspond to *x*, *y*, and *z* components respectively. The temporal resolution of the readings for GIMA magnetometers is 1 second.

The GIMA magnetometer used was from GIMA's Trapper Creek site about 75 miles north of Anchorage (roughly 0.97 degrees geographic latitude and 0.27 degrees geographic longitude) and is roughly similar in magnetic latitude and longitude. This GIMA site was chosen due to its close distance to Anchorage but also due to its overlap in the time the data was taken — it covered all the years of Reeve's SAM-III data from 2010 to 2023. This data was retrieved from GIMA Magnetometer Archive of the Geophysical Institute [11]. The data was downloaded in a .csv file format for each day which contained information on the datetime of the reading and *x*, *y*, and *z* components of the magnetic field. The process of subtracting the start of the day from the daily readings and the coordinate and differential calculations are done the same as the GIMA dataset, converting the GIMA dataset into the same standard format talked about earlier.

67

Scientific and Operational Analyses Datasets

The two other datasets used in the final analysis were the yearly mean total sunspot number and the yearly mean subsurface temperature. The yearly mean total sunspot number dataset was retrieved from the Sunspot Index and Long-term Solar Observations website [12] in a .csv file which covers the years 1700 to the present. The subsurface temperature data was retrieved by the Alaska Road Weather Information System on the Iowa State University website. [13] Multiple stations' subsurface temperature data was retrieved that was nearby either Trapper Creek's GIMA magnetometer or Reeve's SAMIII magnetometer in Anchorage. This data was downloaded as .xlsx files which were then converted to .csv files to be read into Python. Station GWSA2 in Eagle River was selected for the subsurface temperature comparison due to the largest continuous data that overlapped with the years of the magnetometer data. This data covered years 2011 through 2019 with hourly readings which were then averaged together and exported as a .pickle file in the process_temperature_data.ipynb notebook to form the yearly mean subsurface temperature. After each of these datasets was created and processed, they were then read into the make_histograms.py script to start the analysis.

Results

The goal of this project was to analyze the SAM-III dataset scientifically and operationally. This was done by comparing each year and how many days in that year there were readings above a certain threshold and comparing it to sunspot and subsurface temperature data. Figures 3, 4, 5, and 6 show how well SAM-III read *H*-component events over a certain threshold of the strength of the magnetic field compared with the Trapper Creek GIMA magnetometer. Figure 7 shows this for the *z*-component for over a threshold of 100 nT.

These figures were created from the SAM-III and GIMA standard format datasets, where both included datetime *x, y, z, H, D, δH, δt, δH/δt*, information for each reading. Both datasets were first resampled into minute readings for ease of processing time during figure creation since standard format SAM-III data constituted roughly 2 GB of data and standard format GIMA data was roughly 20 GB. Afterwards, these resampled datasets were used in the make_histograms.py script to create the histograms in these figures. This was done by first filtering out the data not within the thresholds then resampling again, instead to daily readings. [6]

H- and *Z*-Component Threshold Analyses

In these plots, you can see the comparison between SAM-III and GIMA and their number of days with readings above 250 nT and 500 nT for each year with the year values for sunspot number and subsurface temperature. The first thing to note is how well SAMIII and GIMA's counts for each component are comparable to each other. Most years have roughly similar counts with GIMA typically having more than SAM-III. The next is readings from SAM-III and GIMA generally show a solar cycle dependence with the solar maximum, the period of greatest solar activity, being around 2015-2016 and the solar minimum, the period of the lowest solar activity, around 2019-2020.
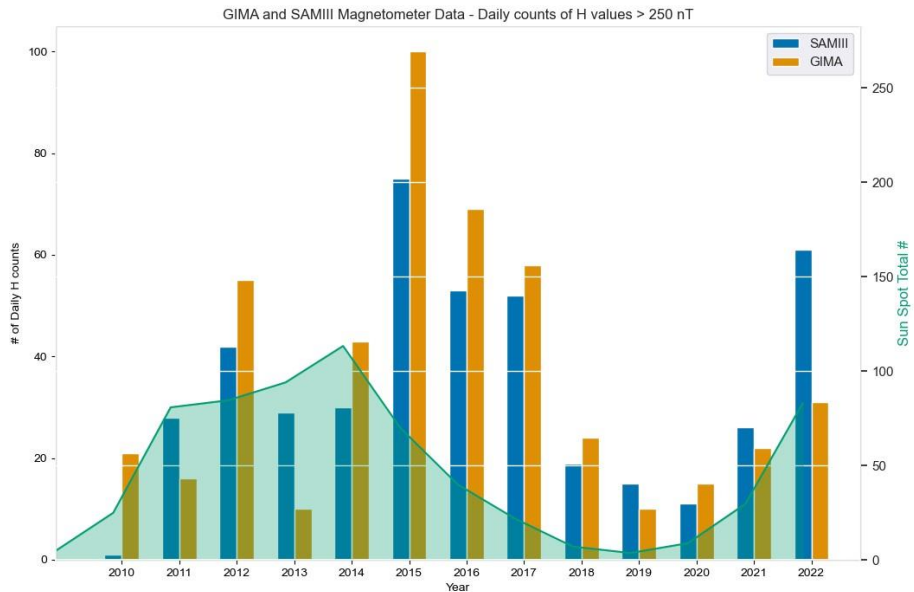
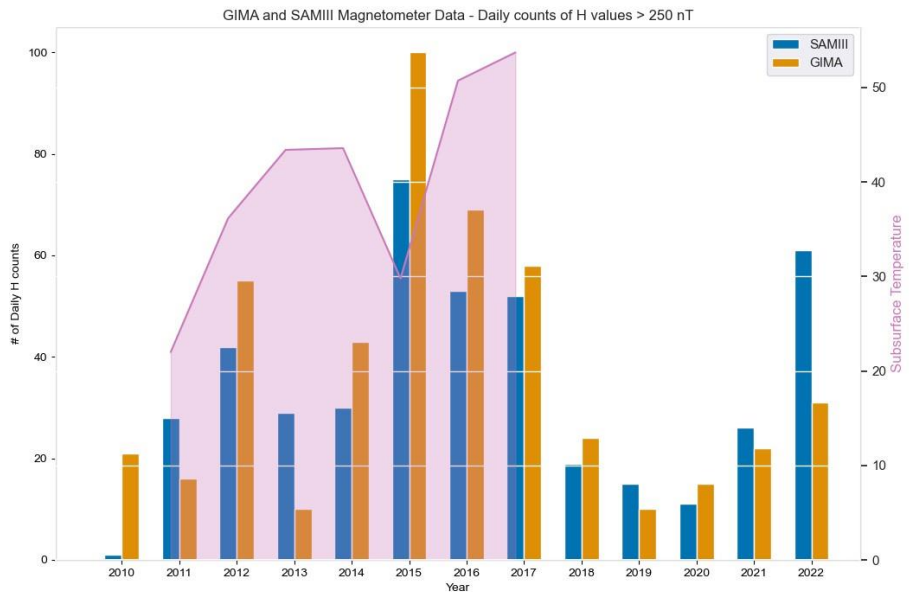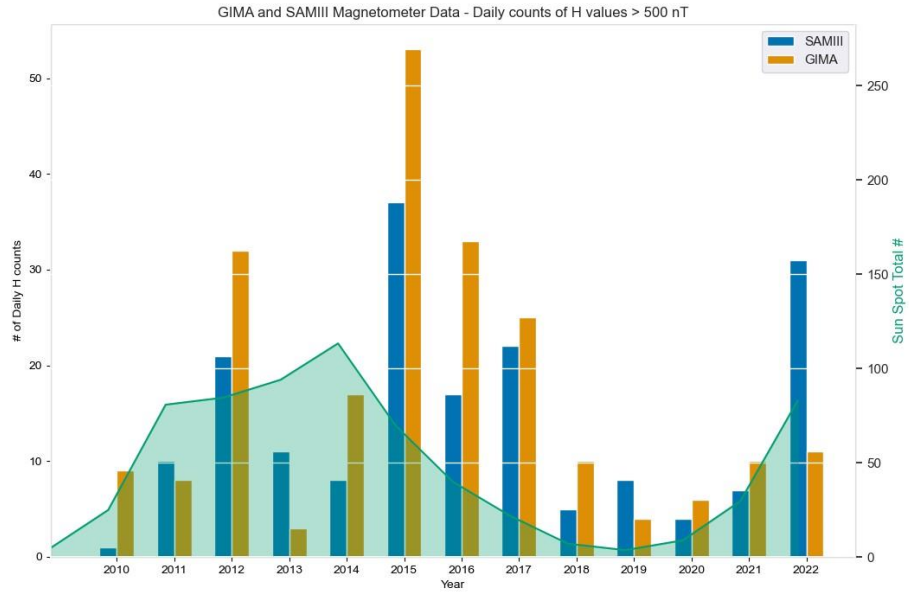Figure 3: Number of days with |H| > 250 nT compared with the sunspot number

Figure 4: Number of days with |H| > 250 nT compared with the subsurface temperature

The peak of that solar cycle was in 2014 when the yearly mean sunspot count is the greatest. However, the counts for both SAM-III and GIMA are at their peak the following year. This is generally seen to be the case and has been shown in other observations [14]. Thus, it seems both SAM-III and GIMA are reliable in providing information on solar activity and space weather events. For the operational analysis, there didn't seem to be any direct correlation between the number of days above the threshold and the yearly mean subsurface temperature

from Eagle River and a more granule look at the temperature data is necessary to better see temperature variation with the SAM-III magnetometer.

Figure 5: Number of days with |H| > 500 nT compared with the sunspot number
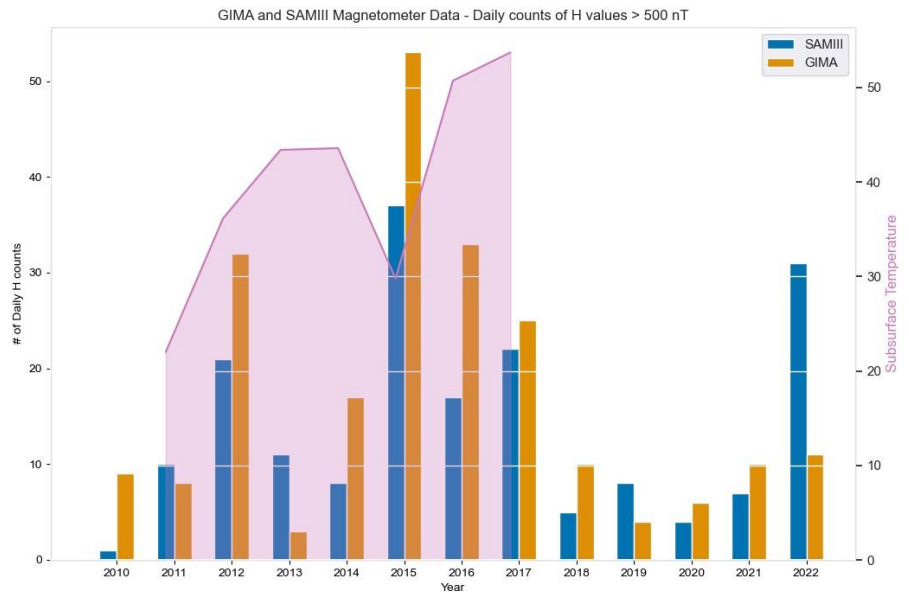
Figure 6: Number of days with |H| > 500 nT compared with the subsurface temperature

δH/δt Threshold Analyses

The next analysis was looking at the change in the magnetic field in time, or *δB/δt*. Purely looking at the horizontal component *H*, we looked at two thresholds, 6 nT/s and 20 nT/s, shown in figures 8 and 9. These thresholds were chosen based on other research that has been done with measuring geomagnetic disturbances. [15]

These sets of plots don't include the subsurface temperature comparison since when *δH/δt* is calculated the baseline dependence of temperature is mostly eliminated in the first order. It's important to note that these plots are in log scale and it can be seen that GIMA's magnetometer readings for both thresholds are roughly an order of magnitude larger than SAM-III readings. This seems to be an issue with the temporal resolutions of both datasets. GIMA's magnetometer data had a temporal resolution of 1 second and this implementation of the SAM-III device had a temporal resolution of 10 seconds. One analysis that could be done to further look into this would be to resample the GIMA dataset into 10-second readings first then calculate *δH/δt.* instead of the inverse, then compare the results of each *δH/δt* .

Anomalies and Erroneous Data

Anomalies

There were two notable anomalies found in this analysis, the first being some of the SAMIII data in the year 2022. In Figure 10 and 11 you can see two anomalous phenomena: a steady increase in magnetometer readings from 6:00 UTC to roughly 16:00 UTC and a discontinuity at 18:00 UTC. The first anomaly is hypothesized to be due to temperature variability with the magnetometer sensor, however further investigation into SAM-III's temperature dependencies is needed before a conclusion can be made. This is actively underway with future SAM-III devices which include a temperature sensor. The second anomaly is unknown, but it seems like it could be that the baseline subtraction calculation made for these plots stopped at 18:00 UTC and so the figure plots the absolute magnetic field. There might be more anomalies in the 2022 data and other years, but these were the first major found near the end of this project.

The latter anomaly doesn't seem like it should have an effect on the dataset that was worked with, since the text files, which measured the absolute magnetic field, were used. However, the former anomaly could possibly lead to many days having counts about the threshold without actual geomagnetic activity happening. This seems to be seen when comparing the day counts of SAM-III and GIMA in the *H-* and *z*-component plots. Most of the years in the *H-* and *z*-component plots have GIMA as having more counts than SAM-III which is expected, however, there are a few other years that also have SAM-III having more counts. In 2013, GIMA had gaps of data missing throughout the year which caused the low count and in 2011 and 2019 SAM-III had more counts but a closer look into the datasets is required to better understand why these occurred. Looking at the *δH/δt* plots, GIMA seemed to have a fairly high count of measurements above both thresholds and further look into why this is, exactly, is also required. It was found that some of these counts were due to erroneous infinity values.

Erroneous Data

The data from 2010 to 2023 was not perfectly continuous and some of the calculations made during the creation of the dataset could've been done incorrectly. These would produce erroneous data consisting of Not-a-Number (NaN) and Infinity (Inf) values in the pandas DataFrame. After resampling both datasets into minute readings, roughly 1.5% (9935 rows) of SAM-III data contained NaN values and 0.00002% (110 rows) contained Inf values. With GIMA, 22% (1449380 rows) of the data contained NaN values and 0.014% (89443 rows) had Inf values. The

NaN values seem to be the cause of missing data and the Inf values could possibly be from some of the calculations performed.
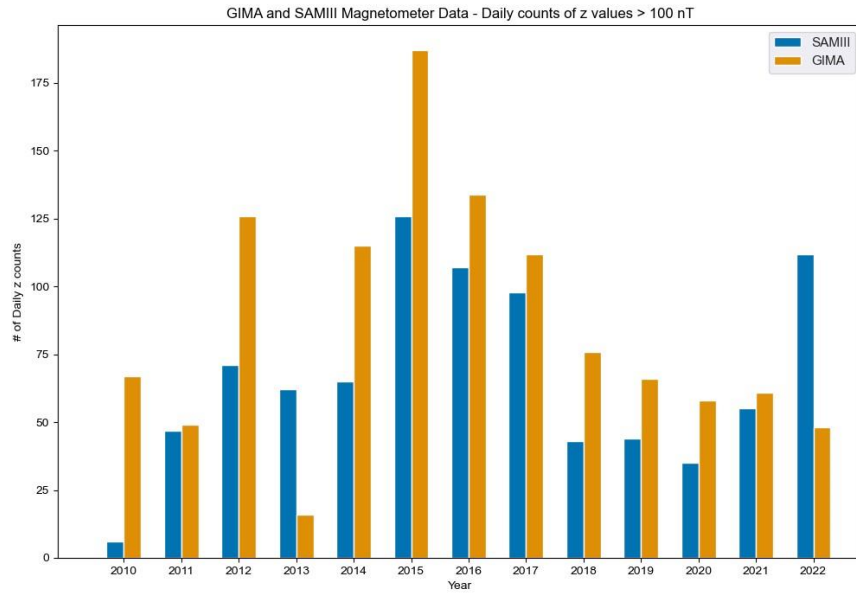

Figure 7: Number of days with |z| > 100 nT compared with the sunspot number
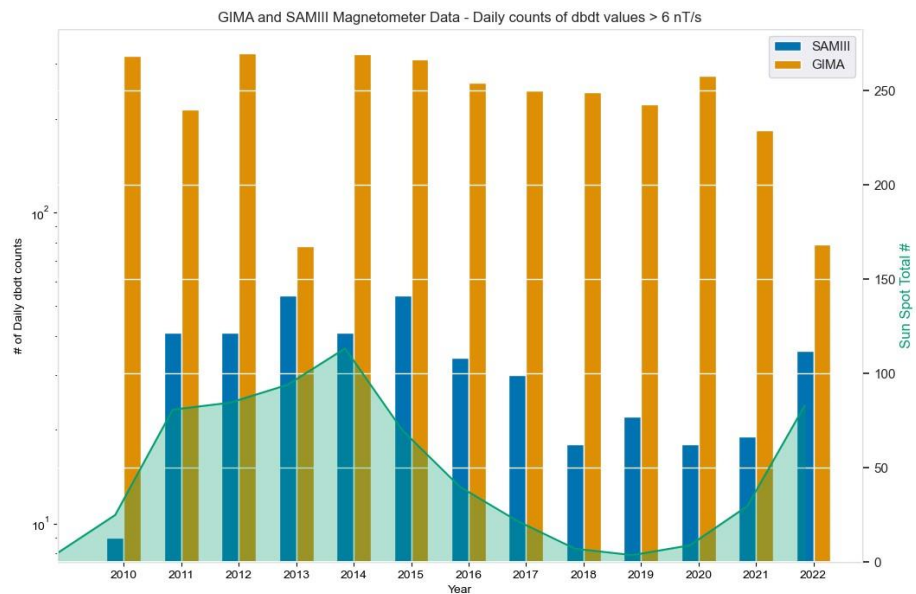

Figure 8: Number of days with $|\delta H/\delta t|$ > 6 nT/s in log scale

Conclusion

As a semi-professional magnetometer, SAM-III seems to reliably measure geomagnetic disturbances as compared to GIMA's Trapper Creek magnetometer in each component in addition to solar activity as shown by the solar cycle dependence with the yearly mean sunspot number. Conclusions cannot be made on the temperature dependencies of SAMIII at the moment and further investigation is required but it is actively being investigated with newly deployed SAM-III devices including a temperature sensor. Based on the $\delta H/\delta t$ performance it is recommended that SAM-III devices be run with the highest temporal resolution possible with this already in action with current deployments of SAM-III taking measurements every 1 second instead of 10 seconds. The future will be promising to study the scientific and operational capabilities of SAM-III with higher temporal resolution in measurements and a temperature sensor in newer SWUG SAM-III deployments.
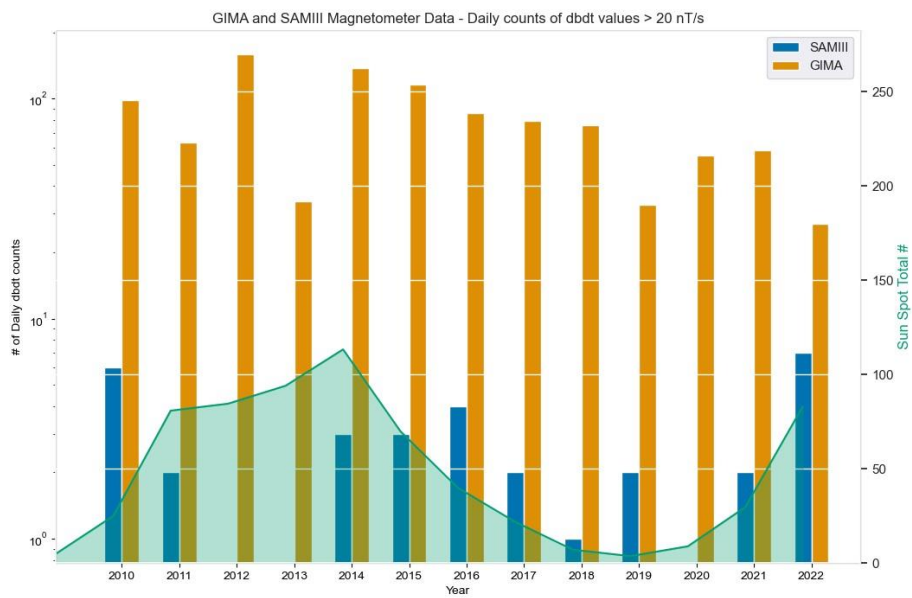
Figure 9: Number of days with $|\delta H/\delta t| > 20$ nT/s in log scale
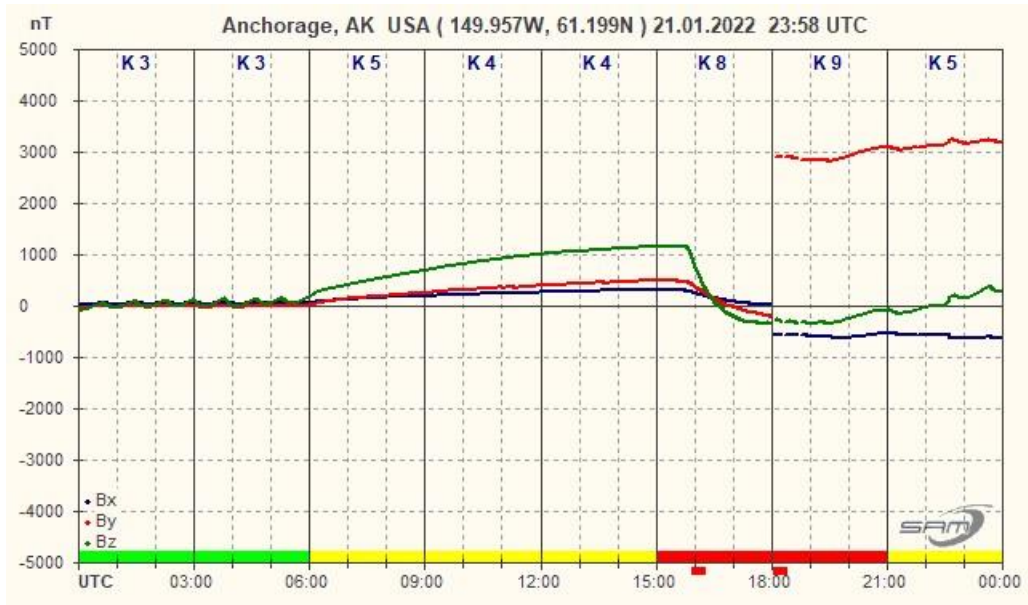
Figure 10: SAM-III - January 21st, 2022
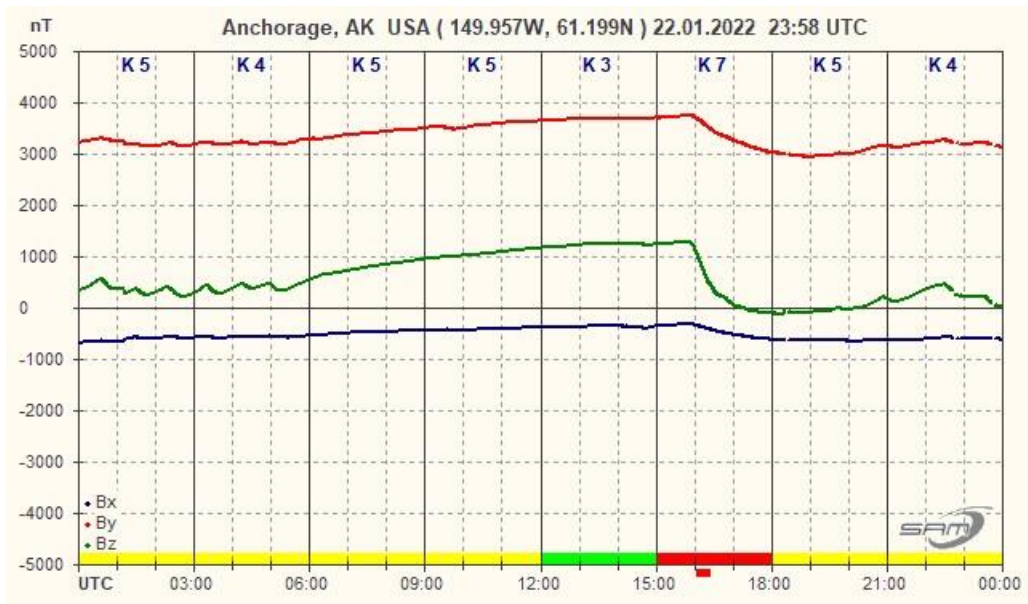
Figure 11: SAM-III - January 22nd, 2022

References

[1]   A. Pulkkinen, E. Bernabeu, A. Thomson, A. Viljanen, R. Pirjola, D. Boteler, J. Eichner, P. J. Cilliers, D. Welling, N. P. Savani, R. S. Weigel, J. J. Love, C. Balch, C. M. Ngwira, G. Crowley, A. Schultz, R. Kataoka, B. Anderson, D. Fugate, J. J. Simpson, and M. MacAlester. Geomagnetically induced currents: Science, engineering, and applications readiness. *Space Weather*, 15(7):828–856, 2017.

[2]   SAM Magnetometer Network. http://www.sam-magnetometer.net/index.html, 2023. Accessed on: 17 5 2023.

[3]   Reeve Engineers. SAM3 Construction Manual. https://reeve.com/Documents/
SAM/SAM3ConstructionManual.pdf, 2023. Accessed on: 17 5 2023.

[4]   Reeve Engineers. Sam3 software setup. https://reeve.com/Documents/SAM/ SAM3SoftwareSetup.pdf,
2023. Accessed on: 10 5 2023.

[5]   The pandas development team. pandas-dev/pandas: Pandas, February 2020.

[6]   Hunter Barndt. Sam-iii parsing and data analysis tools. https://github.com/ whbarndt/samIII-
magnetometer-data-analysis, 2023. Accessed on: 10 5 2023.

[7]   R. Schunk and A. Nagy. *Ionospheres: Physics, Plasma Physics, and Chemistry*. Cambridge Atmospheric and
Space Science Series. Cambridge University Press, 2009.

[8]   B.B. Narod and J.R. Bennest. Ring-core fluxgate magnetometers for use as observatory variometers.
Physics of the Earth and Planetary Interiors, 59(1):23–28, 1990.

[9]   D. Wilkinson and Matt Heavner. Geophysical institute magnetometer array. *AGU Fall Meeting Abstracts*,
01 2006.

[10]   Magnetometer Archive - Geophysical Institute, University of Alaska Fairbanks.
https://www.gi.alaska.edu/monitors/magnetometer/archive, 2023. Accessed on: 17 5 2023.

[11]   Magnetometer data, geophysical institute, uaf. Retrieved from Research Computing Systems 17 3 2023,
2010 - 2022.

[12]   SIDC - Solar Influences Data Analysis Center: The sunspot index and long-term solar observations.
https://www.sidc.be/silso/infosnytot, 2023. Accessed on: 28 3 2023.

[13]   AK RWIS (Alaska road weather information system). https://mesonet.agron.
iastate.edu/request/rwis/fe.phtml?network=AK_RWIS, 2023. Accessed on: 10 5 2023.

[14]   S. E. Milan, S. M. Imber, A. L. Fleetham, and J. Gjerloev. Solar cycle and solar wind dependence of the
occurrence of large dB/dt events at high latitudes. *Journal of Geophysical Research: Space Physics*,
128(4):e2022JA030953, 2023. e2022JA030953 2022JA030953.

[15]   M. J. Engebretson, V. A. Pilipenko, L. Y. Ahmed, J. L. Posch, E. S. Steinmetz, M. B. Moldwin, M. G. Connors,
J. M. Weygand, I. R. Mann, D. H. Boteler, C. T. Russell, and A. V. Vorobev. Nighttime magnetic
perturbation events observed in Arctic Canada: 1. survey and statistical analysis. *Journal of Geophysical
Research: Space Physics*, 124(9):7442–7458, 2019.

Evaluation of RAS 1420 MHz Continuum Frequency Converter and LNA

Written By: Stephen Bentley

Date: 22 Sept 2023

1.0 Preamble

The radio astronomy section of the ASV purchased a product from Radio Astronomy Supplies in the U.S. The product is a neutral hydrogen receiver. The receiver is in 2 parts, the 1420 MHz Continuum Frequency Converter and the Low Noise Amplifier (LNA). The radio astronomy section wishes to use this receiver system on the horn antenna at the LMDSS for general experiments and demonstration of neutral hydrogen reception. A recent operation of the receiver found several issues which were not consistent with the expected performance of the receiver. Detailed schematics or specifications were not supplied for these products. This report provides an evaluation of the continuum converter and the LNA and provides a recommendation for the repair and future use of this receiver.

2.0 Continuum Frequency Converter Measured Performance

Figure 1 shows an internal view of the continuum converter and the labelling attached to the enclosure top lid. The specifications as stated on the converter label indicates a gain of 55dB, noise figure of less than 1dB and a 3dB bandwidth of 6 MHz.

The LNA specifies a gain of 28dB and a noise figure of 0.34dB. Within the continuum converter there is a front end module which converts 1420 MHz down to 70 MHz in a similar manner to the receiver the ASV has for the 8.5 m dish antenna. In addition, the continuum converter includes a further down converter that takes the 70 MHz signal and converts that down to 10 MHz.
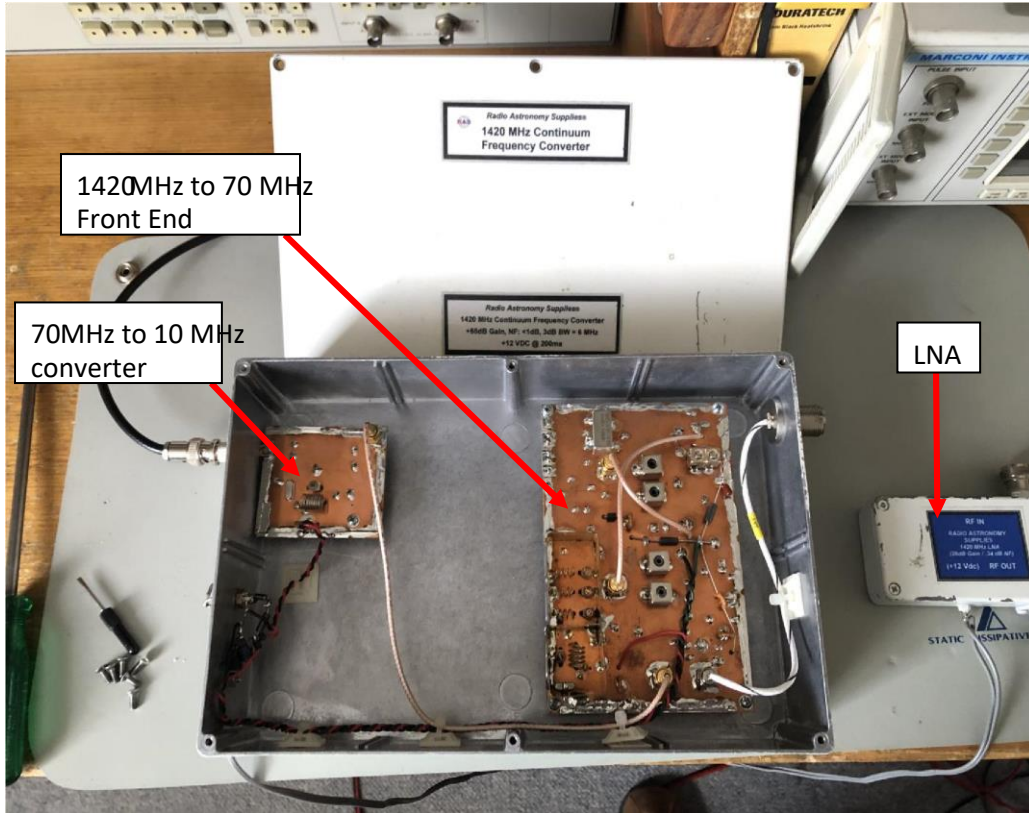
Figure 1: Continuum Frequency Converter and LNA

Figure 2 shows the label on the continuum converter which indicates an output frequency of 10.7 MHz.

Figure 2. Continuum Converter Output label

A basic block diagram of the test setup for the continuum converter is presented in Figure 3 with measured signals and gains as tested using the author's Marconi 2031 RF signal generator and HP8560A spectrum analyzer.
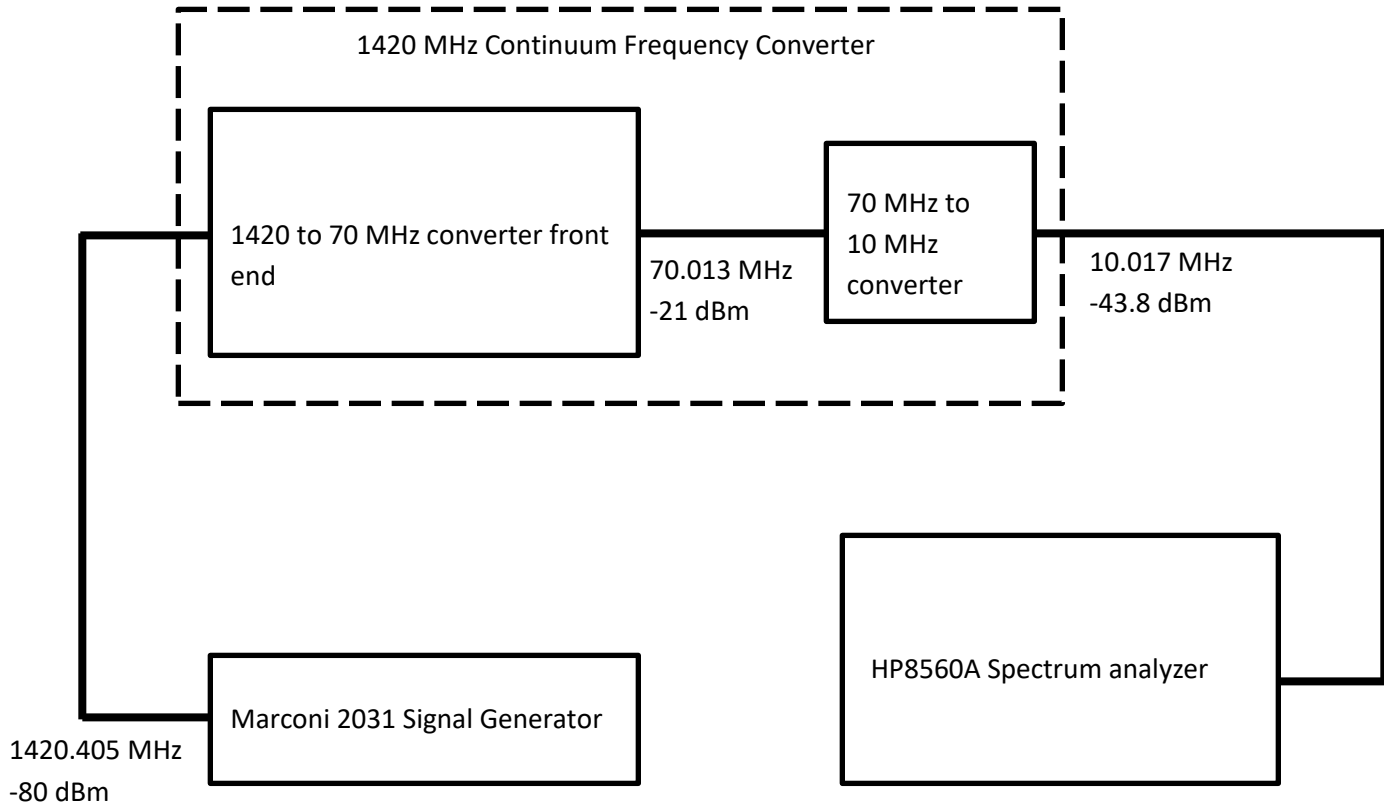
Figure 3. Continuum Converter Test Setup Block Diagram

From the measurements performed with the test setup shown in Figure 3, it appears the overall gain of the continuum converter is (-43.8 − (-80)) = **36.2dB**. This is 18.8dB below the specified 55dB. The front end section appears to have a gain of (-21 − (-80)) = **59dB** which is a respectable result. The other measurement of note was the converted frequency which was expected to be 10.7 MHz at the receiver output. The measured frequency of 10.017 MHz is 683 KHz off tune from the expected output. The second converter was examined in more detail and an image of the component side of the circuit board was captured. Figure 4 shows the 70 MHz to 10 MHz converter.
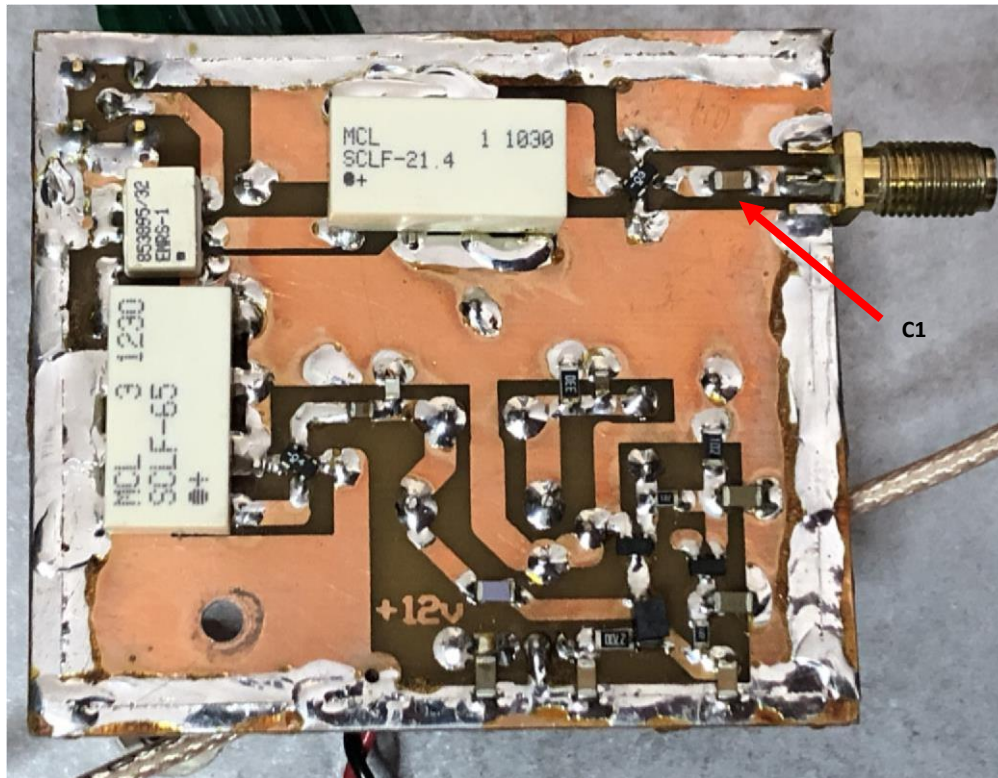
Figure 4. Continuum Converter 70 to 10 MHz Converter Module Component Side View

The 70 MHz to 10 MHz converter appears to be a sophisticated design. The small white block is a Macom wide band mixer, the larger white blocks are Mini-Circuits low pass filters. One filter has a cut-off at 21.4 MHz and the other at 65 MHz. There are also several discrete transistor stages. The use of low pass filters is to ensure the harmonic content from the 60 MHz local oscillator and 10 MHz output frequency is greatly reduced. On the other side of this circuit board is a quartz crystal. The frequency stamped on the crystal is 60.0 MHz. This suggests the second converter is expected to convert the 70 MHz input signal down to 10 MHz rather than 10.7 MHz as indicated by the product label. It is pointed out since the output bandwidth is 6 MHz the small error is not significant however the product labelling is misleading. The measured conversion gain of the second converter in fact is a loss of 22.8dB. Shown in Figure 5 is the author's reverse engineering of part of the 70 to 10 MHz down converter concentrating on the main signal path only.
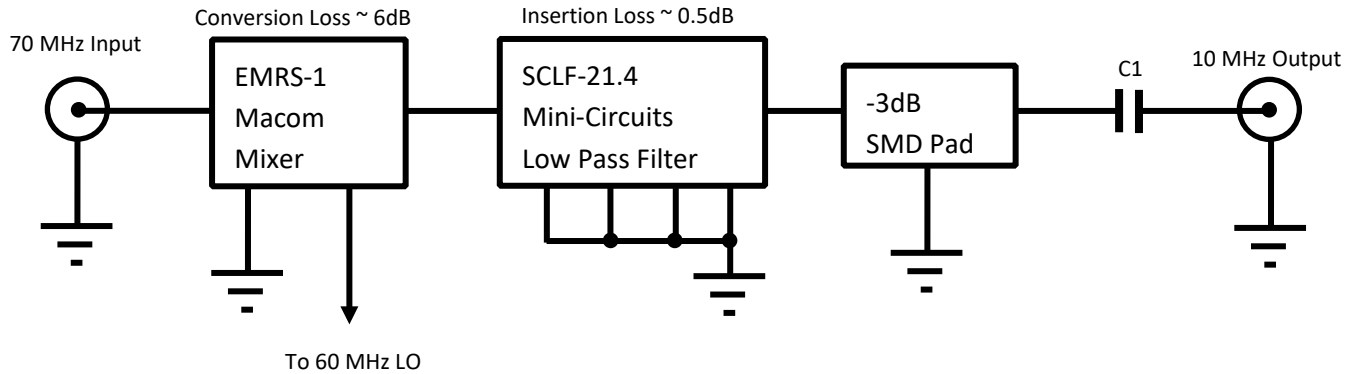
Figure 5. Continuum Converter 70 to 10 MHz Converter Module Main RF Path Block Diagram

Based on the component specifications of the items in the signal path, the overall conversion signal loss is expected to be (6 + 0.5 + 3) = 9.5 dB. The author measured 22.8dB and therefore a fault was evident.

Upon further inspection, the fault appeared to be the coupling capacitor labelled C1 in Figure 5 and also indicated in Figure 4. Slight flexing of the circuit board and the SMA socket attached near C1 caused the signal output to vary by more than 10dB. The faulty C1 was replaced with a discrete 100n Ceramic capacitor which improved the converter which then achieved a conversion loss of 12.5dB. This is still worse than the expected 9.5dB but losses may be occurring in other aspects of the circuit board construction or the quality of the SMA sockets.

The failure of the coupling capacitor C1 has been observed in similar circuits by the author. The combination of a SMD coupling capacitor located close to a board mounted SMA socket appears to risk the effects of small flexing of the SMA socket which mechanically couples to the printed circuit board resulting in strain on the SMD capacitor causing it to fail. Alternatively, the expansion coefficient of the SMA socket is significantly different to the printed circuit board which translates to straining of the SMD capacitor. Another possibility is that the quality of this specific SMD capacitor was inadequate. Either way, it is advised that a different type of capacitor such as a wired discrete capacitor be used or the output socket is installed remotely and connected to the printed circuit board via a coax coupling cable.

The conversion from 1420 MHz to 10 MHz is considered unnecessary for the ASV application. This also results in a signal loss and introduces the potential of degraded receiver intermodulation, dynamic range limitations and spurious responses. The ASV will be better off using the 70 MHz signal output from the front end. A gain improvement of at least 12.5 dB will also be realized. The distance between the horn antenna and the radio astronomy lab where the receiver demonstrations will occur is less than 10 m. Cable loss will be greater using the 70 MHz output compared to 10 MHz however the difference is quite small. For example, a 10 m RG58 cable will have a loss of 0.5 dB at 10 MHz but 1.5 dB at 70 MHz. This is much less than the measured conversion loss of 12.5dB. If the cable was replaced with RG213 the loss at 70 MHz would be 0.6dB.

3.0 LNA Measured Performance

The LNA gain and noise figure was verified using the author's Marconi 2031 RF signal generator and HP8560A spectrum Analyzer. The measured gain of the LNA was 32.17dB. This figure differs slightly from the result the author stated in a report issued on 3rd March 2023. However, the result measured in this report was performed with greater care as the value was also to be used to determine the LNA noise figure. To more accurately measure the LNA gain, the "substitution" test measurement was used where the reading on the spectrum analyses was first set using a short coax cable between the signal generator and the spectrum Analyzer and setting the

generator level to read a precise number on the display marker, in this case -60dBm. The LNA was then placed in the circuit between the signal generator and the spectrum analyses, and the new reading taken, in this case -27.83dBm. Therefore, the gain is the difference between -60 and -27.83 or **32.17dB**.

The noise figure was measured using the spectrum analyzer to measure the LNA output noise power. To perform this measurement the spectrum analyses settings as shown in Table 1 were used. Figure 6 is a screen capture which shows the final result of the noise measurement after the spectrum analyzer had completed 70 trace sweeps to average out the noise variations.

Centre Frequency: 1420 MHz

RF attenuator: 0dB

Span: 10 KHz

Resolution BW: 10 Hz (minimum setting)

Video BW: 1 Hz

Amplitude Scale: 2dB/div.

Video Averaging: On (70 sweeps)

Marker: Noise Measurement

Table 1. Spectrum analyzer Settings for Noise Measurement
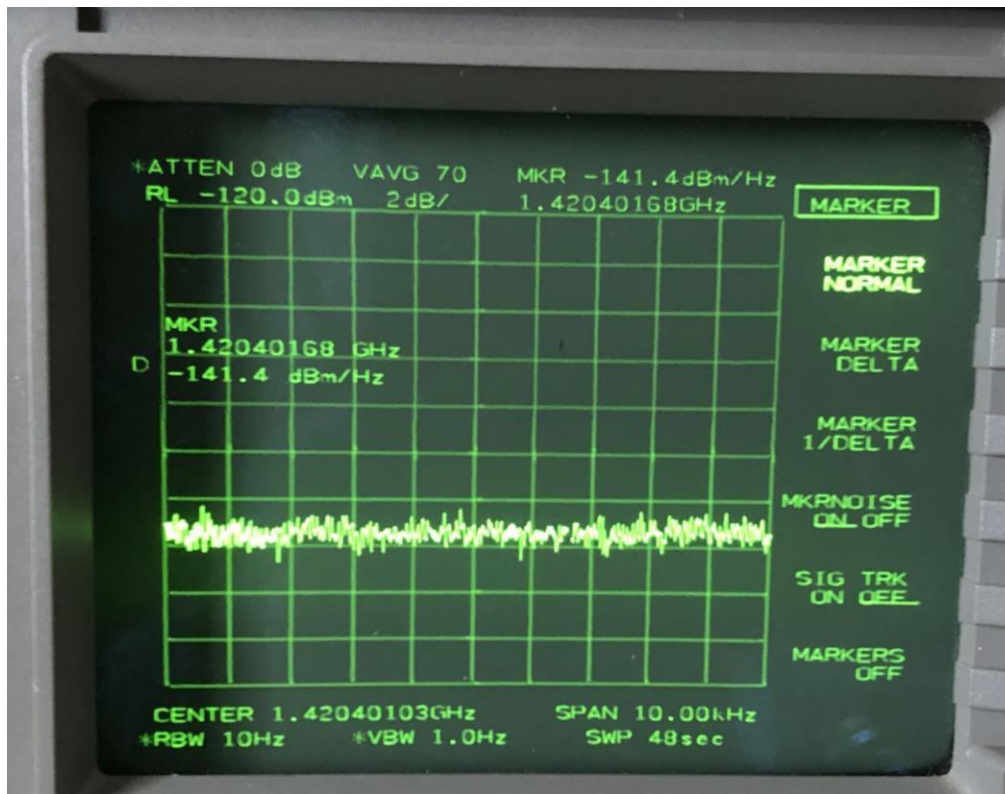
Figure 6. Spectrum analyzer Noise Measurement (100 Sweeps)

To determine the LNA noise figure the formula shown below is used.

$$NF = N_o\,[\text{dBm}] - G\,[\text{dB}] + 174\,dBm$$

Substituting the known values into this equation obtains:-
NF = -141.4dBm -32.17dB + 174dBm = **0.43dB**
This result is slightly worse than the stated value of 0.34dB, however the measurement technique can expect a tolerance of +/-0.2dB.

4.0 Conclusion

The RAS 1420 MHz Continuum Frequency Converter developed a fault. The cause was due to the failure of a surface mount coupling capacitor in the 70 MHz to 10 MHz down converter circuit board. The circuit was repaired, however the stated overall gain of 55 dB was not achieved. When an accurate RF input signal of 1420.405 MHz is applied to the receiver the actual output frequency is 10.017 MHz indicating the product has misleading labelling.

Since the 70 MHz to 10 MHz down converter introduces a significant receiver loss of up to 12.5 dB, it is recommended this module be bypassed and the 70 MHz output signal be used for neutral hydrogen experiments and demonstrations when using the horn antenna. The author will modify the continuum converter to include an additional N-type socket for the 70 MHz output.

The LNA performs well and has sufficient gain and a low noise figure which will be fit for purpose in the horn antenna demonstrations. When the LNA and Continuum Frequency Converter front end are used in conjunction, the overall receiver gain becomes 59 + 32.17 = **91.17dB**. For comparison, the neutral hydrogen receiver front end which will be used on the ASV 8.5 m dish, has a gain of 74dB including the external LNA module.

Optical and Radio Frequency Observations of Twenty Long Period Variable (LPV) Astrophysical Masers

Dave Hinzel

Abstract Astrophysical masers are naturally occurring sources of stimulated spectral line emission, typically in the microwave frequency range of the electromagnetic spectrum. The emission from a maser is stimulated, having the frequency corresponding to the energy difference between two quantum-mechanical energy levels of the molecular species in the gain medium which have been pumped into a non-thermal population distribution. Typical molecules that can produce astrophysical maser emissions include, OH (hydroxyl), water, ammonia, and SiO (silicon monoxide). In the case of SiO, the stimulated frequency is in the 43 GHz frequency band (42373.341-43423.853 GHz, depending on the specific isotope). Observations of SiO masers at 43 GHz will be discussed below. These radio frequency observations will be correlated with the phases of twenty Long Period Variable (LPV) stars that have extensive optical light curves utilizing Johnson-Cousins photometry.

1. Introduction and Background

The American Association of Variable Star Observers, (AAVSO) **(**Kloppenborg 2022, American Association of Variable Star Observers (https://aavso.org)) and the University of New Mexico (Stroh, M. "Circumstellar SiO Masers in the Bulge Asymmetries and Dynamical Evolution Survey" 2019, https://digitalrepository.unm.edu/phyc_etds/216) participated in a cooperative effort to study SiO maser emissions in Long Period Variable (LPV) stars. The maser emissions were observed with the Jansky Very Large Array (JVLA) by the University of New Mexico and the corresponding optical light curves were taken from the AAVSO International Variable Star Index (VSX) (Kloppenborg 2022, American Association of Variable Star Observers International Variable Star Index (https://www.aavso.org/vsx/)). In total, twenty Mira LPV stars were studied with the combination of the light curves and the 43 GHz radio frequency observations. The particular stars selected were based on previous SiO observations as well as a good history of AAVSO coverage. These objects are outlined in Figure 1.

BAaDE Name	Associated Name	R.A. (J2000)	Declination (J2000)	Period (days)	Variable Classification	Previous SiO $v=3$ Detection?
ad3a-18267	TY Cas	00:36:59.42	+63:08:01.7	645	Mira	No
ad3a-17750	FI Per	03:54:56.75	+48:36:01.9	427	Mira	Yes
ad3a-13536	SY Mon	06:37:31.34	-01:23:43.0	423	Mira[a]	No
ad3a-15213	FX Mon	06:45:05.60	+09:02:18.5	428	Mira	No
ad3a-13321	NSVS 12572573	06:45:14.95	-02:26:35.1	375	Mira	Yes
ad3a-16553	V0349 Vul	19:31:10.47	+23:30:33.5	363	Mira	Yes
ad3a-15617	RT Aql	19:38:01.61	+11:43:18.3	327	Mira	No
ad3a-16500	V0353 Vul	19:49:22.06	+22:37:39.8	470	Mira	Yes
ad3a-16952	SX Cyg	20:15:33.53	+31:04:20.1	411	Mira	No
ad3a-17123	AU Cyg	20:18:32.77	+34:23:20.5	435	Mira	Yes
ad3a-17332	V1655 Cyg	20:25:24.02	+38:42:35.6	462	Mira	Yes
ad3a-17830	NSVS J2041274+511326	20:41:27.45	+51:13:29.8	350	Mira	Yes
ad3a-17304	DR Cyg	20:43:41.01	+38:09:56.1	314	Mira	No
ad3a-17802	V0750 Cyg	20:49:21.17	+50:31:51.3	433	Mira	No
ad3a-18063	W Cep	22:36:27.57	+58:25:34.0	350	SRc	Yes
ad3a-18292	VX Cep	22:50:49.45	+64:15:04.7	532	Mira	Yes
ad3a-18081	V0850 Cas	23:37:39.74	+58:50:45.9	365	SR	No
ad3a-18070	AL Cep	22:49:16.89	+58:35:07.1	277	Mira	No
ad3a-18128	V Cas	23:11:40.71	+59:41:58.7	229	Mira	No
ce3a-00250	V0657 Cas	23:52:04.92	+61:48:12.4	607	Mira	Yes

Positions are from the 2MASS associated position. Associated name, period, and variable classification are taken from the VSX catalog (Watson et al., 2006). The last column lists whether SiO $v=3$ emission was found in the original VLA BAaDE observations. [a]This object is also classified as an OH/IR star (Sivagnanam et al., 1988; Szymczak & Le Squeren, 1999).

Figure 1: Twenty SiO Masers Selected (Courtesy M. Stroh)

1.1 Maser Physics and SiO Spectra

The physics of masers, including astrophysical masers is illustrated in Figure 2. The stimulated emission of radiation begins with a molecule in a non-excited state (A). The molecule is excited due to a pumping mechanism that may be due to collisions and/or radiation (B). The molecule is then de-excited to a meta-stable state (C) and an incident photon with the energy equal to the energy of the transition stimulates the molecule causing de-excitation (D). Due to the de-excitation, an additional photon is emitted with the same energy as the incident photon (E).
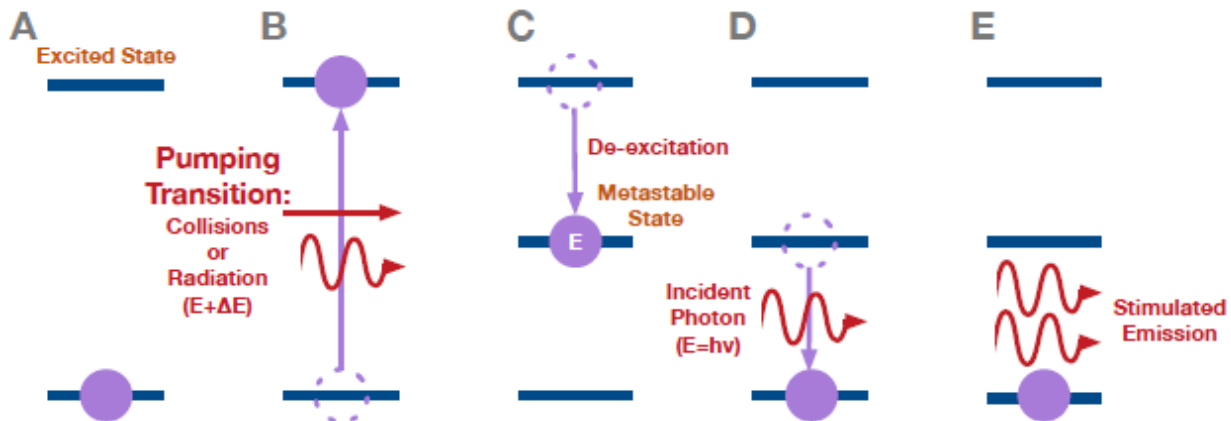
Figure 2: Stimulated Emission of Radiation (Courtesy M. Stroh)

Figure 3 shows the SiO energy levels for the 43 GHz radio frequency signal. SiO maser emission is associated with rotational de-excitation within vibrational states, with the 43 GHz SiO maser lines for the J = 1-0

transitions (42373.341-43423.853 GHz, depending on the specific isotope). Figure 4 shows an example of a JVLA observation around 43 GHz.
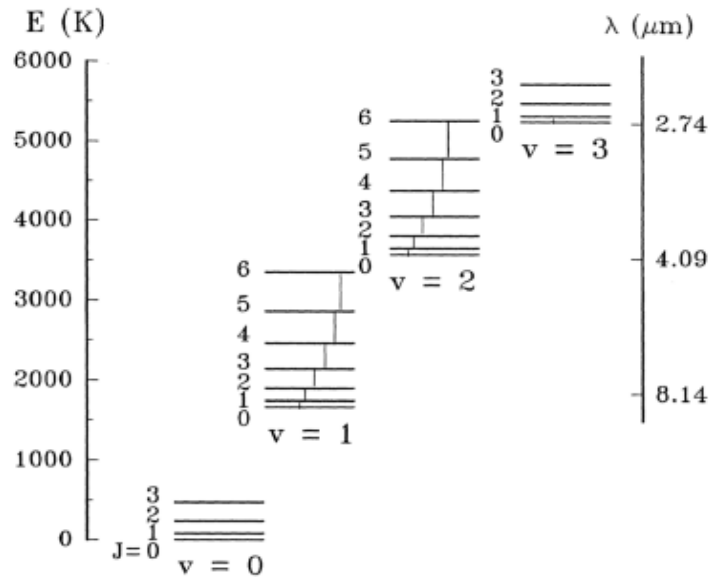
Figure 3: SiO Energy Level Diagram (Elitzur 1992)
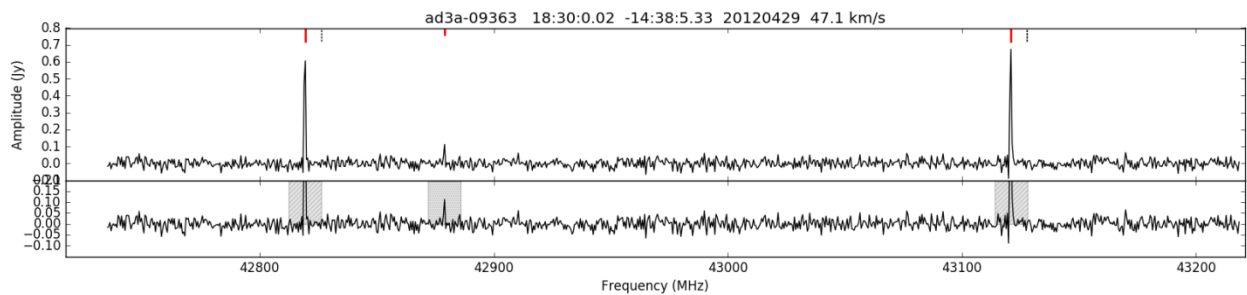
Figure 4: A Sample SiO Maser Spectra with Detection of the 28SiO(1-0) v=1 and v=2 Transitions, and a Weaker Detection of the 29SiO(1-0) v=0 Line. (Courtesy M. Stroh)

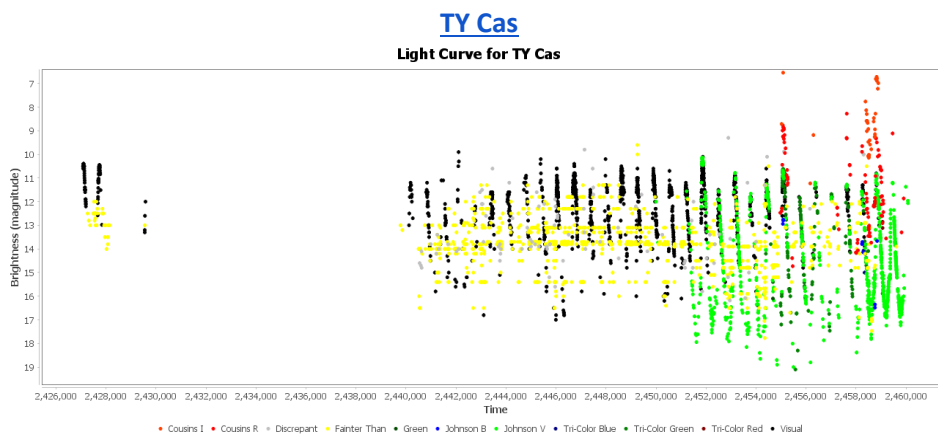**1.2 Mira Variable Stars and Optical Photometry**

Mira or M stars are Ceti-type variables. These are long-period variable giants with a characteristic late-type emission spectra and light amplitudes from 2.5 to 11 magnitudes in the optical V-band (500-700 nanometer wavelength). Their periodicity is well pronounced and the periods lie in the range between 80 and 1000 days. The periods of the twenty Mira SiO masers discussed herein lie between 229 and 645 days. The photometric system employed by the AAVSO for observations in the International Variable Star Index (VSX) is the Johnson-Cousins BVRI system. Johnson B (blue) is in the 400-500 nanometer wavelength range, Johnson V (visual) is in the 500-700 nanometer range, Cousins R (red) is in the 550-800 nanometer range, and Cousins I (infrared) is in the 700-900 nanometer range. The Johnson V or visual is in the optical spectrum to which the human eye is most sensitive.

2.   Methods and Results

The data presented below include the latest complete optical light curve of each LPV maser object in Table 1 from the AAVSO Variable Star Index. Additionally, each object has a clickable direct link to VSX with all of the information in the AAVSO database about that star. Also shown is the portion of the optical light curve that is correlated with the time period of 43 GHz VLA observations (JD 2458249-JD 2458750 or May 10, 2018-September 23, 2019). Finally, the 43 GHz VLA data is shown which includes the AAVSO (and other) optical magnitude plots (a), the integrated flux density of the emission (b), the integrated flux density relative to the SiO v=1 emission (c), the velocity centroid of the emission (d), and the full linewidth at zero maximum, i.e., the width of all emissions (e).

The AAVSO light curves were generated and analyzed by the VStar software (Benn, D. 2012, "Algorithms + Observations = VStar", JAAVSO, v40, n2, pp.852-866 (https://www.aavso.org/vstar)). VStar is a multi-platform variable star data visualization and analysis tool. Specifically, Fourier analysis of the photometric data was performed to yield a detailed periodogram for each of the twenty maser objects from which periodicities and other variations can potentially be identified. VStar utilizes the Date Compensated Discrete Fourier Transform (DCDFT) algorithm (Ferraz-Mello 1981) to produce a power spectrum, a period range, and a resolution. The Date Compensated DFT compensates for gaps in the data, which is common for variable star observations. The resulting analysis can include one or more periods and one or more harmonics. These can be selected to create a model that can also include a polynomial function that is used as a smoothing mechanism to capture key aspects of the data set without all the noise and fine fluctuations. When a model is created, it is subtracted from observations in the series to yield a second series called residuals. The residuals can also be analyzed to look for other signals (periods) in a process called pre-whitening. Periodicities and other potential variations were analyzed utilizing BVRI photometry, models were created from the photometry, mean series computed, and residuals analyzed to obtain all possible variations. In this particular case, the periodicities are not as important as they are normally for variable star research. Rather, the observation time overlap between the optical light curve data and the 43 GHz VLA data is the important feature. Optical and radio frequency data for all maser objects is presented below.

TY Cas

Light Curve for TY Cas

Light Curve for TY Cas During 43 GHz VLA Monitoring

Cousins I • Cousins R • Discrepant • Fainter Than • Johnson B • Johnson V • Tri-Color Blue • Tri-Color Green • Visual
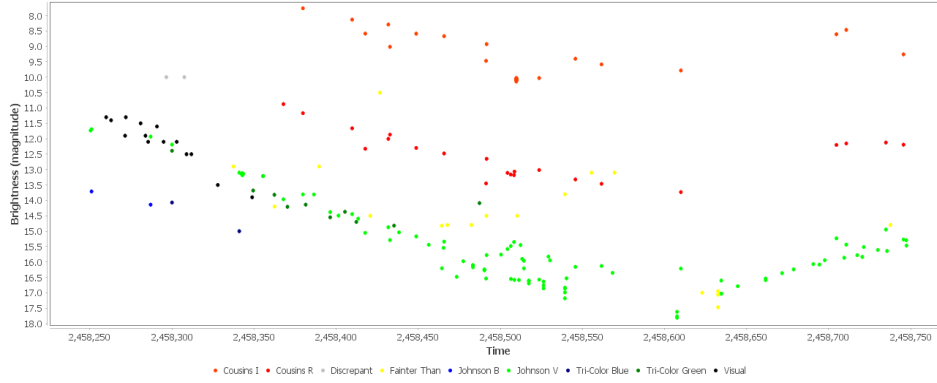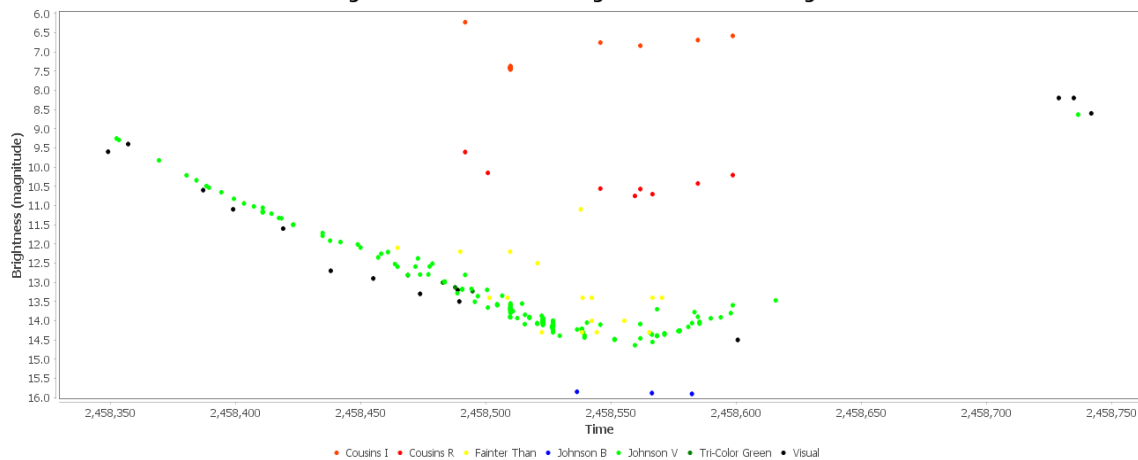

ad3a-18267 = TY Cas

FI Per

Light Curve for FI Per

Cousins I • Cousins R • Discrepant • Fainter Than • Johnson B • Johnson V • Unfiltered with V Zeropoint

87

Light Curve for FI Per During 43 GHz VLA Monitoring
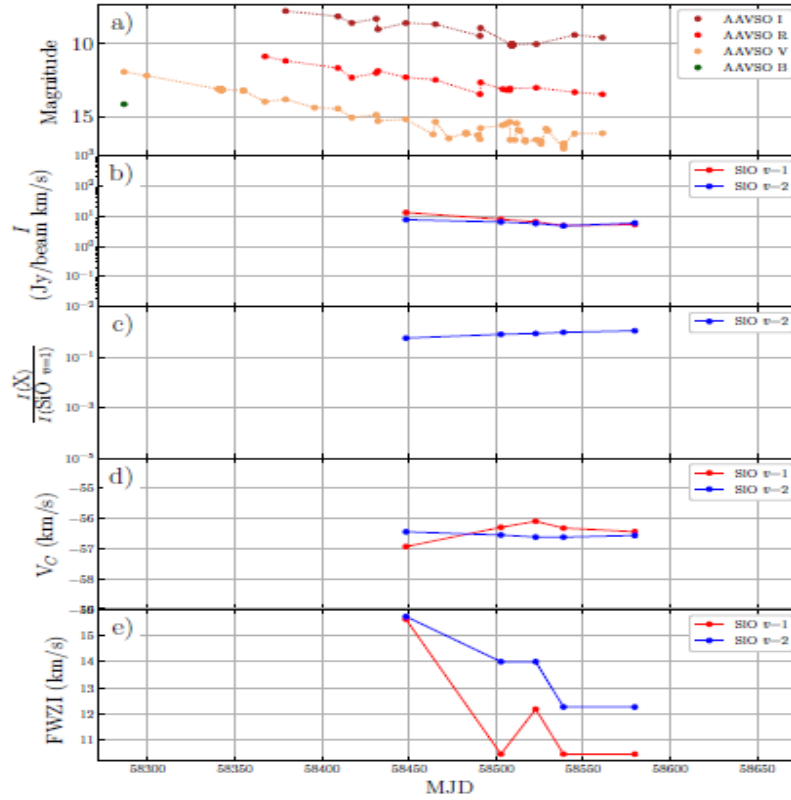
ad3a-17750 = FI Per
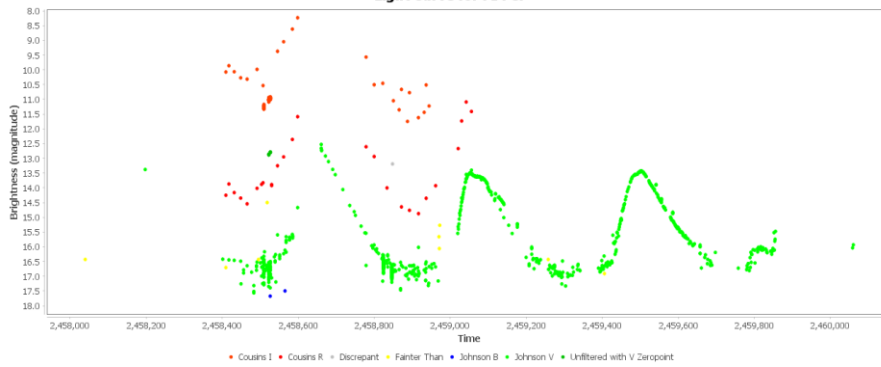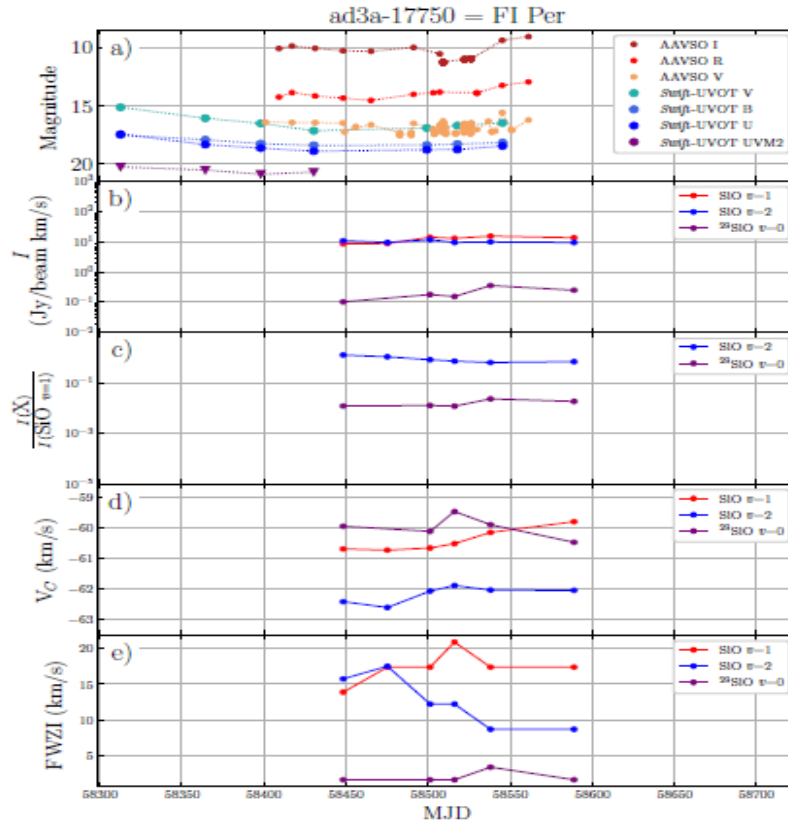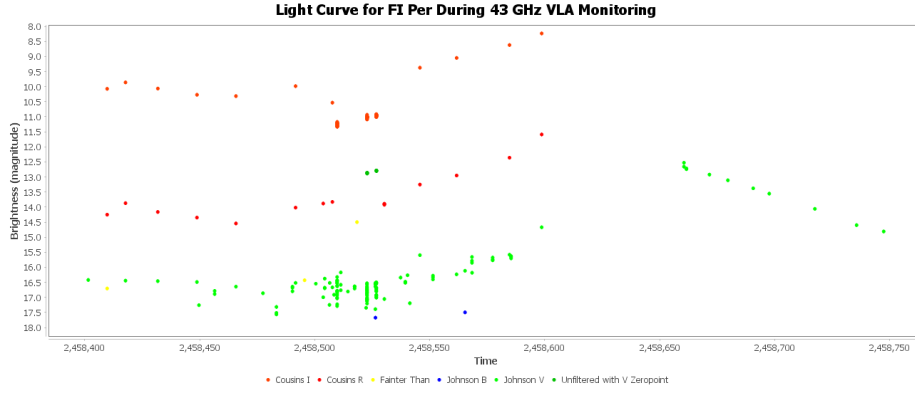
SY Mon

Light Curve for SY Mon

88
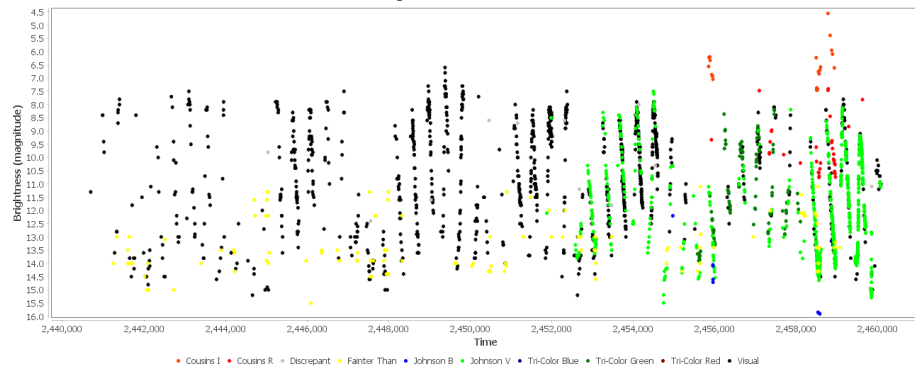
Light Curve for SY Mon During 43 GHz VLA Monitoring

ad3a-13536 = SY Mon
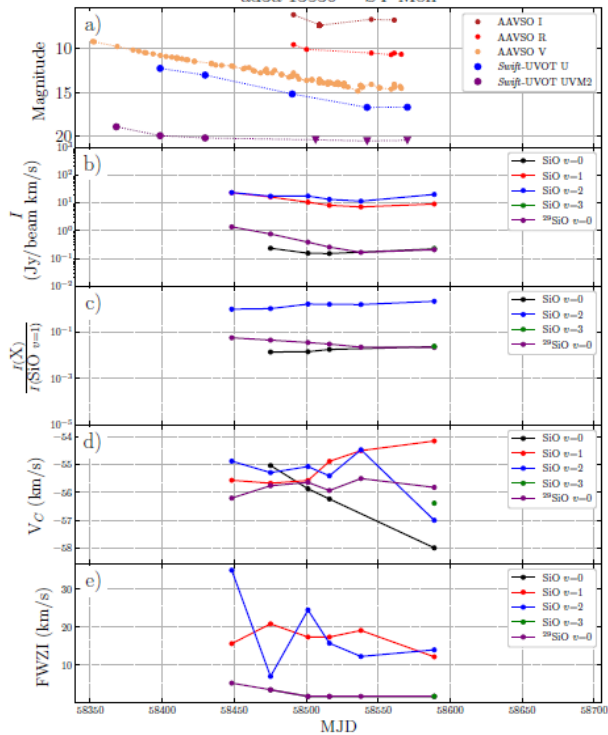
FX Mon

Light Curve for FX Mon
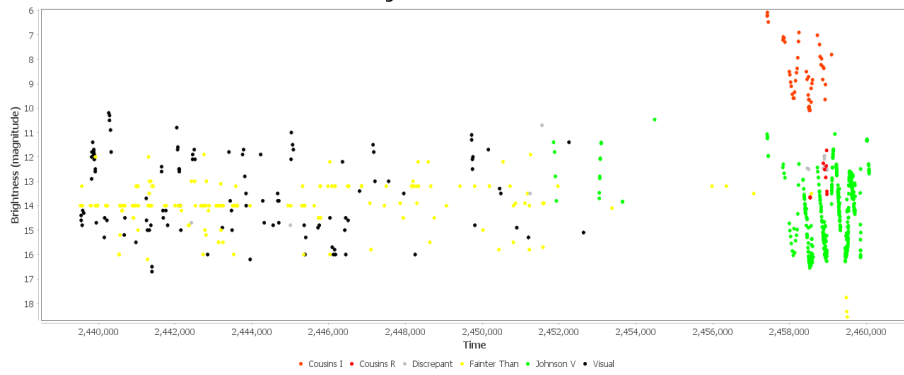
Light Curve for FX Mon During 43 GHz VLA Monitoring
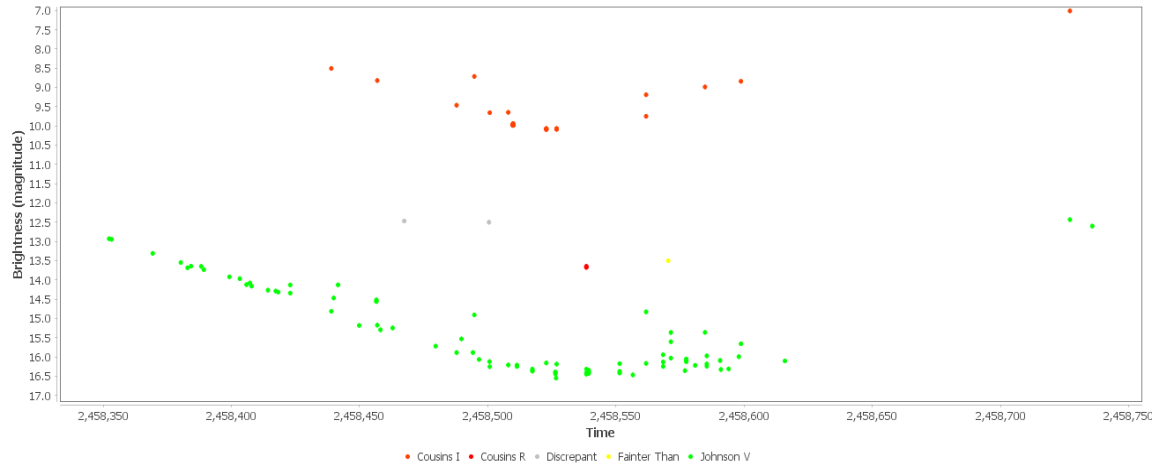
ad3a-15213 = FX Mon
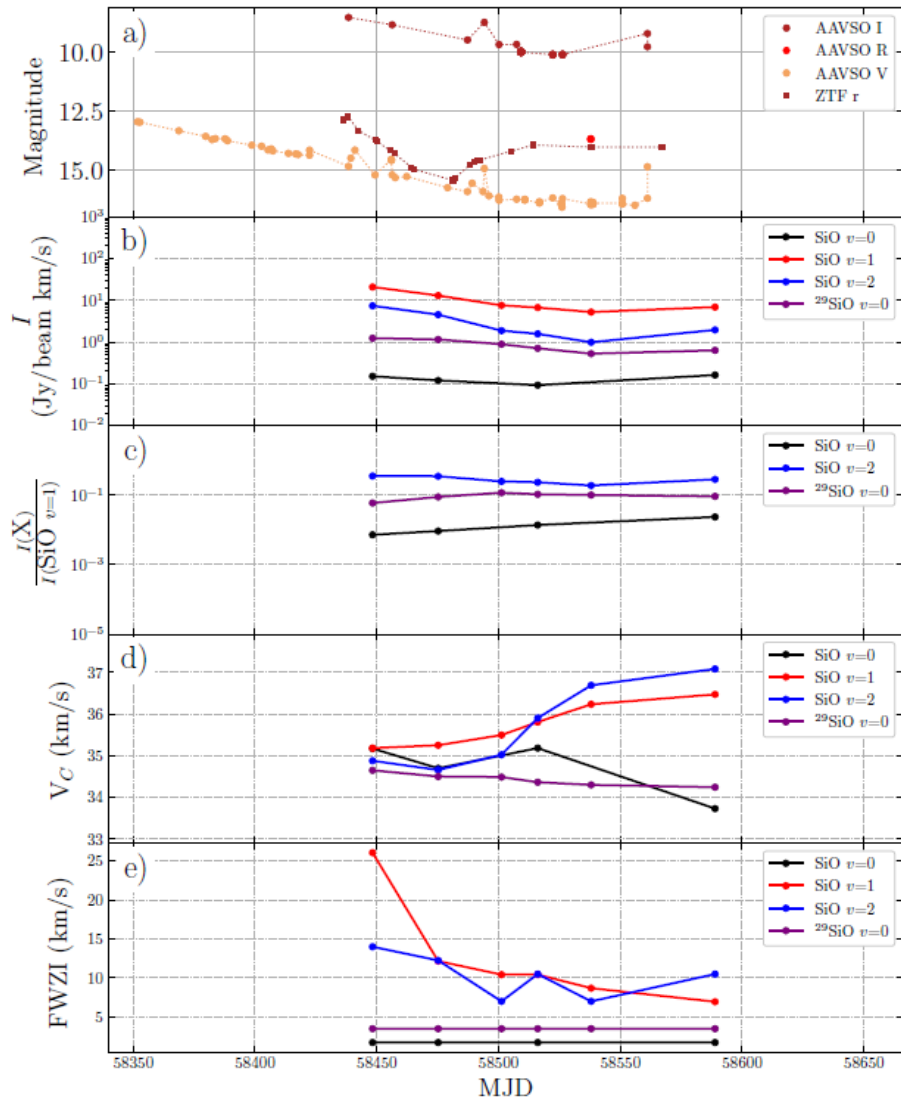
Light Curve for NSVS 12572573
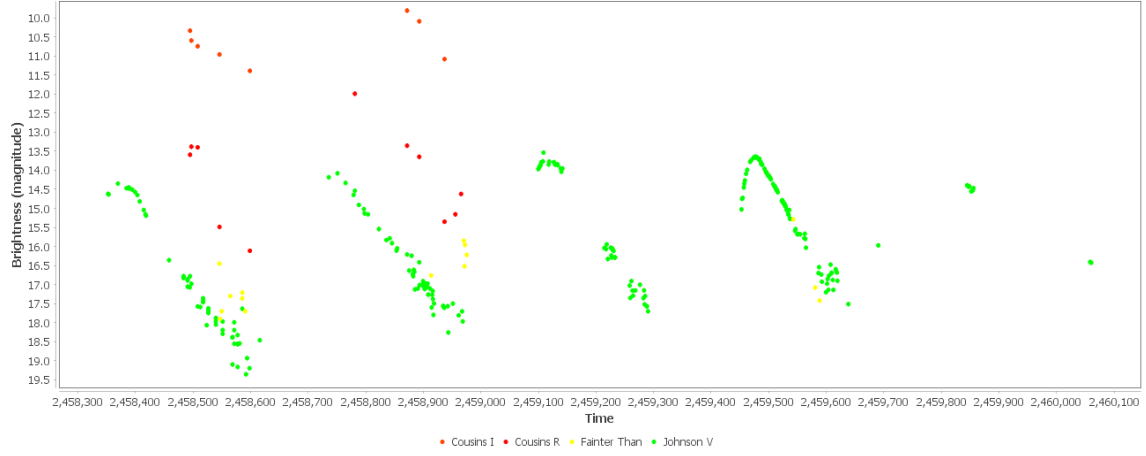
Light Curve for NSVS 12572573 During 43 GHz VLA Monitiring
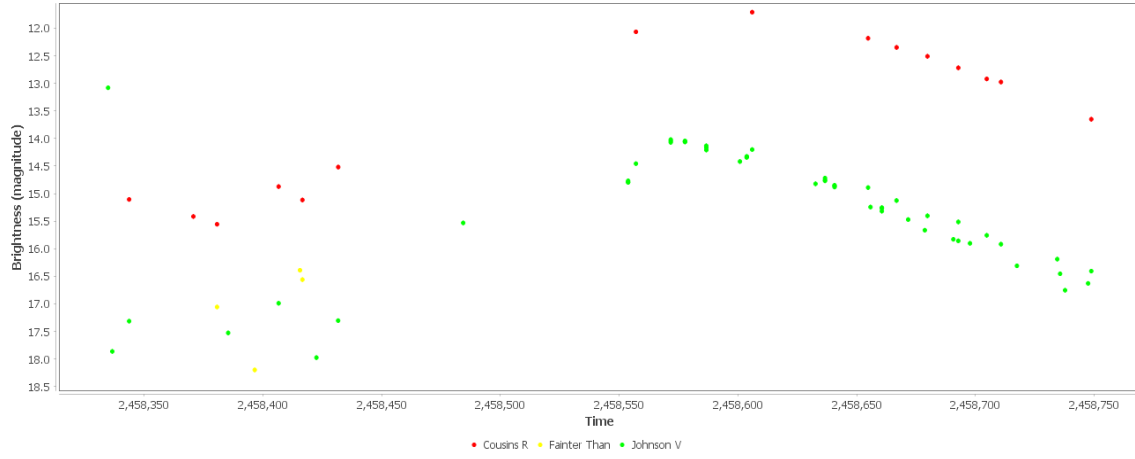
ad3a-13321 = NSVS 12572573

V0349 Vul

Light Curve for V0349 Vul
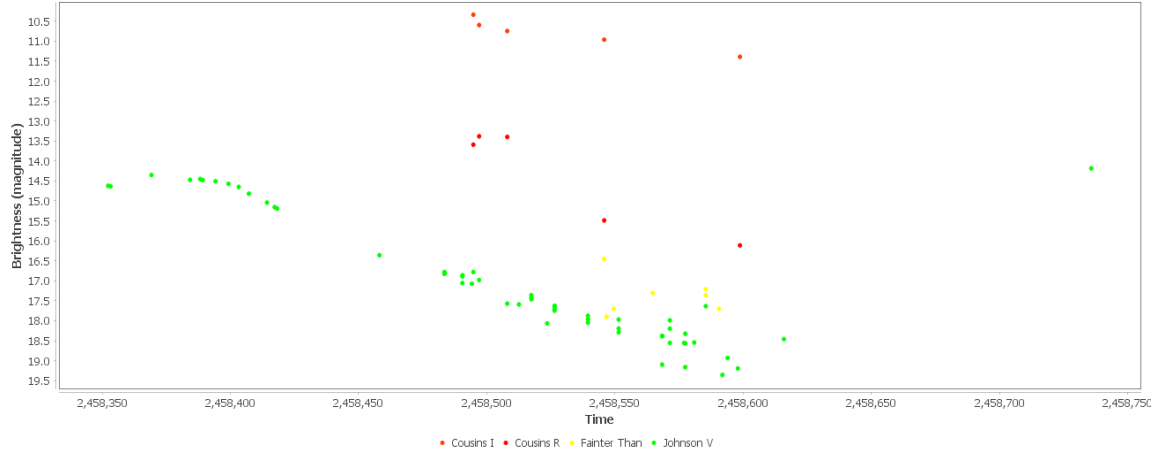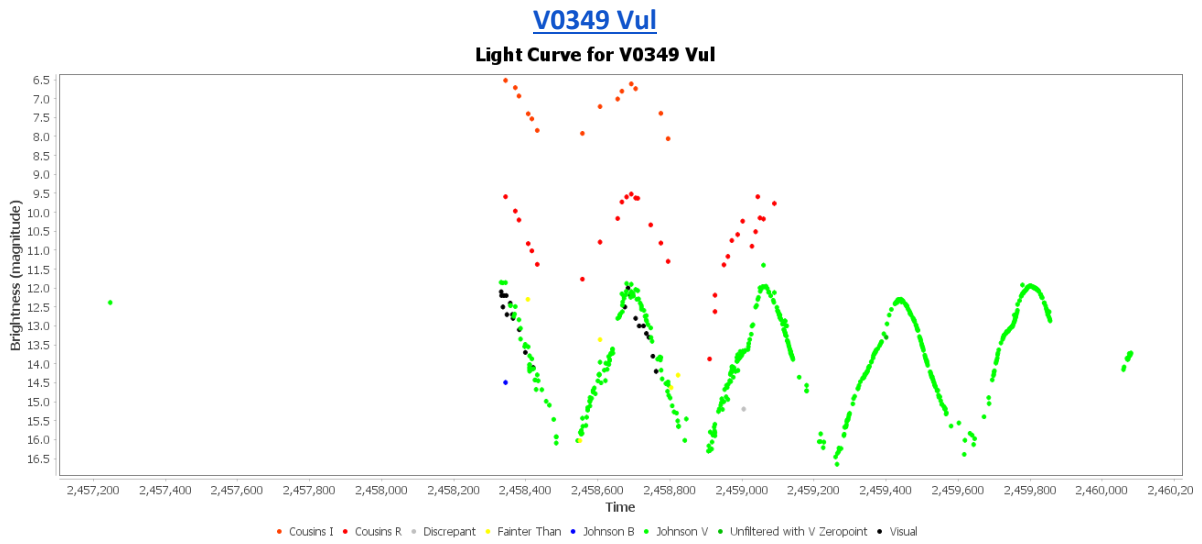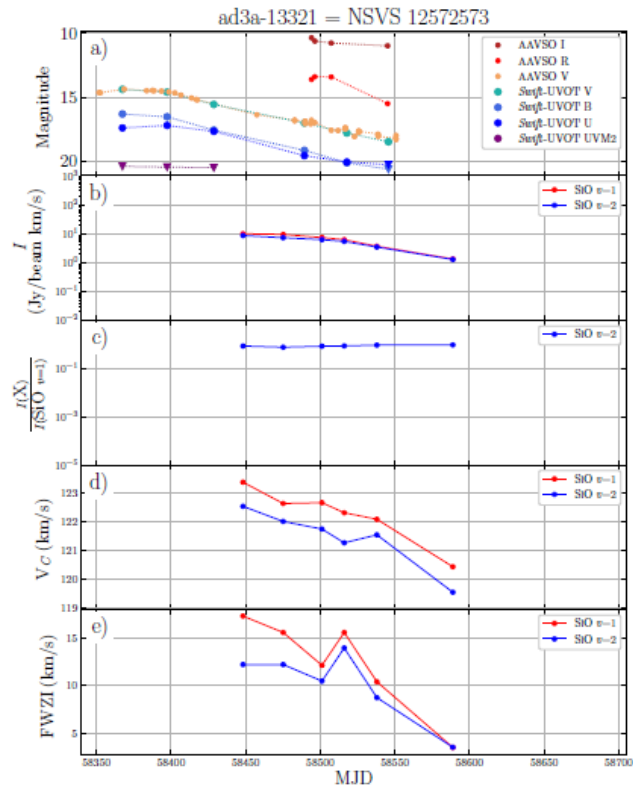
Light Curve for V0349 Vul During 43 GHz VLA Monitoring
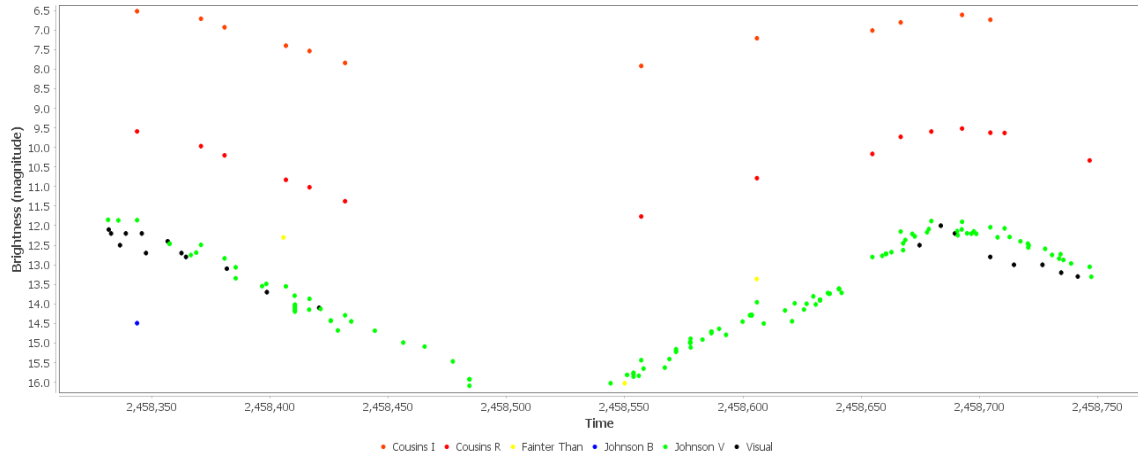
ad3a-16553 = V0349 Vul
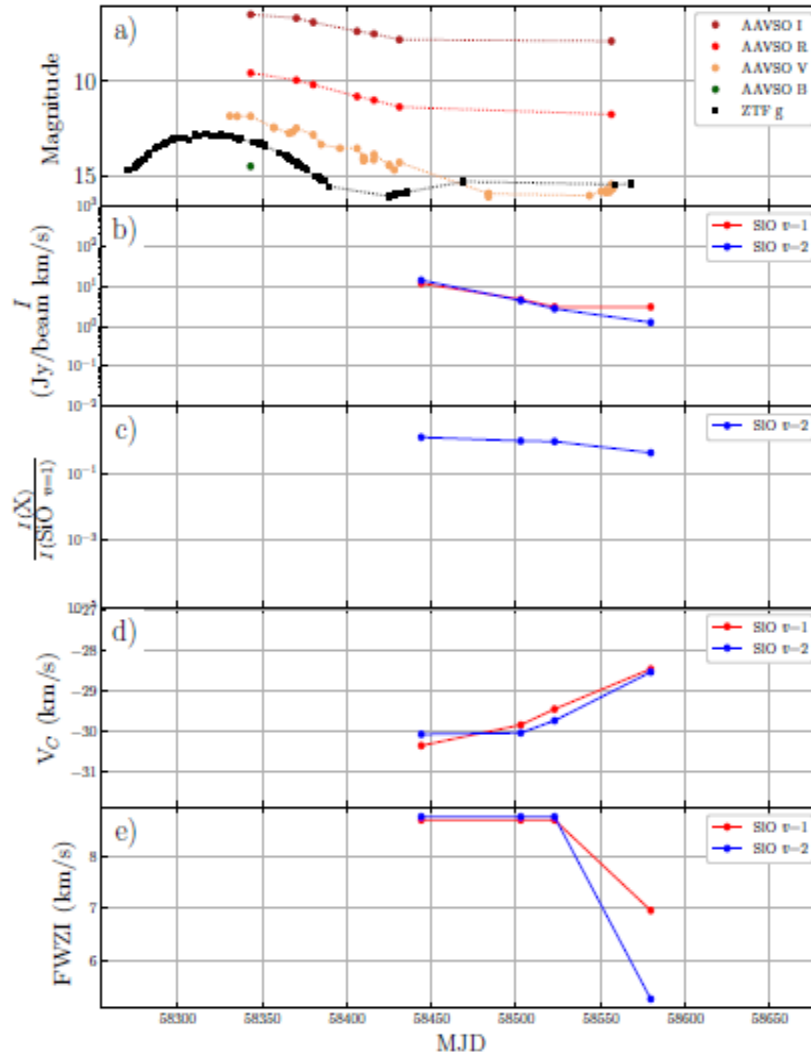
RT Aql

Light Curve for RT Aql
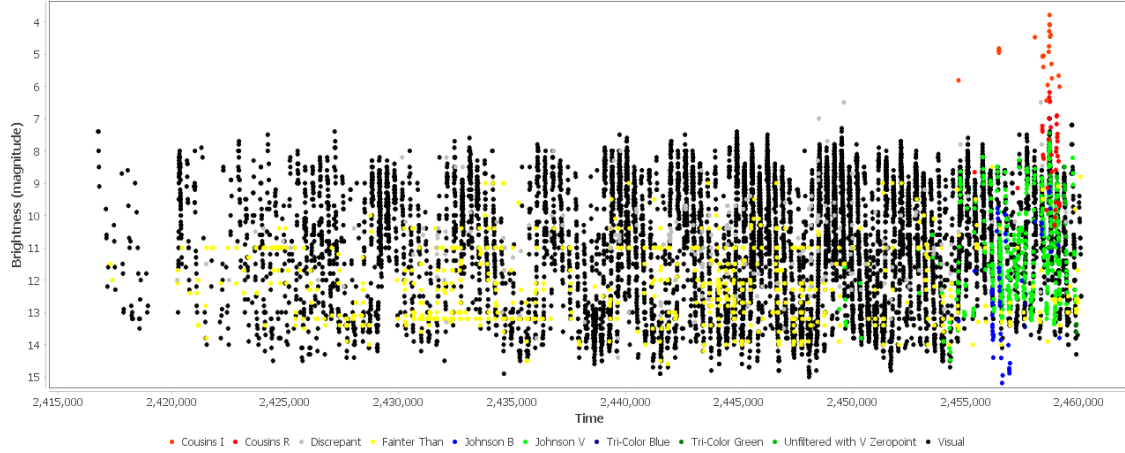
Light Curve for RT Aql During 43 GHz VLA Monitoring
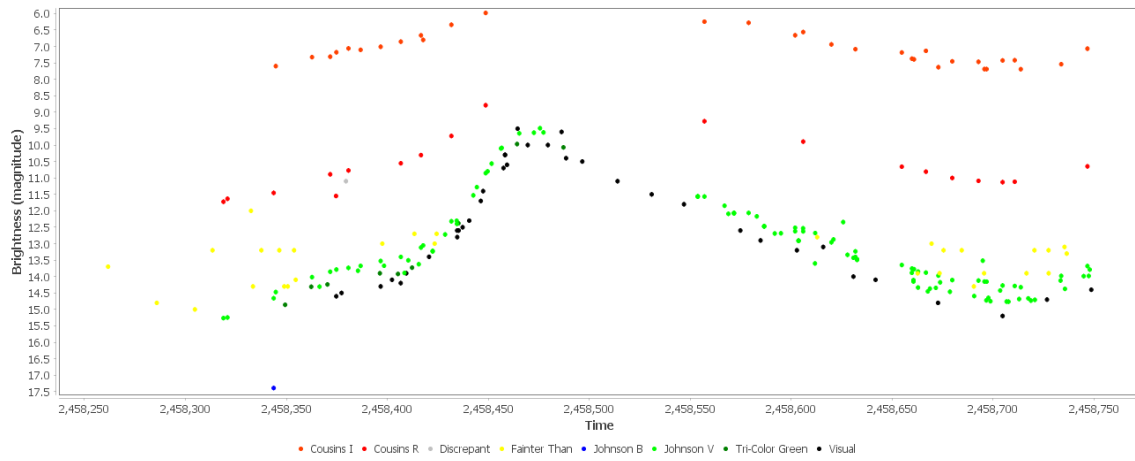
ad3a-15617 = RT Aql
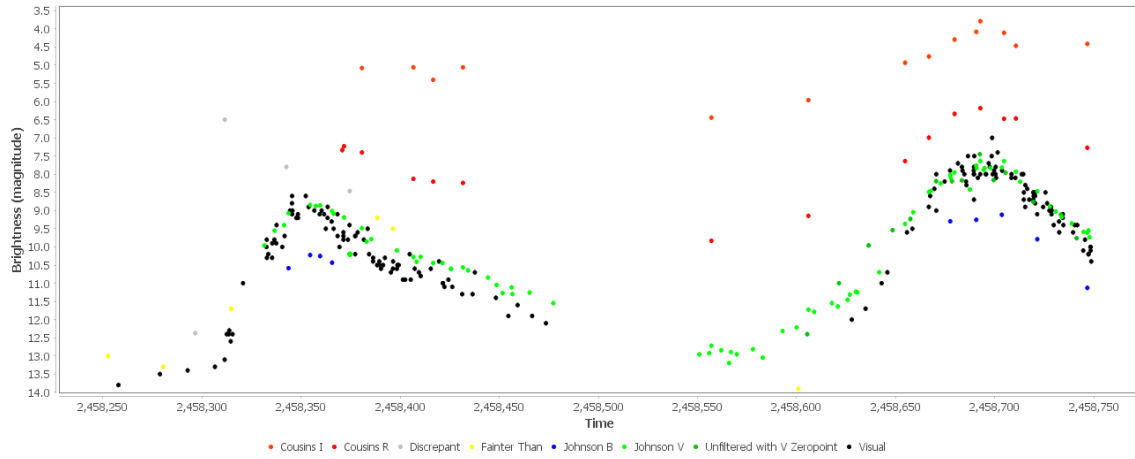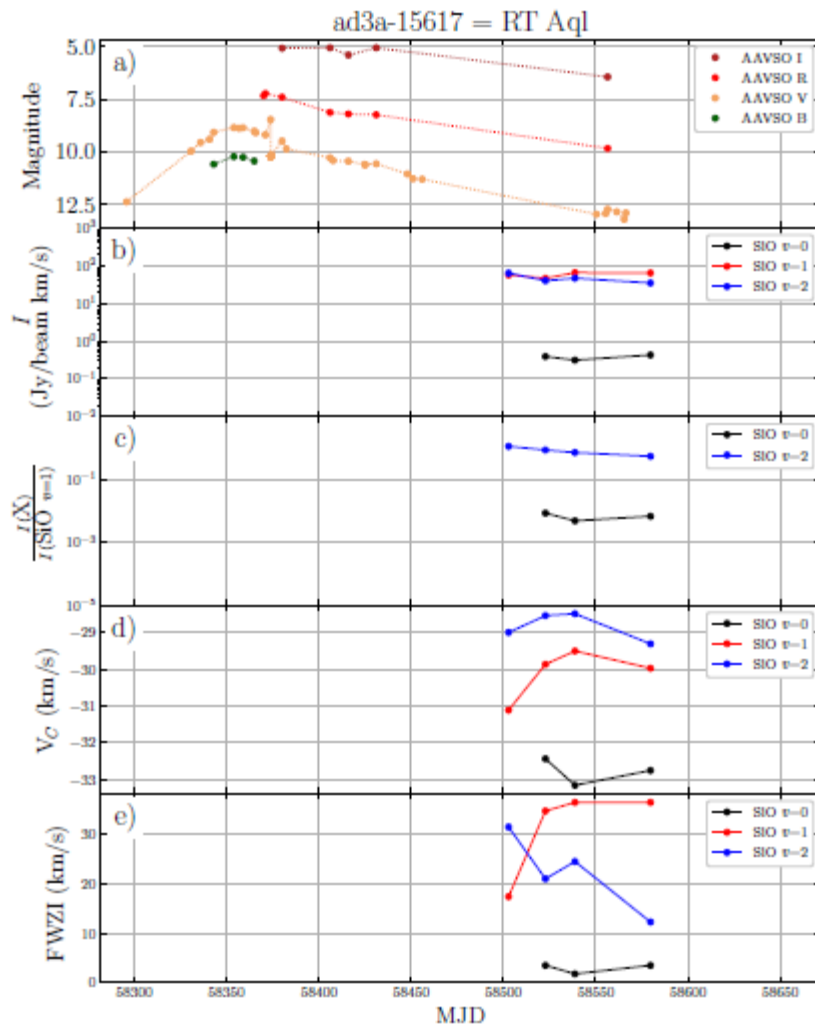
V0353 Vul

Light Curve for V0353 Vul
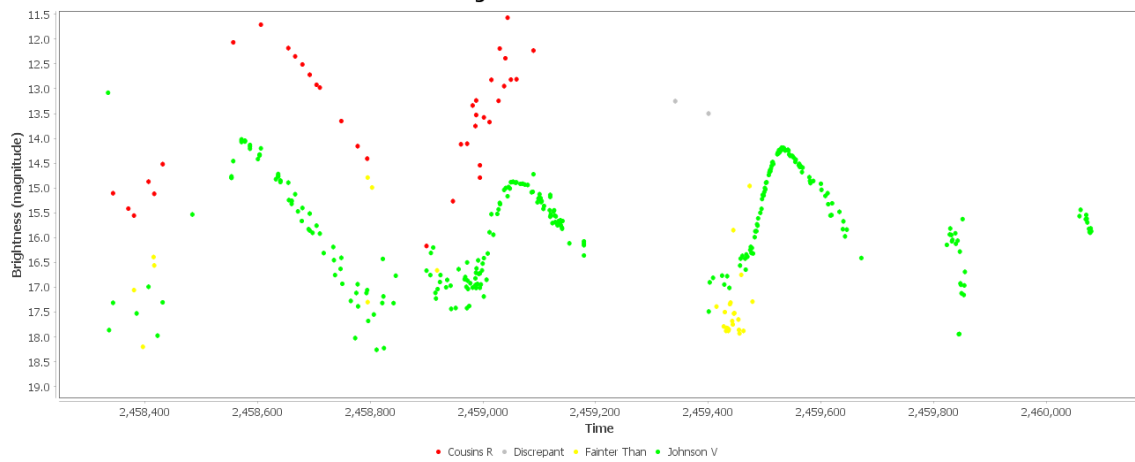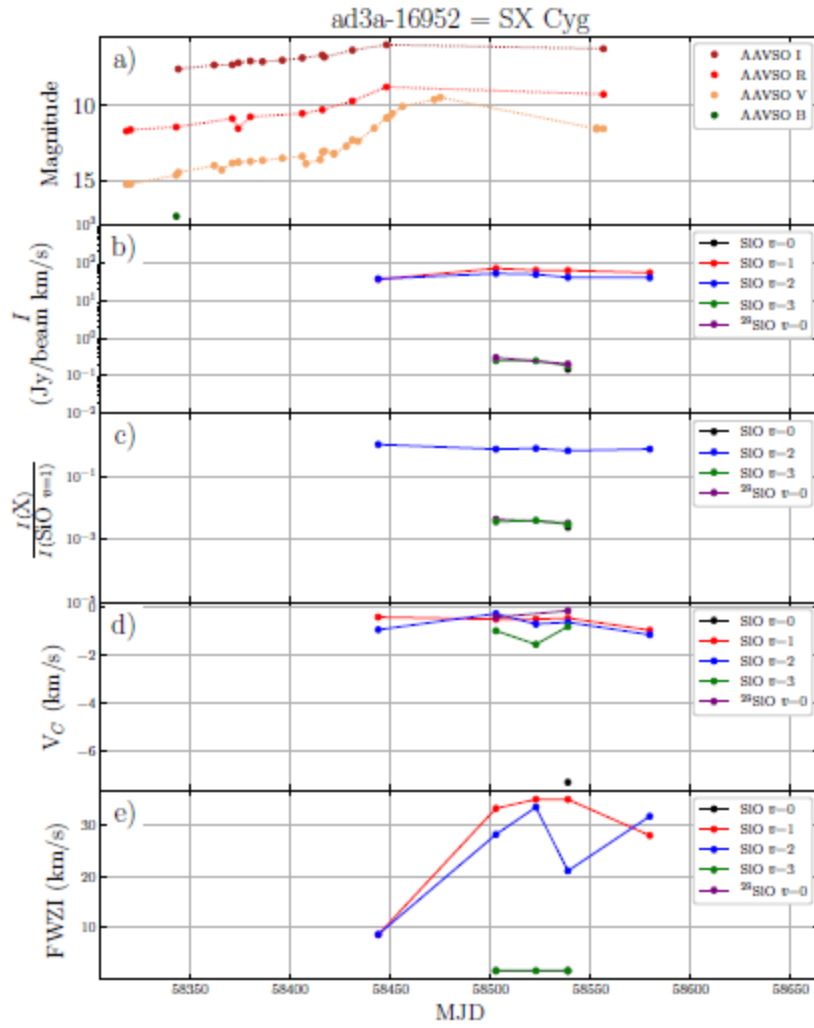
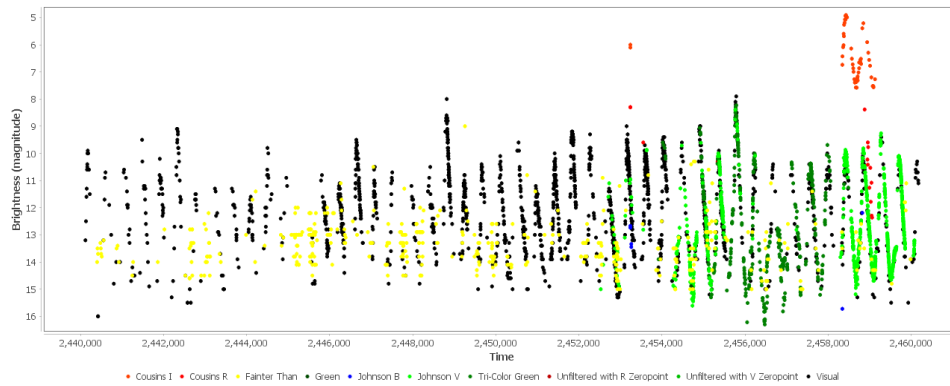Light Curve for V0353 Vul During 43 GHz VLA Monitoring
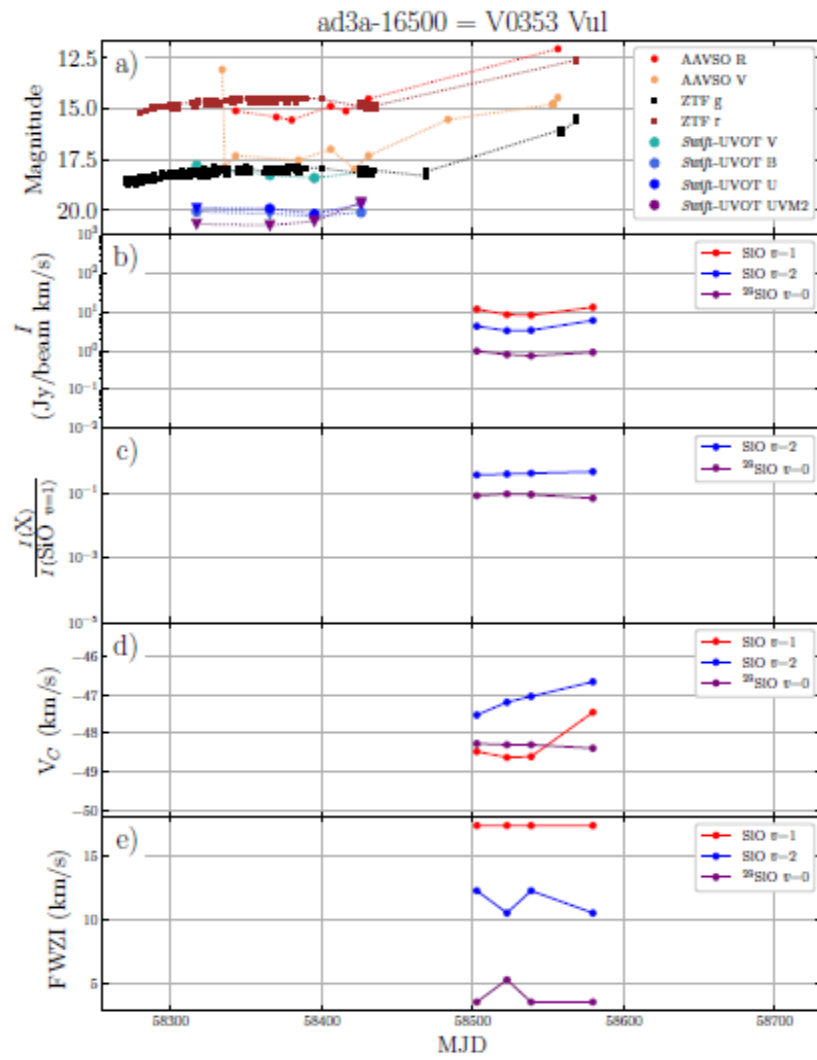
Light Curve for SX Cyg
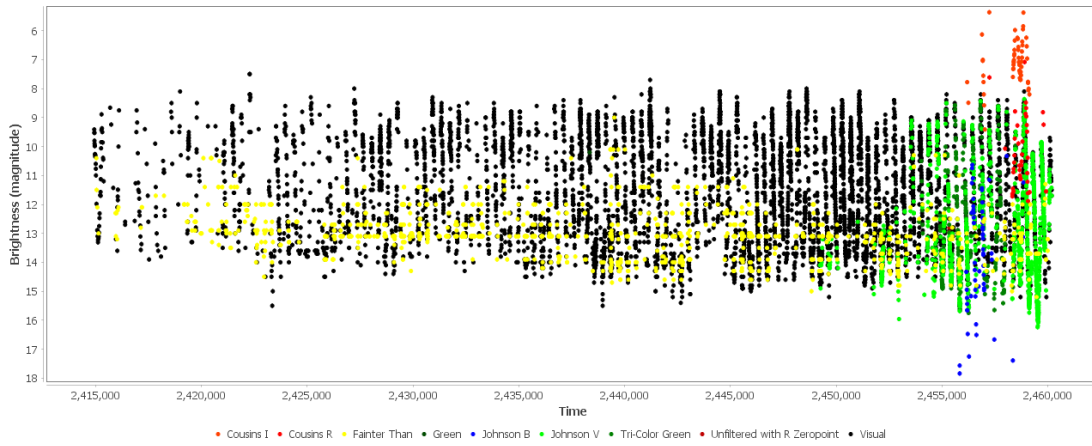
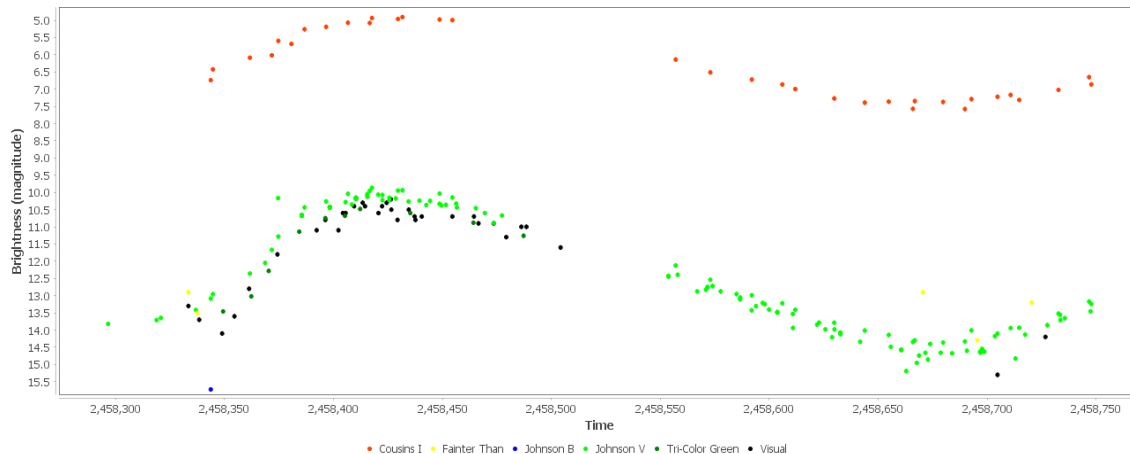**Light Curve for SX Cyg During 43 GHz VLA Monitoring**

ad3a-16952 = SX Cyg

AU Cyg
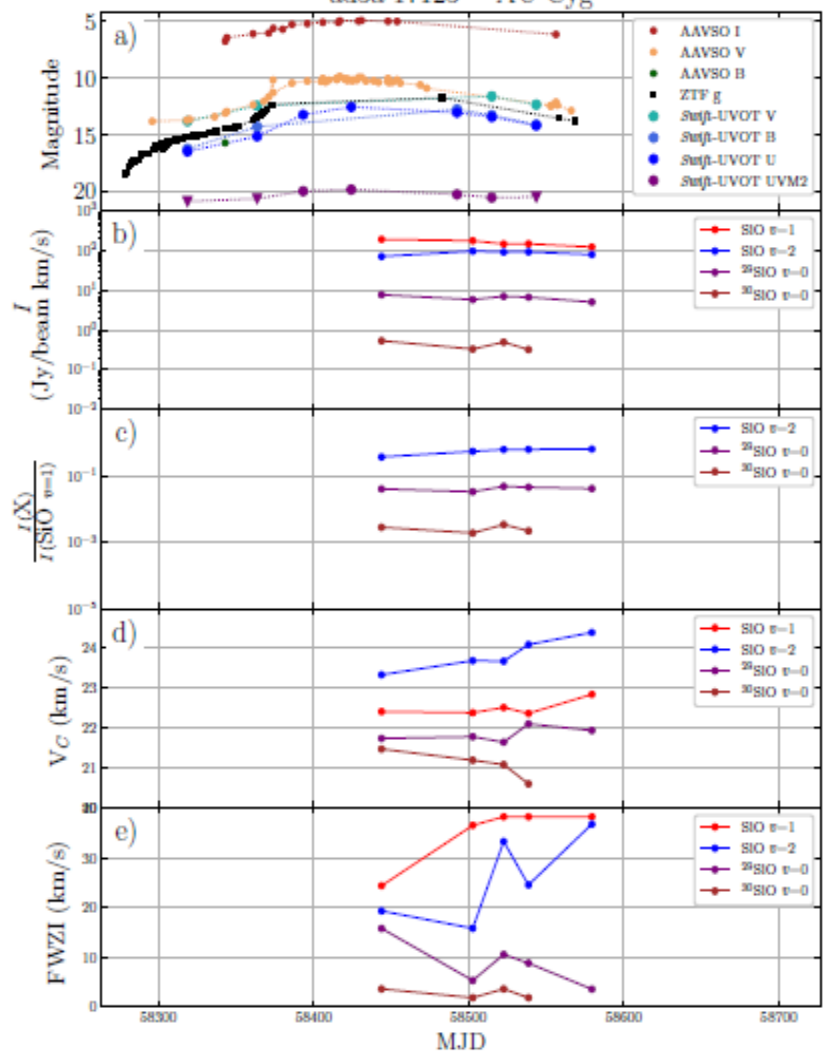
Light Curve for AU Cyg

Light Curve for AU Cyg During 43 GHz VLA Monitoring

ad3a-17123 = AU Cyg

Light Curve for V1655 Cyg

Light Curve for V1655 Cyg During 43 GHz VLA Monitoring

ad3a-17332 = V1655 Cyg

NSVS J2041274+511326

Light Curve for NSVS J2041274+511326
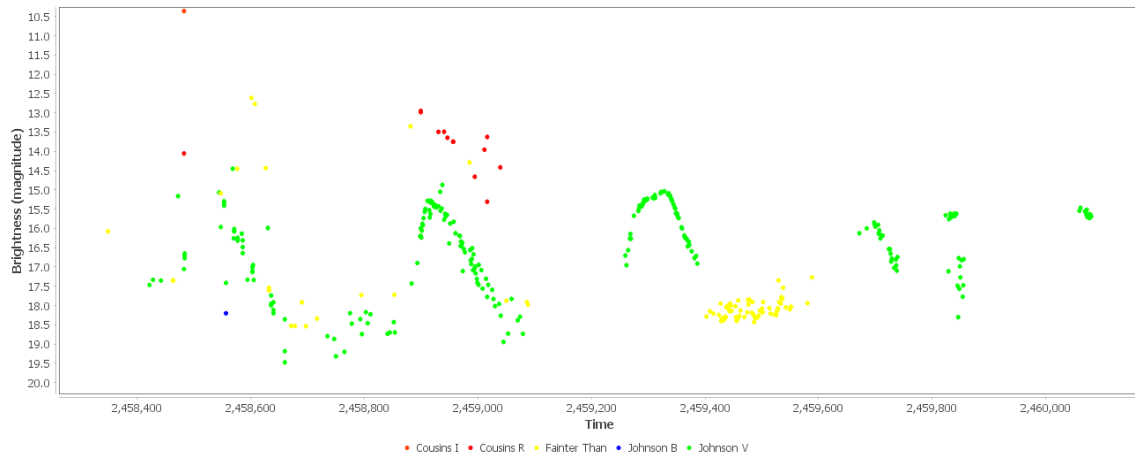
Light Curve for NSVS J2041274+511326 During 43 GHz VLA Monitoring

ad3a-17830 = NSVS J2041274+511326
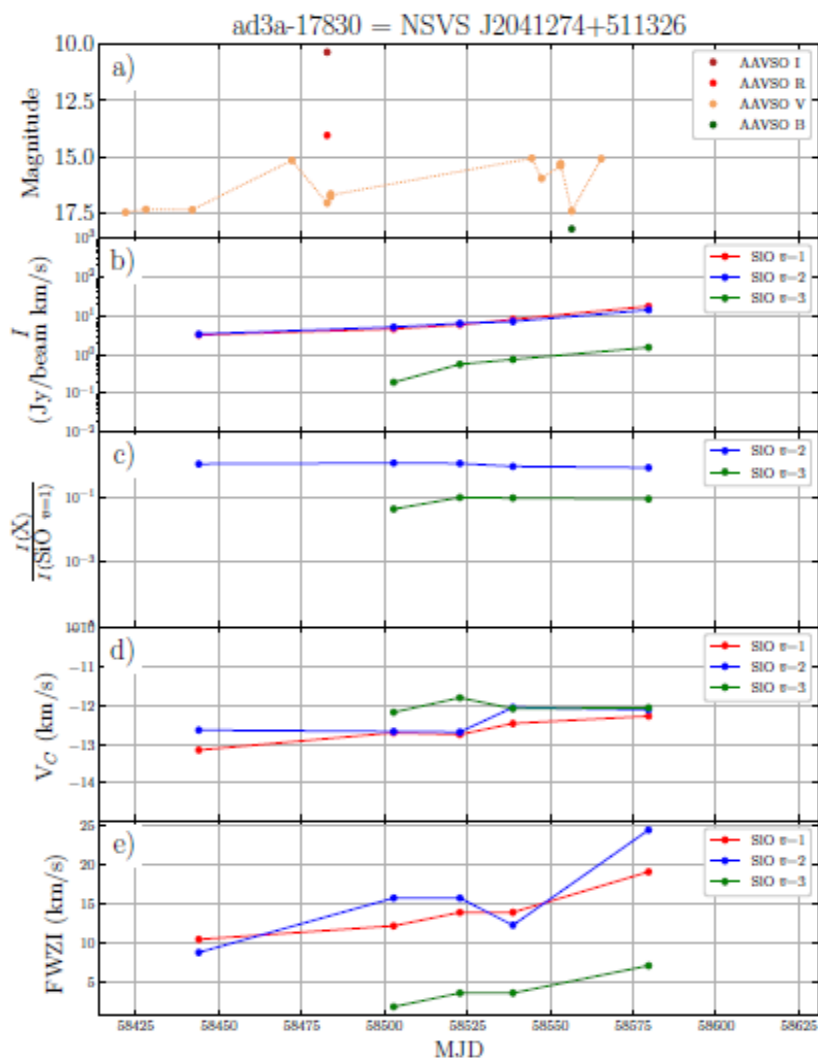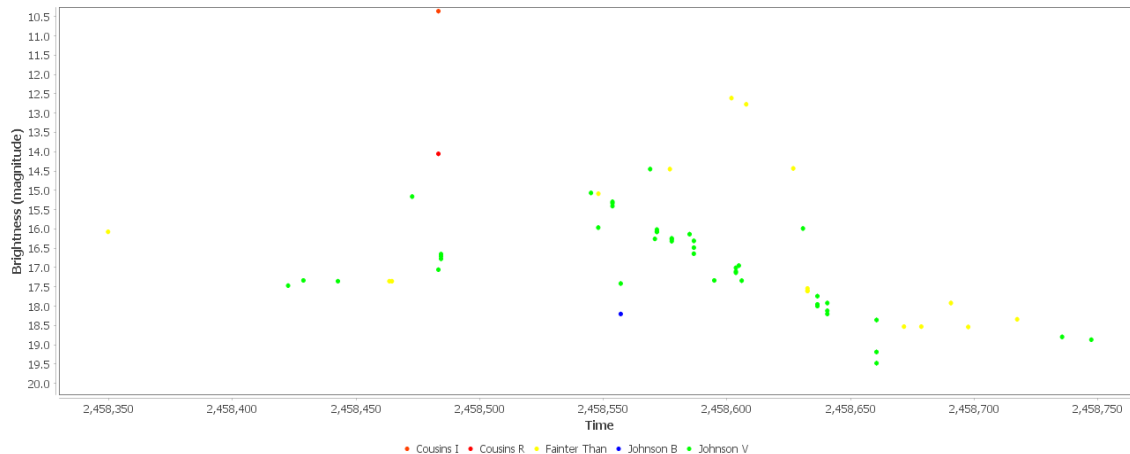
Light Curve for DR Cyg
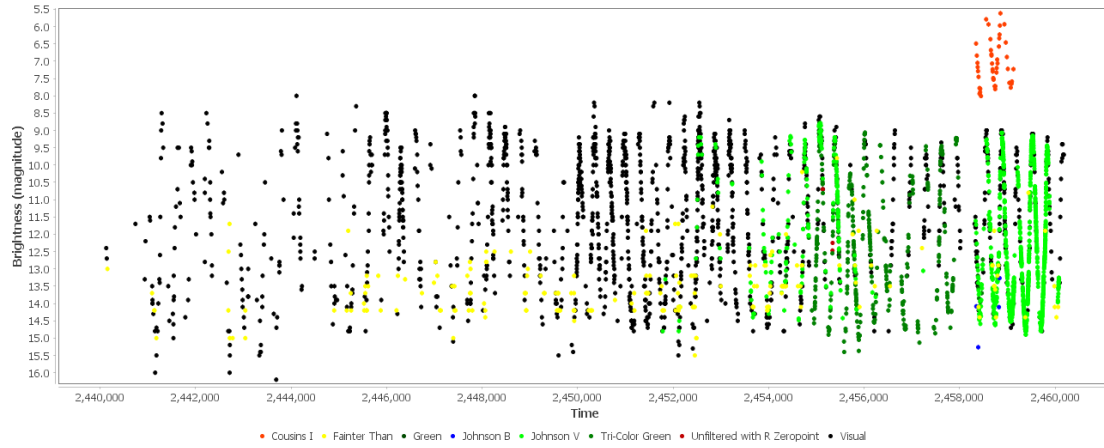
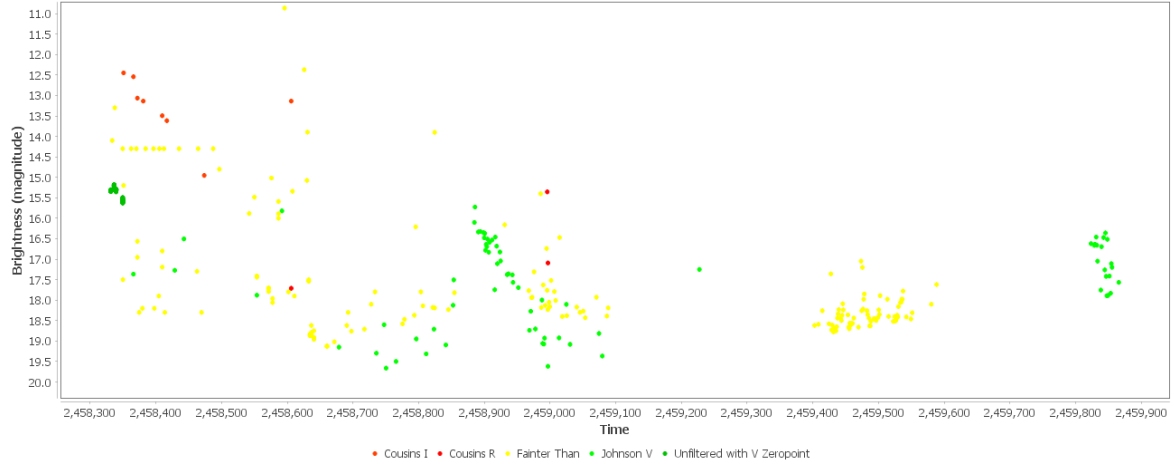**Light Curve for DR Cyg During 43 GHz VLA Monitoring**
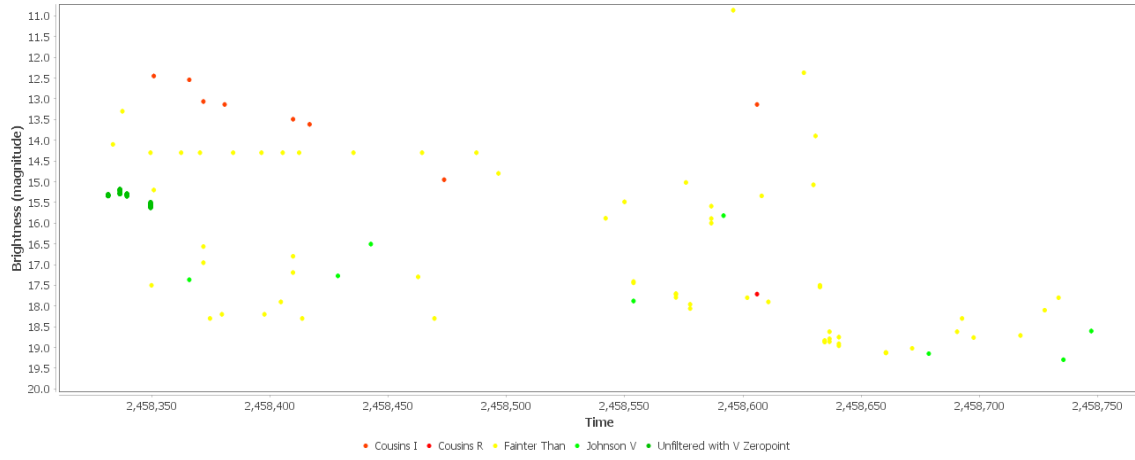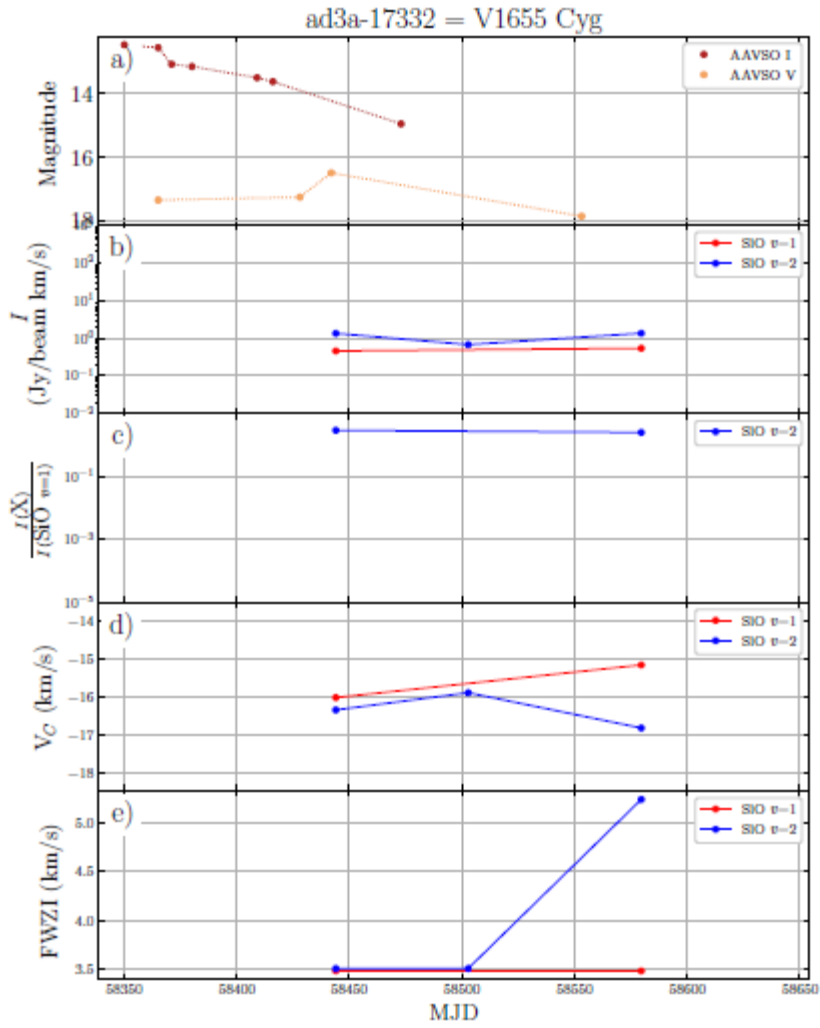

103

ad3a-17304 = DR Cyg
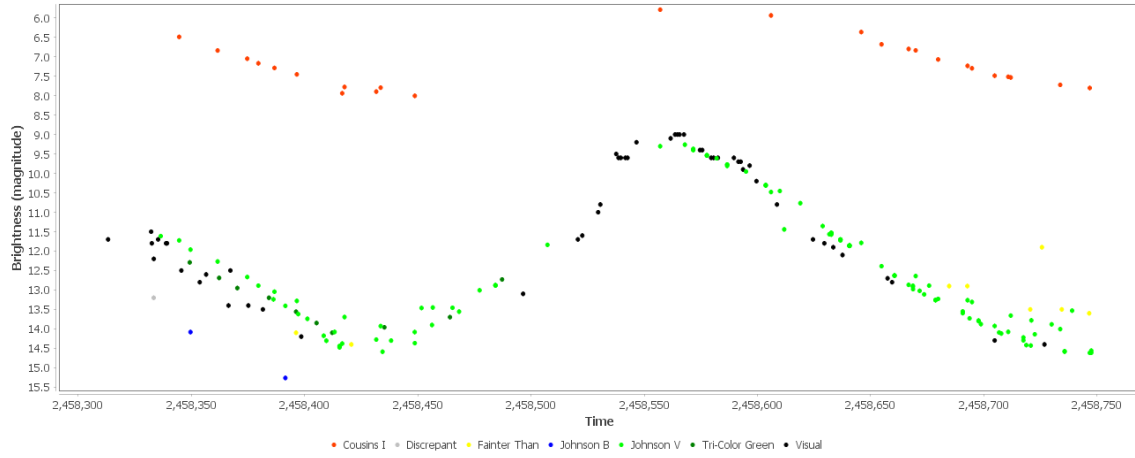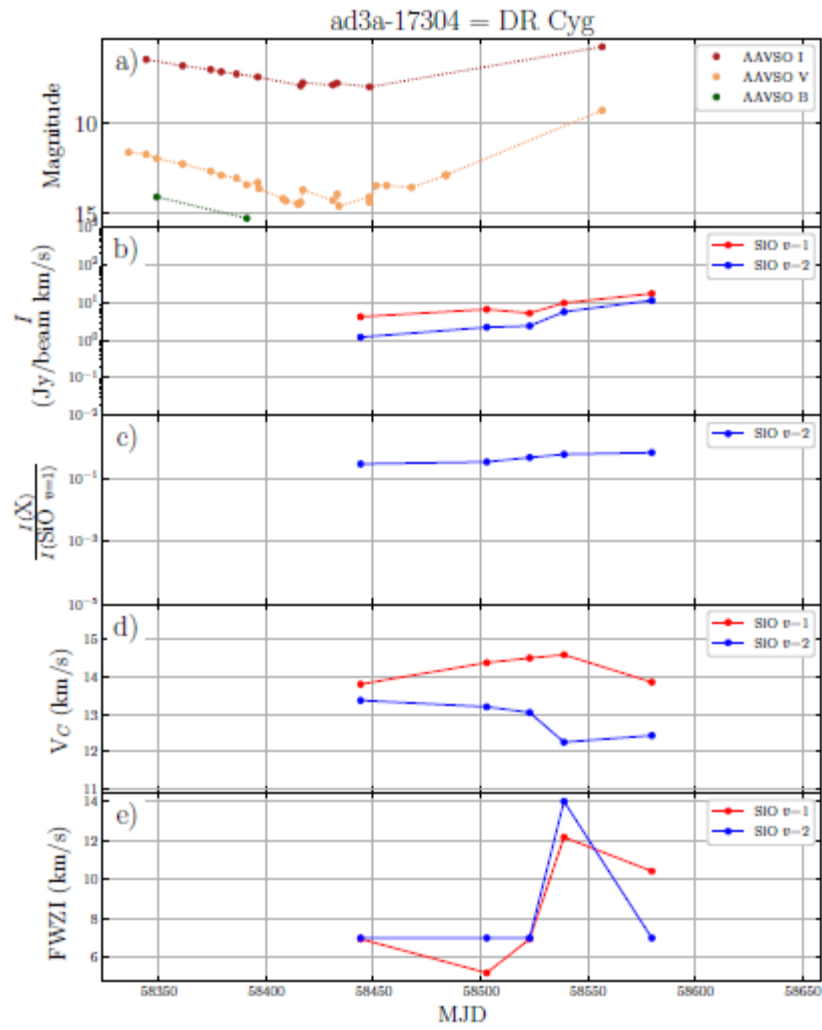
V0750 Cyg

Light Curve for V0750 Cyg
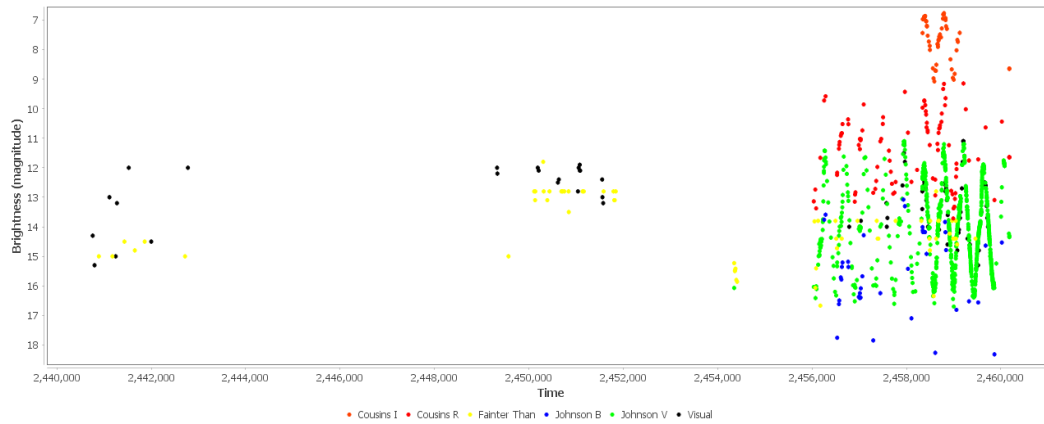
Light Curve for V0750 Cyg During 43 GHz VLA Monitoring

ad3a-17802 = V0750 Cyg

Light Curve for W Cep

Cousins R • Johnson B • Johnson V • Tri-Color Blue • Tri-Color Green • Unfiltered with V Zeropoint • Visual
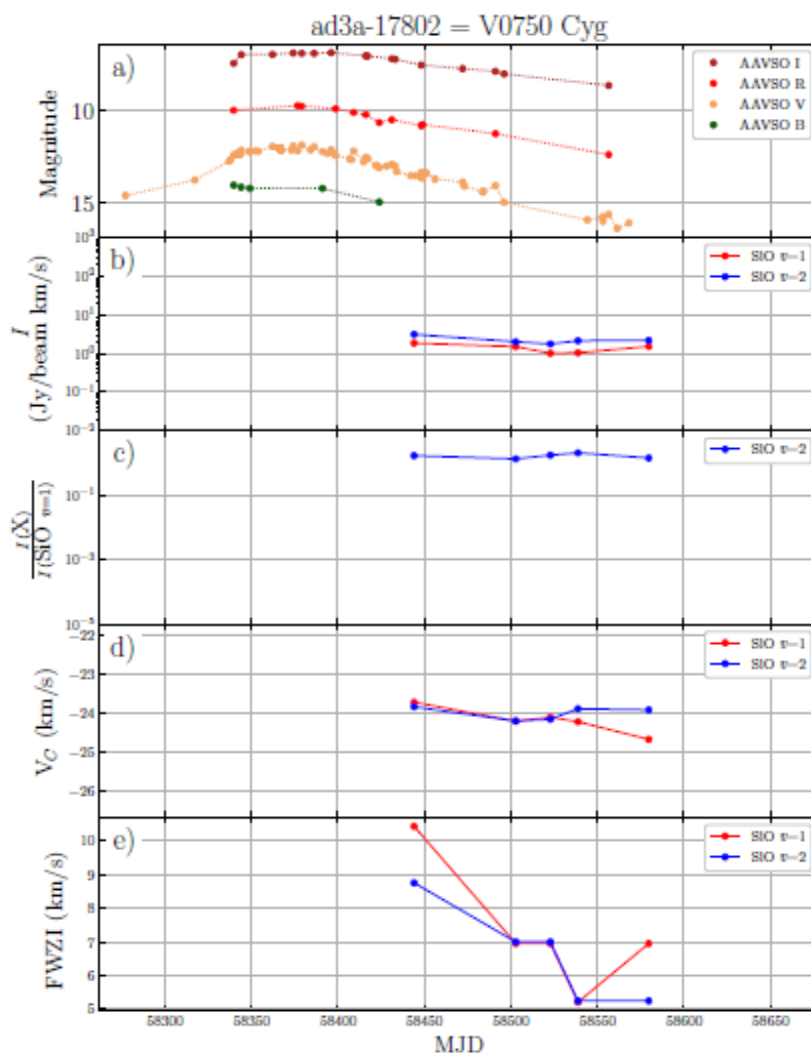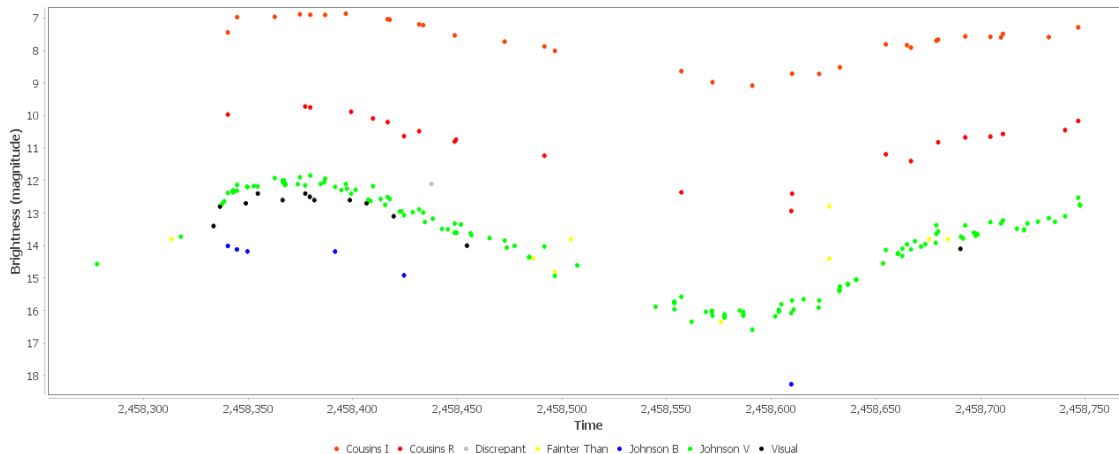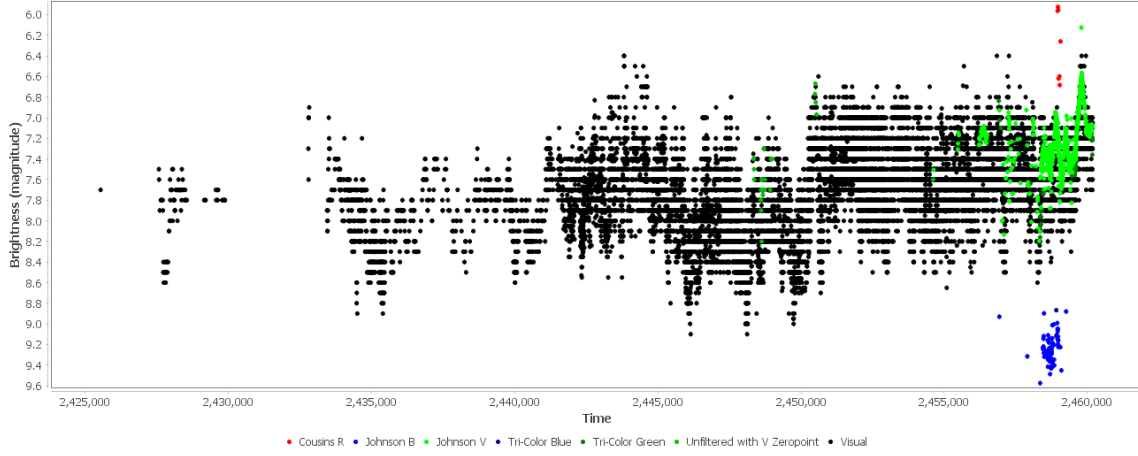
Light Curve for W Cep During 43 GHz VLA Monitoring

Fainter Than • Johnson B • Johnson V • Tri-Color Green • Unfiltered with V Zeropoint • Visual

106

ad3a-18063 = W Cep
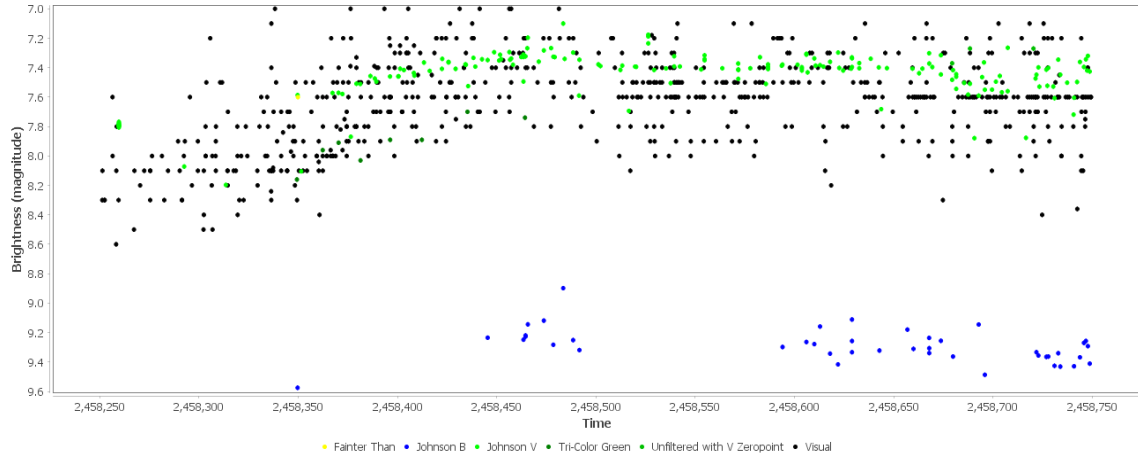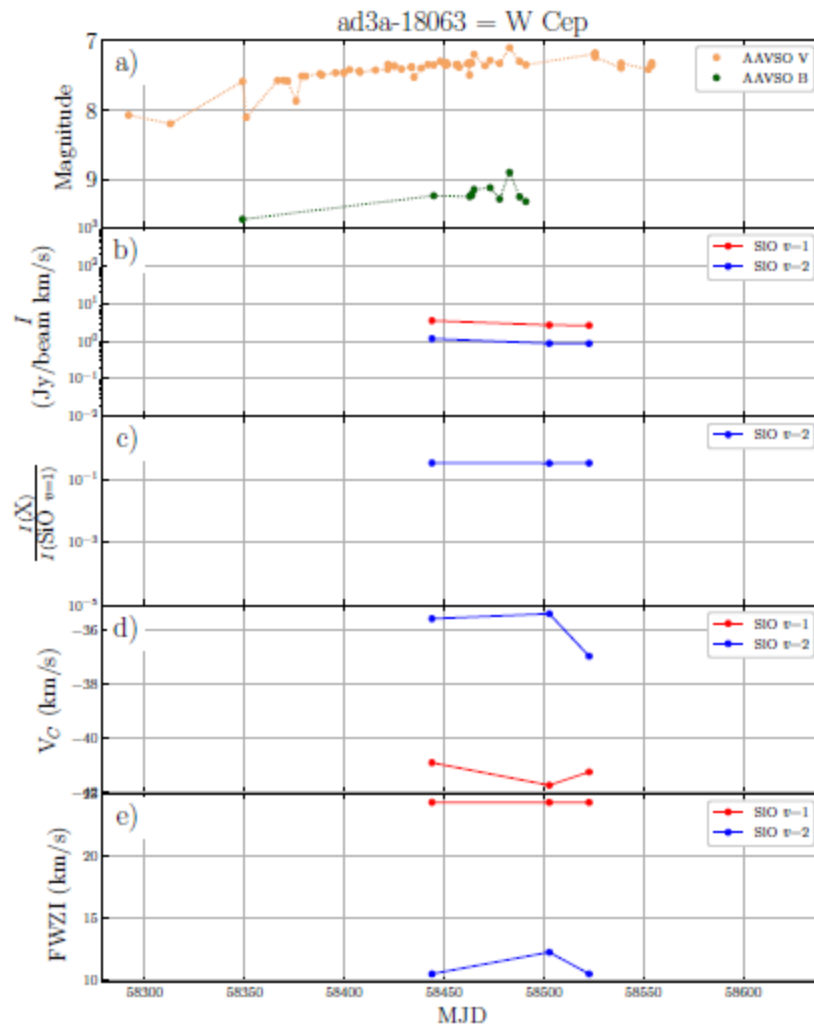
VX Cep

Light Curve for VX Cep

• Cousins I   • Cousins R   • Johnson B   • Johnson V   • Tri-Color Green   • Visual
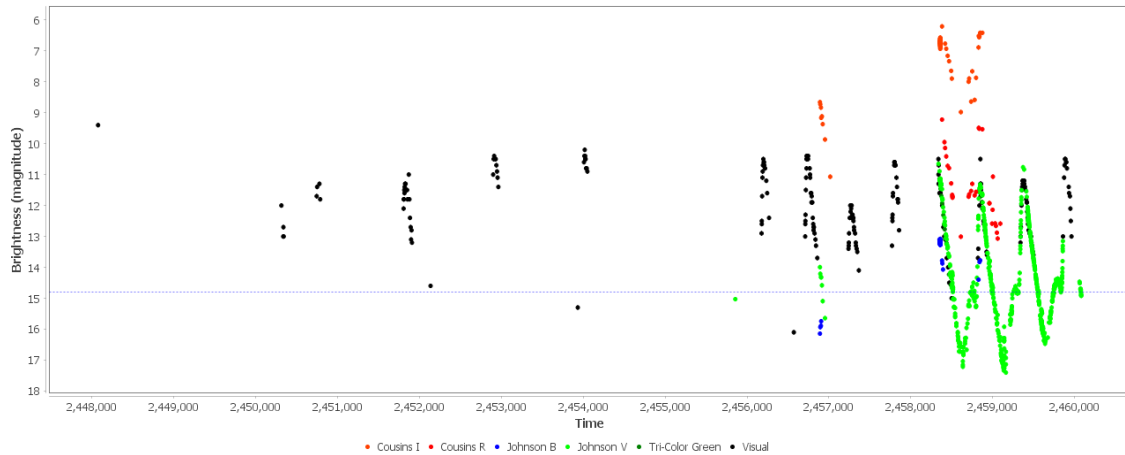
Light Curve for VX Cep During 43 GHz VLA Monitoring

ad3a-18292 = VX Cep
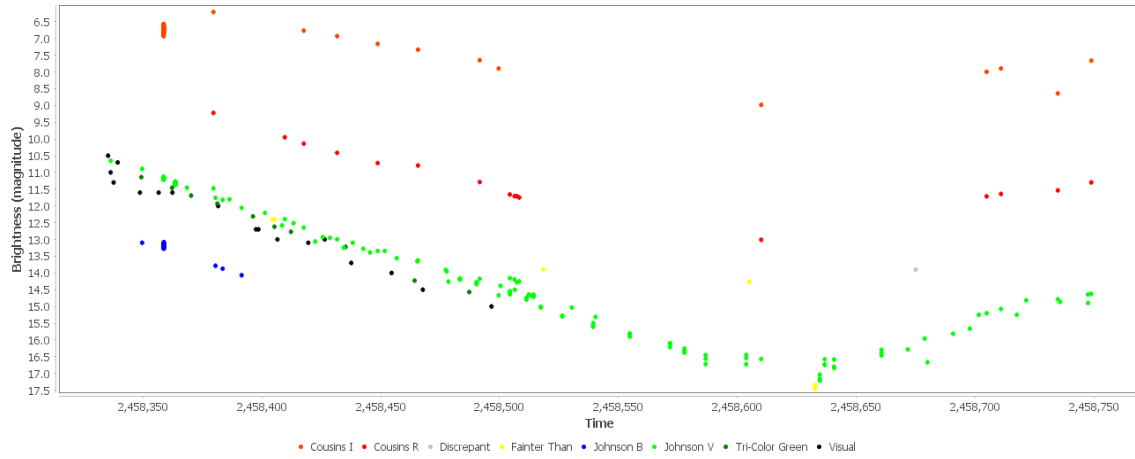
V0850 Cas

Light Curve for V0850 Cas
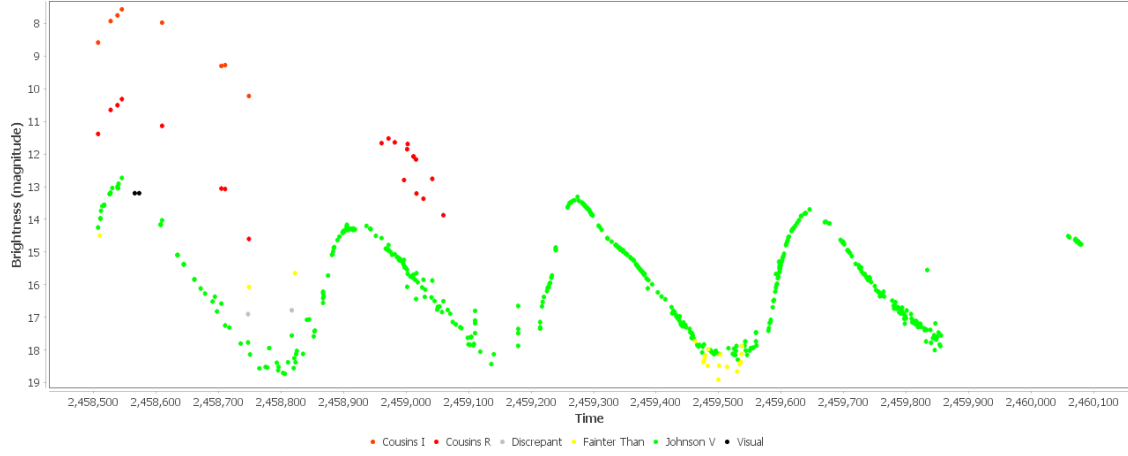
Light Curve for V0850 Cas During 43 GHz VLA Monitoring

109

ad3a-18081 = V0850 Cas
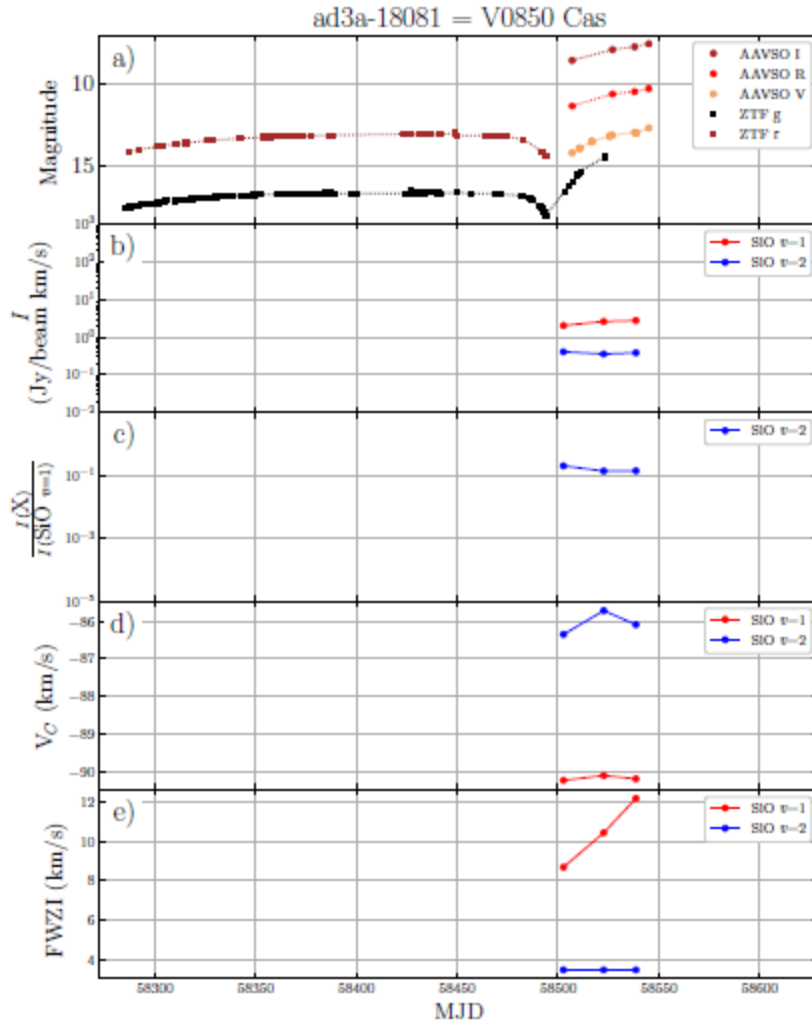
AL Cep

Light Curve for AL Cep
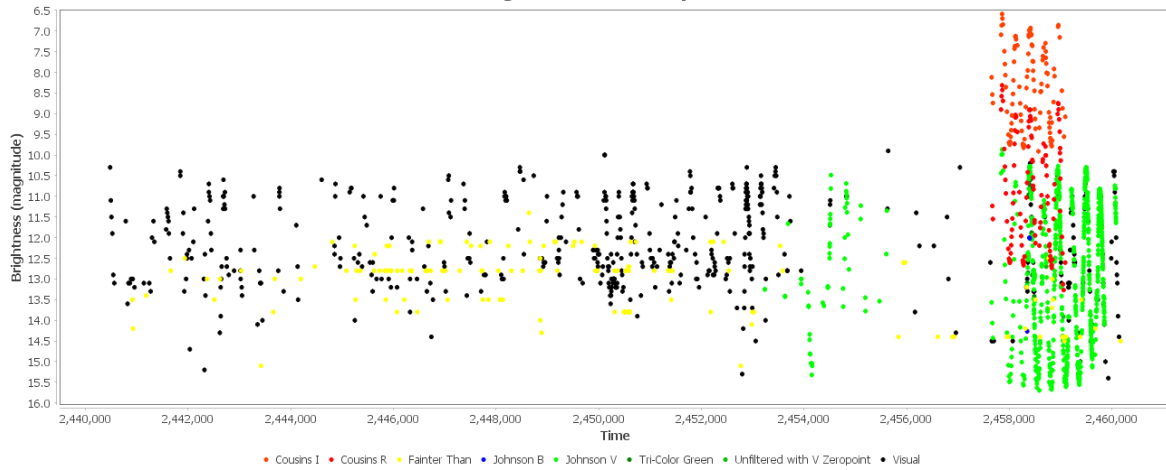
Light Curve for AL Cep During 43 GHz VLA Monitoring
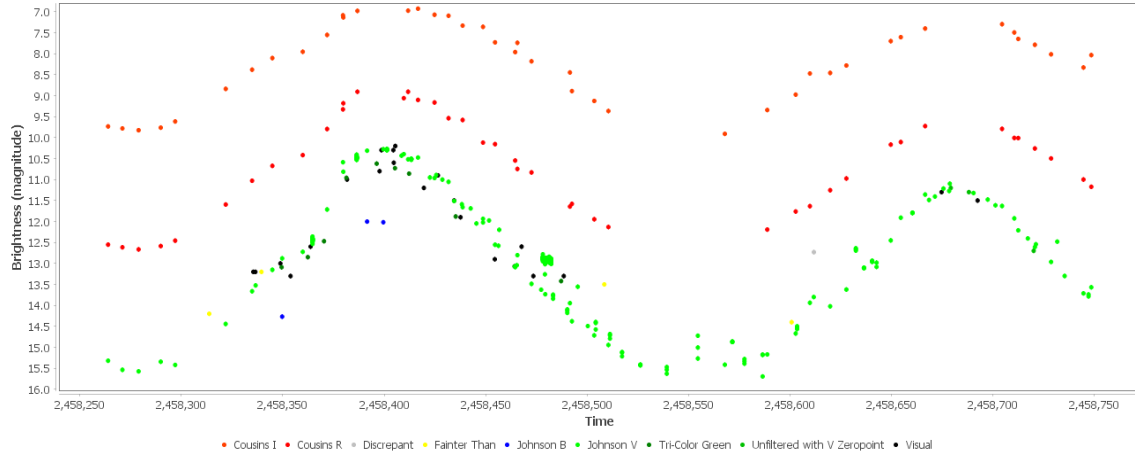
ad3a-18070 = AL Cep

V Cas

Light Curve for V Cas

Light Curve for V Cas During 43 GHz VLA Monitoring
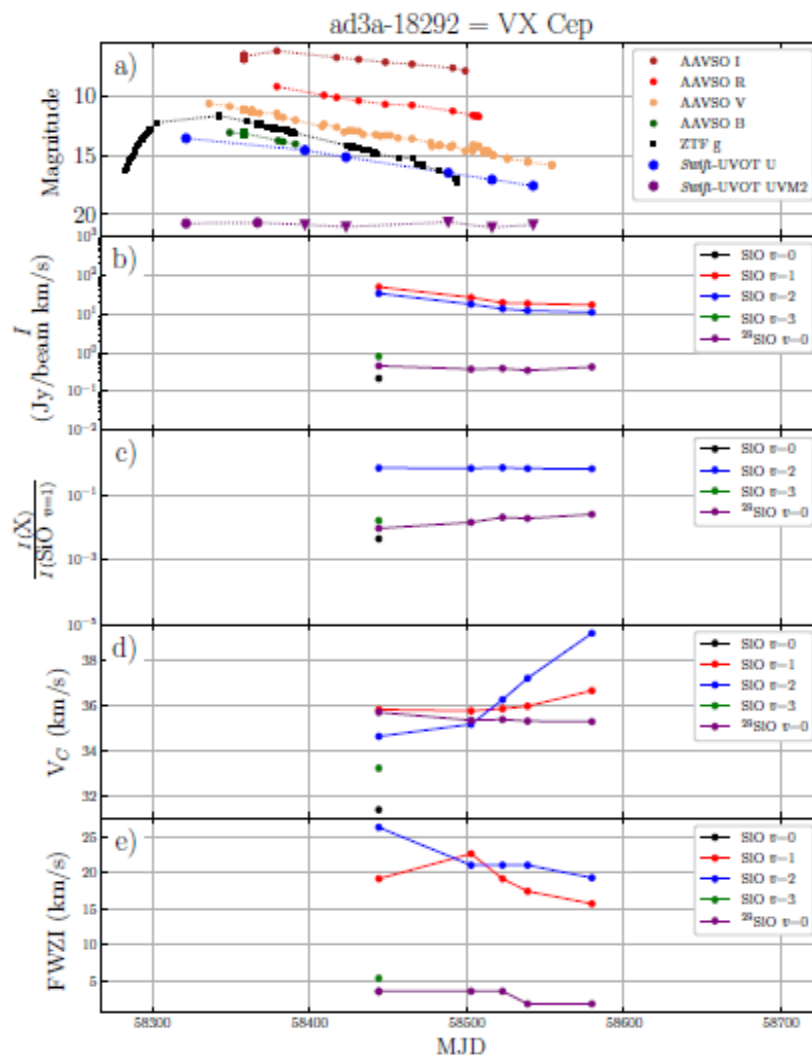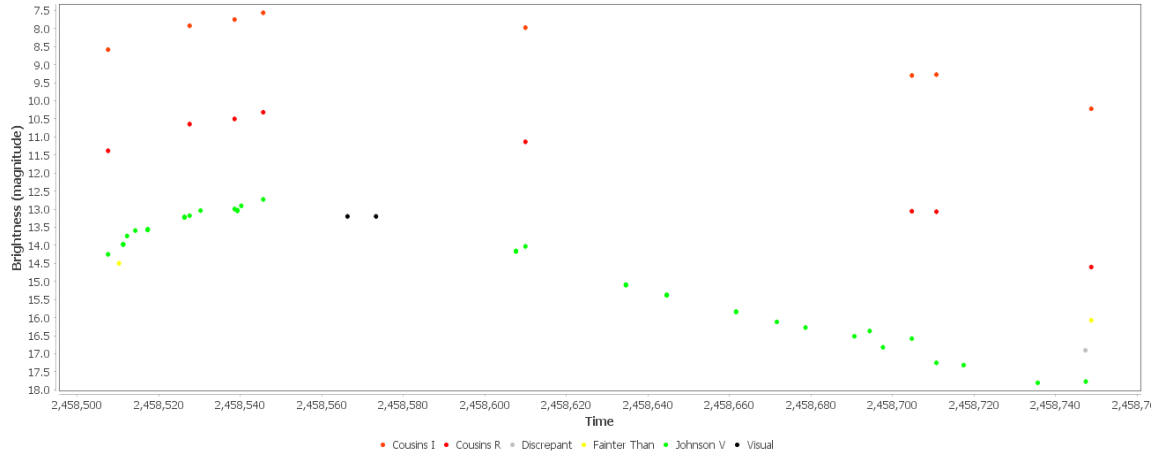
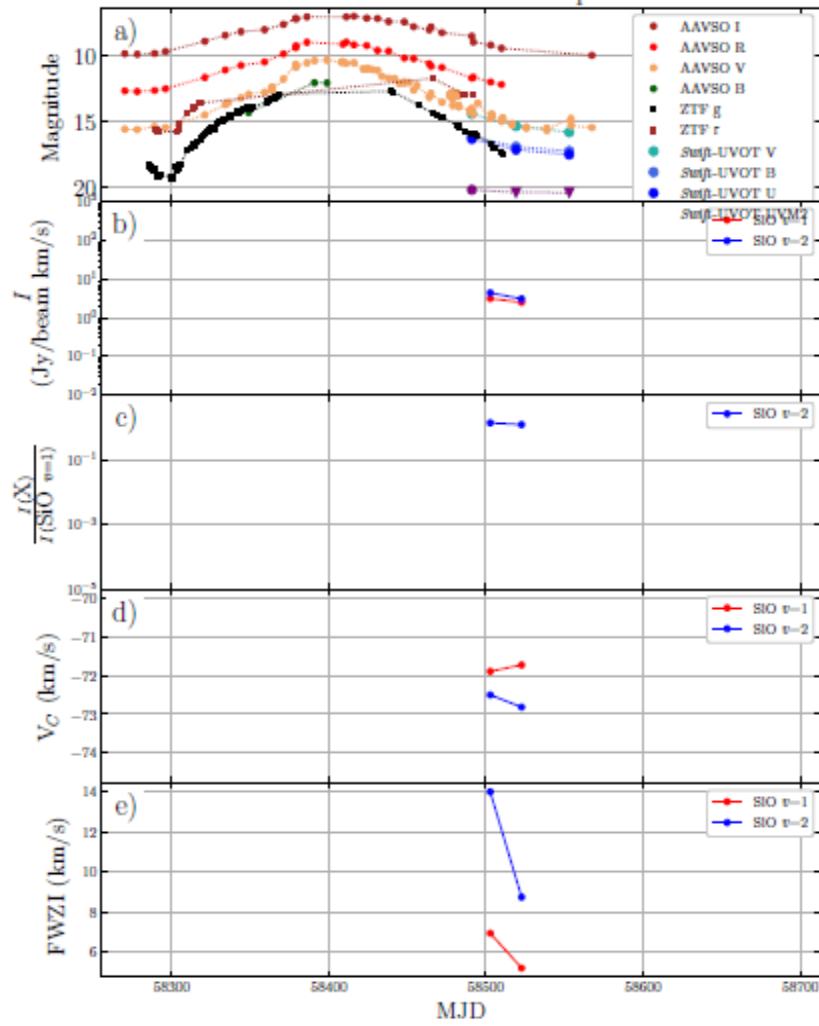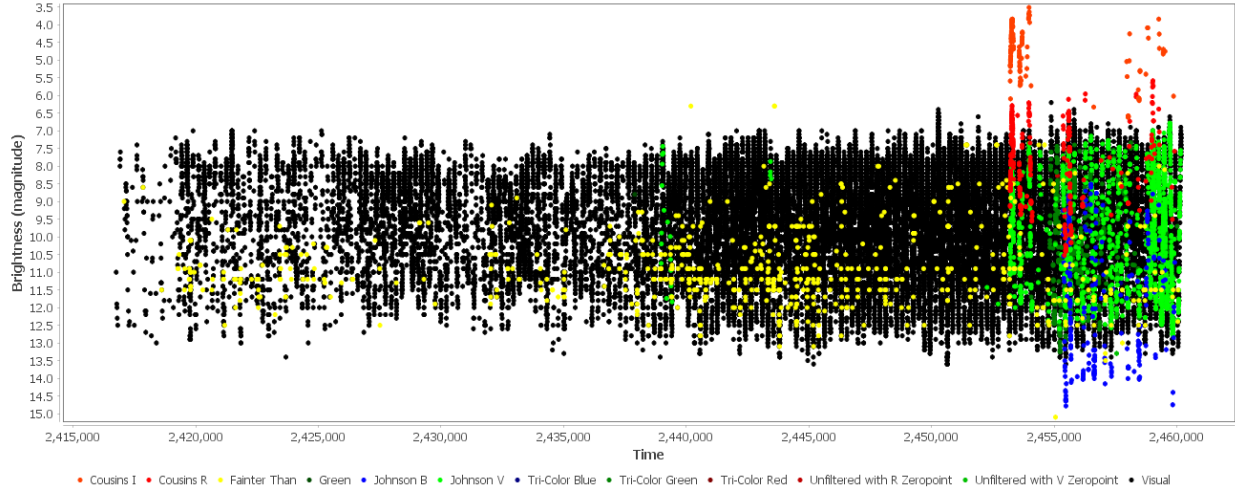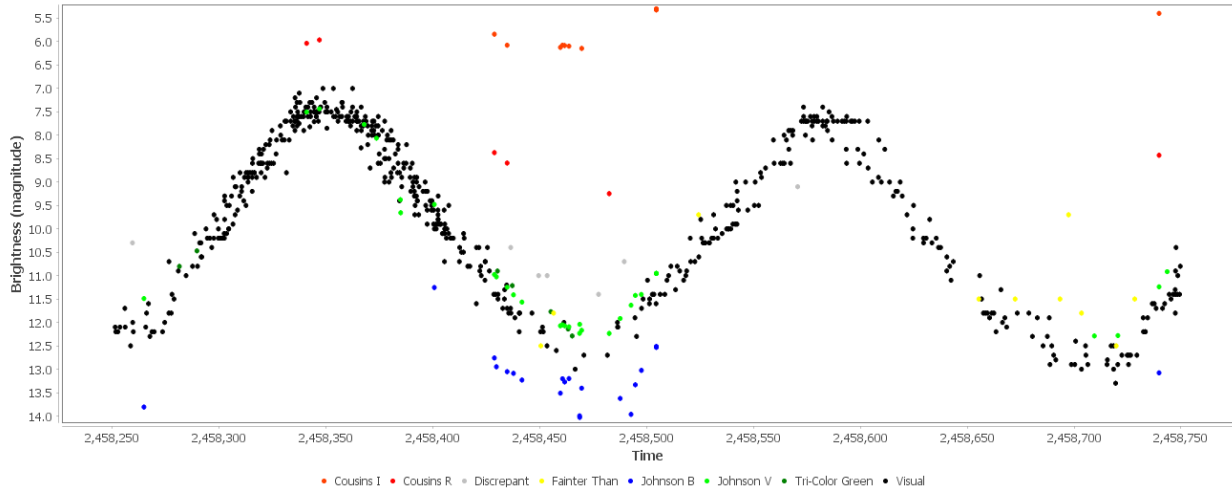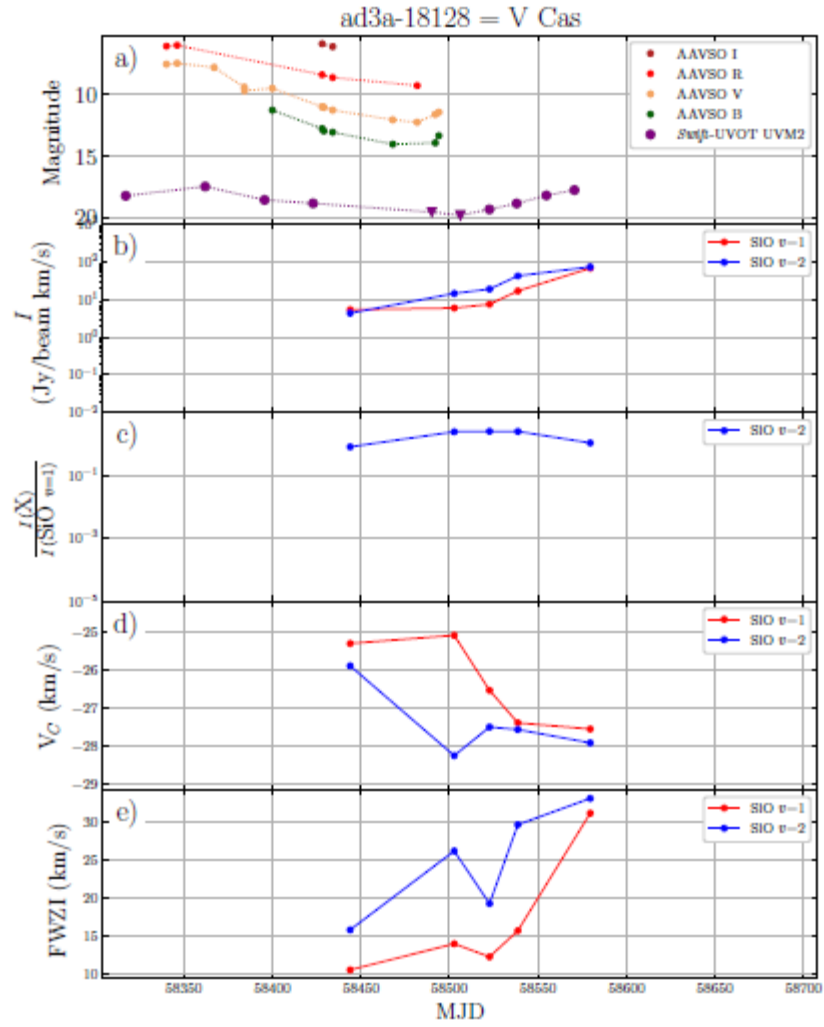ad3a-18128 = V Cas

Light Curve for V0657 Cas

• Cousins I   • Cousins R   • Discrepant   • Fainter Than   • Johnson B   • Johnson V

113

Light Curve for V0657 Cas During 43 GHz VLA Monitoring

ce3a-00250 = V0657 Cas
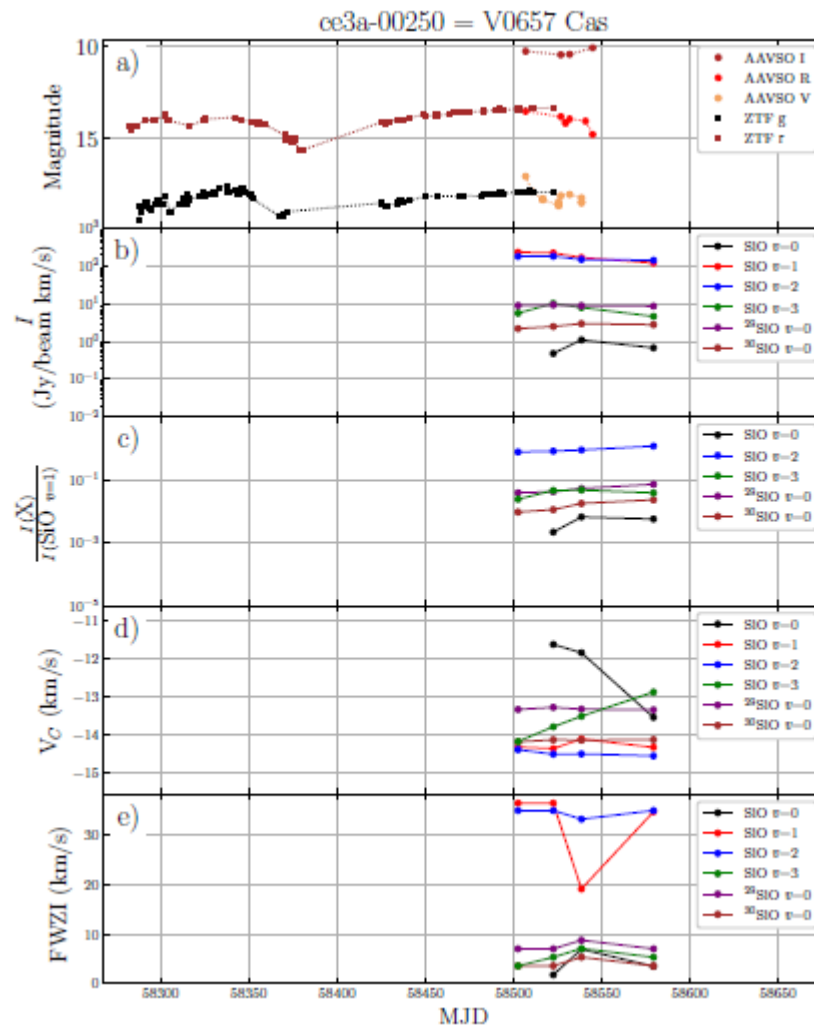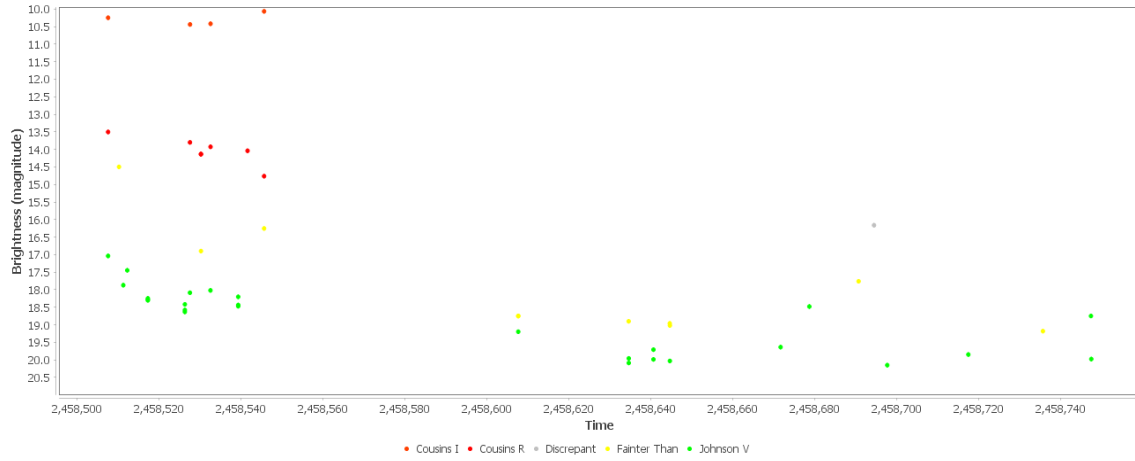
3. **Discussion and Conclusions**

The American Association of Variable Star Observers (Kloppenborg 2022, American Association of Variable Star Observers (https://aavso.org)) and the University of New Mexico (Stroh, M. "Circumstellar SiO Masers in the Bulge Asymmetries and Dynamical Evolution Survey", 2019, https://digitalrepository.unm.edu/phyc_etds/216) participated in a cooperative effort to study SiO maser emissions. The maser emissions were observed with the Jansky Very Large Array (JVLA) by the University of New Mexico. This study surveyed red giant sources in the Galactic bulge and inner Galaxy for SiO maser emission at 7mm and 3mm wavelengths (43 GHz and 86 GHz). At these wavelengths, observations are not hindered by extinction, and extremely accurate stellar velocities (< 1 km/s) and positions can be determined. The survey targeted approximately 28,000 red giant SiO maser sources. In total, twenty Mira Long Period Variable (LPV) stars were studied with the combination of AAVSO light curves and the VLA 43 GHz radio frequency observations. The particular stars selected were based on previous SiO observations as well as a good history of AAVSO coverage. These objects are outlined in Figure 1.

For each of the twenty Mira variables listed in Figure 1, three plots display pertinent optical and radio frequency information. These include the latest overall AAVSO light curve, the portion of the AAVSO light curve that corresponds to the time period in which the VLA was observing the maser activity, and the composite data from the University of New Mexico study. The composite data includes light curves from AAVSO as well as other sensor (e.g., the Swift spacecraft and the Zwicky Transient Facility (ZTF)) data in the top panel. The second panel shows Integrated Flux Density I (Jy/beam km/s), the third panel shows Integrated Flux Density relative to the SiO v=1 emission, the fourth panel shows the velocity centroid of the emission, and the fifth panel shows the full linewidth at zero maximum (i.e., the width of all emissions).

Since the time interval over which the 43 GHz VLA observations were performed (JD 2458249-JD 2458750 or May 10, 2018 - September 23, 2019) is just a small fraction of the overall light curve for the maser object (for example, JD 2414940-JD 2460185 or October 13, 1899 - August 29, 2023 for SX Cyg), it is difficult to draw any firm conclusions without more extensive VLA data. However, examining the AAVSO light curve corresponding to the time of the VLA maser observations as well as the AAVSO and other optical data shown in the top panel of the composite data (Swift and ZTF) indicates that there appears to be a general correlation between the optical data and the VLA intensity I (Jy/beam km/s) for all objects. In some cases, there is a strong correlation while in other cases the correlation is weak. Additionally, the integrated flux density relative to the SiO v=1 emission tracks the intensity I and the optical light curves.

References

Benn, D. 2012, "Algorithms + Observations = VStar", JAAVSO, v40, n2, pp.852-866 (https://www.aavso.org/vstar) AAVSO VStar data analysis software.

Ferraz-Mello, S. 1981, Estimation of Periods From Unequally Spaced Observations, Astron. J., vol 86, p619. (https://adsabs.harvard.edu/full/1981AJ.....86..619F)

Kloppenborg 2022, American Association of Variable Star Observers (AAVSO) (https://aavso.org).

Kloppenborg 2022, American Association of Variable Star Observers (AAVSO) International Variable Star Index (VSX) (https://www.aavso.org/vsx/). This research has made use of the International Variable Star Index (VSX) database, operated at AAVSO, Cambridge, Massachusetts, USA.

Kloppenborg 2022, American Association of Variable Star Observers (AAVSO) Alert Notice 687.

Stroh, Michael Cullen. "Circumstellar SiO Masers in the Bulge Asymmetries and Dynamical Evolution Survey." (2019). https://digitalrepository.unm.edu/phyc_etds/216

Biography

Mr. Hinzel is the Founder, President, and Chief Scientist of Argent Astro Research Institute (AARI). AARI, previously known as Engineering Tecknowledgey Applications, LLC (ETA) is a technical and business professional services firm established to provide high quality engineering, scientific, and business consulting, contracting, and research services to commercial, corporate, and government customers. He has a B.S. in Physics, a B.S. in Mathematics, and a B.S. in Electrical and Computer Engineering, an M.S. in Electrical Engineering, and has completed all course requirements for the Ph.D in Electrical Engineering.

Mr. Hinzel is a member of the American Association of Variable Star Observers (AAVSO) where he is the observing section leader for the AAVSO International High Energy Network (HEN). The HEN is dedicated to the study of high energy astrophysical phenomena in the universe, including Gamma Ray Bursts, Quasi-Stellar Objects, Active Galactic Nuclei, and gravitational waves. He is also a member of the American Astronomical Society (AAS) and the Society for Astronomical Sciences (SAS). He has written several research papers for the AAVSO and the AAS, including:

"Data Mining Analysis for Eclipsing Binary TrES-Cyg3-04450", D. Hinzel. The Journal of the American Association of Variable Star Observers, JAAVSO Volume 43, 2015.

"Unmanned Aerial Systems for Variable Star Astronomical Observations", D. Hinzel. The Journal of the American Association of Variable Star Observers, JAAVSO Volume 46, 2018.

Photometric Observations of Nine High Mass X-Ray Binaries and Analysis of Potential Periodicities and Variations 2022 Res. Notes AAS 7 15; DOI 10.3847/2515-5172/acb5a0

Light Curve Analysis of Nine Algol (EA) Eclipsing Binaries Discovered During the Dauban Survey 2022 Res. Notes AAS 6 231; DOI 10.3847/2515-5172/ac9d9e

Light Curve Analysis of Nine Algol (EA) Eclipsing Binaries Discovered During the Dauban Survey-additional Data 2022 Res. Notes AAS 6 239; DOI 10.3847/2515-5172/aca28f

Applications of CubeSats for Astrophysics Research: Detection of Radio Frequency Counterparts of High Energy Phenomena with Very Long Baseline Interferometry, Journal of the Society of Amateur Radio Astronomers (JSARA), July-August 2023, pp. 66-78.Contact: argentastro22@gmail.com

Investigating the Radiometer T_{SYS} Double Whammy Formula
Peter W East

Abstract

Traditional temperature sensitivity calculations of radio telescope receivers identify two sensitivity loss mechanisms due to unwanted attenuation between the receive antenna and low noise amplifier (LNA) [1]. The first is a straightforward proportional signal loss and the second is an added loss-dependant attenuation noise term. This is often referred to as the double whammy effect of pre-LNA losses [2]. Post-antenna resistive mismatches via connections or with the LNA causing power loss are treated similarly. Reactive mismatches reduce antenna efficiency but deliver no extra noise. Noise factor analysis indicates that a receiver output signal-to-noise ratio (SNR) is only degraded once by the total pre-LNA attenuation. This note follows on from a previous article and explores comparative methods of radiometer temperature sensitivity calculation aiming to resolve the attenuator noise issue and identify reactive load limitations [3].

Introduction

This article examines a number of basic analysis methods used for low noise microwave radiometer receiver chains to explain the derivation and scope of the radiometer system noise temperature sensitivity formula. The standard formula is first introduced implying the double whammy followed by some basic transmission line definitions including discussions on mismatch loss, effect of reactive loads and transmission line loss. Then standard noise factor analysis indicates that the pre-LNA attenuation degrades the combined noise factor only once with single whammy implications. Further sections explain the whammy differences, producing two temperature analysis solutions shown to be mathematical identities where the loss factors can be clearly identified. Later sections cover the radiometer fed from an antenna, Y-factor T_{SYS} measurement and finally presents some examples illustrating the noise contribution of pre-LNA attenuation in practical systems.

The T_{SYS} Double Whammy Formula

For a radiometer with unwanted attenuation between a well-matched antenna and LNA, the usual formula for calculating the receiver system noise temperature performance, referenced to the LNA input is [1],

$$T_{SYS} = AT_S + [1 - A]T_a + T_{LNA} \quad (1)$$

where, T_S is the antenna terminal source equivalent temperature, A is the attenuation/power loss factor ($A < 1$) between the antenna terminal and the LNA input, T_a is the ambient temperature and T_{LNA} is the LNA equivalent input noise temperature (note:- some texts use $L = 1/A$ to describe loss).

The fact that the attenuation factor appears twice in this formula, by linearly reducing the signal power and also adding attenuator-induced extra noise gives rise to the double whammy SNR verdict.

Available Power

All the following derivations are based on available power dissipated in a resistive load. Consider a voltage generator V with a source resistance R_S feeding a load R_L.

The power dissipated in the load from simple circuit theory is given by,

$$P_{load} = \frac{V^2 R_L}{(R_S + R_L)^2} \quad (2)$$

Maximum power is dissipated in the load when $R_L = R_S$ and this is termed the available power from the source = $P_{avail} = V^2/4R_S$. For any other value of the load resistance, R_L, the load power is reduced; this is deemed a mismatch and the power difference termed the mismatch or return loss.

Mismatch Loss Attenuation

For <u>any</u> mismatched cable/component junction with source and load impedances, zs, zl, the voltage reflection coefficient is given by, $\rho = \left| \dfrac{zl - zs}{zl + zs} \right|$.

The mismatch is also specified by the line voltage standing-wave ratio, $vswr = \dfrac{1 + \rho}{1 - \rho}$.

When the load reactance is <u>small</u> compared to the load impedance, the ratio of the power absorbed by the load to the available power from the source, $(1 - \rho^2)$ can be simulated by an equivalent attenuator, where the attenuation loss factor A, is given by,

$$A = \frac{P_{load}}{P_{avail}} = \frac{4 . \mathrm{Re}(zs) . \mathrm{Re}(zl)}{\left(|zs + zl| \right)^2} = (1 - \rho^2) = \frac{4}{\left(\sqrt{vswr} + \dfrac{1}{\sqrt{vswr}} \right)^2} \qquad (3)$$

In summary, at any real microwave circuit junction, even fed by loss-less and correctly source-terminated transmission lines, there is always a resistive load sink that is either matched to the line impedance for no loss, or not matched, for less power to the load constituting the power loss; the loss factor is given by Equation 3, both in terms of reflection coefficient and VSWR.

Effect of Reactive Loads

The presence of large reactive load components can seriously increase the reflection coefficient implying higher signal loss and increased mismatch noise.

In fact, significant signal loss can occur due to reduced available power from the source, but the basic zero reactance resistive noise is only modestly affected up to quite large load reactance values.

With load reactance, X, the available power drops from $P_{avail} = V^2/4R_S$ to,

$$P_{availX} = \frac{V^2 \sqrt{R_S^2 + X^2}}{\left(R_S + \sqrt{R_S^2 + X^2} \right)^2 + X^2}$$
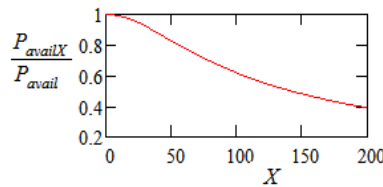
The graph shows that in a 50 Ω system, a 50 Ω load reactance (~2:5 VSWR) can drop the radiometer signal sensitivity by around 20%.

The available power maximum now occurs when $R_L = \sqrt{R_S^2 + X^2}$.

The mismatch attenuation factor P_{load}/P_{availX} is modified to,

$$\frac{P_{load}}{P_{availX}} = A_{rllX} = \frac{2R_L \left(R_S + \sqrt{R_S^2 + X^2} \right)}{\left(R_S + R_L \right)^2 + X^2}$$

118
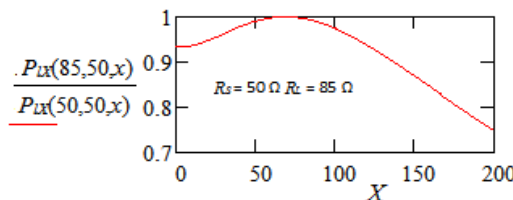
The available power difference is re-radiated by the antenna and is not passed to the LNA or resistive attenuators in the radiometer chain; it reduces the radiometer system sensitivity (see Appendix 2).

Transmission Line Loss Noise
An appreciation of the source and value of the noise generated by an attenuator can be made by considering the effect of transmission line loss.

If the total series resistance is r and the transmission line impedance is Z, feeding an LNA with matched input impedance Z, the line resistance generates thermal noise voltage to the value, $\sqrt{4kT_aBr}$ and delivers a reduced noise power to the LNA input impedance Z of, $\dfrac{4kT_aBrZ}{(r+Z)^2}$.

For example, with series resistance r = 1 Ω, or 10 Ω, and with Z = 50 Ω, the noise power delivered to the LNA = $0.08kT_aB$, or $0.56kT_aB$. These are real measurable values with corresponding attenuation factors A of, 0.923 and 0.444.

Noise Factor Calculation
The IEEE definition of noise factor (NF) is, the ratio of the signal-to-noise power ratio (SNR) at the component input to the SNR at the component output when sourced by a resistive element at standard temperature (290°K). The color codes in Figure 1 indicate the related input and output power components used to calculate the relevant SNRs.

(a)

(b)

(c)
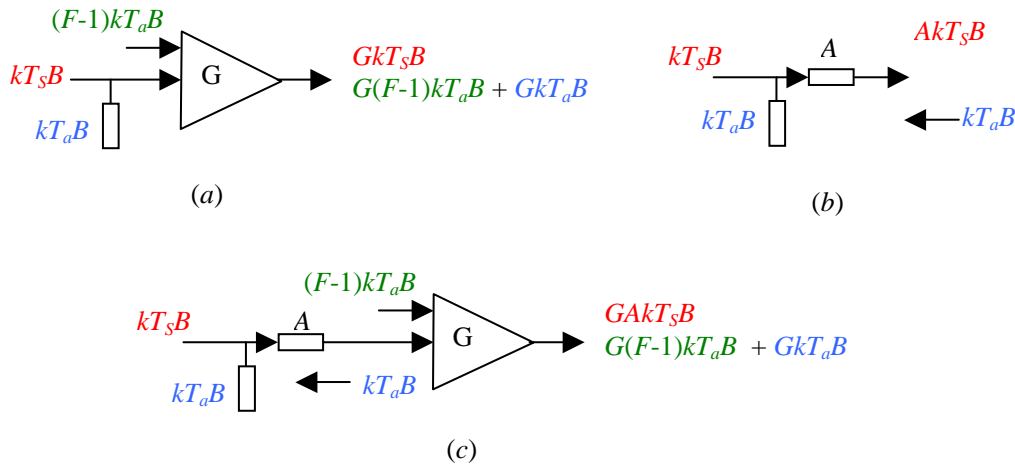
Figure 1. Noise Factor Calculation: (a) Amplifier, (b) Attenuator, (c) Combined Circuits.

The amplifier, power gain G, bandwidth B, in Figure 1(a) is assumed matched at its input with a resistor at ambient temperature T_a providing an <u>available</u> thermal noise input power of kT_aB, where k is Boltzmann's constant. In Figure 1(a), the amplifier internally generated thermal noise relative to the input is represented by, $(F-1)kT_aB$, where, F is the amplifier noise factor.

Both signal power, kT_SB and the noise components are amplified by the amplifier power gain, G producing the obvious signal and noise output power terms as shown.

Applying the IEEE noise factor definition to the amplifier in Figure 1(a), we see that, as might be expected,

$$\text{LNA Noise Factor } = \frac{SNR_{IN}}{SNR_{OUT}} = \frac{kT_SB/kT_aB}{GkT_SB/G(F-1)kT_aB + GkT_aB} = F \qquad (4)$$

For an input-matched attenuator, power attenuation factor, A (<1) in Figure 1(b), all the attenuator internal components are at ambient temperature producing just thermal noise and contain no <u>active</u> noise sources. The input and output available thermal noise power is just kT_aB, so the <u>apparent</u> noise factor is equal to the reciprocal of the power attenuation factor as derived in Equation 5.

$$\text{Attenuator Noise Factor } = \frac{SNR_{IN}}{SNR_{OUT}} = \frac{kT_SB / kT_aB}{AkT_SB / kT_aB} = \frac{1}{A} \qquad (5)$$

Coupling the passive attenuator to the amplifier input with the source load now at the attenuator input as in Figure 1(c), the LNA input available noise power via the attenuator is still kT_aB, due to the matched source impedance, so with $T_S = 0$ °K, the LNA output thermal noise level doesn't change from that observed for Figure 1(a).

In Equation 4, the only term in the denominator that changes is GkT_SB, which modifies to $GAkT_SB$.

The indicated noise factor in the combined attenuator-LNA case, Equation 6, now becomes F/A, but as stated above, the base output noise level (with $T_S = 0$) is <u>unchanged</u> by the presence of the input resistive attenuator which still supplies kT_aB available power.

$$\text{Attenuator + LNA Noise Factor } = \frac{SNR_{IN}}{SNR_{OUT}} = \frac{kT_SB / kT_aB}{GAkT_SB / G(F-1)kT_aB + GkT_aB} = \frac{F}{A} \qquad (6)$$

Single Whammy?
The SNR analysis for Figure 1(c), Equation 6 correctly defines the combined circuit noise factor but shows that the SNR is degraded by the attenuation factor A only once by reducing the input signal power and no sign of any attenuator noise.

The reason for this lies in the noise factor definition, in that it specifies an input source noise power base at 290 °K to standardize the noise factor calculation but its presence and its available power subsumes any following series/parallel resistor/attenuator noise [5].

Radiometers, on the other hand, with well-matched antennas only supply power from sources within the antenna beam and convention measures these as temperatures for comparison with receiver generated noise sources as discussed in the next section.

Noise Factor to Temperature Conversion
Equation 4-6 results are modified here to suit a radiometer by applying the Friis noise factor-to-temperature conversion relation,

$T_{cicuit} = (NF\text{-}1)T_a$

This equation represents the component/circuit <u>added</u> noise temperature at its <u>input</u>, so the equivalent noise temperatures in the three Figure 1 cases:- a) amplifier; b) attenuator; and c) attenuator + LNA combined, are,

    a) $T_{LNA} = (F\text{-}1)T_a$
    b) $T_A = [(1/A)\text{-}1]T_a$
    c) $T_A + T_{LNA} = [(F/A)\text{-}1]T_a$ (7)

Equation 7(b) shows that the resistive attenuator does generate a measurable system noise contribution. Assuming an added target source/antenna temperature of T_S, the equivalent system noise temperature for Figure 1(c) receiver from Equation 7(c), referred to the attenuator input is,

$$T_{SYS}{}^* = T_S + (T_A + T_{LNA}) = T_S + [(F/A)-1]T_a$$

Referring this equation to the LNA input by multiplying all elements by the constant A , we get,

$$T_{SYS} = AT_S + [F - A]T_a \qquad (8)$$

Equation 8 also implies a double whammy impact, now by attenuating the received signal as before but also modifying the LNA noise factor value.
The two Equations 1 and 8 are in fact mathematical identities as is demonstrated later.
Referencing to the LNA input is sensible, as all eventual data measurements are linearly amplified versions of the LNA input noise terms. Equation 1, however, can be more useful for quantifying the effects of lossy components and has distinct advantages in situations where component cooling is implemented and the attenuator noise component genuinely reduced (see the Appendix 1).

Equation 1 T_{SYS} Derivation Using the Friis Noise Factor Combination Formula
The noise factors of both the LNA and attenuator components have been derived individually in Equations 4 and 5 but can be combined using the Friis formula, $[F_{12} = F_1 + (F_2 - 1)/G]$ [4].

Attenuator + LNA Noise Factor $= \frac{1}{A} + \left(\frac{F-1}{A} \right) = \frac{F}{A}$, as before but referenced to the attenuator input.

The equivalent system noise temperature, now the attenuator and LNA components are identified, using the Friis temperature conversion formula becomes,

$$T_{SYS}{}^* = T_S + (T_A + T_{LNA}) = T_S + \left(\frac{1}{A} + \left(\frac{F-1}{A} \right) - 1 \right) T_a$$

Now, changing the reference point to the LNA input terminal by multiplying by the attenuation loss factor A, we get,

$$T_{SYS} = AT_s + A \left(\frac{1}{A} + \left(\frac{F-1}{A} \right) - 1 \right) T_a = AT_S + ((1-A) + (F-1)) T_a \qquad (9)$$

Substituting for the LNA equivalent noise temperature Equation 9 becomes,

$$T_{SYS} = AT_S + [1 - A]T_a + T_{LNA} \qquad (10)$$

Agreeing identically with the original form of Equation 1.

Radiometer SNR Comparison
It may not be obvious that the formula of Equation 8 and the double whammy formulas in Equations 1, 9 and 10 are telling the same story but this can be made clearer by calculating the observed output signal-to-added-noise ratio in both cases, as below.

Equation 8:

$$SNR_O = \frac{AT_S}{(F-A)T_a} \qquad (11)$$

Equation 1:

$$SNR_O = \frac{AT_S}{(1-A)T_a + (F-1)T_a} = \frac{AT_S}{(F-A)T_a} \qquad (12)$$

In fact, the denominator of Equation 12 shows clearly where the loss-dependant noise temperature term is extracted from whilst maintaining the system noise temperature total.

Replacing the Input Source Load with an Ideal Antenna

The input source load in Figure 1 supplies an available power of kT_aB; removing this and connecting a tuned, matched antenna, the available power then depends dominantly on sources illuminated in the antenna main beam.

Of course, placing the antenna in an enclosed space where the walls are all at ambient, $T_a = 290\,°K$ recovers the full kT_aB available power, but with well designed side and back lobes, this can largely be recovered by pointing the main beam to the ground or towards large environmental features at ambient temperature; this procedure is usually performed for Y-factor T_{SYS} estimates.

It was noted earlier that placing a source-matched attenuator in front of an LNA with $T_S = 0\,°K$, causes no change in the LNA base noise output level. However, replacing the source load with a matched antenna pointing in a direction where $T_S = 0\,°K$, together with a zero-loss attenuator link ($A = 1$), immediately drops the LNA output base noise level by GkT_aB (compare Figure 1(c) with Figure 2(a)). This is a measurable quantity.
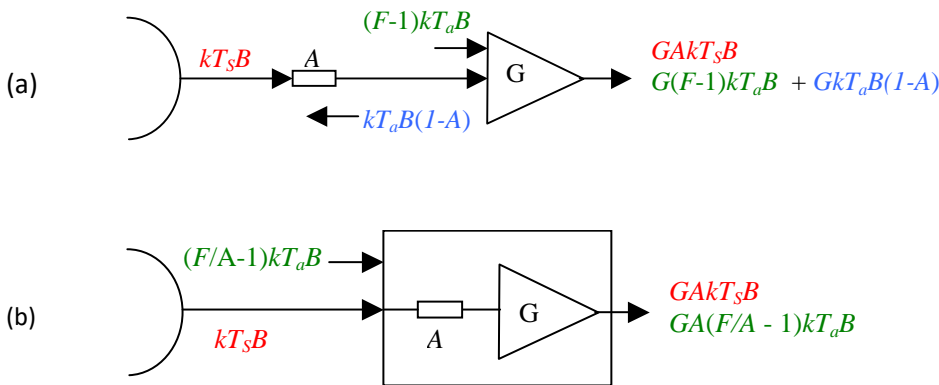
Figure 2. Noise Temperature of the Attenuator + LNA when Driven by an Antenna

Including pre-LNA attenuation as shown in Figure 2(a), the LNA output base noise level is now increased by $GkT_aB(1-A)$; the calculated attenuator noise component of Equation 7b is now referred to the LNA output. Again, this is a measurable quantity.

Figure 2(b) shows the corresponding input and output terms treating the attenuator and LNA as a single unit and whilst the thermal noise output terms appear different they are mathematical identities. This can be verified by simplifying the relevant output terms, for example,

for Figure 2(a), we get,

$AT_S + (1-A)T_a + (F-1)T_a = AT_S + (F-A)T_a$

and for Figure 2(b),

$AT_S + A(F/A -1)T_a = AT_S + (F-A)T_a$

[= $AT_S + (F-A)T_a + T_a - T_a \rightarrow$ **$AT_S + (1-A)T_a + (F-1)T_a$**]

Showing that the representations of Figure 2(a) and 2(b) really are equivalent; duplicating the double whammy formula and again producing the same SNR result,

$$SNR_O = \frac{AT_S}{(F-A)T_a} \qquad (13)$$

Attenuation Effect on Y-Factor T_{SYS} Assessment.

The standard Y-factor method of measuring T_{SYS} is to measure the ratio of the detected power when pointed at the hot ground (T_{gr} = 290 °K) and to a cold part of the sky (T_{sk} = 15 °K), then,

$Y = T_{gr}/T_{sk}$ and the estimated system noise temperature is given by,

$$T_{SYS}{}^* \approx \frac{T_{gr} - Y.T_{sk}}{Y-1} \qquad (14)$$

There are of course some uncertainties in these values anyway but with front-end attenuation, the value of Y actually measured is, $Y = \dfrac{AT_{gr} + T_{SYS}}{AT_{sk} + T_{SYS}}$

Inserting this in Equation 14, we get,

$$T_{SYS}{}^* = \frac{T_{gr}(AT_{sk} + T_{SYS}) - T_{sk}(AT_{gr} + T_{SYS})}{(AT_{gr} + T_{SYS}) - (AT_{sk} + T_{SYS})} = \frac{T_{SYS}(T_{gr} - T_{sk}) + (AT_{gr}T_{sk} - AT_{sk}T_{gr})}{A(T_{gr} - T_{sk})} = \frac{T_{SYS}}{A}$$

Indicating that the Y-factor measurement of T_{SYS} is overestimated due to the total pre-LNA attenuation. The hot ground temperature estimate is usually better than the cold sky measurement especially for broad beam antennas which in the latter case, can have significant side/back-lobe responses or feed spillover. Both reduce the Y-factor value, so increasing the T_{SYS} estimate.

Attenuator Effective Noise Temperature on Cooling

Separating the RF chain component temperature contributions, enables estimation of sensitivity improvements when cooling is applied to the input attenuating components.

This can be understood by noting in Equation 7(b), cooling to T_C, the attenuator noise apparent temperature contribution becomes,

T_{Ac} = $[(1/A)-1]T_C$

Similarly, at the new cooled temperature, Equation 8 simply modifies to,

T_{SYS} = $AT_S + (1 - A)T_C + (F - 1)T_a$ $\qquad$ (15)

In a similar manner further sensitivity improvement is predicted when also cooling the LNA.

Cooling actually reduces the attenuator nominal thermal noise contribution as indicated; this assumes that the attenuator component resistor values are unaffected by temperature, so that the attenuation power ratio stays at A.

Practical Example: T_{SYS} Noise Calculations using Double Whammy, Equation 1
For this example, consider using a LNA with 0.4 dB noise figure with an input VSWR of 1.8 at 50 Ω characteristic impedance, connected to the antenna with a connector loss of 0.1 dB.
The antenna is ideal and directed such the $T_S = 0 \ °K$.
The Mini-Circuits ZX60P33U LNA input impedance at 600 MHz is, 30.8 - j13.5 Ω and VSWR = 1.8.
The antenna measured VSWR is 1.25 and the actual antenna source impedance is 62.5 Ω.
The ambient temperature, T_a is assumed to be 290° K.
Note:- *For 13.5 Ω reactance, the available power reduction is about 1% and is ignored here but is taken into account in the full analysis in Appendix 2*

Calculate the receiver noise temperature when the LNA is,
   1) connected directly to the antenna terminal with 0.1 dB connector loss and,
   2) when using a 50 Ω quarter wave transmission line transformer with 0.2 dB connection loss between the antenna and LNA.

Answer. 1) The LNA noise factor is, $10^{NF/10} = 10^{0.4/10}$ = 1.0965, so the equivalent noise temperature is,
   $(F-1)T_a$ = 27.98° K and the connector loss factor, $A = 10^{-0.1/10} = 0.977$.
   The antenna-LNA voltage reflection coefficient from, $\rho = \dfrac{Z_1 - Z_2}{Z_1 + Z_2}$ *is,* $\dfrac{62.5 - (30.8 - j13.5)}{62.5 + (30.8 - j13.5)} = 0.365$

   The corresponding loss factor is, $1 - \rho^2 = 1 - 0.365^2 = 0.866$
   The loss/mismatch equivalent temperature = $(1 - A(1-\rho^2))T_a = 44.6° K$
   And the total LNA input noise temperature is 27.98 + 44.6 = 72.6° K
   and, $T_{SYSnoise}$ = 72.6 °K

Answer. 2) The LNA noise factor is again, 1.0965 and the noise temperature is, $(F-1)T_a$ = 27.98° K.
   The input impedance of a 50 Ω quarter wave transmission line loaded by an impedance Z is equal to $50^2/Z$, so the transformed LNA input impedance now becomes 68.1+j29.9 Ω.

   The voltage reflection coefficient at the LNA input is now, ρ = $\left|\dfrac{68.1 + j29.9 - 62.5}{68.1 + j29.9 + 62.5}\right| = 0.227$

   The corresponding loss factor is, $1 - \rho^2 = 1 - 0.227^2 = 0.948$
   The connection loss factor is, $A = 10^{-0.2/10} = 0.955$.
   The loss/mismatch equivalent temperature = $(1 - A(1-\rho^2))T_a = 27.4 K$
   The total LNA input noise temperature is 27.98 + 27.4= 55.4K
   Or, $T_{SYSnoise}$ = 55.4 K

Example: T_{SYS} Noise Calculations using Equation 8
1) From Equation 8, the system noise temperature is,
   <u>*Referred to the LNA input,*</u>
   *$T_{SYSnoise} = A(F/A-1)T_a \rightarrow (F - A(1-\rho^2))T_a$ = [1.0965-(0.977*0.866)]x 290 = **72.6° K***
   Agreeing with the double whammy Answer 1 result.

2) From Equation 8, the system noise temperature is,

   Referred to the LNA input,

   $T_{SYSnoise} = A(F/A-1)T_a \rightarrow (F - A(1- \rho^2))T_a = [1.0965-(0.955*0.948]x\ 290 = $ **55.4 K**

   Again agreeing with the double whammy Answer 2 result.

Example Comments

The examples demonstrate that both methods derived produce identical results.

Normally to minimize losses, it is recommended to connect the LNA directly to the antenna terminal. The example above shows that it is worthwhile checking actual impedances for the antenna and LNA to see if a quarter wave transformer is of benefit. If both impedances are greater than or both less than the characteristic impedance, then of course, without detailed matching, direct connection will provide the best overall system noise temperature.

The example calculations assumed negligible reactance components in both the antenna and LNA impedances. This is a fair assumption if the reactive parts are small compared to the impedance magnitude, which is good general design practice. Appendix 2 covers the general reactance case.

Conclusions

The traditional system noise temperature formula shows that attenuation and/or mismatch loss in the antenna-LNA path directly reduces the wanted antenna signal temperature and also adds a further attenuator noise contribution, so degrading the detected signal-to-noise ratio in two ways giving rise to the double whammy red flag.

This article has described the application of basic RF analysis rules to explain the derivation of the double whammy radiometer equation. It shows that although noise factor analysis sports only a single loss factor, proper temperature analysis clearly identifies the signal and attenuator loss terms. Two alternative temperature analysis approaches presented appear to differ but are shown to be mathematical identities.

The example section aimed to show that the results of the two methods agree and noted that knowing the specific antenna and LNA impedances rather than just the component VSWRs, then, by inserting a 50 Ω or maybe 75 Ω quarter-wave length of transmission line it can, in some instances, usefully improve the measured system noise temperature.

Finally, the double whammy formula provides an adequate T_{SYS} result for small reactive LNA loads. Pre-LNA attenuation and resistive mismatch do produce extra noise and also degrade all antenna received signal powers. Load reactance does not appear to generate extra noise but large values reduce the available power from the antenna and so diminish system sensitivity (see Appendix 2).

Acknowledgements

References

[1] Blake LV, Antenna and Receiving System Noise Temperature Calculation, US Naval Research Laboratory Report AD265414. 1961. https://apps.dtic.mil/sti/pdfs/AD0265414.pdf.

[2] Gary Prof DE, Radio Astronomy Lecture #5, New Jersey Institute of Technology.
       https://web.njit.edu/~gary/728/Lecture5.html

[3] East PW, Another Look at the System Noise Temperature of a Radiometer, SARA Journal March/April 2023

[4] Friis formulas for noise, https://en.wikipedia.org/wiki/Friis_formulas_for_noise

[5] McCorkle JW, Noise Figure One and Two, Friis and IEEE,

Appendix 1: Antenna Fed, Attenuator + LNA SNR Characteristics with Cooling
Figure A1 shows the signal and noise terms for calculating the noise factor of an amplifier driven by a cooled attenuator.
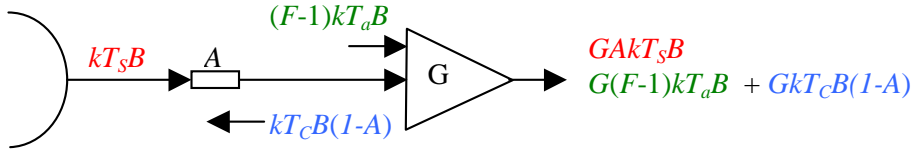
Figure A1 SNR Calculation with a Cooled Attenuator

Derived from the output terms in Figure A1, the output SNR given in Equation A1 is presented in a similar form to Equations 11 and 12 to better show the SNR improvement with attenuator cooling from ambient, T_a to a lower value T_C.

$$SNR_O = \frac{AT_S}{(F-1)T_a + T_C(1-A)} = \frac{AT_S}{(F-A)T_a - (T_a - T_C)(1-A)} \qquad (A1)$$

Indicating that attenuator cooling reduces the noise attributed to the attenuator so increasing the observed SNR. Heating on the other hand increases the attenuator noise, now decreasing the SNR.
When $T_C = 0°K$, the attenuator resistive noise component is reduced to zero as expected, producing an improved SNR reducing Equation A1 denominator by the amount, $(1-A)T_a$.

Appendix 2: Practical Examples - Load Reactance Corrections.
Maximum power is transferred from a resistively matched antenna to a following circuit when the load resistance is equal to that of the antenna. With reactive load components, the presence of the reactance reduces the load current, which in turn reduces the available power absorbed by the load resistance.
With a source impedance rs and load resistance and reactance $rl + jx$, the power absorbed by the load resistance component is,

$$P_{rl} = \frac{V^2 rl}{(rs + rl)^2 + x^2}$$ and the maximum available power with reactance occurs when, $rl^2 = rs^2 + x^2$, so that the

available power now is, $$P_{availX} = \frac{V^2 \sqrt{rs^2 + x^2}}{\left(rs + \sqrt{rs + x^2}\right)^2 + x^2} \qquad (A2)$$

The ratio of the power absorbed by the load resistance to the maximum available power with zero reactance is,
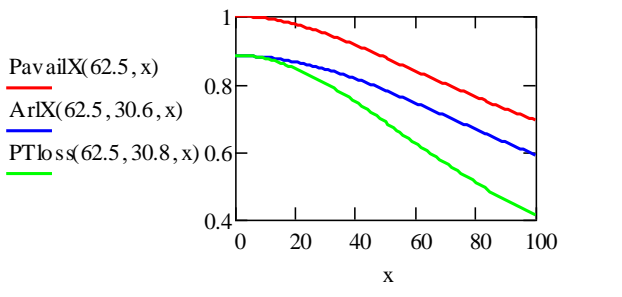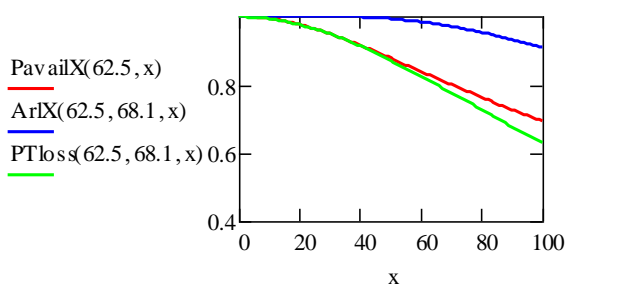
$$P_{Tloss} = \frac{4\, rl\; rs}{(rs + rl)^2 + x_2} \qquad (A3)$$

The ratio of the power absorbed by the load resistance to the available power is a measure of the circuit resistive attenuation and is given by,

$$\frac{P_{rl}}{P_{availX}} = A_{rlX} = \frac{2\, rl\left(rs + \sqrt{rs^2 + x^2}\right)}{(rs + rl)^2 + x^2} \qquad (A4)$$

These relations and example results are summarized in the following table. In the tabled graphs, the red curve plots the fall in available power with increasing load reactance; the blue curve plots the load resistive attenuation; the green curve plots the system total reflected power and is equal to the reported $(1 - \rho^2)$ as in Equation 3.

Example 1.	Example 2
PavailX(62.5, x) — red ArlX(62.5, 30.6, x) — blue PTloss(62.5, 30.8, x) — green *graph: y-axis 0.4 to 1, x-axis 0 to 100*	PavailX(62.5, x) — red ArlX(62.5, 68.1, x) — blue PTloss(62.5, 68.1, x) — green *graph: y-axis 0.4 to 1, x-axis 0 to 100*
PavailX(62.5, 13.5) = 0.989 ArlX(62.5, 30.8, 13.5) = 0.876 PTloss(62.5, 30.8, 13.5) = 0.866 Connector loss = 0.977	PavailX(62.5, 29.9) = 0.949 ArlX(62.5, 68.1, 29.9) = 1 PTloss(62.5, 68.1, 29.9) = 0.948 Connector loss = 0.955

Example calculations and results:-

In Example 1	In Example 2,
T_S Signal loss factor = 0.977 x 0.866 = 0.846	Signal loss factor = 0.955 x 0.948 = 0.905
Attenuation factor = 0.977 x 0.876 = 0.856 --> 41.8°K.	Attenuation factor = 0.955 x 1 = 0.955 --> 13.1°K.
Tsys --> 28 + 41.8 = 69.8°K. (83.8)	*Tsys* --> 28 + 13.1 = 41.1°K. (58.4)
Ts/Tsys --> 69.8/0.846 = 82.5°K.	*Ts/Tsys* --> 41.1/0.905 = 45.4°K.

These results are an improvement on those calculated in the 'Practical Examples' section above (in brackets) and no longer imply noise being generated in the reactance components of the post-antenna circuit, now covered by the loss in available power.

PWE September 2023

Peter East, *pe@y1pwe.co.uk* is retired from a Defense Electronics career in radar and electronic warfare system design. He has authored a book on Microwave System Design Tools. He is a member of the British Astronomical Association since the early '70s and joined SARA in 2013. He has had a lifelong interest in radio astronomy; presently active in amateur detection of pulsars using SDRs, and researching low SNR pulsar recognition and analysis. He has recently released two books, 'Galactic Hydrogen and Pulsars - an Amateurs Radio Astronomy' and 'Small Aperture Pulsar Detection'. He maintains an active RA website at *http://www.y1pwe.co.uk/RAProgs/*

Computer Solar model's how the solar core creates X rays from the Solar Corona

By Rodney Howe

Abstract:
Here we present a computer model of nonlinear differential equations that simulate the Sun's interior and exterior from the solar core to beyond the solar corona where most of the X-ray flux and solar wind originate. We describe the detection of the X-ray flux from VLF wave propagation through the ionosphere wave guide. X-ray flux density e as the high-energy photons interact with free electrons in the upper thermosphere can be derived from the following basic assumption; that the voltage received at the VLF radio telescope is a measure of:

$$f = emc^2$$

f is the X-ray flux density and varies from 10^{-3} to 10^{-7} ergs, averaged over a 10 second interval. Detectable GOES 16 XRA and X-ray flux density energy intensities ranging from perhaps 10^{-7} to ~ 10^{-3} ergs per square centimeter per steradian per second, which may be energetic enough to cause re-emission of free electrons in the thermosphere, can be modeled as producing ultraviolet light and then re-ionization of the ionosphere. Estimates for VLF detection of the gamma ray.

Key words: *nonlinear differential equations, solar core, VLF detection of flares*

Introduction

The computer model described here uses the (Chrong-Yuan, 1997) nonlinear equations for Compton photon density at energy e, scattered by high-energy photons as they descend into the earth's thermosphere and interact with free electrons in the ionosphere. Chrong-Yuan's construct is adapted for earth's thermosphere. (G. R. Blumanthal and R. J. Gould) describe raw XRA or X-ray flux density data collected by the GOES 16 satellite or other satellites are considered conforming to:

$$e = (3pc^3 h^3)^{-1} (3e/4pm_ec)^{kT} \qquad (1)$$

where e is the electron charge, c is the speed of light, h is the Planck's constant, m_e is the mass of the electron being energized from the Compton effect. This model assumes an incoming burst temperature equivalent to 1,200 K per steradian per cm per second, which would be a large event at 10^{-4} ergs, and quiescent thermosphere temperature at `220 K. Compton Effect (CE) photon density at the thermosphere is considered a specific heat in the current model and is measured as *k*T. As the difference between the CE photon burst and thermosphere temperatures increase there is an increase in the amount of re-ionization.

Methods

The nonlinear equation formulae used here is as follows:

1). for h (substitute for Planck's constant)

    h = e((((ln(r)) * pi)-1) cos-1)
    h = 1/ (pi*2)*h

2). for mass m (substitute for m)

    m = e((((ln(r))/.4)-1) cos-1)
    m = 1/m

3). for E2 (substitute for electric charge)

    E2 = (e(atan((ln(pi*m))-1)))-1

4). for Boltzmann's k (substitute for k)

    k = ((e(atan(e(pi*ln(ln(r))))))**3)-1

5). alpha = (h/mc) (Black Body Curve)

6). Inverse Compton Effect (ICE),
    Cumulative (beta dist.)
      ICE=1/(3*pi*(h**3*v**3))*(3*sqrt(E2)/(4*pi*m*v))**(kT)

Where model parameters for input used are;

alpha = ((h/m*c)/ICE)
beta = ((ICE*v)*(m*c))
gamma = ((alpha+beta)**(-ICE))*c2

r = radial distance from the photosphere
v = some Very Low Frequency,
T = microwave temperature being recorded in the transition zone
c = constant for light (distance in cm)

The computer model converts f into voltage measurements. See Figure 2, for voltage values of a VLF telescope less than 1.5 volts, measured as an offset above the 'background' where the value of f ~ 0, there would be no Compton effect thermosphere signal. The model calculates voltage drops below the 1.5 'background' as a large drop in f. This means that any value within the range of 1.75 volts to 2.8 volts as recorded by the VLF radio would potentially represent enough energy to be considered a XRA or X-ray Solar Ionosphere Disturbance (SID) event. However, this is considerably below a calibrated maximum level of 4+ volts for average nighttime ionosphere
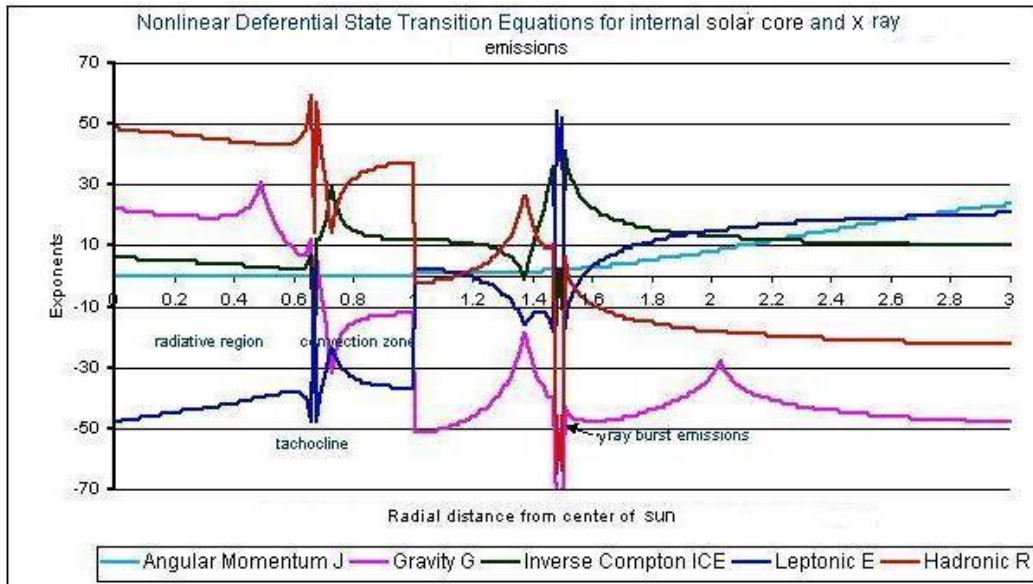
Figure 1, is an example run of the above non-linear equations from the FORTRAN model of Solar environment from the core through the corona, creating gamma and X ray emissions. Notice the intensity of the emissions reach upwards of 10^{53} ergs (y-axis).

measures of VLF radios. At voltage ranges greater than 1.5 to 2.3 the XRA or X-ray flux density would represent a major SID affecting the ionosphere as would a GOES M class flare or above (see Figure 3).
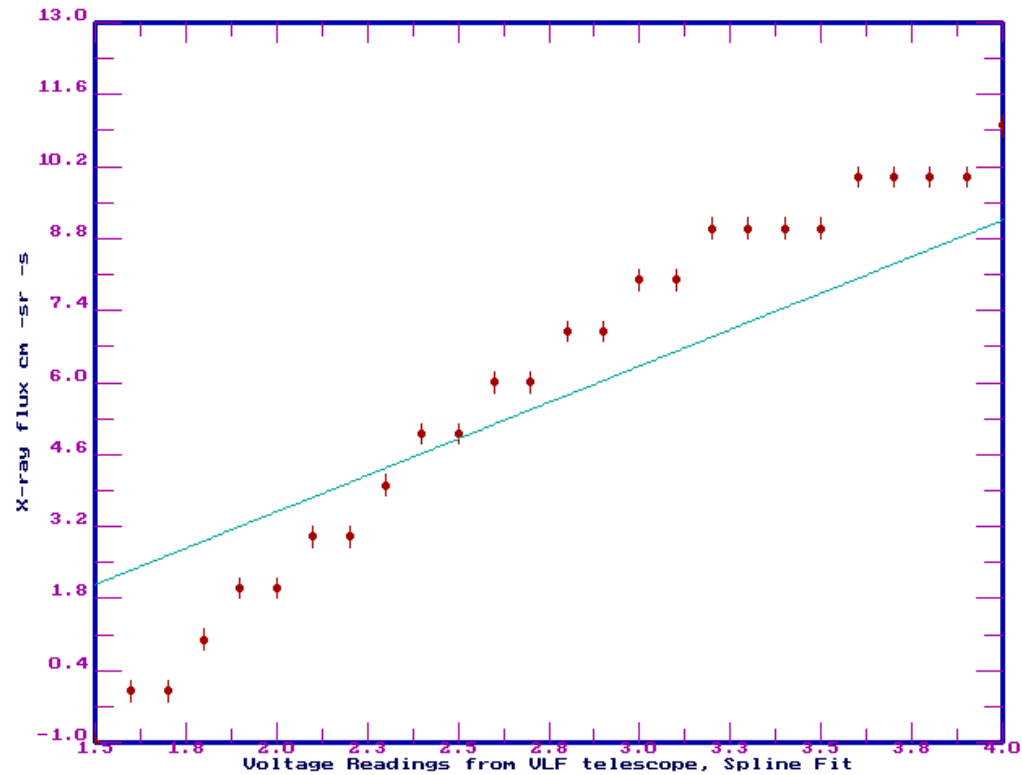
Results

Figure 2, this graph is a model and assumes an incoming burst temperature equivalent to 1,200 K per steradian per cm per second, this would be a large event at 10^{-4} ergs, and quiescent thermosphere temperature at ` 220 K. Compton Effect (CE) photon density at the thermosphere is considered a specific heat in the current model and is measured as kT. As the difference between the CE photon burst and thermosphere temperatures increase there is an increase in the amount of re-ionization. This is measured as flux density per volt recorded at the VLF telescope (red dots). The y-axis, on this graph, estimates the equivalent XRA or X-ray flux density converted to electron volts (eV) in square centimeters per steradian per second. Units on the y-axis are powers of 10 exponents (eV). VLF voltages are on the x-axis. For example: 2 volts on the x-axis, would be approximately 10^2 eV on the y-axis. A XRA or X-ray flux density detected at 2.3 volts on the x-axis would be approximately 10^4 eV on the y-axis. Any XRA or x-ray event at 2.8 volts on the x-axis, 10^6 eV, should be detectable, i.e. above the fitted line.
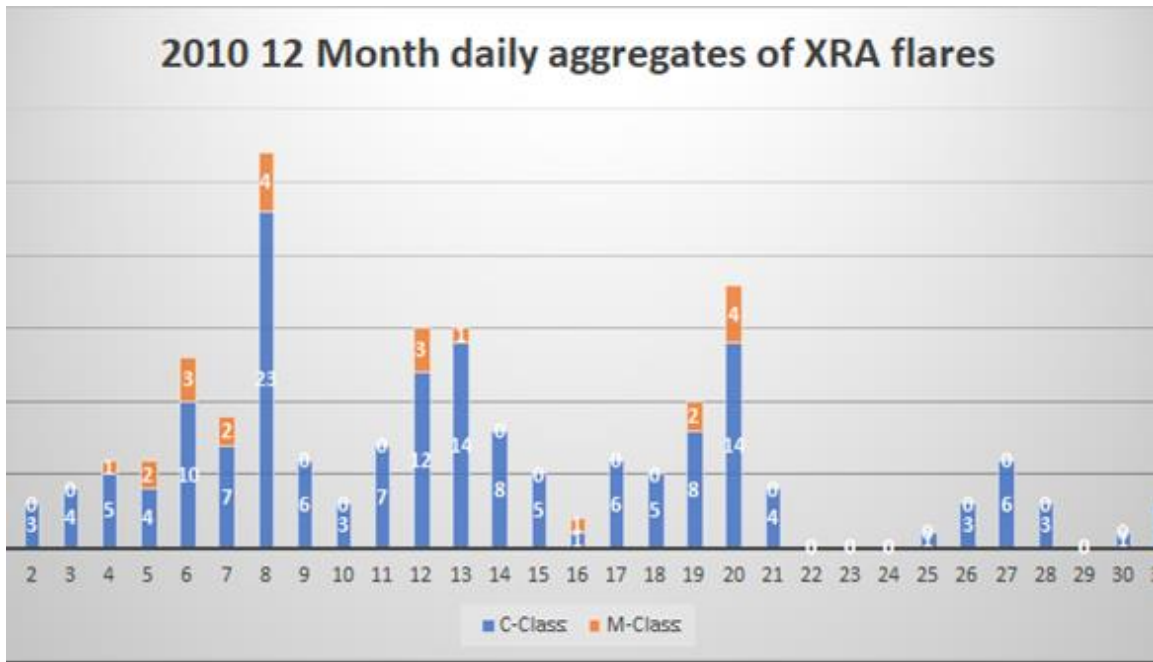
FIGURE 3. GOES -16 XRA FLARES CAPABLE OF DETECTION WITH VLF RECEIVERS

The Solar model expresses the increase of kT, as a Compton Effect (CE) temperature or the re-ionization of the thermosphere. As gamma ray and X-ray photons create emissions in free electrons in the higher layers of the thermosphere creating radiometer temperatures which the VLF radio converts to DC voltages. The VLF model has a low-energy break below 1.57 volts at normal CE thermosphere temperature differences, which might confound detection as noise in the atmosphere layers.

The Solar computer model requires an estimate of the temperature of the incoming burst, expressed in Kelvin's, and an estimate of the ionosphere temperature also measured in Kelvin's. These values are normalized to give a ratio for kT. Boltzmann's constant k is converted to decibels and used as the exponent of e. e the ion energy and is multiplied by mc^2 to estimate the energy of the high-energy x-ray emission as the Compton Effect re-ionizes the thermosphere. Units are in centimeters per steradians per second. All quantum values are measured in the same units and expressed as coupled non-linear equations dependent on the voltage as detected from the VLF telescope. Output from the model, displays an estimate of X-ray flux density on the y-axis of a graph (Figure 2) and the VLF voltage on the x-axis of the graph.

VLF detection of short-hard XRA or X-ray bursts depends on line of sight geometry of the impact with ionosphere layers and the orientation of VLF receiver and transmitter. Intense flux density which impacts the upper thermosphere from coronal mass ejections and other solar plasma phenomena interact with the earth's magnetosphere, thermosphere. With ion-electron plasma interactions from the sun the fraction of the energy that goes into the electrons affects the upper thermosphere and magnetosphere rather than the ionosphere. XRA and X-ray interactions are dependent on ion proportion of heated solar plasma and penetration into the cooler ionized particles at lower layers (Lyon J.G, 2000). Shock waves from X-ray s result in high-energy electrons crossing

into previously ionized cooler layers. The resulting shock waves are influenced by the angular momentum of the earth. Detection of these XRA shock waves depends on the geometry, or line of sight, between the shock wave, receiver and VLF transmitting stations on the ground. Shock waves created from high-energy electron emissions colliding with ionized particles may be twisted in the magnetic field.

Solar X-rays or high energy X-rays from XRA flares penetrate the cooler F, E and D layers through the magnetic field but do not affect direct free electron interaction at the poles (Hill T.W., Dessler A.J, 1991).
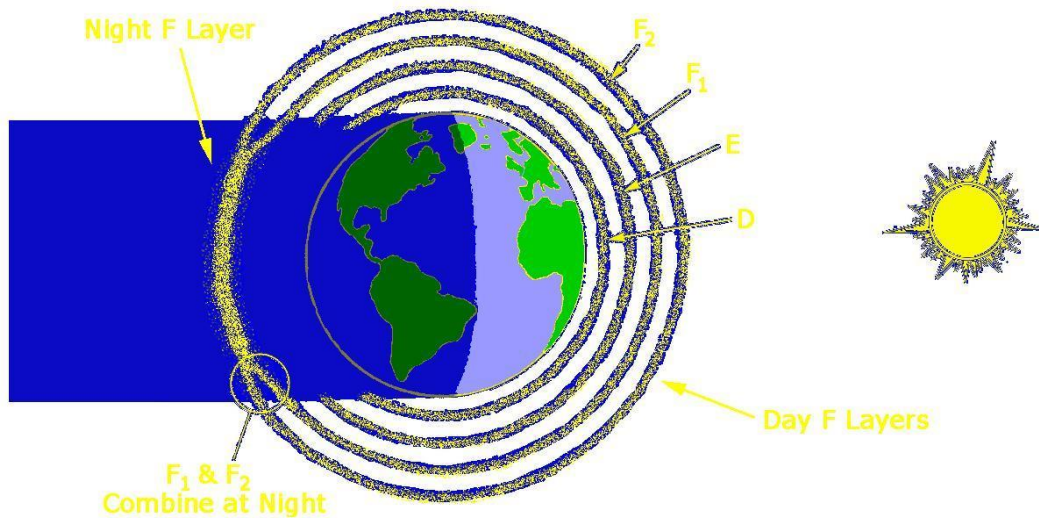

Figure 4, shows the splitting up of the ionosphere during the day into various layers, and reconnection of these layers during the night. (Inan et al., 1999)

Solar plasma interaction is different than interaction of extra-galactic short-hard Gamma Ray Bursts or X-ray s (XRB) from objects like magnetars. A GOES 16 XRA flare will interact with the earth's upper thermosphere directly with much less flux density and are not influenced by the outer magnetosphere like solar plasma from solar coronal mass ejections or proton-electron plasma flares. On the other hand, XRA photons may cause a detectable Compton Effect (CE), which is measurable as electron-volt-flux in square centimeters per steradian per second. As XRA photons interact with free electrons in the upper thermosphere the free electrons re-emit lower frequency ultraviolet-light and perhaps synchrotron radio waves as the result of the Compton Effect. Signatures from the XRA-CE may not create the sudden rise and gentle fall-off often seen in VLF recorded voltages of solar plasma interactions. However, Solar X-ray flares that have the energy to cross into lower F, E and D layers of the ionosphere are detectable as a SID with VLF radios. It is possible XRA, or hard X-ray signatures will show a slight drop in VLF signal during local nighttime hours, although, to-date most VLF detection of XRA and X-ray s have been recorded during the day as a SID type signature. However, any VLF detection of XRA or X-ray rely on the geometry of the incoming flux density and the line of sight arrangement of the receivers and transmitters on the ground.
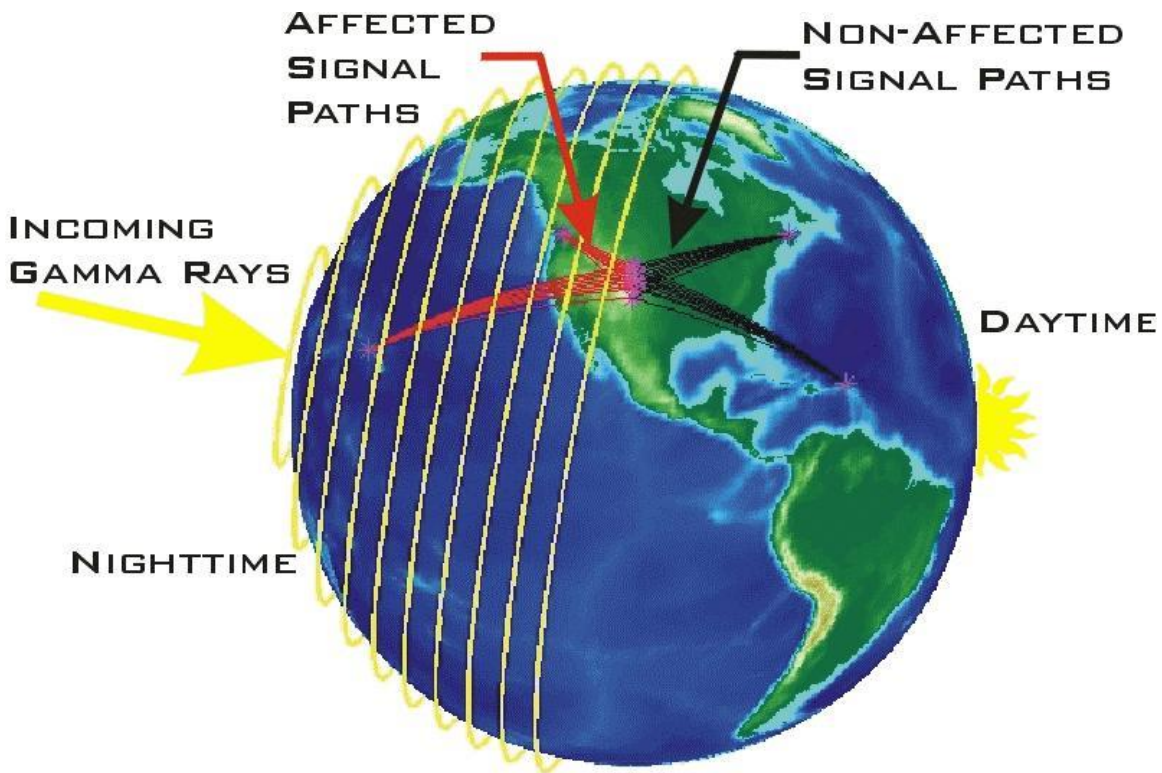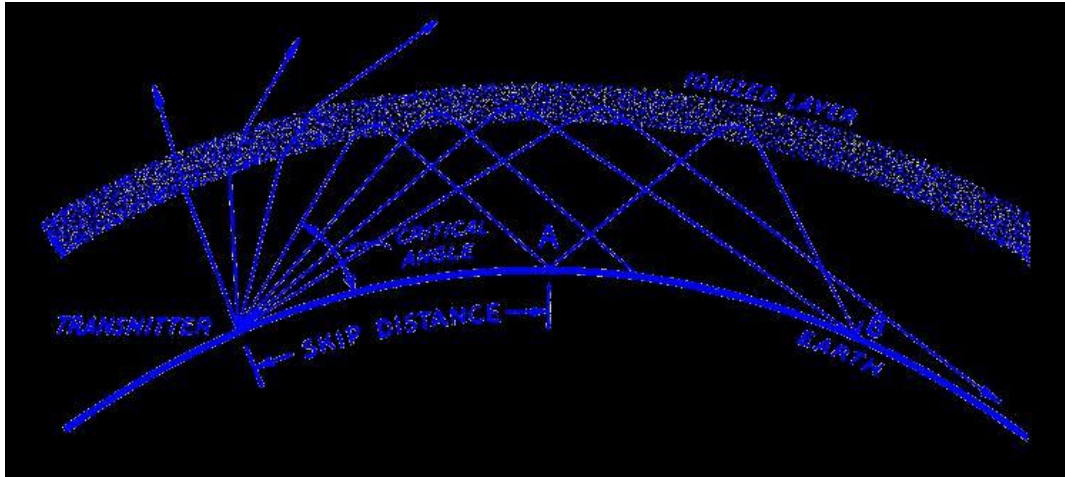
Figure 5, shows the propagation of waves coming in from a gamma ray burst and being in the correct geometry for VLF detection from signals from Hawaii to Colorado, (Inan et al., 1999), University of Stanford's HAIL project: https://vlfstanford.ku.edu.tr/research/ https://vlfstanford.ku.edu.tr/conference_presentat/occurrence-rates-vlf-signatures-lep-events-measured-hail-array/

Conclusions

The Solar computer model proposed in this paper examines a series of interlinked non-linear equations that estimate physical constants and can be used to simulate the placement of the solar core, solar convection zone,

the solar transition zone and the solar corona. It also estimates where in the corona the X-ray flux originates. Gamma ray bursts or X-ray flux from solar flares can be detected by amateur VLF radios. Arguments presented in this paper compare how GOES 16 XRAs created from solar flares events cause detectable signatures as a Sudden Ionospheric Disturbances (SID). High-energy GOES 16 XRA and short X-ray events of solar flare origin affect the upper ionosphere through Compton free electron interaction and not through magnetic field reconnection as local solar plasma might affect the earth's magnetosphere. Gamma ray and X-ray ionization of the upper F2 layer, or thermosphere, should be a measure of ionizing radiation as small as 10^{-6} ergs, yet may not be detectable with amateur VLF radios. High-energy solar plasma interactions causing ionization have larger energy regimes, which impact the lower ionosphere layers. Local atmospherics such as lightening, and sprites also confound detection of XRA.

References
Cameron, P.B., 2005, Nature, **434**, 1112
Peterson, B. A., Price, P. A, 2003, GRB Circ. Network, No. 1985.
Lyon J.G., 2000, Science, **288**, 1987.
Hill T.W., Dessler A.J., 1991, Science, **252**, 410.
Inan, U. S., 1999, *Geophys. Res. Lett.* , **26**, 3357.
Shilling, G., 2002, **Flash**! : the hunt for the biggest explosions in the universe, Cambridge Univ Press.
Ward-Thompson, D., 2002, Science, **295**, 4.
Hossfield C.H., 2002, Solar Bulletin of the AAVSO, **58**, 4.
Uemura, M., et al., 2003, Nature, **423**, 843.
Hwang, Science, 1997, **278**, 1917.
Hurley, K., 2005, Nature, **434**, 1098.
C-Y. Hwang, Science, [Vol. 278], p1917 (1997).

The computer model described in this paper uses the following formulation from G. R. Blumanthal and R. J. Gould, Rev, Mod. Phys. 42. 237(1970) -

Equation (1),
$$e = (3pc^3 h^3)^{-1} (3e/4pm_ec)^{-(p-3)/2}$$

multiplied by equation (2) and equation (3):

$$(kT)^{(p+5)/2} B^{0 \,-(p+1)/2} F(p)/a(p)v^{(p-1)/2} \qquad (2)$$
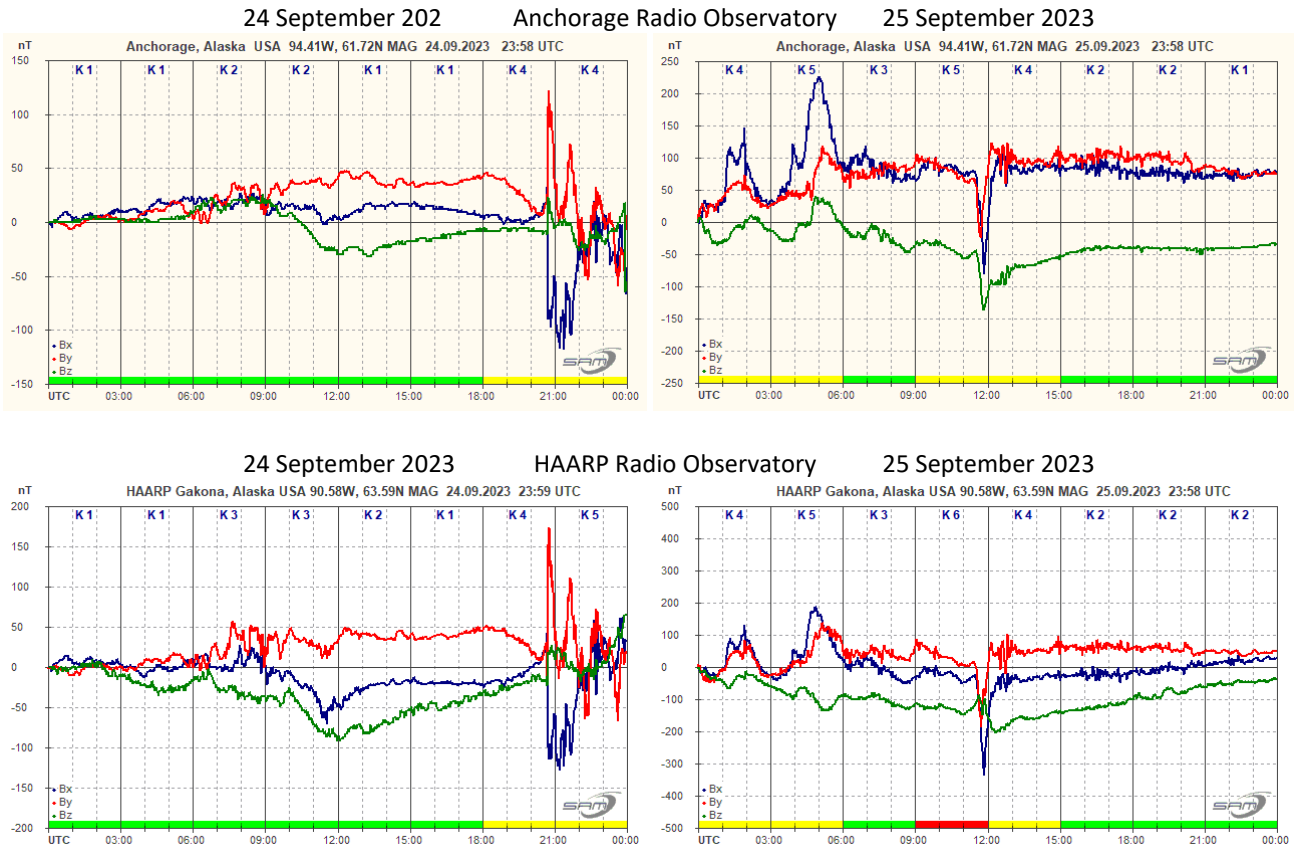
$$Ss(v),^{-(p+1)/2} \qquad (3)$$

XRA photons, where k is Boltzmann's constant, T is the temperature, B^0 is the average magnetic field in the magnetosphere, and F(p) and a(p) are the parameter functions defined by Blumenthal and Gould.

Observations

### Geomagnetic Disturbance Observations in Alaska
Whitham D. Reeve

The magnetograms below were recorded by SAM-III Magnetometers at Anchorage, Alaska and the HAARP facility near Gakona, Alaska on two consecutive days during fall 2023.

24 September 202   Anchorage Radio Observatory   25 September 2023

24 September 2023   HAARP Radio Observatory   25 September 2023

Step-Changes in Natural Phenomena: Natural phenomena, such as geomagnetic field intensities, normally do not change instantly, although the magnetograms above appear to show a step-change at 2041 UTC on 24 September. The rapid changes occurred in all three magnetic field components Bx (blue trace), By (red trace) and Bz (green

trace). However, zooming into the traces shows they do have a relatively steep slopes but are not vertical (12 min of Bx with 10 s resolution shown in plot left).
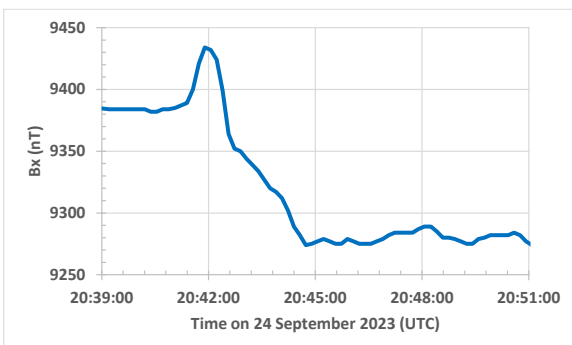
The deflections in Bx and By are much larger than Bz (table below). The field changes likely resulted from rapidly changing auroral electrojet and associated return currents that, in turn, were caused by a *sudden impulse*. The sudden impulse

136

resulted from the collision with Earth's magnetic field of the shock front of a coronal mass ejection (CME) blown away from the Sun on 22 September.

Approximate magnetic field changes during sudden impulse on 24 September

Location	Bx (nT)	By (nT)	Bz (nT)
Anchorage	−80	+110	+40
HAARP-Gakona	−100	+150	+40

Parts of the Sun's magnetic field are carried along with part of the solar wind and coronal mass ejections. If this interplanetary magnetic field (IMF) has a component opposite of Earth's north-south component, the two fields merge and allow the transfer of energy into the geomagnetosphere. This very often leads to a geomagnetic storm as was the case immediately after the sudden impulse and the next day.

Normalization and Vertical Scales: The SAM-III Magnetometer operates as a variometer. The SAM_VIEW software that collects and displays the data from the magnetometers is setup at both sites to *Normalize* the displayed traces at the end of each UTC day such that the three traces are zeroed at 0000 UTC.

The software also is setup to *Autoscale* the displayed vertical axis. The scaling of all three traces is determined by the component with the highest normalized amplitude. Geomagnetic activity at higher latitudes generally has higher amplitudes than lower latitudes. In this case a geomagnetic latitude difference of only about 2° caused the HAARP magnetometer to Autoscale by a factor of 1.3 on 24 September and 2 on 25 September compared to Anchorage. At higher latitudes, the magnetic flux density measured on the ground is heavily influenced by the auroral electrojet. The HAARP magnetometer was closer to the electrojet and more affected by it. The autoscaling appears to lessen the displayed geomagnetic activity the day after the sudden impulse arrival.

K-Index: The K-index shown along the top of the magnetogram indicates the peak-to-peak geomagnetic activity on a quasi-logarithmic scale of K0 to K9 in 3 hour synoptic periods. The higher the K-index, the higher the local magnetic activity. The K-index is a software (computer display) and firmware (SAM-III controller built-in display) function in the SAM-III Magnetometer system. The magnetograms above also show a colored bar along the bottom horizontal scale that corresponds to the K-index.

The K-index thresholds are adjusted at each site to provide approximately the same index value in any given 3-h time period as other sites; for example, if K4 is indicated in the 0300-0600 synoptic period at Anchorage, a K4 is indicated at HAARP and other geomagnetic observatories during the same period even though the magnetic deflection at those observatories was higher or lower due to their different latitudes. Examination of the Anchorage and HAARP magnetograms shows general agreement for almost all synoptic periods.

ULF Waves: ULF Waves are indicated by rapid, periodic changes in the magnetic flux density and have the appearance of noise. Low amplitude ULF Waves can be seen on 25 September in the east-west component By between 0600 and 1000 at Anchorage and between 0600 and 0800 at HAARP. ULF Waves also appear in the north-south component Bx and also By at both Anchorage and HAARP after about 1200 on the same day. The ULF Waves on 25 September probably resulted from the sudden impulse and following geomagnetic storm. No ULF Waves are obvious in the magnetograms for 24 September.

Recent observations of 22.2 GHz H₂O masers with the 1-metre Mini Maser Telescope

Eduard Mol, October 11, 2023

Introduction

The "Mini Maser Telescope" is a small radio telescope made from a 1 metre off- axis satellite TV dish. It is primarily used for the detection of cosmic masers; specifically methanol masers at 12.2 GHz and water masers at 22.3 GHz. A description of the setup, data processing methods and some earlier results can be found on the PARAC website under project EM01 [1] and in the July- August 2022 SARA journal [2].

Masers are essentially the microwave equivalent of lasers: they emit powerful, coherent microwaves at specific spectral line frequencies of the atom or molecule type composing the maser medium [3]. Astrophysical masers occur mostly in dense gas clouds inside star forming regions and around red giant stars. In these environments the molecules needed for maser emission are abundant, while an energy supply in the form of strong infrared radiation or shockwaves provides a pumping mechanism. Masers are often variable on timescales of weeks to years [4]. With the 1 metre dish, maser emission from water vapour at 22.2 GHz is observed most often, since this is the most common and brightest type of maser. Most targets are observed multiple times a few weeks or months apart, in order to check repeatability of observations and to see if there are any changes to the spectrum.

Equipment and data processing

The radio telescope, data collection and processing procedures used for the detection of water masers has been earlier described in [2]. Briefly, the telescope consists of a 1 metre solid offset dish placed on a HEQ5 equatorial mount for sub-degree accuracy pointing and tracking. The front-end is a norsat 9000LD LNB (noise figure 1.5 dB, LO stability ±2 MHz); the back-end is an airspy mini SDR. A GPSDO-based harmonic tone source is mounted on the side of the dish to provide a (weak) pilot tone for post-facto frequency drift correction. During observation sessions spectra are integrated and saved every 60 seconds using SDR# with the IF average plugin. Off-target spectra for bandpass calibration are collected with the dish pointing away from the target, but at approximately the same altitude in order to minimize atmospheric effects. On-target spectra are later divided by the off-target spectra for bandpass correction.

Because the output of IF average is spectral amplitude versus frequency, the vertical axis of the spectra after bandpass correction is amplitude normalized to the background (which consists of spillover, atmospheric, and LNA noise contributions). Since key system parameters like system temperature and aperture efficiency are still poorly constrained, the relative amplitude values are reported here "as is" without converting them to antenna temperature or flux density.

Observation results

W49

W49 was observed in September 2023 as part of an ongoing observation project to monitor for changes in this source. The spectrum of W49 is very complex, because there are over a hundred maser spots in this star forming region located in the outflow of a massive protostar [5].
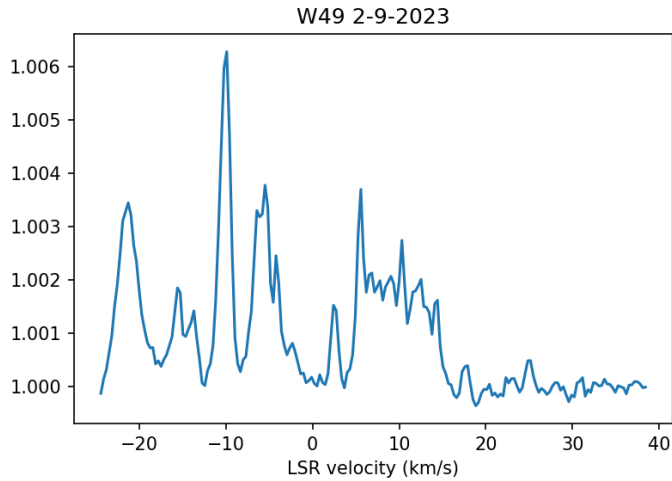

Figure 1: 22.2 GHz water maser spectrum of the W49 star forming region, September 2 2023. Integration time 40 minutes; spectral resolution 23.4 KHz (0.316 km/s)
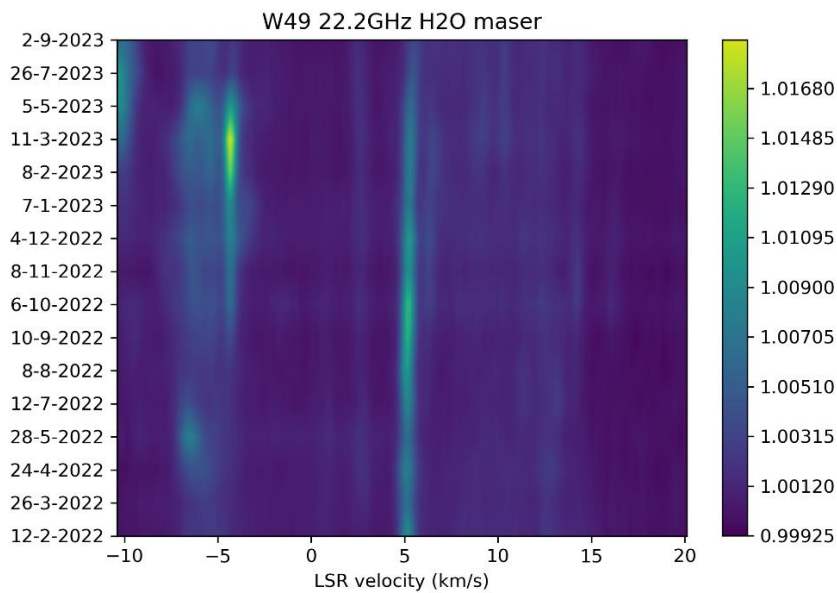

Figure 2: heatmap plot of all spectra of W49 collected in 2022- 2023. Note that the LSR velocity scale of the first three spectra from February- April 2023 is uncertain because the frequency calibrator source was not yet installed back then.

W51

W51 was marginally detected with 30 minutes of integration time on the evening of September 24, 2023. A flaring event reaching 140 KJy, which lasted from fall 2021 to January 2023, was reported in this source by Volvach and colleagues [6]. W51 was one of the strongest sources observed last year but seems to be quiet at the moment.
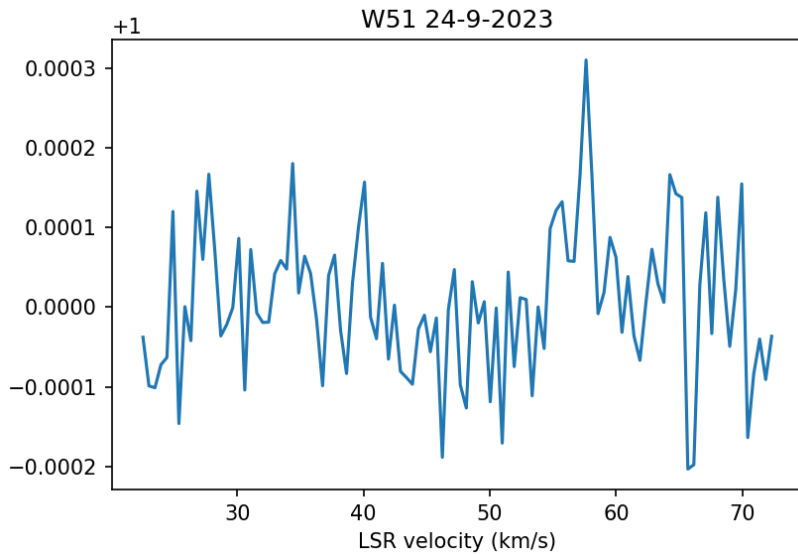

Figure 3: 22.2GHz water maser spectrum of W51. The putative signal at 58 km/s could be from the source. Integration time 30 minutes; spectral resolution 35.2 KHz (0.474 km/s)
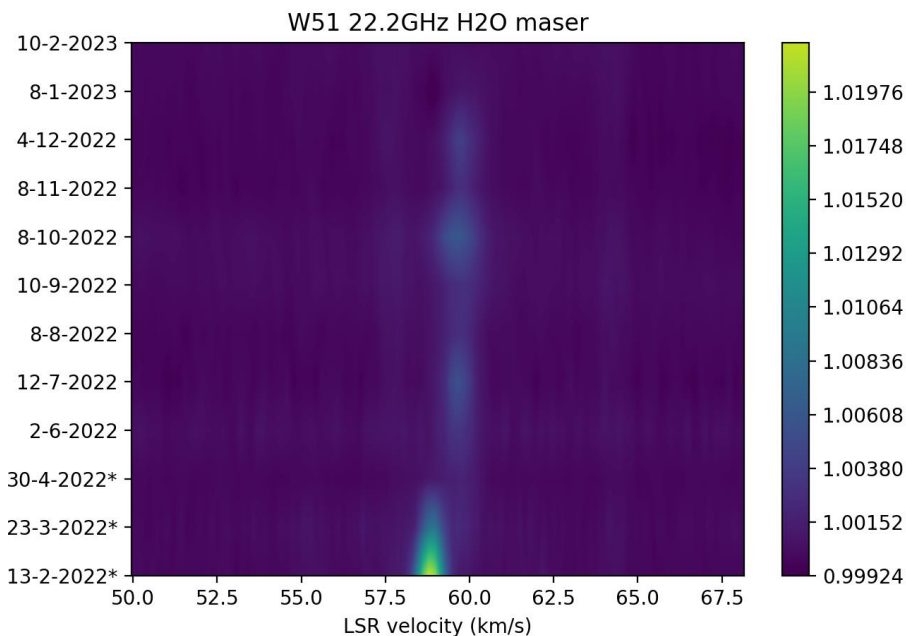

Figure 4: heatmap plot of all spectra of W51 collected between February 2022 and February 2023. Note that the LSR velocity scale of the first three spectra from February- April 2023 is uncertain because the frequency calibrator source was not yet installed back then.

W75

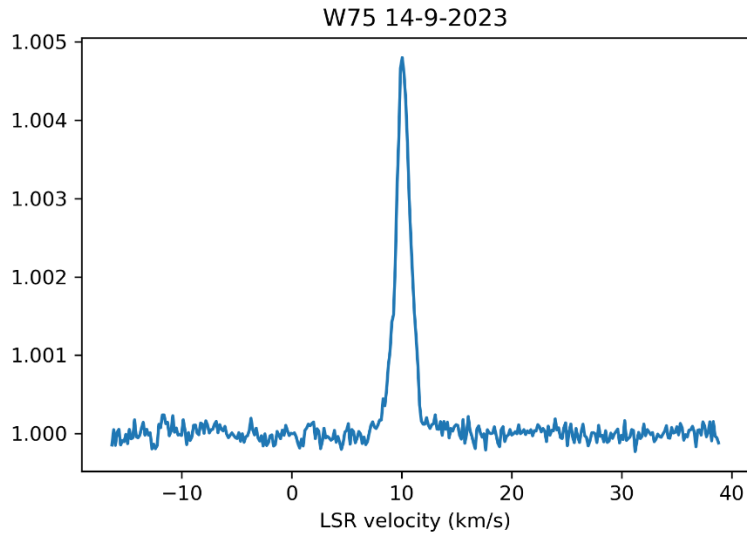W75 has been observed a few times since August 2022. It seems to be gradually getting brighter.

Figure 5: 22.2 GHz water maser spectrum of W75 taken on September 14 2023. Integration time 61 minutes; spectral resolution 11.7 KHz (0.158 km/s).
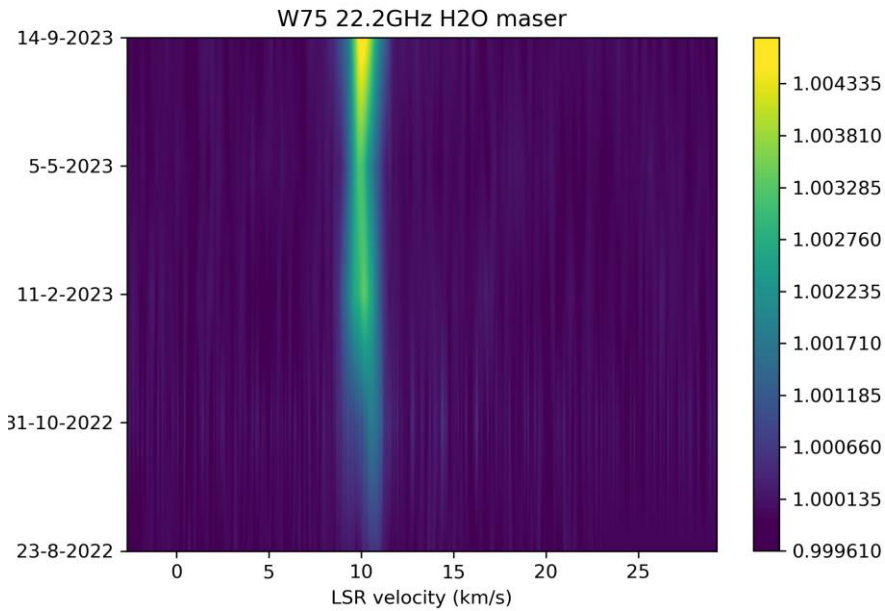

Figure 6: heatmap plot of all spectra of W75 collected in 2022 and 2023.

Cepheus A

Cepheus A was observed for the first time in a year on September 29. Compared to the previous observation in October 2022, the spectrum has changed markedly: instead of a double peak at -9 and -11 km/s its spectrum is now dominated by a single, very narrow feature at -9 km/s.
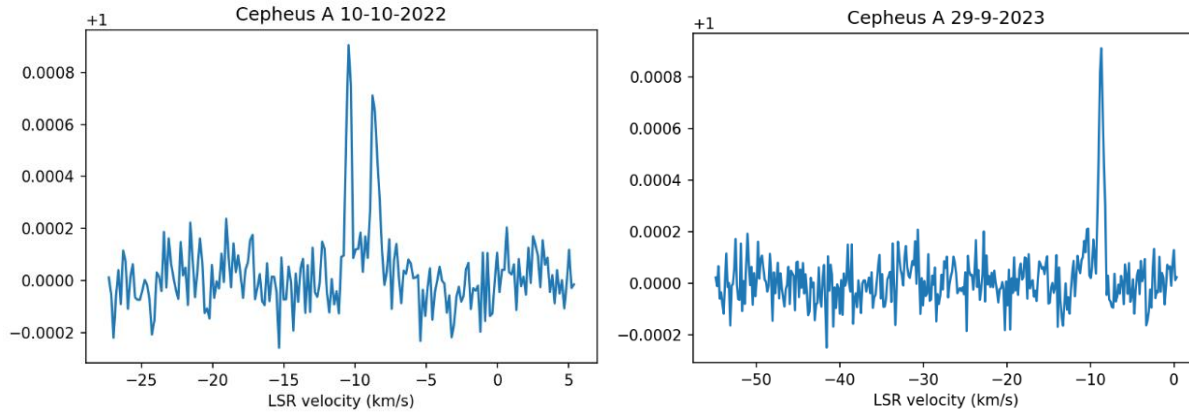

Figure 7: 22.2 GHz water maser spectra of Cepheus A in 2022- 2023. Left: October 10 2022, integration time 65 minutes; spectral resolution 11.7 KHz (0.158 KHz). Right: September 29 2023 observation, integration time 85 minutes; spectral resolution 11.7 KHz (0.158 km/s). The larger velocity range on the horizontal axis of the 29-9-2023 spectrum is due to the use of a different SDR device (airspy mini instead of nooelec NeSDR XTR) with a wider bandwidth.

W3

A quick 30 minute observation run on the W3 region was done on September 29 2023, after finishing the Cepheus A observations. Compared to an earlier observation in March 2023 the -36 km/s feature appears to have become weaker.
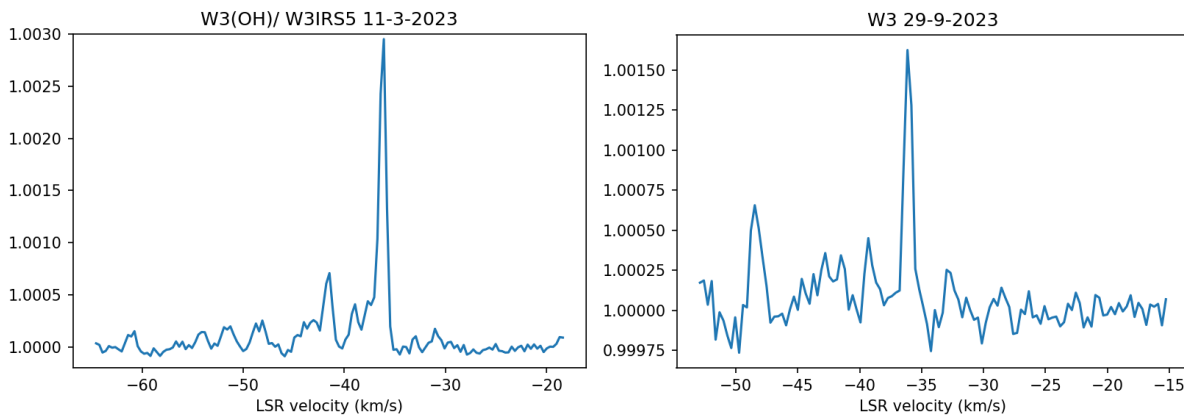

Figure 8: 22.2 GHz water maser spectra of W3. Left: March 11 2023, integration time ca. 180 minutes, spectral resolution 23.4 KHz (0.316 km/s). Right: September 29 2023. Integration time 30 minutes, spectral resolution 23.4 KHz (0.316 km/s).

Orion KL

Orion KL has been detected a few times since February 2022. Shown here are the two most recent observations from February and May 2023.
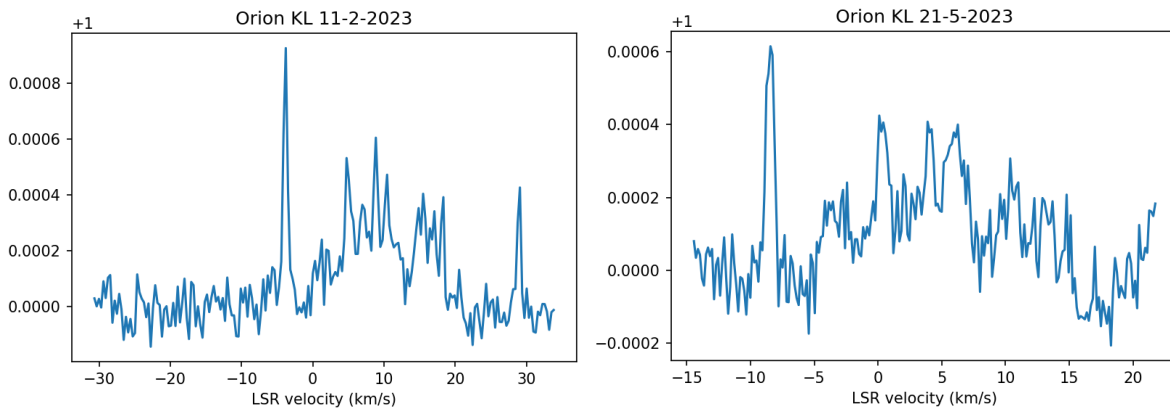

Figure 9: 22.2 GHz water maser spectra of Orion KL. Left: February 11 2023, integration time 65 minutes, spectral resolution 23.4 KHz (0.316 km/s). Right: May 21 2023, integration time 123 minutes, spectral resolution 11.7 KHz (0.158 km/s)

G25.6+1.04

The star forming region G25+694+1.050 (also known as IRAS 18316-0602) hosts one of three known "kilomasers" in our galaxy; these are maser sources which exhibit very intense flaring in the 10^4- 10^6 Jy range (7). Most of the time, however, IRAS 18316-0602 has a flux density of a few hundred Jy and sometimes as low as 10 Jy, so this is a challenging object for small dishes. One has to be lucky to catch it when it is flaring.

IRAS 18316-0602 appears to be quiet at the moment. Last year August this source was not detected. In March 2023 a weak signal was detected at 40 km/s, but I was not able to do a follow-up observation until July 2023. Integration times of both observing sessions are about 1.5 hours.
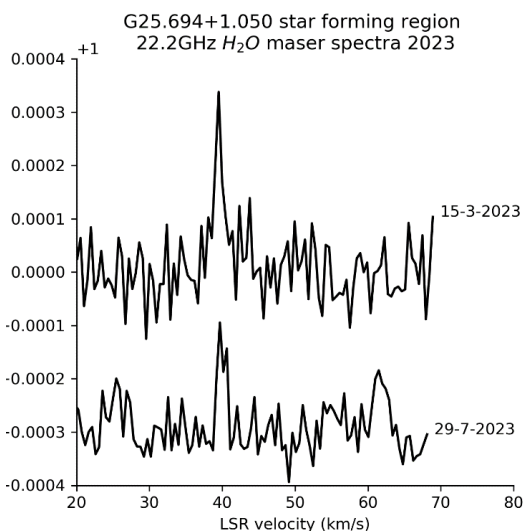

Figure 10: 22.2 GHz water maser spectra of the star forming region G25.694+1.050. Both spectra were made with an integration time of approximately 90 minutes and a spectral resolution of 35.2 KHz (0.474 km/s)

NML Cygni

The possible detection of the red supergiant star NML Cygni at 22.2GHz was a bit of a surprise. The gaseous shell around this star hosts the brightest 1612 MHz OH maser in the sky, which has been observed by amateurs using 3 metre dishes [8, 9]. At 22.2 GHz, however, this object seemed to be well below the detection limit of my 1 metre dish system: the highest flux density reported in the maser database MaserDB was only 134 Jy [10]. Still I decided to aim my dish at this star for about an hour on February 11 2023. Against expectations, a weak signal was detected at -23 km/s. This feature was detected again two weeks later with a much better SNR after a much longer (3 hours) integration time. Another observation in August also appeared to have the same signal. The fact that the signal stayed at the same LSR velocity (after applying LSR correction) over several observations at different times of the year is a strong indication that it is a real signal from outer space and not RFI. The LSR velocity is also broadly consistent with that of the strongest peak of NML Cygni reported in MaserDB, although most of the reported velocities are a bit higher at -17.1 to -21.9 km/s [10].
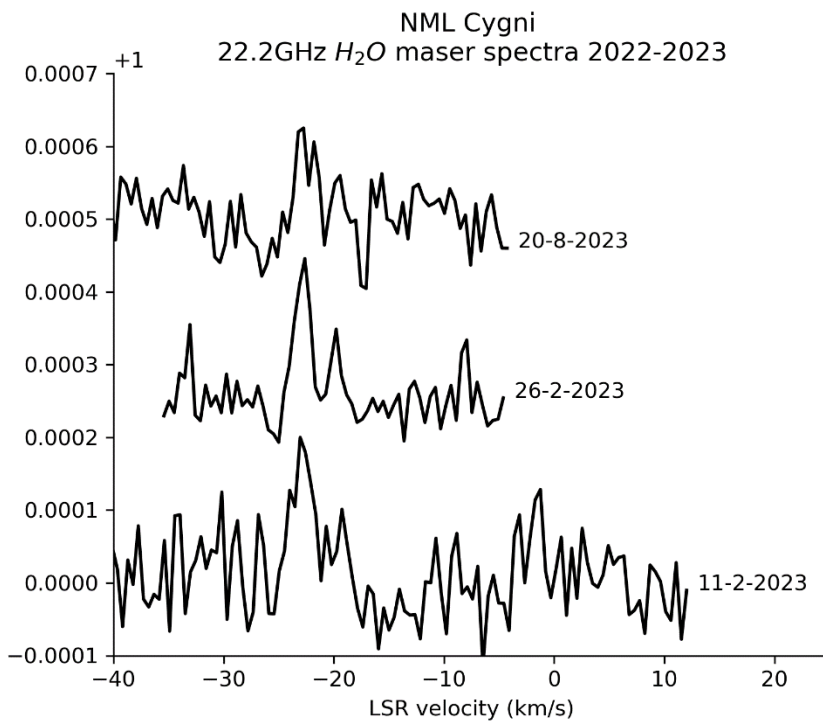

Figure 11: 22.2 GHz water maser spectra of the red supergiant star NML Cygni. Integration times are 60 minutes, 180 minutes and 120 minutes for the observations of 11-2-2022, 26-2-2022 and 20-8-2023 respectively. The spectral resolution is 35.2 KHz (0.474 km/s) for all three spectra.

Future plans

- Continue observations of the strong sources (W49, W75, Orion KL)
- Perform long observing runs on some weaker sources
- Doing an in-depth comparison between the flux density data of W51 presented in [6] and my own data of this source

- Use the flux density data from the Volvach 2023 paper on the water maser in W51 [6] in combination with my own measurements to better constrain key system parameters (aperture efficiency, system temperature)

References

1) https://parac.eu/projectem01.htm
2) Mol, E. (2023). Observations of the water maser sources W49 and W51. August 2023 SARA journal
3) https://astronomy.swin.edu.au/cosmos/m/Masers
4) Felli, M., Brand, J., Cesaroni, R., Codella, C., Comoretto, G., Di Franco, S., … & Valdettaro, R. (2007). Water maser variability over 20 years in a large sample of star-forming regions: the complete database. Astronomy & Astrophysics, 476(1), 373-664.
5) Asanok, K., Gray, M.D., Hirota, T., Sugiyama, K., Phetra, M., Kramer, B.H., Liu, T., Kim, K.T. & Pimpanuwat, B. (2023). Proper Motions of Water Masers in W49 N Measured by KaVA. *The Astrophysical Journal*, *943*(2), 79.
6) Volvach, A. E., Volvach, L. N., & Larionov, M. G. (2023). Unusually Powerful Flare Phenomenon of the Water Maser in W51 and the Possibility of Detecting Gravitational Radiation from It. *The Astrophysical Journal*, *955*(1), 10.
7) Larionov, M. G., MacLeod, G. C., van den Heever, S. P., Wolak, P., Olech, M., Ipatov, A. V., … & Schuller, F. (2019). A Giant Water Maser Flare in the Galactic Source IRAS 18316-0602. Astronomy Reports, 63(1), 49-65.
8) Observations OH @ 18cm, J. J. Maintoux F1EHN: https://www.f1ehn.org/pages_radioastro/Images_Docs/Radioastro_18cm_OH_2019.pdf
9) The 3 metre dish at the "Astropeiler Stockert". Part 2: characterization and observations. https://astropeiler.de/wp-content/uploads/2017/12/Part2_The_3-Meter_Dish_Astropeiler_Stockert_Characterisation_and_Observations.pdf
10) Database of astrophysical masers: https://maserdb.net/

Methanol maser 6.7 GHz in Cepheus A in August-September 2023

by Dimitry Fedorov UA3AVR

This report contains observation data for Cepheus A methanol maser 6.7 GHz obtained in August-September 2023 with small dish 1.8 m. Detected radiation corresponds to the molecular transition $5_1 \rightarrow 6_0$, A^+ methanol molecule type [1] (accurate frequency 6668.5192 MHz). This maser belongs to Class II, i.e. it is pumped to inverse state by the infrared radiation from nearby located stellar objects. The detected line consist of blue-shifted and red-shifted parts with some minor features inside them; these parts are negatively correlated (anti-correlated) in levels. Source coordinates: RA 22:56:17, DEC +62:1:48 (J2000), G109.87078+2.11403. My setup data are collected in Appendix.
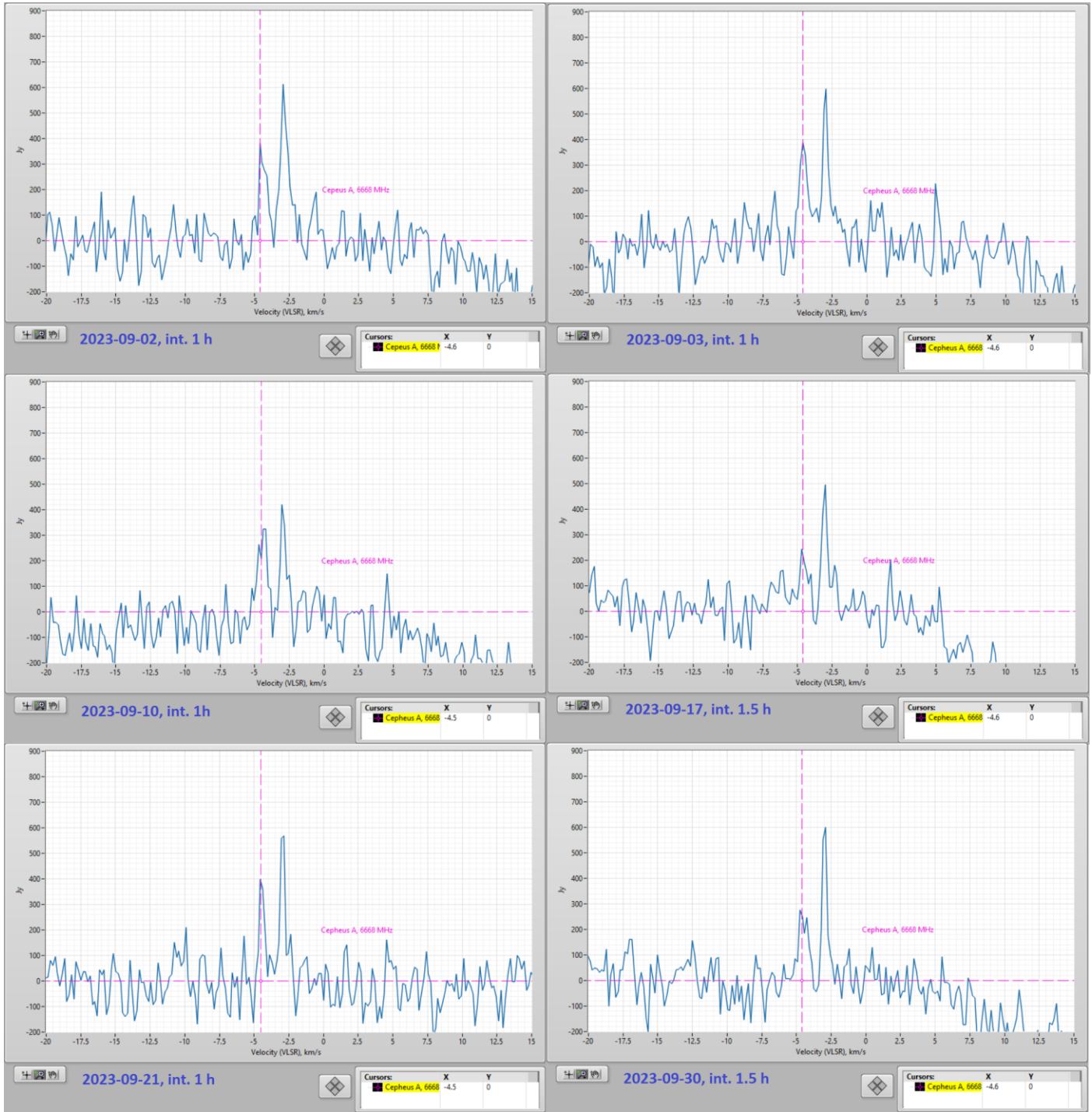
Observed spectrums

Last two months the maser was relatively quiet except the third decade of august with almost vanishing blue-shifted part 2023-08-26. Integration times of observed spectrums were in 1-2 hours.

August 2023 spectrums:

Levels in Jy were calculated with T_{sys}=150 K.

September 2023 spectrums:

2023-09-02, int. 1 h — 2023-09-03, int. 1 h
2023-09-10, int. 1h — 2023-09-17, int. 1.5 h
2023-09-21, int. 1 h — 2023-09-30, int. 1.5 h

Levels in Jy were calculated with T_{sys}=150 K, except last two (2023-09-21 and 2023-09-30) with T_{sys}=180 K.

T_{sys} issues

The system temperature value is needed for spectrum line levels estimation; so, an accurate value for T_{sys} is strongly desirable. The system temperature was measured by the Y-factor method applying a formula

$$T_{sys} = \frac{T_{hot} - Y\, T_{cold}}{Y - 1},\qquad\qquad(1)$$

where $Y=P_{hot}/P_{cold}$, P_{hot} and P_{cold} are the receiver output response in linear power units when the antenna main beam sees radiating objects with T_{hot} and T_{cold} temperatures, respectively. The objects have to fill all the main beam width. Approximate values of temperatures are taken as:

$T_{hot} \approx 280$ K when antenna is directed to the warm brickwall (assumed that the noise temperature of such brickwall is somewhat colder than ambient temperature ≈ 290 K);

$T_{cold} \approx 10$ K when antenna is directed to the sky with elevation about 30-40 deg.

Measured Y-factor = 4.3 dB (2.69 as a power ratio), and we have $T_{sys} \approx 150$ K from the formula (1). This value was actual until September 2023. September measurements have given lesser Y-factor about 3.8 dB; this degraded Y-factor corresponds to $T_{sys} \approx 180$ K. The last two spectrums in September plots were calculated with $T_{sys} \approx 180$ K taking into account possible degradation in T_{sys}.

The system temperature was checked additionally by Moon noise measurements. The Moon is just a heated body in the sky and its radiation is thermal only. It is supposed that the lunar temperature at 6.7 GHz oscillates with the illumination phase weakly ($T_{moon} \approx 230$ K) and the temperature distribution across the disk is uniform. The estimation was done using a simplified formula,
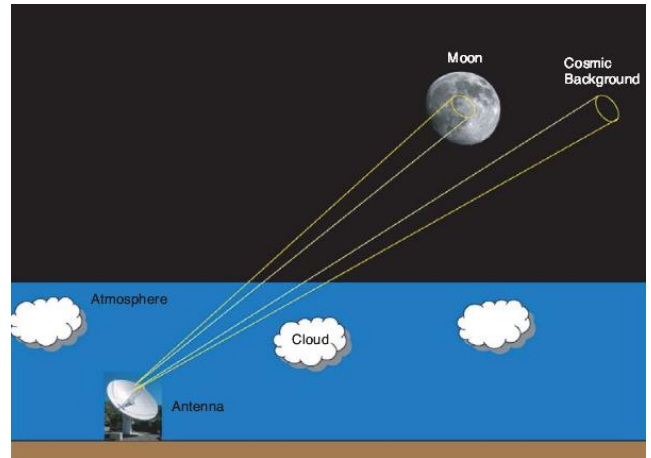
$$T_{sys} = \frac{T_{moon}\left(1 - 2^{-\delta_{moon}^2/\delta_{HPBW}^2}\right)\eta_B}{(Y_{moon} - 1)}.\qquad(2)$$

Here Y_{moon} – is the Moon Y-factor in linear power units measured in comparison to the cold sky (like in the picture right taken from [2]), δ_{moon} – angular size of the Moon ≈ 0.5 deg, δ_{HPBW} - antenna Half-Power Beam Size (1.75 deg for my dish 1.8 m), η_B - antenna Main Beam Efficiency, was taken 0.85 for my dish 1.8 m.

Formula (2) ignores the Cosmic Microwave Background (CMB) radiation, the atmospheric noise and attenuation of the signal along the atmospheric path; it supposes that the Moon temperature is distributed uniformly across the lunar disc and do not change during the lunation cycle. For more accurate formula in illumination phases near the Full Moon (where T_{moon} is the disc center temperature) see [3], eq. (22).

In formula (2) the factor $\left(1 - 2^{-\delta_{moon}^2/\delta_{HPBW}^2}\right)$ represents so called filling factor f_{BEAM} of the Moon in the antenna beam (see 8.2.3 chapter in [4]). This explicit form of the filling factor was derived for Gaussian shape beams [3, 5].

The Main Beam Efficiency η_B was estimated via known Aperture Efficiency η_A using their connection $\eta_A \approx 0.75\,\eta_B$ derived for Gaussian beams [3]. The aperture efficiency was interpreted as a product of taper η_t and spillover η_S efficiencies, $\eta_A \approx \eta_t\,\eta_S$. They are considered as main contributors defining an optimum in the Aperture Efficiency; other components like Ruse term, cross-polarization efficiency or ohmic losses were not taken into account [6], chap. 4. The $\eta_t\,\eta_S$ value was calculated from known far-field pattern of the feed in Comsol software (2D axisymmetric RF module) according to the formula

$$\eta_A \approx \eta_t \eta_S = 2 \cot^2 \frac{\theta_0}{2} \cdot \frac{\left(\int_0^{\theta_0} \sqrt{F(\theta)} \tan \frac{\theta}{2} d\theta \right)^2}{\int_0^\pi F(\theta) \sin \theta \, d\theta}, \tag{3}$$

where $F(\theta)$ corresponds to the axisymmetric far-field pattern of the feed in linear power units, θ_0 – is a half of aperture angle form the feed point. This formula was derived immediately for prime focus dishes and, as I suppose, gives adequate values η_A for offset dishes too.

Result of calculations η_A=0.64, η_B=0.85. The Moon Y-factor value obtained from measurements 0.4 dB. This value corresponds to $T_{sys} \approx 115$ K and appears noticeably lower than obtained from simple Y-factor measurements above.

The difference in results obtained by different methods could be interpreted as uncertainty in T_{sys} measurements; so, the levels in Jy of the maser spectrum lines may be probably lower than they appear on the plots.

Appendix. Setup data

Dish size D = 1.8 m.
Telescope characteristics:

Sensitivity (G, forward gain) – 0.6 mK/Jy;

System temperature (see about T_{sys} issues above in the text):

$T_{sys} \approx 150$ K (by Y-factor method and actual until September 2023);

$T_{sys} \approx 180$ K (by Y-factor method in September 2023);

$T_{sys} \approx 115$ K (estimated by lunar noise measurements in the end of September 2023).

Linear polarization.

Source automatic tracking during the integration time.

Outdoor downconverter:

Terrasat 6.4-7.1 GHz RX module (LO 5.7 GHz) + LNA (NF=1.2 dB, measured in September 2023).

Indoor IF receiver: USRP B200mini, receiver resolution – 5 kHz by noise bandwidth (<0.2 km/s in VLSR), total bandwidth – 1.5 MHz. The indoor IF receiver USRP B200mini is controlled using LabVIEW software with on-fly averaging of spectrum during the integration time (no intermediate data are stored), see more details about IF receiver and post-processing procedures in [7].

References
[1] H.S.P. Mueller et al, *Accurate rest frequencies of methanol maser and dark cloud lines*, arXiv:astro-ph/0408094 (2004)
[2] D. Morabito, M. Gatti, and H. Miyatake, *The Moon as a Calibration Load for the Breadboard Array*, Interplanetary Network (IPN) Progress Report 42-172, pp. 1-21, February 15, 2008, http://ipnpr.jpl.nasa.gov/progress_report/42-172/172G.pdf.
[3] D. Fedorov UA3AVR, *Solar Flux and Temperature at Millimetre Wavelengths*, DUBUS 3/2016, p. 41.
[4] T.L. Wilson, K. Rohlfs, S. Hüttemeister, *Tools of Radio Astronomy*, 6th ed, Springer, 2013.

[5] Joachim Köppen DF3GJ, *A Closer Look at Filling Factors*, DUBUS 4/2021, v 50, p 15.

[6] Jacob W.M. Baars, *The Paraboloidal Reflector Antenna in Radio Astronomy and Communication, Theory and Practice*, Springer, 2007.

[7] D. Fedorov UA3AVR, *Methanol maser lines 12 GHz observations*, Radio Astronomy, Journal of the Society of Amateur Radio Astronomers, September – October 2022, page 71.

About the author

Dimitry Fedorov was first licensed as radio amateur since 1982, as UA3AVR since 1983. In 1990 graduated as MS in electronics in Moscow Power Engineering University. Now works as research and development engineer in wireless industry, LTE/5G NR, RF and microwave modules development. Previous scientific experience in nuclear and particle physics, worked in Moscow State University, Institute of Nuclear Physics and Universität Tübingen, Institut für Theoretische Physik, see profile blog at https://www.researchgate.net/profile/Dimitry-Fedorov-2. Radio Astronomy hobby since 2012, mainly in applications for weak signals reception. You can contact the author at ua3avr@yandex.ru.

Journal Archives and Other Promotions

The rich and diverse legacy of member contributed content is available in the SARA Journal Archives. Table of contents for journals is available online at: SARA-Journal-Master-Index.xlsx (live.com)

The entire set of The Journal of The Society of Amateur Radio Astronomers is available by online download. It goes from the beginning of 1981 to the end of 2022 (over 6000 pages of SARA history!)

All SARA journals and conference proceedings are available through the previous calendar year.

SARA Store (radio-astronomy.org/store.)

SARA offers the above USB drives, DVDs, printed Proceedings and Proceedings on USB drive and other items at the SARA Store: http://www.radio-astronomy.org/e-store. Proceeds from sales go to support the student grant program. Members receive an additional 10% discount on orders over $50 US. Payments can be made by sending payment by PayPal to treas@radio-astronomy.org or by mailing a check or money order to SARA, c/o Brian O'Rourke, 337 Meadow Ridge Rd, Troy, VA 22974-3256

SARA Online Discussion Group
SARA members participate in the online forum at http://groups.google.com/group/sara-list. This is an invaluable resource for any amateur radio astronomer.

SARA Conferences
SARA organizes multiple conferences each year. Participants give talks, share ideas, attend seminars, and get hands-on experience. For more information, visit http://www.radio-astronomy.org/meetings.

What is Radio Astronomy?

Radio Astronomy is just what the name implies…. Astronomy observed at radio wavelengths instead of optical. But why do radio astronomy? Radio astronomy has expanded the knowledge of the universe about as much since its discovery in 1932 as optical has since humans first looked up at the sky. (The sky in the different frequencies or colors of radio are as different and varied as all of the flowers on Earth. Each frequency has its own information about what is happening in the universe.) This knowledge has been gained by both professional astronomers as well as amateurs with amateurs contributing to this day.

Do I need a big dish and expensive equipment?
No. Complete beginner projects are available at the SARA store at very reasonable prices. You can monitor the Sun's effects upon our planet with SuperSID. This information is gathered for Stanford for research into our ionosphere and radio signal propagation. Another project is the detection the hydrogen line just like Dr. Ewen had done in 1951 for a fraction of the cost using the Scope in a Box kit.

That said, radio astronomy is like optical astronomy in that you can spend as much as you want to. Many amateurs push the lower boundaries of cost by using very low-cost receivers and low-noise low-cost amplifiers that were not available even a few years ago. (See the Scope in a Box kit in the store for examples of both.)

Is everything 'plug and play' and boring?
The kits mentioned above are a starting point which are mostly plug-and-play… that gets you started. After you have mastered the basics, where you go from there depends upon your interests. Monitoring pulsars is done by amateurs. (One even noticed a pulsar glitch before the professionals!) These amateurs are pushing the boundaries of what can be done. Papers are being published and discussion had about pulsar detection as well detection of a MASER with a 50-inch dish. Techniques on new detection methods are posted in the SARA forum and elsewhere. You are free to build your own equipment to receive the signals as well as software to collect and analyze the data.

What is SETI?
SETI is the Search for Extra-Terrestrial Intelligence. Some amateurs scan the sky and search for signals that might be from aliens. To date no one has received a definitive alien signal (professional or amateur), but the search continues. The search has resulted not just in better receiving equipment but also wide and lively discussions about how aliens might communicate and how they might be trying to contact us. Some of these techniques have interesting ideas for our own communication techniques here on Earth!

What should I do to get started?
You should start with reading our Introduction to Radio Astronomy and joining our online SARA Forum. Look at the SARA store to get a project to get your feet wet without much expense and minimal risk. We will work with you so you can succeed.

Officers, directors, and additional SARA contacts

The Society of Amateur Radio Astronomers is an all-volunteer organization. The best way to reach people on this page is by email with SARA in the subject line SARA Officers.

President: Dr. Rich Russel, AC0UB, https://www.radio-astronomy.org/contact/President
Vice President: Jay Wilson, https://www.radio-astronomy.org/contact/Vicepresident
Secretary: Bruce Randall, NT4RT, https://www.radio-astronomy.org/contact/Secretary
Treasurer: Tom Jacobs, https://www.radio-astronomy.org/contact/Treasurer
Asst. Treasurer: Donna Hallin, https://www.radio-astronomy.org/contact/Treasurer
Past President: Dennis Farr
Founder Emeritus and Director: Jeffrey M. Lichtman, KI4GIY, jeff@radioastronomysupplies.com

Board of Directors

Name	Term expires	Email
Ed Harfmann	2024	edharfmann@comcast.net
Dr. Wolfgang Herrmann	2025	messbetrieb@astropeiler.de
Paul Butler	2025	paul.butler.melbourne@gmail.com
Charles Osborne	2025	k4cso@twc.com
Bob Stricklin	2024	bstrick@n5brg.com
Steve Tzikas	2024	Tzikas@alum.rpi.edu
Ted Cline	2025	TedClineGit@gmail.com
David Westman	2024	david.westman@engineeringretirees.org

Other SARA Contacts

All Officers	http://www.radio-astronomy.org/contact-sara	
All Directors and Officers	http://www.radio-astronomy.org/contact/All-Directors-and-Officers	
Eastern Conference Coordinator	http://www.radio-astronomy.org/contact/Annual-Meeting	
All Radio Astronomy Editors	http://www.radio-astronomy.org/contact/Newsletter-Editor	
Radio Astronomy Editor	Dr. Richard A. Russel	drrichrussel@radio-astronomy.org
Contributing Editor	Bogdan Vacaliuc	bvaculiuc@iee.org
Educational Co-Chairs	Ken Redcap, Tom Hagen: http://www.radio-astronomy.org/contact/Educational-Outreach	
Grant Committee	Tom Crowley	grants@radio-astronomy.org
Membership Chair	http://www.radio-astronomy.org/contact/Membership-Chair	
Technical Queries (David Westman)	http://www.radio-astronomy.org/contact/Technical-Queries	
Webmaster	Ciprian (Chip) Sufitchi, N2YO	webmaster@radio-astronomy.org

Great Projects to Get Started in Radio Astronomy

Radio Observing Program

The Astronomical League (AL) is starting a radio astronomy observing program. If you observe one category, you get a Bronze certificate. Silver pin is two categories with one being personally built. Gold pin level is at least four categories. (Silver and Gold level require AL membership which many clubs have membership. For the bronze level, you need not be a member of AL.)

Categories include
  1) SID
  2) Sun (aka IBT)
  3) Jupiter (aka Radio Jove)
  4) Meteor back-scatter
  5) Galactic radio sources

This program is a collaboration between NRAO and AL. Steve Boerner is the Lead Coordinator and a SARA member.

For more information:
Steve Boerner
2017 Lake Clay Drive
Chesterfield, MO 63017
Email: sboerner@charter.net
Phone: 636-537-2495
http://www.astroleague.org/programs/radio-astronomy-observing-program

Radio Jove

The Radio Jove Project monitors the storms of Jupiter, solar activity and the galactic background. The radio telescope can be purchased as a kit, or you can order it assembled. They have a terrific user group you can join.
http://radiojove.gsfc.nasa.gov/

INSPIRE Program

The INSPIRE program uses build-it-yourself radio telescope kits to measure and record VLF emissions such as tweeks, whistlers, sferics, and chorus along with man-made emissions. This is a very portable unit that can be easily transported to remote sites for observations.
 http://theinspireproject.org/default.asp?contentID=27

SARA/Stanford SuperSID

Stanford Solar Center and the Society of Amateur Radio Astronomers have teamed up to produce and distribute the SuperSID (Sudden Ionospheric Disturbance) monitor. The monitor utilizes a simple pre-amp to magnify the VLF radio signals which are then fed into a high-definition sound card. This design allows the user to monitor and record multiple frequencies simultaneously. The unit uses a compact 1-meter loop antenna that can be used indoors or outside. This is an ideal project for the radio astronomer that has limited space. To request a unit, send an e-mail to supersid@radio-astronomy.org

Radio Astronomy Online Resources

SARA YouTube Videos: https://www.youtube.com/channel/UC-SzptAQZ-20c9CkRb9ZPxw/videos	Pisgah Astronomical Research Institute: www.pari.edu
AJ4CO Observatory – Radio Astronomy Website: http://www.aj4co.org/	A New Radio Telescope for Mexico - ORION 2021 01 20. Dr. Stan Kurtz https://www.youtube.com/watch?v=Q9aBWr1aBVc
Radio Astronomy calculators https://www.aj4co.org/Calculators/Calculators.html	National Radio Astronomy Observatory http://www.nrao.edu
Introduction to Amateur Radio Astronomy (presentation) http://www.aj4co.org/Publications/Intro%20to%20Amateur%20Radio%20Astronomy,%20Typinski%20(AAC,%202016)%20v2.pdf	NRAO Essential Radio Astronomy Course http://www.cv.nrao.edu/course/astr534/ERA.shtml
RF Associates Richard Flagg, rf@hawaii.rr.com 1721-1 Young Street, Honolulu, HI 96826	Exotic Ions and Molecules in Interstellar Space -- ORION 2020 10 21. Dr. Bob Compton https://www.youtube.com/watch?v=r6cKhp23SUo&t=5s
RFSpace, Inc. http://www.rfspace.com	The Radio JOVE Project & NASA Citizen Science – ORION 2020.6.17. Dr. Chuck Higgins https://www.youtube.com/watch?v=s6eWAxJywp8&t=5s
CALLISTO Receiver & e-CALLISTO http://www.reeve.com/Solar/e-CALLISTO/e-callisto.htm	UK Radio Astronomy Association http://www.ukraa.com/
Deep Space Exploration Society http://DSES.science	CALLISTO software and data archive: www.e-callisto.org
Deep Space Object Astrophotography Part 1 -- ORION 2021 02 17. George Sradnov https://www.youtube.com/watch?v=Pm_Rs17KIyQ	Radio Jove Spectrograph Users Group http://www.radiojove.org/SUG/
European Radio Astronomy Club http://www.eracnet.org	Radio Sky Publishing http://radiosky.com
British Astronomical Association – Radio Astronomy Group http://www.britastro.org/baa/	The Arecibo Radio Telescope; It's History, Collapse, and Future - ORION 2020.12.16. Dr. Stan Kurtz, Dr. David Fields https://www.youtube.com/watch?v=rBZlPOLNX9E
Forum and Discussion Group http://groups.google.com/group/sara-list	Shirleys Bay Radio Astronomy Consortium marcus@propulsionpolymers.com
GNU Radio https://www.gnuradio.org/	SARA Twitter feed https://twitter.com/RadioAstronomy1
SETI League http://www.setileague.org	SARA Web Site http://radio-astronomy.org
NRAO Essential Radio Astronomy Course http://www.cv.nrao.edu/course/astr534/ERA.shtml	Simple Aurora Monitor: Magnetometer http://www.reeve.com/SAMDescription.htm
NASA Radio JOVE Project http://radiojove.gsfc.nasa.gov Archive: http://radiojove.org/archive.html https://groups.io/g/radio-jove	Stanford Solar Center http://solar-center.stanford.edu/SID/
National Radio Astronomy Observatory http://www.nrao.edu	

At the SARA online store: radio-astronomy.org/store.

SARA Polo Shirts

New SARA shirts have arrived.

We now have a good selection of X, XX, and XXX shirts available in all colors including white!

Shirts are $20 at the conference and $25 shipped.

Contact the treasurer at treas@radio-astronomy.org for availability and shipping.

Scope in a Box

radio-astronomy.org/store.

Kit of parts and software to build a working Radio Telescope to detect Hydrogen Line emissions. Available to USA addresses only at this time.

SuperSID Complete Kit
radio-astronomy.org/store.

SARA Publication, Journals and Conference Proceedings (various prices)
radio-astronomy.org/store.

SARA Journal Online Download
radio-astronomy.org/store.

The USB drive covers the society journal "Radio Astronomy" from the founding of the organization in 1981 thru 2020. Articles cover a wide range of topics including: cosmic radiation, pulsars, quasars, meteor detection, solar observing, Jupiter, Radio Jove, gamma ray bursts, the Itty Bitty Telescope (IBT), dark matter, black holes, the Jansky antenna, methanol masers, mapping at 408 MHz and more. This CD contains all of the above and more with over 4800 pages of articles on radio astronomy. Also included is a copy of Grote Reber's handwritten, 34-page document "Carriage and Mirror Detail" of his historic antenna now on display at the National Radio Astronomy Observatory (NRAO) in Greenbank, WV. You also get an electronic copy of the 109 page "Basics of Radio Astronomy" from JPL Goldstone-Apple Valley Radio Telescope. Also included is the NRAO 40-foot radio telescope "Operators Manual", which by the way, you get to operate if you attend the Eastern SARA conference in July.

SARA Advertisements

There is no charge to place an ad in Radio Astronomy; but you must be a current SARA member. Ads must be pertinent to radio astronomy and are subject to the editor's approval and alteration for brevity. Please send your "For Sale," "Trade," or "Wanted" ads to edit@radio-astronomy.org. Please include email and/or telephone contact information. Please keep your ad text to a reasonable length. Ads run for one bimonthly issue unless you request otherwise.

Radio-Astro-Machine, zzblac@gmail.com
Elevation rotation adapter plate for Scope in a Box and custom machining. For further information visit https://radio-astro-machine.wixsite.com/my-site or send an email.

Typinski Radio Astronomy, Inc., info@typinski.com
Antenna systems and feed line components for HF radio astronomy

Jeff Kruth, WA3ZKR, kmec@aol.com
RF components from HF to MMW, various types including mixers, RF switches, amplifiers, oscillators, coaxial components, waveguide components, etc. I have a very large collection of stuff and the facilities to test and provide data. Please email with your needs and I will see if I have something for you. Have fun!

Stuart and Lorraine Rumley, sales@valontechnology.com
The Valon Technology 2100 Downconverter, when combined with our 5009 frequency synthesizer module, provides a high-performance, compact receiver downconverter system. Applications include hydrogen line studies at 1420MHz and radio astronomy in the protected 30MHz segment of the 21 cm band. For more information visit http://www.valontechnology.com/2100downconverter.html or send an email.

Radio2Space, filippo.bradaschia@primalucelab.com
SPIDER radio telescopes and turn-key-systems designed specifically for education.
https://www.radio2space.com
We developed our SPIDER radio telescopes as turn-key-system just to avoid the problem you perfectly highlighted in your website: "Purchasing a radio telescope isn't like buying an optical telescope. They are harder to find, and usually require assembly and software troubleshooting. In some cases, a radio telescope must be built from components." Our SPIDER radio telescopes are not designed for amateurs that prefer to build a radio telescope but to schools, universities, museums, and other science institutes that needs for a complete and ready-to-use system, just like the optical telescopes they can normally buy!

SARA Brochure

Society of Amateur Radio Astronomers, Inc.

Founded 1981

Membership supported, nonprofit [501(c) (3)] Educational and Radio Astronomy Organization

Knowledge through Common Research, Education and Mentoring

Membership Information

Annual SARA dues Individual $20, Classroom $20, Student $5 (US funds) anywhere in the world. Membership includes a subscription to Radio Astronomy, the bimonthly Journal of The Society of Amateur Radio Astronomers, delivered electronically (via a secure web link, emailed to you as each new issue is posted). We regret that printing and postage costs prevent SARA from providing hardcopy subscriptions to our Journal.

We would appreciate the following information included with your check or money order, made payable to SARA:

Name: _____

Email Address : _____
(required for electronic Journal delivery)

Ham call sign: _____ (if applicable)

Address: _____

City: _____

State: _____

Zip: _____

Country: _____

Phone: _____

Please include a note of your interests. Send your application for membership, along with your remittance, to our Treasurer.
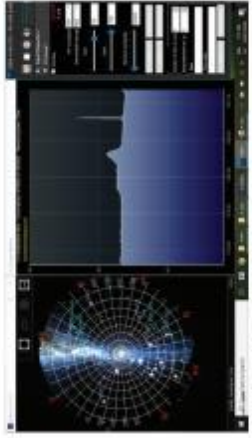
For further information, see our website at:
http://radio-astronomy.org/membership

How to get started?

SARA has a made a kit of software and parts to detect the Hydrogen line signal from space. This is an excellent method to get started in radio astronomy. It teaches the principles of antenna design, signal detection, and signal processing. Read more about this and other projects on our web site.

Why Radio Astronomy?

Because about sixty five percent of our current knowledge of the universe has stemmed from radio astronomy alone. The discovery of quasars, pulsars, black holes, the 3K background from the "Big Bang" and the discovery of biochemical hydrogen/carbon molecules are all the result of professional radio astronomy.

http://radio-astronomy.org

SARA members have been privileged to use this forty foot diameter drift-scan hydrogen line radio telescope every year at their annual meeting in Green Bank.

The Society of Amateur Radio Astronomers

SARA was founded in 1981, with the purpose of educating those interested in pursuing amateur radio astronomy.

The society is open to all, wishing to participate with others, worldwide.

SARA members have many interests, some are as follows:

SARA Areas of Study and Research:

- Solar Radio Astronomy
- Galactic Radio Astronomy
- Meteor Detection
- Jupiter
- SETI
- Gamma Ray/High Energy Pulse
- Detection
- Antennas
- Design of Hardware / Software

The members of the society offer a friendly mentor atmosphere. All questions and inquiries are answered in a constructive manner. No question is silly!

SARA offers its members an electronic bi-monthly journal entitled Radio Astronomy. Within the journal, members report on their research and observations. In addition, members receive updates on the professional radio astronomy community and, society news.

Once a year SARA meets for a three-day conference at the Green Bank Observatory in Green Bank West Va.

There is also a spring conference held at various cities in the Western USA. Previous meeting have been at the VLA in Socorro, NM and at Stanford University.

How do I get started?

Just as a long journey begins with the first step, the project you elect must start with a clear idea of your objectives. Do you wish to study the sun? Jupiter? Make meteor counts? Do you wish to engage in imaging radio astronomy? What you decide will not only determine the type of equipment you will need, but also the local radio spectrum.

How do amateurs do radio astronomy?

Radio astronomy by amateurs is conducted using antennas of various shapes and sizes, from smaller parabolic dishes to simple wire antennas. These antennas are connected to receivers and most of these receivers are software defined radios these days. Data from the receivers are collected by computers, and the received signals will be displayed as charts, graphs or maybe even sky maps. As diverse as the observed objects, so is are the instruments and tools used. SARA members will always be supportive to find good solutions for what one wishes to observe.

Is amateur radio astronomy instrumentation expensive?

Technical information freely circulated in our monthly journal helps amateurs to obtain good low noise equipment from off the shelf assemblies, or to build their own units. The actual cash investment in radio astronomy equipment need not exceed that of any other hobby.

What are amateurs actually looking for in the received data?

The aim of the radio amateur is to find something new and unusual. Just as an amateur optical observer hopes to notice a supernova or a new comet, so does an amateur radio observer hope to notice a new radio source, or one whose radiation has changed appreciably.

The Reber Telescope at NRAO. Constructed by Grote Reber in 1937 in his back yard in Wheaton, Illinois

SARA Members discussing the IBT
(Itty Bitty Telescope)